Springer Theses
Recognizing Outstanding Ph.D. Research

Yan Wang

First-stage LISA Data Processing and Gravitational Wave Data Analysis

Ultraprecise Inter-satellite Laser Ranging, Clock Synchronization and Novel Gravitational Wave Data Analysis Algorithms

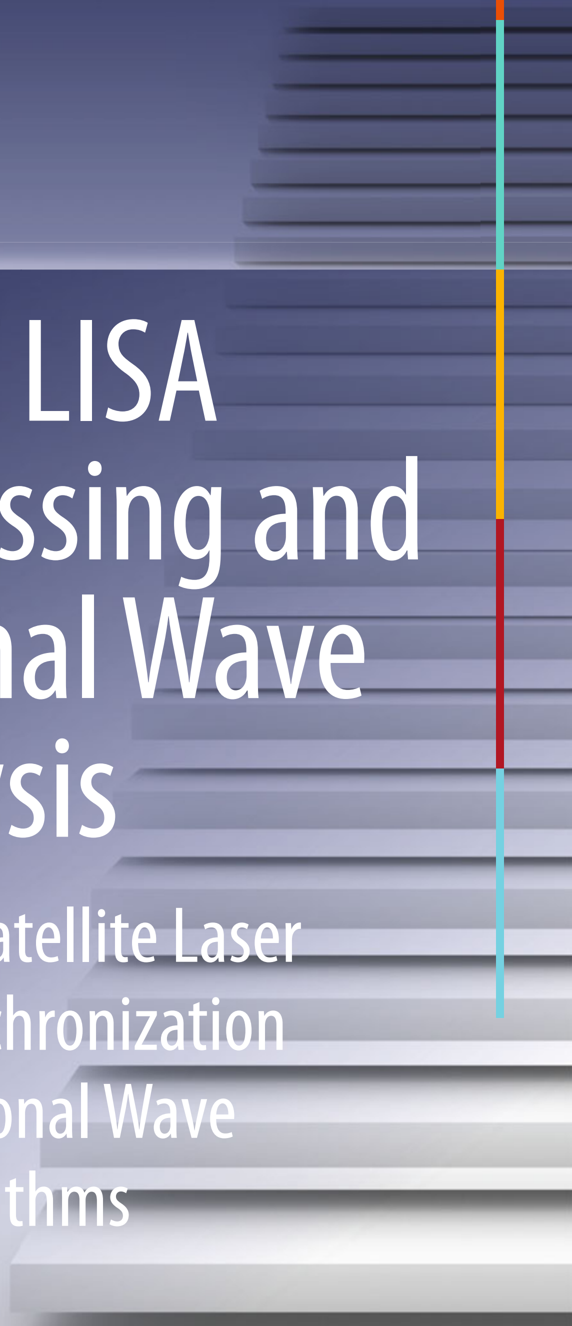

Springer

Springer Theses

Recognizing Outstanding Ph.D. Research

Aims and Scope

The series "Springer Theses" brings together a selection of the very best Ph.D. theses from around the world and across the physical sciences. Nominated and endorsed by two recognized specialists, each published volume has been selected for its scientific excellence and the high impact of its contents for the pertinent field of research. For greater accessibility to non-specialists, the published versions include an extended introduction, as well as a foreword by the student's supervisor explaining the special relevance of the work for the field. As a whole, the series will provide a valuable resource both for newcomers to the research fields described, and for other scientists seeking detailed background information on special questions. Finally, it provides an accredited documentation of the valuable contributions made by today's younger generation of scientists.

Theses are accepted into the series by invited nomination only and must fulfill all of the following criteria

- They must be written in good English.
- The topic should fall within the confines of Chemistry, Physics, Earth Sciences, Engineering and related interdisciplinary fields such as Materials, Nanoscience, Chemical Engineering, Complex Systems and Biophysics.
- The work reported in the thesis must represent a significant scientific advance.
- If the thesis includes previously published material, permission to reproduce this must be gained from the respective copyright holder.
- They must have been examined and passed during the 12 months prior to nomination.
- Each thesis should include a foreword by the supervisor outlining the significance of its content.
- The theses should have a clearly defined structure including an introduction accessible to scientists not expert in that particular field.

More information about this series at http://www.springer.com/series/8790

Yan Wang

First-stage LISA Data Processing and Gravitational Wave Data Analysis

Ultraprecise Inter-satellite Laser Ranging, Clock Synchronization and Novel Gravitational Wave Data Analysis Algorithms

Doctoral Thesis accepted by
Max Planck Institute for Gravitational Physics, Germany

Springer

Author
Dr. Yan Wang
School of Physics
The University of Western Australia
Perth
Australia

Supervisor
Prof. Karsten Danzmann
Institut für Gravitationsphysik der Leibniz Universität
Hannover
Germany

ISSN 2190-5053 ISSN 2190-5061 (electronic)
Springer Theses
ISBN 978-3-319-26388-5 ISBN 978-3-319-26389-2 (eBook)
DOI 10.1007/978-3-319-26389-2

Library of Congress Control Number: 2015957100

Printed on acid-free paper

This Springer imprint is published by SpringerNature
The registered company is Springer International Publishing AG Switzerland

Supervisor's Foreword

With the advent of the expected first detection of gravitational waves in the near future, a completely new window will be opened up to the Universe. By then, gravitational waves, as a new powerful tool, will lead to the prosperity of gravitational wave astronomy. The proposed space-borne detector (e)LISA, whose pathfinder is to be launched later in 2015, aims at detection of gravitational waves at mHz band, which comprise the richest fascinating sources of gravitational waves: galactic white dwarf binaries, super-massive black hole binaries, extreme mass ratio inspirals (a stellar mass compact object orbiting a massive black hole), and stochastic background radiation from the early Universe. Detection and precise parameter estimation of such sources will improve our understanding of the Universe to an unprecedented level.

The major part of this monograph makes the first ever step to bridge the missing link between the 0-level satellite raw data and the pre-processed data that can be used to extract astrophysical information. It paves the way to establishing an entire first-stage data analysis of (e)LISA, which monitors the data quality, deals with various emergent issues, and prepares the 0-level data for subsequent astrophysical data analysis. Specifically, the framework and the algorithms designed in this monograph successfully improved the inter-satellite ranging accuracy and reduced the time errors of the clocks in the three satellites of (e)LISA, which is crucial to the success of the detector.

Since gravitational wave signals are usually very weak, buried deeply in the detector noise, it is challenging and computationally expensive to extract the signal from the measured data. The second part of the monograph focuses on novel space-borne gravitational wave detector design and methods of efficient detection and parameter estimation in the astrophysical data analysis stage. These innovative novel algorithms are completely new in gravitational wave data analysis. They try to tackle the difficult problem from a new angle and should be followed by further investigation in the future.

November 2015

Prof. Karsten Danzmann
Director at the Max Planck Institute
for Gravitational Physics
Albert Einstein Institute
Hannover, Germany

Preface

In brief, the first half of this book is about first-stage data analysis—the analysis of 0-level data, of the space-based gravitational wave detector (e)LISA, with the help of various types of Kalman filters and other algorithms, and to achieve ultra-precise inter-satellite ranging and clock synchronization for (e)LISA. The second half is about the design of a novel space-based gravitational wave detector and a few novel gravitational wave data analysis algorithms.

Gravitational waves are propagating space-time ripples on the static space-time background. Laser Interferometer Space Antenna (LISA) is a space-based GW detector concept, which consists of three spacecraft forming an equilateral triangle orbiting the Sun trailing the Earth. The proper distances between the spacecraft are modulated by gravitational waves, which will be measured by (e)LISA through heterodyne interferometers. Thus, the gravitational wave signals are encoded in the phase evolution of the lasers. The phasemeter raw data of (e)LISA are not directly usable for time-delay interferometry techniques and astrophysical data analysis, since clock jitter contaminates the ranging measurements and introduces noise into the time stamps of the measurements. This has been a long-lasting gap and needs to be solved in the first-stage data analysis of (e)LISA.

Chapters 2–9 focus on the development of 0-level data analysis algorithms for (e)LISA, which calibrate and synchronize the phasemeter raw data, estimate the inter-spacecraft distances and the clock errors, and hence make the raw measurements usable for time-delay interferometry techniques and astrophysical data analysis algorithms. An introduction to an entire LISA data processing chain is presented in Chap. 2, followed by an exemplary application of the basic Kalman filter on a single laser link of LISA in Chap. 3. In Chaps. 4 and 5, the inter-satellite measurements are precisely modelled and a hybrid-extended Kalman filter is applied to the (e)LISA problem. In Chaps. 6 and 8, different state vectors and their corresponding dynamic equations are designed and investigated, which has been found to be crucial to the efficiency and success of the first-stage data analysis. Emergent cases with different combination of broken laser links are studied in Chap. 7 via a sequential Kalman filter, while the posterior measurements are used to improve the estimates via an RTS filter. In Chap. 9, the effect of the clock errors on both the measurements and recording time stamps is studied. A combination of different algorithms is designed and investigated, in order to make the Kalman filter variant work for measurements sampled at different time, with erroneous time stamps contaminated by different timing errors of the three different clocks. The relative ranging accuracy achieved is around 10^{-11} in the end.

In the second part, several aspects of gravitational wave detection and data analysis, in general not restricted to (e)LISA, are studied. For the first time, an octahedral displacement-noise-free space-based GW detector is proposed and studied in Chap. 10. A phenomenological waveform is proposed for the most challenging type of sources for (e)LISA—extreme-mass-ratio inspirals in Chap. 11. A data analysis pipeline, including particle swarm optimization, Markov chain Monte Carlo, genetic algorithm, and clustering algorithms is designed to search for the extreme-mass-ratio inspiral signals. As an innovation, the detection and the parameter estimation are in two separatestages. In Chap. 12, a novel method based on compressed sensing is designed, which can quickly detect gravitational wave signals with moderate to high signal-to-noise ratios and estimate the parameters automatically. In the final chapter, the likelihood transform is defined, which gradually modifies and traces the geometry of the likelihood surface, and hence makes the search for weak signals in noisy data, such as gravitational wave signals, easier.

Contents

List of Figures

List of Tables

Notation

Einstein summation convention: Repeated lower and upper indices are summed over. Unless otherwise specified, we assume this convention throughout the thesis.

ds	Space-time interval or proper distance
c	Speed of light
$g_{\mu\nu}$	Space metric, defined as $ds^2 = g_{\mu\nu}dx^{\mu}dx^{\nu}$
$\eta_{\mu\nu}$	Minkowski metric or flat space metric $(-, +, +, +)$
G	Newton constant $G = 6.6738 \times 10^{-11}\,\mathrm{m}^3\mathrm{kg}^{-1}\mathrm{s}^{-2}$
$R^{\lambda}_{\mu\nu\sigma}$	Riemann tensor
$R_{\mu\nu}$	Ricci tensor $R_{\mu\nu} = R^{\lambda}_{\mu\lambda\nu}$. The Ricci scalar is $R = g^{\mu\nu}R_{\mu\nu}$
$T_{\mu\nu}$	The energy-momentum tensor
$h_{\mu\nu}$	Metric perturbation or gravitational wave, defined as $g_{\mu\nu} = \eta_{\mu\nu} + h_{\mu\nu}$. Usually, $\lvert h_{\mu\nu}\rvert \ll 1$
$\Box$	The flat space d'Alembertian, defined as $\Box = \eta_{\mu\nu}\partial_{\mu}\partial_{\nu}$

Abbreviations

ADC	Analog-to-digital converter
AU	Astronomical unit $1\,\mathrm{AU} = 1.496 \times 10^{11}\,\mathrm{m}$
BBO	Big Bang Observer
BH	Black hole
CBC	Compact binaries coalescence
CW	Continuous wave
DAC	Digital-to-analog Converter
DFACS	Drag-free and attitude control system
DFI	Displacement-noise free interferometry
DSN	Deep Space Network

DWS	Differential wavefront sensing
EMRI	Extreme-mass-ratio inspiral
EOM	Electro-optic modulator
FEEP	Field emission electric propulsion
FPGA	Field programmable gate array
GA	Genetic algorithm
GPS	Global positioning system
GW	Gravitational wave
IMRI	Intermediate-mass-ratio inspiral
LISA	Laser Interferometer Space Antenna
LSB	Lower sideband
MBH	Massive black hole
MCMC	Markov chain Monte Carlo
MLDC	Mock LISA data challenge
NGO	New Gravitational Observatory
NS	Neutron star
OGO	Octahedral Gravitational Observatory
PN	Post Newtonian
PSD	Power spectral density
PSO	Particle Swarm Optimization
PRN	Pseudo-random noise
S/C	Spacecraft
SA	Simulated Annealing
SNR	Signal-to-noise ratio
SSB	Solar system barycenter
TDI	Time-delay interferometry
TM	Test mass
USB	Upper sideband
USO	Ultra stable oscillator
UTC	Coordinated universal time
WDB	White dwarf binary
WSS	Wide-sense stationary

Chapter 1
Introduction

Abstract This first chapter begins with a brief introduction to gravitational waves, and their basic formulas in linearized general relativity, followed by a short review of various types of gravitational wave sources and current gravitational wave detectors. In the rest part, the basics of gravitational wave data analysis is described in a pedagogical way.

1.1 Gravitational Wave Physics

Albert Einstein's general theory of relativity was published in 1916. It predicts the existence of gravitational waves (GWs). Analogous to electromagnetic waves, which are time-varying electromagnetic fields, GWs are nothing but varying gravitational fields. Phenomenologically, a GW can be viewed as a space-time ripple propagating on the static space-time background as a wave, see Fig. 1.1.

The existence of GW was predicted almost a century ago, and the mathematical description as well as the foundations were being refined for many more years [1, 2]. Due to the extreme mathematical complexity, especially the nonlinearity, of general relativity, we still do not even have a full solution of a two-body system today. In many cases, it seems impossible to find the exact solution. Instead, people constructed many approximate solutions and are continuously trying to extend and improve them.

Peters and Mathews derived the gravitational radiation from a nonrelativistic binary system of two point masses in 1963 [3], where they assumed Keplerian orbits and computed the GW with the so-called quadrupole formula. Mark Zimmermann and Eugene Szedenits, Jr. first computed the gravitational radiation from rotating and processing bodies with a simplified model in 1979 [4].

The post-Newtonian treatment of the source leads to more accurate results. Nonrelativistic sources are characterized by $v/c \ll 1$, which is a small quantity. Thus, one can in principle expand the Einstein equations in orders of v/c and solve them order by order. Although the post-Newtonian approximation was already introduced by Einstein himself almost a century ago, there were still many practical difficulties when applying it to gravitational radiation. Early works on this aspect were done after the 1970s [5–7]. Many techniques have been invented to compute additional

Y. Wang, *First-stage LISA Data Processing and Gravitational Wave Data Analysis*,
Springer Theses, DOI 10.1007/978-3-319-26389-2_1

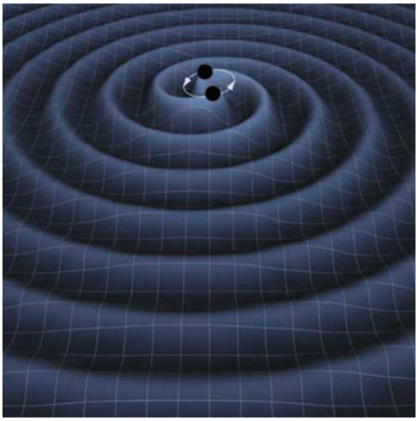

Fig. 1.1 Illustration of gravitational waves from a binary as a space-time ripple propagating on the static space-time background. (Image: T. Carnahan)

terms and extend the results to higher post-Newtonian order, such as the DIRE (direct integration of the relaxed Einstein equation) method [8–12], the Blanchet–Damour approach [13–18], the ADM-Hamiltonian formalism [19–21], etc. Post-Newtonian waveforms have been calculated to the third post-Newtonian order in the conserved energy [22–27] and 3.5 post-newtonian order in the energy flux [25, 28–30]. Since there are still other free choices, the same post-Newtonian order can lead to different phase evolutions in gravitational waveforms. T. Damour et al. [31] and A. Buonanno et al. [32, 33] have compared different waveforms for data analysis consideration.

As one goes to higher and higher post-Newtonian order, post-Newtonian waveforms are more and more accurate in the non-relativistic case (or even in mildly relativistic cases). But in the strongly relativistic case, when the typical velocity is approaching a significant fraction of the speed of light, the post-Newtonian approximation fails. The effective-one-body approach [34–37] has been developed to effectively solve for the behaviour near the last stable orbit, bridging the adiabatic [38] inspiral and the plunge.

In the extreme-mass-ratio inspiral (so-called EMRI) case with mass ratios of about 1:100,000–1:1000,000, one can also expand the Einstein equation in term of the small mass ratio. This approach is valid even when the velocity of the small compact body is a large fraction of the speed of light. But there are other issues to be solved in this approach. We will come to EMRIs in detail later.

One can also try to solve the Einstein equations numerically, which leads to an important branch of general relativity—numerical relativity [39–42]. Although numerical relativity can in principle solve a relativistic system accurately and provide precise gravitational waveforms, it is computationally very expensive, hence often requiring supercomputers. The first stable, relatively long-term evolution and merger of a binary black hole system was obtained in 2005 by Frans Pretorius [39]. Up to now, numerical relativity waveforms are still too expensive for data analysis use.

The very short review of gravitational waveform calculation above is by no means exhaustive. There are still many aspects left in this field, which I did not have a chance to mention in this introduction. Instead, I will describe the very basic formulae in the next section.

1.2 Gravitational Waves in Linearized General Relativity

The famous Einstein equations read as follows

$$R_{\mu\nu} - \frac{1}{2}g_{\mu\nu}R = \frac{8\pi G}{c^4}T_{\mu\nu}, \tag{1.1}$$

where the cosmological constant has been set to zero for what is to follow. It basically says that matter ($T_{\mu\nu}$) tells the spacetime how to curve and the spacetime ($R_{\mu\nu}$, $g_{\mu\nu}$) curvature tells the matter how to move. In linearized theory, Eq. (1.1) can be cast into the following form

$$\Box\bar{h}_{\mu\nu} = -\frac{16\pi G}{c^4}T_{\mu\nu}, \tag{1.2}$$

where $\bar{h}_{\mu\nu} = h_{\mu\nu} - \frac{1}{2}\eta_{\mu\nu}h$, and we have assumed the harmonic gauge (sometimes also called the Lorentz gauge)

$$\partial^{\nu}\bar{h}_{\mu\nu} = 0. \tag{1.3}$$

Notice that the linearization takes place around the Minkowski space and the indices are raised and lowered by using the Minkowski metric. Equation 1.2 can be solved with the help of the so-called *retarded Green's function* [43], and the solution is

$$\bar{h}_{\mu\nu}(t, \vec{x}) = \frac{4G}{c^4}\int \mathrm{d}x'^3 \frac{1}{|\vec{x} - \vec{x}'|}T_{\mu\nu}\left(t - \frac{|\vec{x} - \vec{x}'|}{c}, \vec{x}'\right). \tag{1.4}$$

In GW physics, it is convenient to work in the transverse-traceless gauge (TT gauge),

$$h^{0\mu} = 0, \tag{1.5}$$

$$h^{\mu}{}_{\mu} = 0, \tag{1.6}$$

$$\partial^{j}h_{ij} = 0. \tag{1.7}$$

These conditions reduces the 10 degrees of freedom of $h_{\mu\nu}$ to 2 degrees of freedom, namely $h_+, h_\times$, which are usually referred to as the 'plus'-polarization and the 'cross'-polarization. In the transverse plane, the GW in the TT gauge takes the following form

$$h^{TT}_{ab} = \begin{pmatrix} h_+ & h_\times \\ h_\times & -h_+ \end{pmatrix} \tag{1.8}$$

For a certain propagation direction $\vec{n}$, we can define a projector

$$P_{ij} = \delta_{ij} - n_i n_j, \tag{1.9}$$

where δ_{ij} is the Kronecker delta function. With the help of this projector P_{ij}, GWs in TT gauge can be easily expressed as

$$h_{ij}^{TT} = \left(P_{ik}P_{jl} - \frac{1}{2}P_{ij}P_{kl}\right)h_{kl}, \tag{1.10}$$

$$= \left(P_{ik}P_{jl} - \frac{1}{2}P_{ij}P_{kl}\right)\bar{h}_{kl}. \tag{1.11}$$

Therefore, we have the solution of the linearized Einstein equation in the TT gauge

$$h_{ij}^{TT}(t, \vec{x}) = \frac{4G}{c^4}\left(P_{ik}P_{jl} - \frac{1}{2}P_{ij}P_{kl}\right)\int \mathrm{d}x'^3 \frac{1}{|\vec{x} - \vec{x}'|}T_{kl}\left(t - \frac{|\vec{x} - \vec{x}'|}{c}, \vec{x}'\right). \tag{1.12}$$

Usually, one can make use of the following condition: the distance between the detector and the gravity source is much longer than the scale of the gravity source, i.e. $|\vec{x} - \vec{x}'| \gg |\vec{x}'|$. This would allow us to replace the distance $|\vec{x} - \vec{x}'|$ by a single averaged distance r and to make a Taylor expansion to the leading order of $|\vec{x}'|/r$. For non-relativistic sources, the typical velocity inside the gravity system is much smaller the speed of light. Basically, this tells us that the wavelength of the GW is much longer than the size of the gravity source. Hence, we do not need to know the finer structure of the gravity source. In this approximation, it gives rise to the famous quadrupole formula [3]

$$h_{ij}^{TT}(t, \vec{x}) = \frac{1}{r}\frac{2G}{c^4}\left(P_{ik}P_{jl} - \frac{1}{2}P_{ij}P_{kl}\right)\ddot{Q}_{kl}(t - r/c), \tag{1.13}$$

$$\equiv \frac{1}{r}\frac{2G}{c^4}\ddot{Q}_{ij}^{TT}(t - r/c), \tag{1.14}$$

where the traceless quadrupole moment Q_{ij} is defined as

$$Q^{ij} = \frac{1}{c^2}\int \mathrm{d}x^3 T^{00}(t, \vec{x})\left(x^i x^j - \frac{1}{3}r^2\delta^{ij}\right). \tag{1.15}$$

It is instructive to make an order of magnitude estimation

$$h \sim \frac{1}{r}\frac{2G}{c^4}Mv^2 \sim 2\left(\frac{GM}{c^2 r}\right)\left(\frac{GM}{c^2 R}\right), \tag{1.16}$$

which is roughly the product of the dimensionless internal gravitational potential and the dimensionless external gravitational potential. The external potential mainly depends on the distance from the gravity source. The internal potential depends on how compact the gravity source is. So compact gravity sources tend to be easier to detect by a GW detector.

For a compact binary in fixed circular orbit, the GW form in Newtonian approximation reads [43]

$$h_+(t) = \frac{4}{r}\left(\frac{GM_c}{c^2}\right)^{5/3}\left(\frac{\pi f}{c}\right)^{2/3}\frac{1+\cos^2\iota}{2}\cos(2\pi f t + \Phi_0), \tag{1.17}$$

$$h_\times(t) = \frac{4}{r}\left(\frac{GM_c}{c^2}\right)^{5/3}\left(\frac{\pi f}{c}\right)^{2/3}\cos\iota\sin(2\pi f t + \Phi_0), \tag{1.18}$$

where

$$M_c = \frac{(m_1 m_2)^{3/5}}{(m_1+m_2)^{1/5}} \tag{1.19}$$

is the so-called *chirp mass*, and ι is the inclination angle. The GW frequency f is twice the orbital frequency. In practice, the orbit is shrinking due to the energy loss caused by the emission of GWs. As a result, there will be a frequency drift

$$\dot{f} = \frac{96}{5}\pi^{8/3}\left(\frac{GM_c}{c^3}\right)^{5/3} f^{11/3}. \tag{1.20}$$

It depends only on f and M_c. That is why M_c is named *chirp mass*. From Eqs. (1.17) and (1.18), we find that $\frac{4}{r}\left(\frac{GM_c}{c^2}\right)^{5/3}$ serves as a common amplitude in the two polarizations. This implies that one cannot distinguish between the distance r and the *chirp mass* M_c. Luckily, there is always a frequency chirp in the GW signal. After determining this chirp, Eq. (1.20) helps to break the degeneracy between the distance and the *chirp mass*.

1.3 Gravitational Wave Astronomy and Sources

GW astronomy aims at collecting information about astrophysical sources using GWs. The significance of GW astronomy is undoubted. In fact, the GW spectrum provides very distinct and complementary astrophysical information compared to electromagnetic waves (γ-ray, X-ray, optical, infrared, radio, etc.). See the GW spectrum in Fig. 1.2. Sathyaprakash and Schutz gave a nice explanation as follows,

> The primary emitters of electromagnetic radiation are charged elementary particles, mainly electrons; because of overall charge neutrality, electromagnetic radiation is typically emitted in small regions, with short wavelengths, and conveys direct information about the physical conditions of small portions of the astronomical sources. By contrast, GWs are emitted by

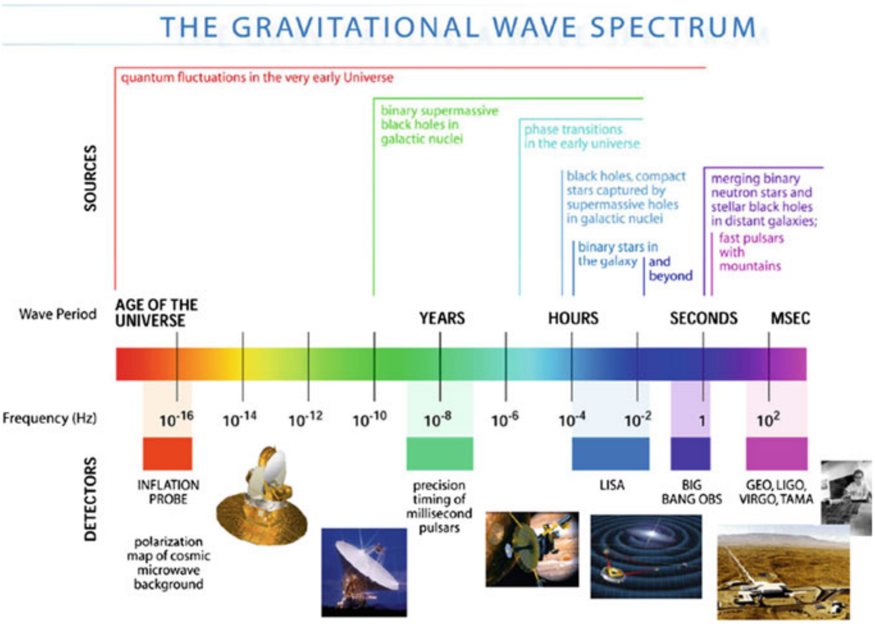

Fig. 1.2 The GW spectrum from extremely low frequency to high frequency. (Image: Chris Henze)

> the cumulative mass and momentum of entire systems, so they have long wavelengths and convey direct information about large-scale regions. Electromagnetic waves couple strongly to charges and so are easy to detect but are also easily scattered or absorbed by material between us and the source; GWs couple extremely weakly to matter, making them very hard to detect but also allowing them to travel to us substantially unaffected by intervening matter, even from the earliest moments of the Big Bang [2].

The most important category of GW sources is binary systems. The frequency of the emitted GW largely depends on the mass of the binary. A super massive black hole (SMBH) is indicated by observations to reside in the center of every galaxy. Since SMBH binaries have a total mass of 10^6–$10^9\ M_\odot$, they are the strongest binary GW sources. Usually, SMBH binaries can be detected from a cosmological distance. Thus, SMBH binary signals provide cosmological information as well as information of the SMBHs. The frequency range of these sources is from nHz to mHz. An intermediate-mass black hole (IMBH) lies in the mass range 100–$10^6\ M_\odot$, with a frequency in the mHz–10 Hz range. Currently, IMBH is still a hypothetical class of black hole s. Observations of GWs from such sources bring information about galaxy formation, merger trees [44–46] etc. Stellar mass black hole binaries are in the frequency range of 1 Hz–kHz. They are important sources for ground-based interferometric detectors.

Extreme-mass-ratio inspirals (EMRIs) stand for the systems that consist of an MBH or SMBH and a stellar mass compact object captured by it. The mass ratio is about 1:10^6. Near the SMBH in the galactic center there are expected to be a large amount of stellar mass neutron stars and black holes. So it is very likely that from time to time one of these compact objects is captured by the SMBH, forming an EMRI system. A more extensive introduction to EMRIs is given in Chap. 11.

White dwarf binaries are believed to be important GW sources in the frequency range 0.1 mHz–0.1 Hz. Since the GWs from these sources are weaker than those from the sources mentioned above, these sources are only visible within our galaxy to the space-based detector LISA. There are so many such systems in our galaxy that the unresolved can form a stochastic astrophysical gravitational foreground [47]. One other stochastic GW signal is the cosmological background. It was generated by various mechanisms in the early universe [48–50]. We will talk about this later in detail.

The neutron star—neutron star binary coalescence, neutron star—(stellar-mass) black hole binary coalescence and (stellar-mass) black hole—(stellar-mass) black hole binary coalescence are the main GW sources for ground-based detectors, such as LIGO. Since these systems are more massive than white dwarf binaries and a binary system in the merger phase emits much stronger GWs than in the inspiral phase, the event horizon of these compact binary coalescence for ground-based detectors, such as LIGO and VIRGO, is about a few tens of Mpc.

Spinning neutron stars are also GW sources. When there is asymmetry in the mass distribution of the spinning neutron star, it radiates GWs. They are important sources for ground-based detectors. Since the asymmetric mass distribution is constrained to be very small ($\epsilon < 10^{-6}$ [51]), this kind of GWs is relatively weak. So it needs to be observed for quite a long time to accumulate sufficient SNR. Beside the GW sources mentioned above, there are other sources, such as burst gravitational radiation from gravitational collapses, cosmic string cusps, quasi-normal modes of black holes, etc.

1.4 Gravitational Wave Detectors

Due to the weakness of typical GWs $h \sim 2\Delta L/L \sim 10^{-22}$, there is no direct detection yet since the first attempt by Joseph Weber in the 1960s, when he built resonant-bar detectors to search for cosmic GWs [52, 53]. During those early years, people had very limited knowledge about the strength of the cosmic GWs. A resonant-bar detector has a relatively narrow detection band and poor sensitivity. In today's point of view, there is almost no matching source of GWs except the very unexpected violent events. Later on, people started to use large interferometers as GW observatories, which in general have much better sensitivities and broader detection bands. However, they were still not sensitive enough to have a reasonable detection rate. After decades of hard work, the sensitivity of the large interferometers is improved dramatically, and close to the guaranteed GW sources for the first time. In this section, we will briefly review different kinds of existing and planned GW detectors.

Fig. 1.3 MiniGrail, the first spherical GW detector, is operating in 2–4 kHz high frequency range at Leiden University in the Netherlands

1.4.1 Bar Detectors

The first GW detector was built by Joseph Weber in the 1960s. It was a large metal bar, hence being referred as a bar detector or Weber bar. The metal bar is well isolated from outside perturbing forces. When there are GWs of proper frequencies passing by, the bar will be exited at the resonant frequency, thus amplifying the effect and allowing the detection of GWs through sensitive displacement sensors. Modern bar detectors are even cryogenically cooled down to extremely low temperatures (e.g. a few K to mK) to reduce the thermal noise, e.g. the ALLEGRO detector [54–56]. MiniGrail [57–59] is the first spherical GW detector operating in 2–4 kHz high frequency range at Leiden University in the Netherlands, see Fig. 1.3. Generally, bar or spherical metal detectors aim at high frequency sources (around or above kHz).

1.4.2 Ground Based Interferometers

Currently, large laser interferometers are the most sensitive GW detectors. There are already several existing ground-based detectors all around the world.

LIGO (Laser Interferometer Gravitational-Wave Observatory) [60, 61] is the largest ground-based GW detector for the time being. LIGO has two sites: One is located in Hanford near Richland in Washington state, see Fig. 1.4; the other is in

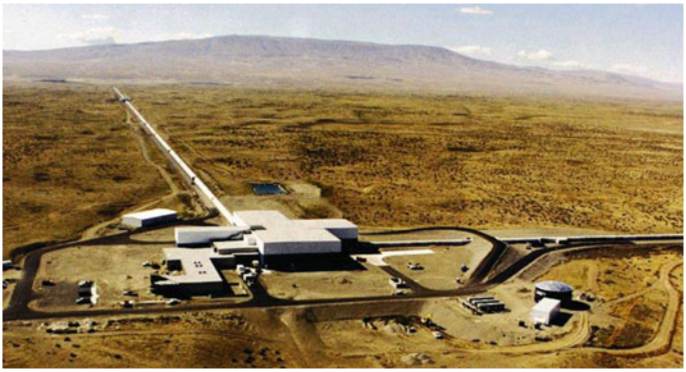

Fig. 1.4 Laser Interferometer Gravitational-Wave Observatory (LIGO) at Hanford

Fig. 1.5 Laser Interferometer Gravitational-Wave Observatory (LIGO) at Livingston

Livingston, Louisiana, see Fig. 1.5. Each site has an L-shape ultra high vacuum chamber, holding a 4 km armlength Michelson-type laser interferometer in it. Figure 1.6 shows the strain sensitivity of the LIGO detectors from science run 1 to science run 6. Notice that each curve is the sensitivity of either LIGO Livingston or LIGO Hanford (but not the joint sensitivity). Science run 1 began in 2002, and science run 6 ended in 2010. Each science run has an improved sensitivity compared to previous sensitivity, by implementing better techniques. Science run 5 roughly fulfilled the design sensitivity of initial LIGO. Science run 6 has outperformed the initial LIGO sensitivity high-frequency range with the help of techniques such as homodyne detection, output mode cleaner, in-vacuum readout hardware, increased laser power etc. [62]. Thus, science run 6 is sometimes referred to as enhanced LIGO. LIGO has many noise sources. Contributions from all these noise sources add up to the sensitivity curve in Fig. 1.6. The main limiting noise sources for initial LIGO and most other current ground-based interferometric detectors are: 1. seismic noise, which limits the

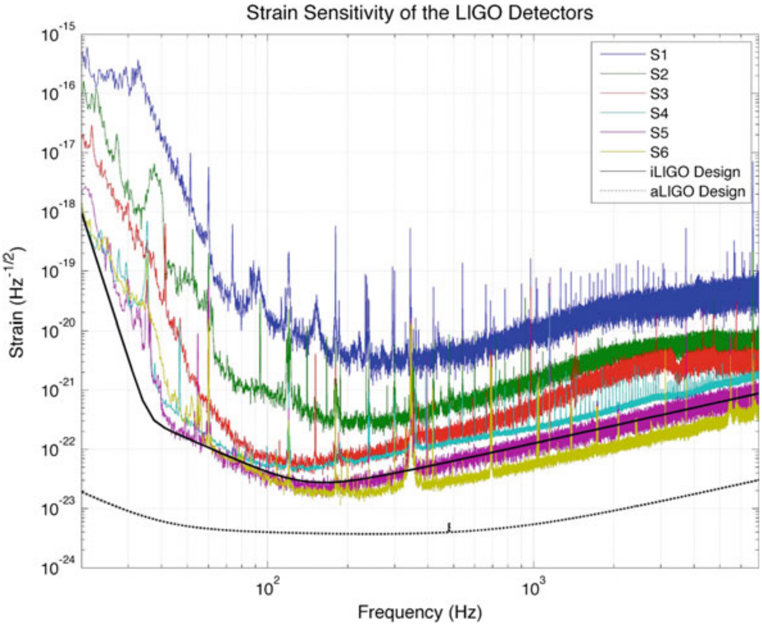

Fig. 1.6 Strain sensitivity of the LIGO detectors from science run 1 to science run 6 [63]

low-frequency sensitivity; 2. shot noise, which is the quantum mechanical photon counting noise at the photon detector, limiting the sensitivity at high frequency; 3. thermal noise, which limits the sensitivity in the middle frequency range. Currently, LIGO is being upgraded to advanced LIGO. Advanced LIGO intends to outperform the initial LIGO sensitivity by a factor of 10, hence increasing the detectable volume by a factor of 1000, see Fig. 1.6. Hopefully, advanced LIGO will have the first GW detection when it reaches its design sensitivity. This will open up a new era of GW astronomy.

VIRGO [64, 65] is an L-shape Michelson interferometer located in Italy with an armlength of 3 km, see Fig. 1.7. VIRGO has been operating since 2007. It has a sensitivity comparable to LIGO. Currently, it is being upgraded to advanced VIRGO.

GEO600 [66] is another GW detector with an armlength of 600 m, located near Sarstedt in Hannover, Germany, see Fig. 1.8. Since GEO600 has a shorter armlength than LIGO and VIRGO, its sensitivity is worse than LIGO's and VIRGO's at low frequencies and comparable to LIGO at high frequencies. Many advanced techniques have been developed at and applied to GEO600, such as squeezing etc.

TAMA300 is a Japanese GW detector. Since it has an arm length of 300 m, its sensitivity is not comparable to any of the above detectors.

There are also planned second-generation ground-based GW detectors. Besides advanced LIGO and advanced VIRGO mentioned before, GEO-HF [67] is an upgrade version of GEO 600. LIGO-India, a joint India-US advanced GW detector to be

Fig. 1.7 VIRGO interferometer located near Pisa in Italy

Fig. 1.8 GEO600 detector, with an armlength of 600 m, located at Sarstedt near Hannover, Germany

located in India, has been proposed. The Kamioka Gravitational Wave Detector (KAGRA) [68], formerly called the Large Scale Cryogenic Gravitational Wave Telescope (LCGT), is a planned Japanese GW detector. It has been approved in 2010. Now it is under construction. Einstein Telescope (ET) [69] is a proposed third-generation ground-based GW detector. Unlike other ground-based detectors, ET forms an equilateral triangular shape underground. See Fig. 1.9 for the comparison of sensitivity curves of different existing and planned ground-based GW detectors.

1.4.3 Space-Borne Interferometers

LISA [71, 72] is short for Laser Interferometer Space Antenna, which is a space-based detector with three spacecraft forming an equilateral triangular constellation with 5×10^9 m arm length orbiting the Sun trailing behind the Earth, see Fig. 1.10.

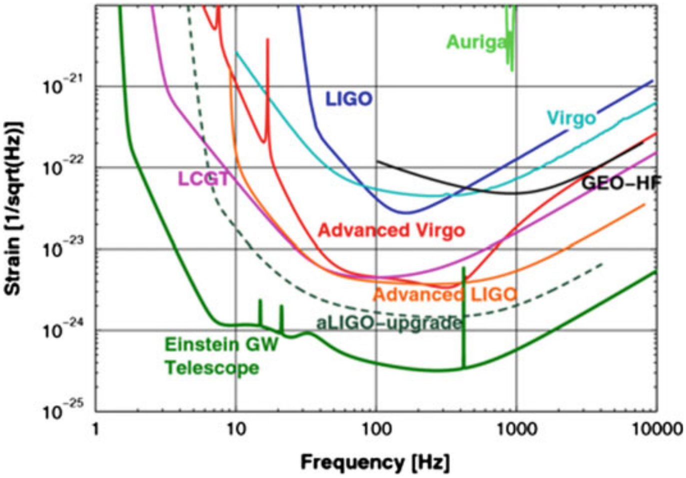

Fig. 1.9 Comparison of design sensitivity curves of different ground-based GW detectors [70]

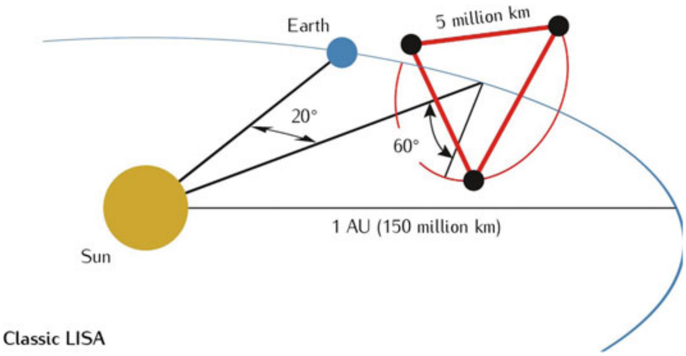

Fig. 1.10 Orbits and configuration of classic LISA [78]. (Image: S. Barke)

Some variations of the LISA concept are called eLISA [73, 74] or NGO (New Gravitational wave Observatory). Unlike ground-based detectors, LISA operates at the richest GW signal band 0.1 mHz−0.1 Hz, where there are plenty of gravitational wave signals, including massive black hole mergers, extreme mass ratio inspirals, white dwarf binaries, GW cosmic background etc. LISA data analysis is more a question of astrophysical parameter estimation than of mere detection. As for the experimental preparation, LISA/eLISA is much more mature than other space-based detectors (or space-based detector concepts) that we are going to talk about below. We will discuss LISA in more details in the next chapters. LISA pathfinder [75–77] is planned to be launched by the end of 2015. When it is successful in demonstrating the key technologies required by LISA, LISA itself (or eLISA) will hopefully be launched in twenty years.

DECIGO (DECI-Hertz Interferometer Gravitational wave Observatory) [79, 80] is a proposed Japanese space-borne GW detector. It consists of four equilateral triangular constellations, with an armlength of 1000 km each. It plans to use a Fabry–Pérot cavity along each arm to increase the effective armlength and the sensitivity. However, Fabry–Pérot cavities in space set much more demanding requirements. DECIGO is designed to be sensitive in the 0.1 Hz–10 Hz band.

ALIA (Advanced Laser Interferometer Antenna) and BBO (Big Bang Observer) [81] are follow-on concepts to LISA. ALIA requires moderately better techniques than LISA, while BBO requires much better techniques than LISA. So, BBO is actually a far-future space-borne concept, which gives excellent sensitivity. ALIA is an intermediate concept bridging the LISA concept and BBO.

ASTROD-GW (Astrodynamical Space Test of Relativity using Optical Devices) [82] is also a proposed space-based detector. It consists of three spacecraft, that are located near Lagrange points L3, L4, and L5. Thus, ASTROD-GW has a much longer armlength (about 1.7 AU) compared to other space-based detectors. So, it is sensitive in a lower frequency band than LISA.

OGO (Octahedral Gravitational Observatory) is a recently proposed space-borne gravitational wave detector [83]. Unlike other space-borne detectors, OGO consists of 6 spacecraft forming a 3-dimensional octahedron configuration with an armlength of about 1400 km, see Fig. 1.11. The acceleration noise is a limiting noise for space-borne detectors; and, the drag-free system for space detectors is one of the bottleneck difficult technologies. With 6 spacecraft, OGO has the ability to remove the acceleration noise while retaining GW signals. Thus, in principle, OGO needs no drag-free systems, which greatly simplifies the engineering technology. An alternative OGO configuration with 2×10^9 m armlengths is also proposed in paper [83].

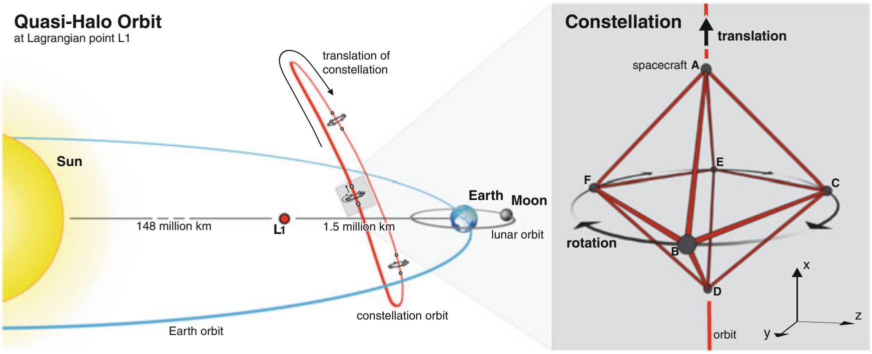

Fig. 1.11 OGO (Octahedral Gravitational Observatory), a newly proposed space-borne GW detector [83]

1.4.4 Pulsar Timing Array

A PTA (Pulsar Timing Array) uses a set of millisecond pulsars to detect GWs [84]. Since millisecond pulsars are emitting pulses to the Earth extremely regularly, they can be viewed as an emitter and the Earth's radio telescope can be viewed as a receiver. So each pulsar forms an arm with the Earth (more precisely, with the radio telescope). When there is a GW passing through these arms, the time of arrival of the pulses is altered. Thus, the GW signal is encoded in the time of arrival of these pulses. Since the distance between the Earth and the pulsar is astronomically long, the armlength formed by them is in turn much longer than man-made GW detectors. In principle, the sensitive frequency range determined by these armlengths can extend to extremely low frequencies. However, in practice, the observation time is limited to the order of 10 years. Therefore, the actual sensitive frequency range of PTA is usually from nHz to μHz.

Currently, there are three major PTAs operating and recording data: (i) the European Pulsar Timing Array (EPTA) [85], (ii) the North American Nanohertz Observatory for Gravitational waves (NANOGrav) [86] and (iii) the Parkes Pulsar Timing Array (PPTA) [87]. The collaboration of these three PTAs is called the International Pulsar Timing Array (IPTA) [84], which has better sensitivity than any of the three individual PTAs.

1.4.5 Doppler Tracking

Doppler tracking of spacecraft has been also used to search for GWs [88, 89]. Similar to PTA, the method takes the Earth as one end and the deep space spacecraft as the other, hence forming an arm between the two by sending and receiving signals. The distance between the spacecraft and the Earth is of the order of about 1 AU, thus the sensitive frequency band of Doppler tracking is similar to that of ASTROD-GW.

1.4.6 High Frequency Detectors

There are two high frequency GW detectors for the time being. One of them is located at INFN Genoa, in Italy. The other [90] is located at the University of Birmingham in England. They are aiming at MHz to GHz range GW signals. Another high frequency detector [91] is proposed by Fangyu Li at Chongqing University, China. This detector aims to detect relic gravitational radiation around 10^{10} Hz.

1.5 Gravitational Wave Data Analysis

GW data analysis [92, 93] is a crucial integral part of GW astronomy. Due to the weakness of GWs, most of the time GW signals are buried in strong detector noise. One needs to design sophisticated algorithms and efficient codes to detect GW signals. Even when the signal is strong (e.g. massive black hole mergers for LISA), one still needs to design sophisticated data analysis algorithms to extract physical information (e.g. the masses of the black holes, the spins, the sky positions) from the observed signals. Generally speaking, the analysis of the measurement data of GW detectors mainly involves two stages:

1. The pre-processing stage (or the data preparation stage), whose main task is to use various auxiliary measurement data (e.g. the data channel that is used to monitor the environment surrounding the GW detectors) or additional information to calibrate the science data (i.e. the data stream that is supposed to contain GW signals and used to detect GW signals) and to reduce or remove various noise in the science data. Chapters 2–9 of this thesis are devoted to this kind of data analysis for (e)LISA. Since the pre-processing stage is different for different kinds of GW detectors, such as space-borne interferometers, ground-based interferometers, PTAs, the background knowledge for LISA data preparation is specific. Its introduction will be given in Chaps. 2 and 3.
2. The astrophysical data analysis stage (or the 'usual' GW data analysis), in which we try to detect GW signals from the science data and estimate the physical parameters of the detected GW signals. The works in Chaps. 10–13 are of this type of data analysis. Since the astrophysical data analysis for space-borne interferometers, ground-based interferometers and PTAs, relies on more or less common background knowledge and techniques, we will give a general introduction below.

1.5.1 The General Problem in Astrophysical Data Analysis

The general problem in the astrophysical data analysis stage is to detect the GW signal from the detector output $x(t)$ and estimate the (physical) parameters $\boldsymbol{\theta}$ that describe the GW signal. For a compact binary, these parameters $\boldsymbol{\theta}$ can be the masses, the spins, the sky position of the binary, the angle between the orbital momentum of the binary and the line of sight, etc. The detector output $x(t)$ can usually be expressed as

$$x(t) = s(t, \boldsymbol{\theta}) + n(t), \tag{1.21}$$

where $n(t)$ denotes the noise time series, $s(t, \boldsymbol{\theta})$ the detector response to a gravitational wave signal $h(t, \boldsymbol{\theta})$. For linear measurement system, $s(t, \boldsymbol{\theta})$ equals the convolution of the gravitational wave signal $h(t, \boldsymbol{\theta})$ and the impulse response of the system. In the next subsections, we will look in detail into the detector response and the noise, which are the two important elements of the detector output.

1.5.2 Properties of a Random Process

The detection and parameter estimation algorithms depend largely on the property of the noise n(t), which is a random process. The property of a random process is usually characterized by its moments. The first moment is defined as the mean of the process

$$\mu(t) =< n(t) >, \tag{1.22}$$

where $< \cdots >$ denotes the ensemble average. The second moment is also known as the autocorrelation

$$A(t,\tau) =< n(t)n(t+\tau) > . \tag{1.23}$$

The higher moments are defined as

$$\begin{aligned} &< n(t)n(t+\tau_1)n(t+\tau_2) >, \\ &< n(t)n(t+\tau_1)n(t+\tau_2)n(t+\tau_3) >, \\ &\qquad \ldots \end{aligned}$$

A random process is said to be stationary if its joint probability distribution is invariant under a shift in time. Therefore, for a stationary random process, its moments do not depend on the time t. If only its mean and autocorrelation do not change when shifted in time, the random process is call wide-sense stationary (WSS).

The Wiener–Khinchin theorem [94, 95] states that if a noise process $n(t)$ is WSS, the Fourier transform of its autocorrelation $A(\tau)$ exists

$$\begin{aligned} S_n(f) &\equiv \int_{-\infty}^{\infty} A(\tau) e^{i2\pi f\tau} \mathrm{d}\tau, \\ &= \int_{-\infty}^{\infty} < n(t)n(t+\tau) > e^{i2\pi f\tau} \mathrm{d}\tau, \end{aligned} \tag{1.24}$$

where $S_n(f)$ is usually called the two-sided power spectral density (PSD) of the noise process, and we have adopted the following convention of the Fourier transform $\tilde{x}(f) = \int x(t) e^{i2\pi f t} \mathrm{d}t$. With the help of inverse Fourier transform, we can easily obtain the variance of the noise process

$$\begin{aligned} < n(t)^2 > &= A(0), \\ &= \int_{-\infty}^{\infty} S_n(f) \mathrm{d}f. \end{aligned} \tag{1.25}$$

A random process is called Gaussian, if it is uniquely characterized by its first and second moments. In GW data analysis, the noise process $n(t)$ is usually assumed to be Gaussian stationary with a zero mean. Such a noise process is uniquely characterized by its autocorrelation function, hence by its PSD.

In the following, we will discuss the noise process in a more intuitive and less rigorous way, which assumes the Fourier transform $\tilde{n}(f)$ of the Gaussian stationary noise process $n(t)$ exists. It is easy to verify that

$$\begin{aligned} < \tilde{n}^*(f')\tilde{n}(f) > &= \int\int < n(t_1)n(t_2) > e^{-i2\pi f' t_1} e^{i2\pi f t_2} \mathrm{d}t_1 \mathrm{d}t_2, \\ &= \int\int < n(t_1)n(t_1+\tau) > e^{i2\pi(f-f')t_1} e^{i2\pi f\tau} \mathrm{d}t_1 \mathrm{d}\tau, \\ &= S_n(f)\delta(f-f'), \end{aligned} \tag{1.26}$$

which is the usual definition of the two-sided PSD of the Gaussian stationary noise in GW literatures. For a total observation time T, the above equation leads to

$$S_n(f) = \frac{1}{T} < |\tilde{n}(f)|^2 >, \tag{1.27}$$

which can be used to quickly estimate the PSD of the noise. For white-Gaussian stationary noise process, another useful formula can be obtained from Eq. (1.25)

$$S_n(f) = \sigma^2 \Delta t, \tag{1.28}$$

where σ is the standard deviation of the noise process, Δt the sampling interval. This can be used to simulate white-Gaussian noise at a given PSD level. Simulation of noise with arbitrary PSD will be discussed in Chap. 9.

1.5.3 *Detector Responses*

Now let us calculate the response of the basic element of an arbitrary interferometer—a single (laser) link to a gravitational wave signal. Suppose the emitter locates at $\boldsymbol{X}_{(j)}$, where subscript $j = 1, 2, 3\ldots$ indicates the jth spacecraft for space-borne detectors, the jth vertex of ground-based detectors, or the jth pulsar for PTAs. Similarly, we denote the location of the receiver as $\boldsymbol{X}_{(k)}$ and the unit vector pointing from the emitter to the receiver by $\boldsymbol{n}_{(jk)} = (\boldsymbol{X}_{(k)} - \boldsymbol{X}_{(j)})/L_{(jk)}$, where the so-called armlength $L_{(jk)} = |\boldsymbol{X}_{(k)} - \boldsymbol{X}_{(j)}|$ is the distance between the emitter and the receiver. Without loss of generality, we assume the gravitational wave propagates along $\boldsymbol{e}_z$ direction, which can be expressed as

$$\mathbf{h}(t, \boldsymbol{X}) = h_+(t - \boldsymbol{e}_z \cdot \boldsymbol{X}/c)\boldsymbol{e}_+ + h_\times(t - \boldsymbol{e}_z \cdot \boldsymbol{X}/c)\boldsymbol{e}_\times, \tag{1.29}$$

where $\boldsymbol{e}_+ = (\boldsymbol{e}_x \otimes \boldsymbol{e}_x - \boldsymbol{e}_y \otimes \boldsymbol{e}_y)/2$, $\boldsymbol{e}_\times = (\boldsymbol{e}_x \otimes \boldsymbol{e}_y + \boldsymbol{e}_y \otimes \boldsymbol{e}_x)/2$ are the two polarization tensors, c is the speed of light. The detector response to gravitational radiations can be strictly derived with the help of the three Killing vectors of the radiation field, which lead to three constants of motion. See [89, 96] for more details. Up to the leading order in h, the phase change induced by GWs to a single-way laser link is

$$\Delta\phi_{(jk)}(t_e) = \sum_{p=+,\times} F^p_{(jk)} \int_0^{L_{(jk)}/c} h_p[(t_e - \boldsymbol{e}_z \cdot \boldsymbol{X}_{(j)}/c) + (1 - \boldsymbol{e}_z \cdot \boldsymbol{n}_{(jk)})t']\omega_L dt' \tag{1.30}$$

where $F^+_{(jk)} = [\boldsymbol{n}_{(jk)} \otimes \boldsymbol{n}_{(jk)}] : \boldsymbol{e}_+$, $F^\times_{(jk)} = [\boldsymbol{n}_{(jk)} \otimes \boldsymbol{n}_{(jk)}] : \boldsymbol{e}_\times$ are the antenna pattern functions of the single-way link, ':' denotes tensor contraction, ω_L is the angular frequency of the laser, and t_e is the time of emission. The reception time can be written as $t_r = t_e + L_{(jk)}/c$. Physically, this equation means the total phase change results from the summation of gravitational perturbation of different phases along the laser link. The dimensionless response of the detector is also quite useful in many cases, which is given by

$$s_{(jk)}(t_e) = \sum_{p=+,\times} F^p_{(jk)} \int_0^{L_{(jk)}/c} h_p[(t_e - \boldsymbol{e}_z \cdot \boldsymbol{X}_{(j)}/c) + (1 - \boldsymbol{e}_z \cdot \boldsymbol{n}_{(jk)})t'] \frac{cdt'}{L_{(jk)}}. \tag{1.31}$$

The antenna pattern functions in these responses basically indicate which directions the gravitational wave detector is sensitive to. Figure 1.12 shows the antenna

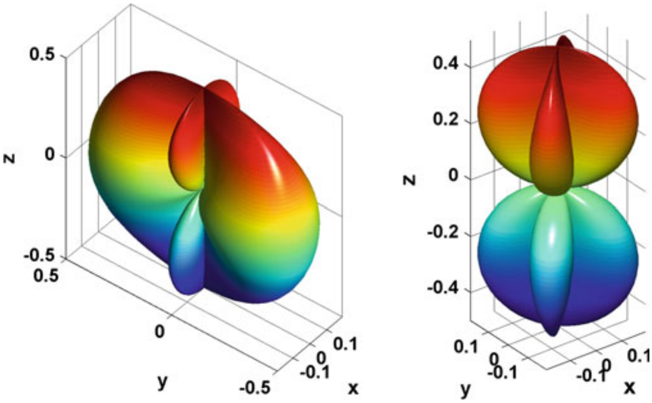

Fig. 1.12 Antenna pattern functions of a single laser link. (*Left*) Antenna pattern function for h_+ polarization, $F^+ = \frac{1}{2}(\cos^2\theta\cos^2\varphi - \sin^2\varphi)$. (*Right*) Antenna pattern function for $h_\times$ polarization, $F^\times = \cos\theta\cos\varphi\sin\varphi$

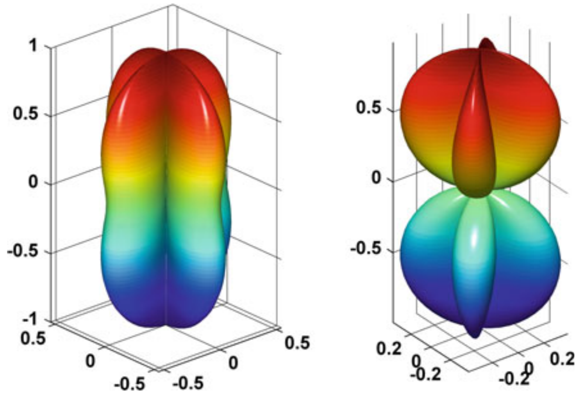

Fig. 1.13 Antenna pattern functions of a Michelson interferometer. (*Left*) Antenna pattern function for h_+ polarization, $F^+ = \frac{1}{2}(\cos(2\varphi)(1+\cos^2\theta))$. (*Right*) Antenna pattern function for $h_\times$ polarization, $F^\times = \sin(2\varphi)\cos\theta$

pattern functions of a single laser link. Figure 1.13 shows the antenna pattern functions of a Michelson interferometer, which has two orthogonal arms. It is apparent from these figures that gravitational wave detectors are sensitive to a very large fraction of the sky, hence they are usually referred to as omni-directional detectors.

The Fourier transform of the dimensionless response can be obtained easily

$$\tilde{s}_{(jk)}(f) = \sum_{p=+,\times} F^p_{(jk)} \frac{\exp\{2\pi i f[1-\boldsymbol{e}_z\cdot\boldsymbol{n}_{(jk)}]L_{(jk)}/c\}-1}{2\pi i f[1-\boldsymbol{e}_z\cdot\boldsymbol{n}_{(jk)}]L_{(jk)}/c} e^{-2\pi i \boldsymbol{e}_z\cdot\boldsymbol{X}_{(j)}}\tilde{h}_p(f). \tag{1.32}$$

Let us consider a special case when the laser beam is along x-axis ($\boldsymbol{e}_x$), GWs propagate in $\boldsymbol{e}_z$ direction and have only the plus polarization $h = h(t)\boldsymbol{e}+$. Then the detector response in frequency domain can be simplified as

$$\begin{aligned}\tilde{s}_{(jk)}(f) &\equiv T(f)\tilde{h}(f)\\ &= \frac{1}{2}\frac{\exp\{2\pi i f L_{(jk)}/c\}-1}{2\pi i f L_{(jk)}/c} e^{-2\pi i \boldsymbol{e}_z\cdot\boldsymbol{X}_{(j)}}\tilde{h}(f),\end{aligned} \tag{1.33}$$

where

$$T(f) = \frac{1}{2}\frac{\exp\{2\pi i f L_{(jk)}/c\}-1}{2\pi i f L_{(jk)}/c} e^{-2\pi i \boldsymbol{e}_z\cdot\boldsymbol{X}_{(j)}} \tag{1.34}$$

is the transfer function. Figure 1.14 shows the amplitude of the transfer function for an arm length $L = 5\times 10^9$m (LISA arm length). If the detector is limited by some noise floor with a PSD $S_n^{\mathrm{floor}}(f)$, the effective strain sensitivity can then be written as

$$\sqrt{S_n(f)} = \frac{\sqrt{S_n^{\mathrm{floor}}(f)}}{|T(f)|}. \tag{1.35}$$

Figure 1.15 shows an example of the strain sensitivity.

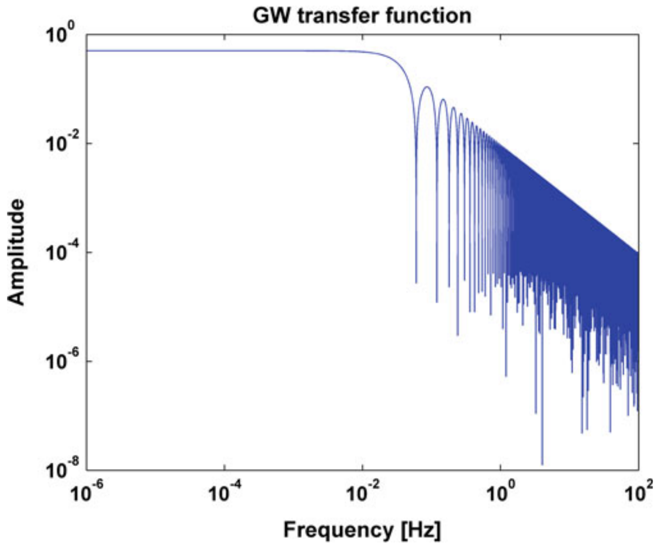

Fig. 1.14 Transfer function of a single-link one-way detector

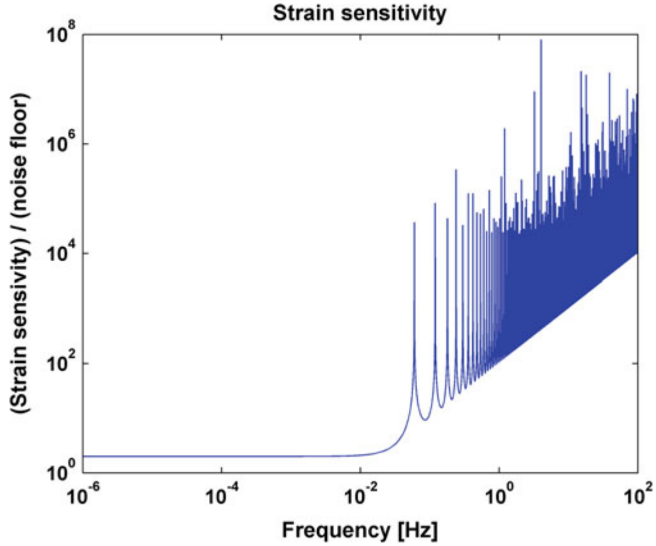

Fig. 1.15 Strain sensitivity of a single-link one-way detector with an arm length of $L = 5 \times 10^9$m. Here we assume the sensitivity of the detector is limited only by white noise

In more general case, the transfer function depends on the propagation direction of GWs, while the noise floor usually does not. We need to average the gravitational wave transfer function over all directions. The strain sensitivity of a GW detector is then given by

$$\sqrt{S_n(f)} = \sqrt{\frac{S_n^{\text{floor}}(f)}{< |T(f)|^2 >_{\text{sky}}}}, \tag{1.36}$$

where $< \cdots >_{\text{sky}}$ means averaging over all sky positions. Next we give an simple example of the sensitivity of a GW detector. According to [97], mock LISA data challenge (MLDC) adopts a simplified model to characterize LISA noise. The one-sided PSD of the position noise is modelled as

$$S_{\text{pos}}^{1/2}(f) = 20 \times 10^{-12}\text{m}/\sqrt{\text{Hz}}. \tag{1.37}$$

The one-sided PSD of the acceleration noise is modelled as

$$S_{\text{acc}}^{1/2}(f) = 3 \times 10^{-15}\sqrt{1 + (10^{-4}Hz/f)^2}\ \text{m/s}^2/\sqrt{\text{Hz}}. \tag{1.38}$$

Then, the total noise floor can be calculated as

$$S_n^{\text{floor}}(f) = \sqrt{S_{\text{pos}}(f)/L^2 + S_{\text{acc}}(f)/(4\pi^2 f^2 L)^2}. \tag{1.39}$$

By inserting this into Eq. (1.36), we obtain LISA strain sensitivity of a single-link averaged over all sky positions plotted in Fig. 1.16. In practice, we need to eliminate the otherwise overwhelming laser frequency noise through post-processing, which will be discussed in Chap. 2. The post-processing algorithms will introduce a small correction to the sensitivity curve, which accounts for the small difference between the single-link sensitivity curve here and the official LISA sensitivity curve.

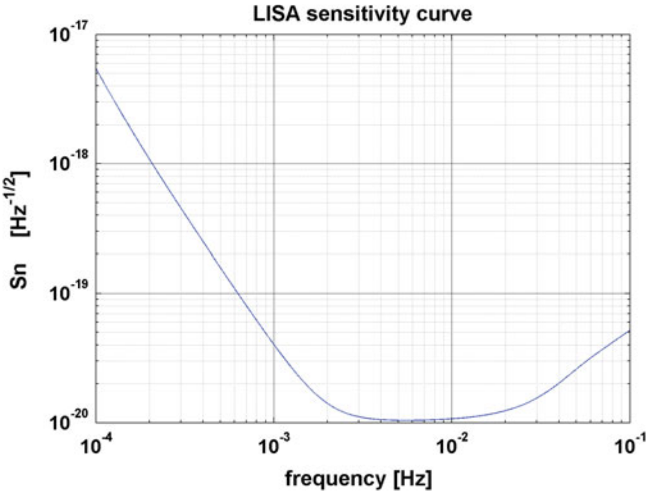

Fig. 1.16 Strain sensitivity of a single-link one-way detector with an arm length of $L = 5 \times 10^9$m averaged over all sky positions

1.5.4 Detection Statistic

In the following, we follow the Bayesian approach to construct a detection statistic [98, 99]. We denote the conditional probability of realizing $x(t)$ in the absence of the signal as $P(x|0)$. The conditional probability of realizing $x(t)$, when a signal $s(t)$ is present, is denoted by $P(x|s)$. Similarly, the conditional probability of realizing $x(t)$, when the signal $s(t, \boldsymbol{\theta})$ characterized by parameters $\boldsymbol{\theta}$ is present, is denoted by $P(x|s(\boldsymbol{\theta}))$. The a priori probabilities that no signal is present in the data and a signal $s(t)$ is present in the data are denoted by $P(0)$ and $P(s)$ respectively. The a priori probability density of the signal parameters is denoted by $P(\boldsymbol{\theta})$. According to the law of total probability, we can express the probability of measuring $x(t)$ as

$$\begin{aligned} P(x) &= P(x|0)P(0) + P(x|s)P(s), \\ &= P(x|0)P(0) + P(s)\int d^N\boldsymbol{\theta} P(\boldsymbol{\theta})P(x|s(\boldsymbol{\theta})), \end{aligned} \tag{1.40}$$

where N is the dimension of the parameter space. By inserting this into the relation given by the Bayes' theorem, we obtain the probability that a signal is present given the data $x(t)$

$$\begin{aligned} P(s|x) &= \frac{P(x|s)P(s)}{P(x)}, \\ &= \frac{\Lambda}{\Lambda + P(0)/P(s)}, \end{aligned} \tag{1.41}$$

where we have defined

$$\Lambda = \int d^N\boldsymbol{\theta}\Lambda(\boldsymbol{\theta}), \tag{1.42}$$

$$\Lambda(\boldsymbol{\theta}) = P(\boldsymbol{\theta})\frac{P(x|s(\boldsymbol{\theta}))}{P(x|0)}. \tag{1.43}$$

Since $P(0)/P(s)$ is a positive constant in Eq. (1.41), $P(s|x)$ is a monotone increasing function of the likelihood ratio Λ. In addition, since $P(0)/P(s)$ does not depend on any physical parameters, Λ is a sufficient statistic. Ideally, it is nice to use Λ as a detection statistic. However, the high dimensional integral over the signal parameters $\boldsymbol{\theta}$ is usually computationally prohibitive. Instead, one uses $\Lambda(\boldsymbol{\theta})$ as a detection statistic. In practice, one calculates this likelihood ratio $\Lambda(\boldsymbol{\theta})$ for many possible parameters $\boldsymbol{\theta}$. If the maximum $\Lambda(\boldsymbol{\theta})$ is above a certain prescribed threshold, we claim a detection. And the parameter set $\boldsymbol{\theta}_*$ that maximize the likelihood ratio is usually taken as the estimate of the parameters. This procedure is called the maximum likelihood estimator in statistics.

1.5.5 Matched Filtering

Now we try to express the probability densities explicitly. In the absence of the signal, the data should follow the probability distribution of the noise, which is usually assumed to be Gaussian with a zero mean. Suppose there are M discrete measurements x_j, where $j = 1, 2, \ldots, M$. Notice that these measurements can be nonuniform in time. The autocorrelation matrix of the corresponding noise n_j is denoted by

$$A_{jk} =< n_j n_k >, \tag{1.44}$$

whose inverse matrix is denoted by A^{-1}_{jk}, which satisfies

$$\sum_{k=1}^{M} A_{jk} A^{-1}_{kl} = \delta_{jl}. \tag{1.45}$$

Then the probability density of the data x_j in the absence of the signal is

$$P(x|0) = \frac{1}{\sqrt{\| 2\pi A_{jk} \|}} \exp\left[-\frac{1}{2} \sum_{j,k} x_j A^{-1}_{jk} x_k \right], \tag{1.46}$$

where $\| \cdots \|$ denotes the determinant. Similarly, the probability of observing x_j, when the signal s_j is present, can be expressed as

$$P(x|s) = \frac{1}{\sqrt{\| 2\pi A_{jk} \|}} \exp\left[-\frac{1}{2} \sum_{j,k} (x_j - s_j) A^{-1}_{jk} (x_k - s_k) \right]. \tag{1.47}$$

The likelihood ratio can be easily calculated from the above two equations. If this likelihood ratio is above a prescribed threshold, a detection is claimed. In this procedure, the calculation of the inverse of the large autocorrelation matrix and the matrix production is computationally expensive, especially when the number of samples is large. PTA data analysis, whose data is unevenly sampled, usually adopts the above procedure.

For ground-based and space-borne interferometers, the measurements are usually uniformly sampled. Assuming the noise is Gaussian stationary, there is a much more efficient way to evaluate the exponents in the above two equations. In the limit of the total observation time $T \to \infty$ and the sampling interval $\Delta t \to 0$, it is straightforward to prove [98]

$$\sum_{j,k} x_j A^{-1}_{jk} x_k \to \int_{-\infty}^{\infty} \frac{\tilde{x}^*(f)\tilde{x}(f)}{S_n(f)} df, \tag{1.48}$$

where $S_n(f)$ is the two-sided PSD of the noise. In this way, one can avoid calculating the inverse of large matrices. It is convenient and traditional to define a inner product of two time series $a(t)$, $b(t)$ as follows

$$\langle a|b\rangle = \int_{-\infty}^{\infty} \frac{\tilde{a}^*(f)\tilde{b}(f)}{S_n(f)}df = 2\mathrm{Re}\left[\int_{0}^{\infty} \frac{\tilde{a}^*(f)\tilde{b}(f)}{S_n(f)}df\right], \tag{1.49}$$

where Re denotes the real part. Insert the data and the GW signal into this inner product, we have

$$\langle x|s(\boldsymbol{\theta})\rangle = \int_{-\infty}^{\infty} \tilde{x}^*(f) \times \frac{\tilde{s}(f,\boldsymbol{\theta})}{S_n(f)}df, \tag{1.50}$$

which can also be written in time-domain as a convolution. This is a linear time-invariant filter, which is the optimal linear filter in the sense that it maximizes the signal-to-noise ratio (SNR). It is usually called the matched filter in GW literatures. Essentially, it is a Wiener filter [100]. The optimal SNR for a signal $s(\boldsymbol{\theta})$ present in the data is

$$\mathrm{SNR}^2 = \langle s(\boldsymbol{\theta})|s(\boldsymbol{\theta})\rangle = \int_{-\infty}^{\infty} \frac{|\tilde{s}(f,\boldsymbol{\theta})|^2}{S_n(f)}df. \tag{1.51}$$

With the help of the inner product, the probability of observing the measurements $x(t)$ in the absence and presence of the signal can be reexpressed as

$$P(x|0) = e^{-\frac{1}{2}\langle x|x\rangle}, \tag{1.52}$$
$$P(x|s(\boldsymbol{\theta})) \propto e^{-\frac{1}{2}\langle x-s(\boldsymbol{\theta})|x-s(\boldsymbol{\theta})\rangle}. \tag{1.53}$$

Up to a constant, the likelihood ratio can be reexpressed as

$$\begin{aligned}\Lambda(\boldsymbol{\theta}) &\propto P(\boldsymbol{\theta})\frac{P(x|s(\boldsymbol{\theta}))}{P(x|0)}\\ &\propto P(\boldsymbol{\theta})e^{\langle x|s(\boldsymbol{\theta})\rangle-\frac{1}{2}\langle s(\boldsymbol{\theta})|s(\boldsymbol{\theta})\rangle}.\end{aligned} \tag{1.54}$$

Since the exponential function is a monochromatically increasing function, one usually uses the log likelihood ratio as the detection statistic

$$\begin{aligned}L(\boldsymbol{\theta}) &\equiv \log\Lambda(\boldsymbol{\theta}),\\ &= \langle x|s(\boldsymbol{\theta})\rangle - \frac{1}{2}\langle s(\boldsymbol{\theta})|s(\boldsymbol{\theta})\rangle + \log P(\boldsymbol{\theta}).\end{aligned} \tag{1.55}$$

For a uniform a priori probability density, the last term in the above equation vanishes.

1.5.6 Parameter Estimation

For a given parameter space, one needs to evaluate the log likelihood ratio at all possible parameter sets $\mathbb{\theta}$ in the parameter space and identify the parameters $\mathbb{\theta}_*$ that maximize the log likelihood ratio as the most probable parameters of the signal (assuming its likelihood ratio is above some threshold). As mentioned before, this is called the maximum likelihood estimator. In practice, it is computationally extremely intensive to do this for all the parameters. Actually, some of the parameters in the parameter set $\mathbb{\theta}$ can be maximized over analytically. These parameters are usually called extrinsic parameters in GW literatures. The parameters that cannot be maximized over analytically are called intrinsic parameters. The extrinsic parameters usually do not modulate the phase of the GW signals, while the intrinsic parameters do. In the following, we give a few typical examples of maximization over extrinsic parameters.

Consider $\mathbb{\theta} = (\Theta,\ A)$, where the amplitude A of the signal is an extrinsic parameter. The rest parameters are denoted by Θ. The signal is $s = Ah(t, \Theta)$ and the detector output is $x = Ah(t, \Theta) + n$, where $h(t, \Theta)$ is the normalized signal $\langle h|h\rangle = 1$. We assume a uniform a priori probability density $P(\mathbb{\theta})$ throughout this subsection. Then, the log likelihood ratio is

$$\begin{aligned} L(\mathbb{\theta}) &= \langle x|s(\mathbb{\theta})\rangle - \frac{1}{2}\langle s(\mathbb{\theta})|s(\mathbb{\theta})\rangle, \\ &= \langle x|h(\Theta)\rangle A - \frac{1}{2}A^2. \end{aligned} \tag{1.56}$$

Let $\partial L/\partial A = 0$, we obtain $A = \langle x|h(\Theta)\rangle$. Therefore, we have

$$L(\Theta) \equiv \max_A L(\mathbb{\theta}) = \frac{1}{2}\langle x|h(\Theta)\rangle^2. \tag{1.57}$$

This implies that $L'(\Theta) \equiv \langle x|h(\Theta)\rangle$ is a sufficient statistic for the maximum likelihood estimator, hence we only need to calculate the inner product of the data and the normalized signal.

Now let us consider $\mathbb{\theta} = (\Theta,\ A,\ \phi_a,\ t_a)$, where the initial phase ϕ_a of the signal is also an extrinsic parameter, t_a denotes the time of arrival, and the rest parameters are denoted by Θ. (Notice that the following algorithm works equally for the coalescence time t_c and the coalescence phase ϕ_c.) The Fourier transform of the signal can now be expressed as

$$\tilde{s}(f; \Theta, A, \phi_a, t_a) = A\tilde{h}(f; \Theta)e^{i2\pi f t_a + i\phi_a}. \tag{1.58}$$

The maximization over the extrinsic parameters and the fast parameter t_a can be done as follows

$$\begin{aligned}
\max_{A,\phi_a,t_a} L(\mathbb{\Theta}) \rightarrow &\max_{\phi_a,t_a} L'(\Theta,\phi_a,t_a), \\
&= \max_{\phi_a,t_a} < x|h(\Theta,\phi_a,t_a) >, \\
&= 2\max_{\phi_a,t_a} \mathrm{Re}\left[\int_0^\infty \frac{\tilde{x}^*(f)\tilde{h}(f;\Theta)}{S_n(f)} e^{i2\pi f t_a + i\phi_a} df\right], \\
&= 2\max_{t_a} \left|\int_0^\infty \frac{\tilde{x}^*(f)\tilde{h}(f;\Theta)}{S_n(f)} e^{i2\pi f t_a} df\right|, \qquad (1.59)
\end{aligned}$$

which is simply twice the largest absolute value of the Fourier transform of $\tilde{x}^*(f)\tilde{h}(f;\Theta)/S_n(f)$. Therefore, the maximization over the parameter t_a can be efficiently calculated via a fast Fourier transform.

Next we consider $\mathbb{\Theta} = (\Theta, A^\mu)$, where $A^\mu = (A^1, A^2, \dots, A^n)$ are extrinsic parameters, and the signal is in the following form

$$s(t,\mathbb{\Theta}) = A^\mu h_\mu(t,\Theta), \qquad (1.60)$$

where we have assumed Einstein summation convention, and $h_\mu(t,\Theta)$ are functions of the intrinsic parameters Θ. The corresponding log likelihood ratio of this type of signals can be expressed as

$$\begin{aligned}
L(\mathbb{\Theta}) &= \langle x|s(\mathbb{\Theta})\rangle - \frac{1}{2}\langle s(\mathbb{\Theta})|s(\mathbb{\Theta})\rangle, \\
&= A^\mu\langle x|h_\mu(\Theta)\rangle - \frac{1}{2}A^\mu\langle h_\mu(\Theta)|h_\nu(\Theta)\rangle A^\nu, \\
&= A^\mu x_\mu - \frac{1}{2}A^\mu M_{\mu\nu}A^\nu, \qquad (1.61)
\end{aligned}$$

where we have defined $x_\mu(\Theta) \equiv \langle x|h_\mu(\Theta)\rangle$ and $M_{\mu\nu}(\Theta) \equiv \langle h_\mu(\Theta)|h_\nu(\Theta)\rangle$. This is a quadratic form of the parameters A^μ, hence it can be maximized easily. Let $\partial L/\partial A^\mu = 0$, we obtain $A^\mu = (M^{-1})^{\mu\nu}x_\nu$. Therefore, we have

$$\max_{A^\mu} L(\mathbb{\Theta}) = \frac{1}{2}x_\mu(\Theta)(M^{-1})^{\mu\nu}(\Theta)x_\nu(\Theta). \qquad (1.62)$$

This is the so-called F-statistic in GW literatures. See more discussions on it in Chap. 11.

All in all, the maximization over extrinsic parameters helps a lot in accelerating the search for the signal. However, the exploration in the intrinsic parameter space is still computationally very expensive. There are mainly two categories of search algorithms for the intrinsic parameters: (i) the incoherent and semi-coherent search and (ii) the coherent search. The incoherent and semi-coherent search are computationally more efficient, but they are less sensitive to the signals. Time-frequency methods (see Chap. 11 for more details about this method), short Fourier transforms, and wavelet transforms all belong to this category. The coherent search is more sensitive to the signals, but it is computationally more expensive. There are mainly two types of algorithms in this category: (i) grid-based algorithms and (ii) stochastic algorithms. The grid-based algorithms employ a mesh grid in the intrinsic parameter space, and calculate the likelihood ratio for each of the parameter set on the grid. This kind of algorithms is very sensitive to the signals, but it is computationally extremely expensive. Therefore, it is usually run on big clusters. Sometimes, grid-based algorithms are computationally prohibitive. In this case, one could turn to stochastic algorithms, which are computationally more efficient. These heuristic algorithms include Markov chain Monte Carlo, particle swarm optimization, genetic algorithms, etc. See more discussions about these algorithms and coherent searches in Chaps. 11–13.

The uncertainty of the parameter estimation is usually characterized by the Fisher matrix [101], which is defined by

$$F_{jk}(\mathbb{\theta}) =< \partial_j \log P(x|s(\mathbb{\theta}))\partial_k \log P(x|s(\mathbb{\theta})) >, \tag{1.63}$$

where $\partial_j \equiv \partial/\partial\theta^j$ denotes the partial derivative with respect to the jth component in $\mathbb{\theta}$. With the help of the definitions of $P(x|s(\mathbb{\theta}))$ and the noise PSD, it is straightforward to prove that

$$F_{jk}(\mathbb{\theta}) = \langle \partial_j s|\partial_k s\rangle. \tag{1.64}$$

The inverse of the Fisher matrix $F^{-1}_{jk}(\mathbb{\theta})$ serves as a lower bound, which is well-known as the Cramér–Rao bound [101], for the parameter-estimation error of all unbiased estimators.

One other important concept, that is closely related to the Fisher matrix, is the metric on the likelihood surface [102]. Let us consider the mismatch between two normalized signals (which satisfy $\langle s|s\rangle = 1$) separated by a small distance $\mathrm{d}\mathbb{\theta}$ in the parameter space.

$$\langle s(\mathbb{\theta})|s(\mathbb{\theta}+\mathrm{d}\mathbb{\theta})\rangle = 1 + \frac{1}{2}\langle s(\mathbb{\theta})|\partial_j\partial_k s(\mathbb{\theta})\rangle \mathrm{d}\theta^j \mathrm{d}\theta^k + \cdots, \tag{1.65}$$

where the linear order vanishes due to the fact that the inner product has its maximum at $\mathrm{d}\mathbb{\theta} = 0$, and we have assumed Einstein summation over repeated indices. By taking the second partial derivative of $\langle s|s\rangle = 1$, it is easily obtained that

$$\langle s(\mathbb{\theta})|\partial_j\partial_k s(\mathbb{\theta})\rangle = -\langle \partial_j s(\mathbb{\theta})|\partial_k s(\mathbb{\theta})\rangle. \tag{1.66}$$

Therefore, the mismatch up to the second order in $\mathrm{d}\theta$ can be expressed as

$$1-\langle s(\theta)|s(\theta+\mathrm{d}\theta)\rangle = \frac{1}{2}\langle\partial_j s(\theta)|\partial_k s(\theta)\rangle \mathrm{d}\theta^j \mathrm{d}\theta^k, \\ = G_{jk}\mathrm{d}\theta^j\mathrm{d}\theta^k, \tag{1.67}$$

where the metric G_{jk} is one half of the Fisher matrix F_{jk}. At a given mismatch (say 0.03), the metric describes a hyper ellipse in the parameter space, which is used to place the templates in the parameter space [102]. The hyper ellipse determines the resolution of a template bank, and the ratio between the volume of the parameter and the volume of the hyper ellipse determines the number of templates required by a given mismatch. See more discussions in Chap. 13.

References

1. C.W. Misner, K.S. Thorne, J.A. Wheeler, *Gravitation* (W.H. Freeman, San Francisco, 1973)
2. B.S. Sathyaprakash, B.F. Schutz, Physics, astrophysics and cosmology with gravitational waves, Living Rev. Relat. **12**, 2 (2009). http://www.livingreviews.org/lrr-2009-2
3. P.C. Peters, J. Mathews, Gravitational radiation from point masses in a Keplerian orbit. Phys. Rev. **131**, 435–440 (1963)
4. M. Zimmermann, E. Szedenits, Jr., Gravitational waves from rotating and precessing rigid bodies: simple models and applications to pulsars. Phys. Rev. D **20**, 351–355 (1979)
5. R. Epstein, R.V. Wagoner, Post-Newtonian generation of gravitational waves. Astrophys. J. **197**, pt. 1, 717–723 (1975)
6. R.V. Wagoner, C.M. Will, Post-Newtonian gravitational radiation from orbiting point masses, Astrophys. J. **210**, pt. 1, 764–775 (1976)
7. K.S. Thorne, Multipole expansions of gravitational radiation. Rev. Mod. Phys. **52**, 299–339 (1980)
8. A.G. Wiseman, C.M. Will, Christodoulou's nonlinear gravitational-wave memory: evaluation in the quadrupole approximation. Phys. Rev. D **44**, R2945–R2949 (1991)
9. A.G. Wiseman, Coalescing binary systems of compact objects to (post)5/2-Newtonian order. II. Higher-order wave forms and radiation recoil. Phys. Rev. D **46**, 1517–1539 (1992)
10. A.G. Wiseman, Coalescing binary systems of compact objects to (post)5/2-Newtonian order. IV. The gravitational wave tail, Phys. Rev. D **48**, 4757–4770 (1993)
11. C.M. Will, A.G. Wiseman, Gravitational radiation from compact binary systems: gravitational waveforms and energy loss to second post-Newtonian order. Phys. Rev. D **54**, 4813–4848 (1996)
12. L.E. Kidder, C.M. Will, A.G. Wiseman, Coalescing binary systems of compact objects to (post)5/2-Newtonian order. III. Transition from inspiral to plunge. Phys. Rev. D **47**, 3281–3291 (1993)
13. T. Damour, The problem of motion in Newtonian and Einsteinian gravity, *Three Hundred Years of Gravitation* (Cambridge University Press, Cambridge, 1987)
14. T. Damour, B.R. Iyer, Multipole analysis for electromagnetism and linearized gravity with irreducible Cartesian tensors. Phys. Rev. D **43**, 3259–3272 (1991)
15. L. Blanchet, T. Damour, Post-Newtonian generation of gravitational waves. Annales de l'IHP Physique théorique (1989)
16. L. Blanchet, T. Damour, B.R. Iyer, C.M. Will, A.G. Wiseman, Gravitational-radiation damping of compact binary systems to second post-Newtonian order. Phys. Rev. Lett. **74**, 3515–3518 (1995)

17. L. Blanchet, T. Damour, B.R. Iyer, Gravitational waves from inspiralling compact binaries: energy loss and waveform to second-post-Newtonian order. Phys. Rev. D **51**, 5360–5386 (1995)
18. L. Blanchet, Gravitational radiation from post-Newtonian sources and inspiralling compact binaries. Living Rev. Relat. **9**, 4 (2006)
19. P. Jaranowski, G. Schäfer, Binary black-hole problem at the third post-Newtonian approximation in the orbital motion: static part. Phys. Rev. D **60**, 124003 (1999)
20. P. Jaranowski, G. Schäfer, The binary black-hole dynamics at the third post-Newtonian order in the orbital motion. Annalen der Physik, **512**(Series 8, Vol. 9)(3), 378–383 (2000)
21. P. Jaranowski, G. Schäfer, Third post-Newtonian higher order ADM Hamilton dynamics for two-body point-mass systems. Phys. Rev. D **57**, 7274–7291 (1998)
22. T. Damour, P. Jaranowski, G. Schäfer, Dimensional regularization of the gravitational interaction of point masses. Phys. Lett. B **513**, 147 (2001)
23. T. Damour, P. Jaranowski, G. Schäfer, Equivalence between the ADM-Hamiltonian and the harmonic-coordinates approaches to the third post-Newtonian dynamics of compact binaries. Phys. Rev. D **63**, 044021 (2001)
24. L. Blanchet, T. Damour, G. Esposito-Farese, Dimensional regularization of the third post-Newtonian dynamics of point particles in harmonic coordinates. Phys. Rev. D **69**, 124007 (2004)
25. L. Blanchet, T. Damour, G. Esposito-Farse, B.R. Iyer, Gravitational radiation from inspiralling compact binaries completed at the third post-Newtonian order. Phys. Rev. Lett. **93**, 091101 (2004)
26. V.C. de Andrade, L. Blanchet, G. Faye, Third post-Newtonian dynamics of compact binaries: Noetherian conserved quantities and equivalence between the harmonic-coordinate and ADM-Hamiltonian formalisms. Class. Quantum Gravity **18**, 753 (2001)
27. Y. Itoh, T. Futamase, New derivation of a third post-Newtonian equation of motion for relativistic compact binaries without ambiguity. Phys. Rev. D **68**, 121501 (2003)
28. L. Blanchet, T. Damour, G. Esposito-Farese, B. Iyer, Dimensional regularization of the third post-Newtonian gravitational wave generation from two point masses. Phys. Rev. D **71**, 124004 (2005)
29. L. Blanchet, B.R. Iyer, Hadamard regularization of the third post-Newtonian gravitational wave generation of two point masses. Phys. Rev. D **71**, 024004 (2005)
30. L. Blanchet, G. Faye, B.R. Iyer, B. Joguet, Gravitational-wave inspiral of compact binary systems to 7/2 post-Newtonian order. Phys. Rev. D **65**, 061501 (2002)
31. T. Damour, B. Iyer, B. Sathyaprakash, Comparison of search templates for gravitational waves from binary inspiral. Phys. Rev. D **63**, 044023 (2001)
32. A. Buonanno, Y. Chen, M. Vallisneri, Detection template families for gravitational waves from the final stages of binaryCblack-hole inspirals: nonspinning case. Phys. Rev. D **67**, 024016 (2003)
33. A. Buonanno et al., Comparison of post-Newtonian templates for compact binary inspiral signals in gravitational-wave detectors. Phys. Rev. D **80**, 084043 (2009)
34. T. Damour, Coalescence of two spinning black holes: an effective one-body approach. Phys. Rev. D **64**, 124013 (2001)
35. A. Buonanno, T. Damour, Effective one-body approach to general relativistic two-body dynamics. Phys. Rev. D **59**, 084006 (1999)
36. A. Buonanno, T. Damour, Transition from inspiral to plunge in binary black hole coalescences. Phys. Rev. D **62**, 064015 (2000)
37. T. Damour, P. Jaranowski, G. Schäfer, Determination of the last stable orbit for circular general relativistic binaries at the third post-Newtonian approximation. Phys. Rev. D **62**, 084011 (2000)
38. A. Pound, E. Poisson, B.G. Nickel, Limitations of the adiabatic approximation to the gravitational self-force. Phys. Rev. D **72**, 124001 (2005)
39. F. Pretorius, Evolution of binary black-hole spacetimes. Phys. Rev. Lett. **95**, 121101 (2005)

40. J.G. Baker, J. Centrella, D. Choi, M. Koppitz, J. van Meter, Gravitational-wave extraction from an inspiraling configuration of merging black holes. Phys. Rev. Lett. **96**, 111102 (2006)
41. M. Campanelli, C.O. Lousto, P. Marronetti, Y. Zlochower, Accurate evolutions of orbiting black-hole binaries without excision. Phys. Rev. Lett. **96**, 111101 (2006)
42. J.G. Baker et al., Getting a kick out of numerical relativity, Astrophys. J. Lett. **653**, L93 (2006)
43. M. Maggiore, Theory and experiments, *Gravitational Waves*, vol. 1 (Oxford University Press, Oxford, 2008)
44. M. Volonteri, F. Haardt, P. Madau, The assembly and merging history of supermassive black holes in hierarchical models of galaxy formation. Astrophys. J. Lett. **582**, 559 (2003)
45. A. Sesana, M. Volonteri, F. Haardt, The imprint of massive black hole formation models on the LISA data stream. Mon. Not. R. Astron. Soc. **377**(4), 1711–1716 (2007)
46. K.G. Arun et al., Massive black-hole binary inspirals: results from the LISA parameter estimation taskforce. Class. Quantum Gravity **26**, 094027 (2009)
47. A.J. Farmer, E.S. Phinney, The gravitational wave background from cosmological compact binaries. Mon. Not. R. Astron. Soc. **346**, 1197 (2003). arXiv:astro-ph/0304393
48. R. Brustein, M. Gasperini, M. Giovannini, G. Veneziano, Relic gravitational waves from string cosmology. Phys. Lett. B **361**, 45 (1995). arXiv:hep-th/9507017
49. M.S. Turner, Detectability of inflation produced gravitational waves. Phys. Rev. D **55**, 435 (1997). arXiv:astro-ph/9607066
50. K.N. Ananda, C.Clarkson, D. Wands, The cosmological gravitational wave background from primordial density perturbations. Phys. Rev. D **75**, 123518 (2007). arXiv:gr-qc/0612013
51. G. Ushomirsky, C. Cutler, L. Bildsten, Deformations of accreting neutron star crusts and gravitational wave emission. Mon. Not. R. Astron. Soc. **319**, 902–932 (2000)
52. J. Weber, Detection and generation of gravitational waves. Phys. Rev. **117**, 306 (1960)
53. K.S. Thorne, Gravitational radiation, in *300 Years of Gravitation*, ed. by S. Hawking, W. Israel (Cambridge University Press, Cambridge, 1987)
54. M.P. Mchugh et al., The Allegro gravitational wave detector. Int. J. Mod. Phys. D **09**, 229 (2000)
55. E. Mauceli et al., The Allegro gravitational wave detector: data acquisition and analysis. Phys. Rev. D **54**, 1264–1275 (1996)
56. I.S. Heng et al., Allegro: noise performance and the ongoing search for gravitational waves. Class. Quantum Gravity **19**, 1889 (2002)
57. A. de Waard et al., MiniGRAIL progress report 2001: the first cooldown. Class. Quantum Gravity **19**, 1935 (2002)
58. A. de Waard et al., MiniGRAIL, the first spherical detector. Class. Quantum Gravity **20**, S143 (2003)
59. A. de Waard et al., MiniGRAIL progress report 2004. Class. Quantum Gravity **22**, S215 (2005)
60. A. Abramovici et al., LIGO: the laser interferometer gravitational-wave observatory. Science **256**(5055), 325–333 (1992)
61. B.P. Abbott et al., LIGO: the laser interferometer gravitational-wave observatory. Rep. Prog. Phys. **72**, 076901 (2009)
62. http://en.wikipedia.org/wiki/LIGO
63. LIGO Laboratory Home Page for Interferometer Sensitivities, project homepage, LIGO/California Institute of Technology
64. B. Caron et al., The Virgo interferometer. Class. Quantum Gravity **14**(6), 1461 (1997)
65. B. Caron et al., The VIRGO interferometer for gravitational wave detection. Nucl. Phys. B, Proc. Suppl. **54** 167 (1997)
66. B. Willke et al., The GEO 600 gravitational wave detector. Class. Quantum Gravity **19**, 1377 (2002)
67. B. Willke et al., The GEO-HF project. Class. Quantum Gravity **23**, S207 (2006)
68. K. Somiya, Detector configuration of KAGRACthe Japanese cryogenic gravitational-wave detector. Class. Quantum Gravity **29**, 124007 (2012)

69. M. Punturo et al., The Einstein telescope: a third-generation gravitational wave observatory. Class. Quantum Gravity **27**, 194002 (2010)
70. S. Hild, Beyond the second generation of laser-interferometric gravitational wave observatories. Class. Quantum Gravity **29**, 124006 (2012)
71. The LISA Study Team, Laser interferometer space antenna for the detection and observation of gravitational waves: pre-phase a report. Max-Planck-Institute for Quantum Optics (1998)
72. K. Danzmann, the LISA Study Team, LISA - An ESA cornerstone mission for the detection and observation of gravitational waves. Adv. Space Res. **32**, 12331242 (2003)
73. The Gravitational Universe, The eLISA Constortium, Whitepaper submitted to ESA for the L2/L3 Cosmic Vision call. arXiv:1305.5720
74. P. Amaro-Seoane et al., eLISA: astrophysics and cosmology in the millihertz regime. GW Notes **6**, 4–110 (2013). arXiv:1201.3621
75. P. McNamara, S. Vitale, K. Danzmann, (on behalf of the LISA Pathfinder Science Working Team), LISA Pathfinder. Class. Quantum Grav. **25**, 114034 (2008)
76. M. Armano et al., LISA pathfinder: the experiment and the route to LISA. Class. Quantum Gravity **26**, 094001 (2009)
77. F. Antonucci et al., LISA pathfinder: mission and status. Class. Quantum Gravity **28**, 094001 (2011)
78. LISA Metrology System - Final Report, ESA ITT AO/1-6238/10/NL/HB. http://www.esa.int/Our_Activities/Observing_the_Earth/Copernicus/Final_reports
79. S. Kawamura et al., The Japanese space gravitational wave antennaDECIGO. Class. Quantum Gravity **23**, S125 (2006)
80. M. Ando et al., DECIGO and DECIGO pathfinder. Class. Quantum Gravity **27**, 084010 (2010)
81. J. Crowder, N.J. Cornish, Beyond LISA: exploring future gravitational wave missions. Phys. Rev. D **72**, 083005 (2005)
82. W. Ni, ASTROD-GW: overview and progress. Int. J. Mod. Phys. D **22**, 1341004 (2013)
83. Y. Wang et al., Octahedron configuration for a displacement noise-canceling gravitational wave detector in space. Phys. Rev. D **88**, 104021 (2013)
84. G. Hobbs et al., The international pulsar timing array project: using pulsars as a gravitational wave detector. Class. Quantum Gravity **27**, 084013 (2010)
85. G.H. Janssen et al., 40 years of pulsars: millisecond pulsars, magnetars and more, in *Proceedings of the AIP Conference*, vol. 983, ed. by C. Bassa, Z. Wang, A. Cumming, V.M. Kaspi (AIP, New York, 2008), pp. 633–635
86. F.A. Jenet et al., The North American Nanohertz observatory for gravitational waves.arXiv:0909.1058
87. R.N. Manchester, 40 years of pulsars: millisecond pulsars, magnetars and more, in *Proceedings of the AIP Conference*, vol. 983, ed. by C. Bassa, Z. Wang, A. Cumming, V.M. Kaspi (AIP, New York, 2008), pp. 584–592
88. J.W. Armstrong, Low-frequency gravitational wave searches using spacecraft Doppler tracking, Living Rev. Relat. **9**, 1 (2006)
89. F.B. Estabrook, H.D. Wahlquist, Response of Doppler spacecraft tracking to gravitational radiation, Gen. Relat. Gravit. **6**(5), 439–447 (1975)
90. A.M. Cruise, An electromagnetic detector for very-high-frequency gravitational waves. Class. Quantum Gravity **17**, 2525 (2000)
91. F.-Y. Li, M.-X. Tang, D.-P. Shi, Electromagnetic response of a Gaussian beam to high-frequency relic gravitational waves in quintessential inflationary models. Phys. Rev. D **67**, 104008 (2003)
92. P. Jaranowski, A. Królak, Gravitational-wave data analysis. Formalism and sample applications: the Gaussian case, Living Rev. Relat. **8**, 3 (2005)
93. N.J. Cornish, Gravitational wave astronomy: needle in a haystack (2012). arXiv:1204.2000v1
94. C. Kittel, *Elementary Statistical Physics* (Wiley, New York, 1958)
95. C. Chatfield, *The Analysis of Time Series-An Introduction*, 4th edn. (Chapman and Hall, London, 1989), pp. 94–95

96. R.W. Hellings, Spacecraft-Doppler gravity-wave detection. I. Theory. Phys. Rev. D **23**, 832–843 (1981)
97. K.A. Arnaud et al., (the MLDC Task Force), A how-to for the mock LISA data challenges. AIP Conf. Proc **873**, 625 (2006)
98. L.S. Finn, Detection, measurement, and gravitational radiation. Phys. Rev. D **46**, 12 (1992)
99. G.E.P. Box, G.C. Tiao, *Bayesian Inference in Statistical Analysis* (Addison-Wesley Publishing Co., Reading, 1973)
100. N. Wiener, *Extrapolation, Interpolation, and Smoothing of Stationary Time Series* (Wiley, New York, 1949)
101. M. Vallisneri, Use and abuse of the Fisher information matrix in the assessment of gravitational-wave parameter-estimation prospects. Phys. Rev. D **77**, 042001 (2008)
102. B. Owen, Search templates for gravitational waves from inspiraling binaries: choice of template spacing. Phys. Rev. D **53**, 6749 (1996)

Chapter 2
LISA Data Processing Chain

Abstract The complete LISA data processing chain is described in this chapter, which consists of the simulation of the orbits, the simulation of gravitational wave signals, the simulation of various LISA measurements, the pre-processing stage, the time-delay interferometry techniques, and the astrophysical data analysis. The role and the goal of the pre-processing stage—first stage of LISA data analysis—is established and discussed for the first time.

2.1 Introduction

LISA (Laser Interferometer Space Antenna) [1, 2] is a proposed space-borne gravitational wave (GW) detector, aiming at various kinds of GW signals in the low frequency band between 0.1 mHz and 1 Hz. LISA consists of three identical spacecraft (S/C), each individually following a slightly elliptical orbit around the sun, trailing the Earth by about 20°. These orbits are chosen such that the three S/C retain, as much as possible, an equilateral triangular configuration with an arm length of about 5×10^9 m. This is accomplished by tilting the plane of the triangle by about 60° out of the ecliptic. Graphically, the triangular configuration makes a cartwheel motion around the Sun. As mentioned before, eLISA [3, 4] is a (evolving) variation of LISA, which consists of one mother S/C and two daughter S/C, separated from each other by 1×10^9 m. Although the configurations are slightly different, the principles and the techniques are equally applicable. Therefore, we will mainly focus on LISA hereafter.

Since GWs are propagating spacetime perturbations, they induce proper distance variations between test masses (TMs) [5], which are free-falling references inside the S/C shield. LISA measures GW signals by monitoring distance changes between the S/C. Spacetime is very stiff. Usually, even a fairly strong GW still produces only spacetime perturbations of order about 10^{-21} in dimensionless strain. This strain amplitude can introduce distance changes at the pm level in a 5×10^9 m arm length. Therefore, a capable GW detector must be able to monitor distance changes with this accuracy. The extremely precise measurements are supposed to be achieved by large laser interferometers. LISA makes use of heterodyne interferometers with coherent

Y. Wang, *First-stage LISA Data Processing and Gravitational Wave Data Analysis*,
Springer Theses, DOI 10.1007/978-3-319-26389-2_2

offset-phase locked transponders [6]. The phasemeter [7] measurements at each end are combined in postprocessing to form the equivalent of one or more Michelson interferometers. Information of proper-distance variations between TMs is contained in the phasemeter measurements.

Unlike the several existing ground-based interferometric GW detectors [8–12], the armlengths of LISA are varying significantly with time due to celestial mechanics in the solar system. As a result, the arm lengths are unequal by about 1 % (5×10^7 m), and the dominating laser frequency noise will not cancel out. The remaining laser frequency noise would be stronger than other noises by many orders of magnitude. Fortunately, the coupling between distance variations and the laser frequency noise is very well known and understood. Therefore, we can use time-delay interferometry (TDI) techniques [13–21], which combine the measurement data series with proper time delays, in order to cancel the laser frequency noise to the desired level.

However, the performance of TDI [18, 22] depends largely on the knowledge of armlengths and relative longitudinal velocities between the S/C, which are required to determine the correct delays to be adopted in the TDI combinations. In addition, the raw data are referred to the individual spacecraft clocks, which are not physically synchronized but independently drifting and jittering. This timing mismatch would degrade the performance of TDI variables. Therefore, they need to be referred to a virtual common "constellation clock" which needs to be synthesized from the inter-spacecraft measurements. Simultaneously, one also needs to extract the inter-spacecraft separations and synchronize the time-stamps properly to ensure the TDI performance.

2.2 Simulating the Whole LISA Data Processing Chain

In this section, I will talk about the perspective of a complete LISA simulation. The future goal is to simulate the entire LISA data processing chain as detailed as one can, so that one will be able to test the fidelity of the LISA data processing chain, verify the science potential of LISA and set requirements for the instruments. The flow chart of the whole simulation is shown in Fig. 2.1. In the following, I will discuss the role and the main task of each step.

2.2.1 LISA Orbits Simulator

The first step is to simulate LISA orbits under the solar system dynamics. It should provide the position and velocity of each TM, or roughly S/C, as functions of some nominal time, e.g. UTC (Coordinated universal time) for subsequent simulations. Since TDI requires knowledge of the delayed armlengths (or light travel times) to meter accuracies [23], and the pre data processing algorithms could hopefully determine the delayed armlengths to centimeter accuracies, the provided position

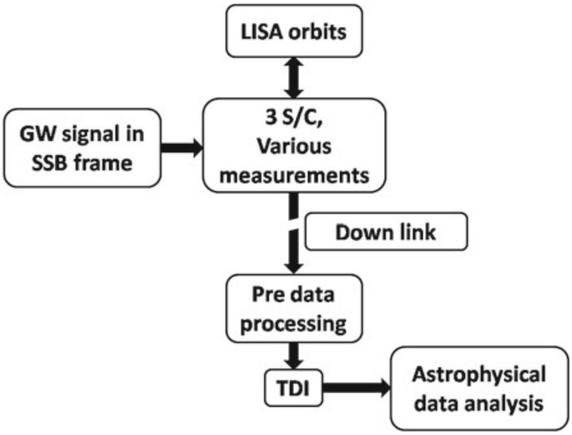

Fig. 2.1 LISA data processing chain

information should be more accurate than centimeters. Recall that 1 AU is of order 10^{11} m. The dynamic range here is 13 orders of magnitude, which is smaller than the machine accuracy (15–16 digits). However, the GW-induced arm-length variation for LISA is at the picometer level [23], which is 25 orders of magnitude smaller than 1 AU. One could in principle use extended precision, but that might be computationally too expensive. Luckily, GWs in the TT gauge do not change the coordinates of the TMs. Thus, one can ignore GWs when simulating LISA orbits.

One other issue is the sampling rate. The LISA onboard measurements will be down-sampled and transferred to the Earth at about Hz sampling rate (e.g. 3 Hz). So the position and velocity information should be provided to the centimeter precision at Hz sampling rate. In one year, there are about 10^8 samples at this sampling rate. One can design an orbit integrator with sub second integration time-steps, but it is inefficient. Instead, one can design an orbit integrator with adaptive large integration steps and then interpolate the orbits to centimeter precision. However, the accuracy of the interpolation scheme needs to be checked carefully.

The last issue in this step is to choose a model of dynamics. In principle, one should use the best known ephemeris (with trajectories of all the solar system planets) and the solar system dynamics to a sufficient PN order [24]. For simplicity and speed concern, sometimes one can also use Kepler orbits, or even simpler, analytical orbits (Taylor expansion of Kepler orbits to certain order of eccentricity) in the right place. One should make sure that it is consistent with all other steps.

2.2.2 Simulating GWs

The second step is to simulate GWs. There are various kinds of GW sources [23, 25] in the LISA band, such as massive black hole (MBH) binaries, extreme-mass-ratio inspirals (EMRIs), intermediate-mass-ratio inspirals (IMRIs), galactic white dwarf binaries (WDBs), gravitational wave cosmic background etc. In the source frame, these GW waveforms are generated either from the dynamic equations or phenomenological waveform models. For some purposes, one can also simply use sinusoidal GW signals as test signals.

2.2.3 Simulating Measurements

The third step is to simulate the measurements as detailed as needed, which in turn requires the simulation of the evolution of the S/C internal environments, e.g. how does the attitude of TMs evolve, how does the frequency of the ultra-stable oscillator (USO) evolve, how does the temperature evolve, how does the laser frequency evolve? Since there are many sources of disturbance [26–28], one should first only take into account the critical ones. The less critical features can be ignored selectively. The irrelevant features should be ignored.

The TMs are drag-free in only one dimension each, which is along the direction of the laser beam. The other two transverse dimensions are controlled. Hence, their actual orbits may deviate from geodesics (i.e. orbits of three dimensional drag-free TMs). The deviation is small over short periods, but sizable after a few months accumulation.

Usually, these deviations are ignored in simulations. If one wants to simulate this effect, the orbits calculation and the measurements simulation must be integrated. Whenever the TMs tends to fall off the orbits, one should make corrections and calculate the new orbits. Mathematically, the equations of motion are augmented with the equations of the active control and the disturbances. The whole set of differential equations should be solved and evolved together.

There are many measurements in LISA. The main ones are science measurements, ranging measurements, clock side band beatnotes, S/C positions and clock offsets observed by the deep space network (DSN). There are many more measurements, such as various auxiliary measurements, incident beam angle measured by differential wavefront sensing (DWS). In principle, all the relevant measurements need to be simulated. The simulation in turn can guide the experiments and the design, telling us which measurements are useful and which ones need to be transferred back to the Earth at which sampling rate.

Another important issue is to simulate various kinds of noise sources, such as the laser-frequency noise, clock jitters, the readout noise, the acceleration noise. These noises are generated either from their PSD or from physical models. In the end, the noises and the GWs signals are both added to the measurements. For simplicity, usually stationary Gaussian noise (white or colored) is used, although real instruments in general produce more complicated noise.

2.2.4 Down Link

The ‘down link’ is referred to as a procedure of transferring the onboard measurement data back to Earth, which is also an important step in the simulation. Since the beatnotes between the incoming laser beam and the local laser are in the MHz range, the sampling rate of ADCs should be at least twice that, i.e. at least 40–50 MHz. The phasemeter prototype developed in the Albert Einstein Institute Hannover for ESA uses 80 MHz [29]. Due to the limited bandwidth of the down link to Earth, measurement data at this high sampling rate cannot be transferred to Earth. Instead, they are low-pass filtered and then down-sampled to a few Hz (e.g. 3 Hz). The raw data received on Earth are at this sampling rate.

For simulation concerns, generating measurement data at 80 MHz with a total observation time of a few years is computationally expensive and unnecessary. Instead, these measurements are simulated at a few tens to a few hundreds of Hz.

It is worth clarifying that, up to this point, the simulation of the S/C and GWs was done with complete knowledge of ‘mother nature’. From the next subsection ‘pre data processing’ on, comes the the simulated processing of the down-linked data, where we have only the raw data received on Earth, but other informations such as the S/C status are unknown.

2.2.5 Pre Data Processing

The next step is the so-called pre data processing. The main task is to synchronize the raw data received at the Earth station and to determine the armlength accurately. In addition, pre data processing aims to establish a convenient framework to monitor the system performance, to compensate unexpected noise and to deal with unexpected cases such as when one laser link is broken for a short time.

The armlength information is contained in the ranging measurements, which compare the laser transmission time at the remote S/C and the reception time at the local S/C. Since these two times are measured by different clocks (or USOs), which have different unknown jitters and biases, the ranging data actually contain large biases. For instance, high-performance (not necessarily the best) space-qualified crystal oscillators, such as oven controlled crystal oscillators [30], have a frequency stability of about 10^{-7--8}. This would lead to clock biases larger than one second in three years, which would result in huge biases in the ranging measurements.

In fact, all the measurements taken in one S/C are labeled with the clock time in that S/C. This means all the time series contain clock noise. Time series from different S/C contain different clock noise. These unsynchronized, dirty and noisy time series need to be pre-processed in order to become usable for TDI.

Pre data processing has been ignored for long. It is one of the main topics of this thesis.

2.2.6 TDI Simulation

As mentioned previously, TDI has been well studied in the literature [14–21]. Laser frequency noise is the frequency instability of the laser source. For a normal Michelson interferometer, the laser beams travelling in the two arms originate from the same laser source, thus they share common laser frequency noise. At the photon detector, one measures the phase (or frequency) variation of the beatnote of the two laser beams. The frequency noise is canceled out when the two arms have the same length, hence not degrading the measurements.

However, in the LISA case, the S/C are far apart. The telescope can capture only a very small fraction of the remote laser beam, thus it is impossible to reflect the same laser light back to the remote S/C. The local photon detector measures the beatnote between the received weak laser beam and the local laser. Without the offset phase locking scheme, the two laser beams are generated by different laser sources, hence they contain different frequency noise. As a consequence, the laser frequency remains in the measurements. With the offset phase locking scheme [6], the laser frequency noise still remains, due to the unequal arm lengths. Its power spectral density is about 8–9 orders of magnitude higher than the designed sensitivity. Currently, the only solution is to phase-lock the remote laser, record each single-way measurement, properly recombine these single-way measurements in the TDI post-processing stage, virtually forming an equal-arm Michelson interferometer. In this step, one uses the ranging and the time information from pre data processing to properly shift the phasemeter measurements accordingly and recombine them.

2.2.7 Astrophysical Data Analysis

In this final step, the task is to dig out GW signals from the data and extract astrophysical information—in short, detection and parameter estimation. At this stage, we have relatively clean and synchronized data labeled with UTC time stamps. Still, the GW signals are weak compared to the remaining noise. As a result, one needs to implement matched filtering techniques to obtain optimal SNR. We will come to this again in detail in other chapters.

References

1. The LISA Study Team, Laser interferometer space antenna for the detection and observation of gravitational waves: Pre-phase a report. Max-Planck-Institute for quantum optics (1998)
2. K. Danzmann the LISA Study Team, LISA—an ESA cornerstone mission for the detection and observation of gravitational waves. Adv. Space Res. **32**, 12331242 (2003)
3. The Gravitational Universe, The eLISA constortium, Whitepaper submitted to ESA for the L2/L3 cosmic vision call. arXiv:1305.5720

4. P. Amaro-Seoane et al., eLISA: Astrophysics and cosmology in the millihertz regime. GW Notes **6**, 4–110 (2013). arXiv:1201.3621
5. L. Carbone et al., Achieving geodetic motion for lisa test masses: ground testing results. Phys. Rev. Lett. **91**, 151101 (2003)
6. P.W. McNamara, Weak-light phase locking for LISA. Class. Quantum Gravity **22**, S243–S247 (2005)
7. D. Shaddock, B. Ware, P. Halverson, R.E. Spero, B. Klipstein, Overview of the LISA phasemeter. 6th international LISA symposium, Greenbelt, Maryland, 19–23 June 2006
8. A. Abramovici et al., LIGO: the laser interferometer gravitational-wave observatory. Science **256**(5055), 325–333 (1992)
9. B.P. Abbott et al., LIGO: the laser interferometer gravitational-wave observatory. Rep. Prog. Phys. **72**, 076901 (2009)
10. B. Willke et al., The GEO 600 gravitational wave detector. Class. Quantum Gravity **19**, 1377 (2002)
11. B. Willke et al., The GEO-HF project. Class. Quantum Gravity **23**, S207 (2006)
12. B. Caron et al., The VIRGO interferometer for gravitational wave detection. Nucl. Phys. B, Proc. Suppl. **54**, 167 (1997)
13. G. de Vine, B. Ware, K. McKenzie, R.E. Spero, W.M. Klipstein, D.A. Shaddock, Experimental demonstration of time-delay interferometry for the laser interferometer space antenna. Phys. Rev. Lett. **104**, 211103 (2010)
14. T. Massimo, D. Shaddock, J. Sylvestre, J. Armstrong, Implementation of time-delay interferometry for LISA. Phys. Rev. D **67**, 122003 (2003)
15. J.W. Armstrong et al., Time-delay interferometry for space-based gravitational wave searches. ApJ **527**, 814–826 (1999)
16. N.J. Cornish, R.W. Hellings, The effects of orbital motion on LISA time delay interferometry. Class. Quantum Gravity **20**, 4851 (2003)
17. D.A. Shaddock, B. Ware, R.E. Spero, M. Vallisneri, Postprocessed time-delay interferometry for LISA. Phys. Rev. D **70**, 081101(R) (2004)
18. M. Vallisneri, Synthetic LISA: simulating time delay interferometry in a model LISA. Phys. Rev. D **71**, 022001 (2005)
19. T.A. Prince, M. Tinto, S.L. Larson, J.W. Armstrong, LISA optimal sensitivity. Phys. Rev. D **66**, 122002 (2002)
20. M. Tinto, S.V. Dhurandhar, Time-delay interferometry, Living Rev. Relativ. 8(4) (2005). arXiv:gr-qc/0409034. http://www.livingreviews.org/lrr-2005-4
21. M. Otto, G. Heinzel, K. Danzmann, TDI and clock noise removal for the split interferometry configuration of LISA. Class. Quantum Gravity **29**, 205003 (2012)
22. A. Petiteau et al., LISACode: a scientific simulator of LISA. Phys. Rev. D. **77**, 023002 (2008)
23. LISA International Science Team 2011, LISA assessment study report (Yellow Book) (European Space Agency) ESA/SRE(2011) 3. http://sci.esa.int/science-e/www/object/index.cfm?fobjectid=48364
24. E.M. Standish et al., Orbital ephemerides of the Sun, Moon, and Planets, in *Explanatory Supplement to the Astronomical Almanac*, ed. by P.K. Seidelmann (University Science Books, Mill Valley, 1992), pp. 279–323
25. S. Babak et al., Report on the second mock LISA data challenge. Class. Quantum Gravity **25**, 114037 (2008)
26. P.L. Bender, LISA sensitivity below 0.1 mHz. Class. Quantum Gravity **20**, S301–S310 (2003)
27. R.T. Stebbins et al., Current error estimates for LISA spurious accelerations. Class. Quantum Gravity **21**, S653–S660 (2004)
28. W.M. Folkner, F. Hechler, T.H. Sweetser, M.A. Vincent, P.L. Bender, LISA orbit selection and stability. Class. Quantum Gravity **14**, 1405–1410 (1997)
29. O. Gerberding et al., Phasemeter core for intersatellite laser heterodyne interferometry: modelling, simulations and experiments. Class. Quantum Gravity **30**(235029), 16 (2013)
30. Space oven controlled crystal oscillator. http://www.q-tech.com/assets/datasheets/spaceOCXO.pdf

Chapter 3
Applying the Kalman Filter to a Simple Case

Abstract The very basic formulas of a Kalman filter with discrete time are derived in this chapter. A simplified LISA problem is considered as an introductory example, where the pseudo-ranging measurements and the Doppler measurements from a single laser link of LISA are processed via a standard Kalman filter. The clock errors have been ignored in this simple example. The simulation results show that the Kalman filter is able to reduce the ranging noise under these assumptions.

3.1 Introduction

As mentioned in the previous chapter, in the whole LISA data processing chain, pre data processing is a crucial step, which has been ignored for long time. It is one of the main tasks of this thesis. The main goal of this step is to synchronize the clocks and to extract the ranging information. We expect this problem to be solved by an optimal filter (Kalman-like) [1, 2], since we know the dynamic model of the whole LISA constellation (i.e. solar system dynamics, the power spectral density of clock jitters, etc.). This kind of knowledge is complementary to phasemeter raw measurements [3]. Thus, if one combines the information from the measurements and that from the system model, it is possible to continuously calculate optimal estimates for the armlengths, the Doppler velocities and the clock jitters. In this chapter, we will introduce the basic form of Kalman filter, and then apply it to a simplified LISA ranging problem.

3.2 Kalman Filter

A very natural and clever way to combine complementary information is the famous Kalman filter, a data analysis technique named after Rudolf E. Kalman. Kalman filter is the optimal linear filter in the least square error sense on condition that both the dynamics of the system and the observation function are linear and the noises are white Gaussian. To be specific, the linearly dependent dynamics can be expressed as

Y. Wang, *First-stage LISA Data Processing and Gravitational Wave Data Analysis*,
Springer Theses, DOI 10.1007/978-3-319-26389-2_3

$$x_k = F_{k-1}x_{k-1} + B_{k-1}u_{k-1} + w_{k-1} \tag{3.1}$$

where x_k is the state vector (a column vector here) of the system at time $t = t_k$, describing the instantaneous state of the system (e.g. the positions, the velocities, the clock jitters); u_k is the so-called control vector with known components, which can be ignored in the simplified case; w_k is the process noise vector and assumed to be a zero-mean white-Gaussian random variable with known covariance matrix; F_k and B_k are matrices of proper size (determined by the dimension of x_k and u_k) which describe how the control input and the state at an earlier time affect the state at present. Furthermore, if the observations are linearly dependent on the state vector, they can be modeled as

$$y_k = H_k x_k + v_k \tag{3.2}$$

where H_k is a matrix of proper size, describing the relation between the state vector x_k and the measurements y_k; v_k is the measurement noise which is also zero-mean, white-Gaussian, and in addition uncorrelated with w_k. Hereafter, we denote the covariance matrices of w_k and v_k respectively by W_k and V_k. Furthermore, we denote the estimates of the state vector along with their covariance matrices at time t_k excluding and including the measurements at that time respectively by

$$\hat{x}_k^- = E[x_k | y_1, y_2, \ldots, y_{k-1}], \tag{3.3}$$

$$P_k^- = E[(x_k - \hat{x}_k^-)(x_k - \hat{x}_k^-)^T] \tag{3.4}$$

and

$$\hat{x}_k^+ = E[x_k | y_1, y_2, \ldots, y_k], \tag{3.5}$$

$$P_k^+ = E[(x_k - \hat{x}_k^+)(x_k - \hat{x}_k^+)^T]. \tag{3.6}$$

If we can propagate the estimate from $\hat{x}_{k-1}^+$ to $\hat{x}_k^-$ then to $\hat{x}_k^+$, we should be able to filter all the data set step by step starting from an initialization such as $\hat{x}_0^+ = E[x_0]$, $P_0^+ = E[(x_0 - \hat{x}_0^+)(x_0 - \hat{x}_0^+)^T]$. It's quite straightforward to calculate $\hat{x}_k^-$ from $\hat{x}_{k-1}^+$. In this step, there are no additional measurements taken, hence the only thing we can make use of is the dynamic equation. Since w_k is zero-mean white Gaussian, its most probable value is $w_k = 0$. Therefore,

$$\hat{x}_k^- = F_{k-1}\hat{x}_{k-1}^+ + B_{k-1}u_{k-1}, \tag{3.7}$$

$$P_k^- = F_{k-1}P_{k-1}^+ F_{k-1}^T + W_{k-1}. \tag{3.8}$$

To obtain $\hat{x}_k^+$ from $\hat{x}_k^-$, we need to minimize the trace of P_k^+, which is the sum of the squares of the estimation errors after including the measurements at time t_k. A linear filter can be put into the following form

$$\hat{x}_k^+ = \hat{x}_k^- + K_k(y_k - H_k\hat{x}_k^-), \tag{3.9}$$

which means that if the prediction $H_k \hat{x}_k^-$ perfectly matches the measurements y_k, the estimates after the observation of y_k should be the same as before this observation. K_k is a matrix to be determined. (It is usually called Kalman gain when determined.) It can be easily shown that

$$\begin{aligned} P_k^+ &= E[(x_k - \hat{x}_k^+)(x_k - \hat{x}_k^+)^T] \\ &= (I - K_k H_k) P_k^- (I - K_k H_k)^T + K_k V_k K_k \end{aligned} \tag{3.10}$$

Letting $\partial\,(\mathrm{tr} P_k^+)/\partial K_k = 0$, we obtain

$$K_k = P_k^- H_k^T (H_k P_k^- H_k^T + V_k)^{-1} \tag{3.11}$$

With this Kalman gain, we can update $\hat{x}_k^-$ and P_k^- to $\hat{x}_k^+$ and P_k^+. Up to now, we have derived all the formulae of the standard Kalman filter.

For a given discrete system model,

$$x_k = F_{k-1} x_{k-1} + B_{k-1} u_{k-1} + w_{k-1}, \tag{3.12}$$
$$y_k = H_k x_k + v_k, \tag{3.13}$$
$$E(w_k w_j^T) = W_k \delta_{k,j}, \tag{3.14}$$
$$E(v_k v_j^T) = V_k \delta_{k,j}, \tag{3.15}$$
$$E(w_k v_j^T) = 0, \tag{3.16}$$

we summarize the basic Kalman filter formulae as follows:

1. Initialize the state vector and the covariance matrix

$$\hat{x}_0^+, P_0^+. \tag{3.17}$$

2. Calculate the a priori estimate of the subsequent state

$$\hat{x}_k^- = F_{k-1} \hat{x}_{k-1}^+ + B_{k-1} u_{k-1}, \tag{3.18}$$
$$P_k^- = F_{k-1} P_{k-1}^+ F_{k-1}^T + W_{k-1}. \tag{3.19}$$

3. Calculate the Kalman gain

$$K_k = P_k^- H_k^T (H_k P_k^- H_k^T + V_k)^{-1}. \tag{3.20}$$

4. Correct the a priori estimate with the new measurements

$$\hat{x}_k^+ = \hat{x}_k^- + K_k (y_k - H_k \hat{x}_k^-), \tag{3.21}$$
$$P_k^+ = (I - K_k H_k) P_k^- (I - K_k H_k)^T + K_k V_k K_k^T. \tag{3.22}$$

3.3 A GPS Example

The Kalman filter derived above is extremely useful in the tracking problem in global positioning system (GPS) [4, 5] user data processing. The goal here is to estimate the user's position and clock bias continuously. The measurements can be formulated as follows

$$\rho_i = |(\vec{x}_i - \vec{x}_u)| + c\delta t_u, \tag{3.23}$$

where the so-called pseudo-range ρ_i $(i = 1, 2, \ldots, n_{\text{sat}}, \text{ with } n_{\text{sat}} \geq 4)$ are the ranging measurements from four different satellites, $\vec{x}_i$ are the position of these satellites, $\vec{x}_u$ and δt_u are the position and clock bias of the user. There are four unknowns in the state vector (three components of $\vec{x}_u$ and δt_u) to be estimated and at least four measurements. These unknowns are functions of the same time or time step. Thus, the problem is quite well posed for a Kalman filter after a straightforward linearization of the observation equations. However, we will see in the next section that the LISA system is way more complicated.

3.4 The LISA Case

LISA consists of three identical spacecraft sending laser beams to each other. Each spacecraft in the constellation follows a nearly ellipsoidal orbit. For that reason, the whole constellation appears to proceed in a cartwheel motion. Hence, the travel time of the laser beam transmitted from spacecraft i to spacecraft j differs from that of the laser beam traveling in the opposite direction (the so-called Sagnac effect). Consequently, there are six laser links in total, monitoring the inter-spacecraft quantities. For the convenience of data analysis, we model these quantities respectively as the arm lengths L_{ij} , the longitudinal Doppler velocities v_{ij} , the differences of clock jitters (derived from clock sideband to clock sideband beat note) c_{ij} , measured by the laser traveling from spacecraft i to spacecraft j, where $i, j = 1, 2, 3, i \neq j$. There is additive measurement noise in all of these quantities. In addition, c_{ij} contains the difference of clock bias, which also can be treated as noise sometimes. The final goal is now to suppress all this noise and estimate the difference of the clock bias in order to make TDI variables work properly.

In principle, if we want to reduce the noise in the measurements purely through data analysis techniques, we need additional information or knowledge. What we have in hand are the LISA orbits, which are determined by the dynamics of the solar system, as well as the power spectral density (PSD) of the clock jitter, which can be measured on the earth before launch. Besides, we temporarily assume all the measurement noise to be zero-mean white Gaussian noise. Under this assumption, we may somehow roughly estimate the covariance matrices of the noise by analyzing the raw data, because gravitational wave signals are much weaker than the noise sources before the cancelation of laser frequency noise and the annual change caused by the solar system dynamics is out of band. In fact, we can also get some very rough idea of these noise spectra even from the experiments on the earth. With the help of this additional information, we have somehow complementary knowledge about the whole LISA system.

The next thing to do is to fuse all the information to get less noisy estimates with a Kalman filter. As indicated before, the Kalman filter for LISA is much more complicated than that for GPS ranging. The raw ranging measurements of LISA in Newton limit can be put into the following form

$$\begin{aligned}\rho_{ij} &= |(\vec{x}_j(T+\delta t_j(T)) - \vec{x}_i(T+\delta t_j(T) - L_{ij}/c)| \\ &\quad + c(\delta t_i(T+\delta t_j(T) - L_{ij}/c)) - \delta t_j(T)) \end{aligned} \tag{3.24}$$

where ρ_{ij}, $(i, j = 1, 2, 3, i \neq j)$ stands for the raw ranging data measured by the laser link from spacecraft i to spacecraft j, T is the unknown fiducial time, δt_i is the clock jitter of each clock, c is the speed of light and the position of spacecraft i is denoted by $\vec{x}_i$ which of course is a function of time. Obviously, the position and the clock jitter of each spacecraft appear at three different unknown times. Thus, there are in total $3 \times 4 \times 3 = 36$ unknowns while only 6 measurements are performed. Mathematically, this means the system is not fully determined. Physically, the change in position and orientation of the LISA triangle as a whole in fact does not affect the results of ranging measurements, so they can not be determined purely from ranging measurements. Another problem is that the state of each spacecraft (the position and the clock jitter as functions of time) appears several times at different unknown time. This makes the LISA problem significantly different from the standard Kalman filter model. Furthermore, the strong nonlinearity also make the problem more complicated.

3.5 Simulation Results

As a first step, we build a separate Kalman filter for each link. Therefore, there are in total six Kalman filters running separately. The state vector in each Kalman filter consists of the position, velocity and clock jitter of the receiver spacecraft at present and that of the transmitter spacecraft at an unknown delayed time. If we artificially shift the time of the transmitter to make it roughly the same as the receiver, the state vector specified for each laser link involves only the status of two spacecrafts at the same time step. The advantage of this method is that it fits in the Kalman filter form (3.1) and (3.2) while keeps closely tracking the states of the pair of spacecrafts. However, it has the disadvantage that different Kalman filters for different laser links do not exchange information even though they have at least one spacecraft in common. The number of components of the state vector is still much bigger than the number of measurements for each laser link.

In the simulation, we temporarily ignore the DC values of all clock biases and focus on the noise suppression in armlengths and Doppler velocities, since six separate Kalman filters without communication between the small filters would not be adequate for clock biases correction.

Figures 3.1 and 3.2 show the simulation results of noise reduction for armlength measurements and Doppler velocity measurements. In Fig. 3.2, the blue points display the deviation of the raw measurements from the true longitudinal velocities, while the red points show the differences between the filter outputs and the true values. It can be seen clearly that the filter outputs converge very fast to the true Doppler velocities. The standard deviation of the filtered Doppler velocities is more than an order of magnitude below the raw measurements. Figure 3.1 shows roughly the same behavior for the armlength estimation except for the small bump of the red line in the beginning part. This is because the influence of the dynamics on the armlengths

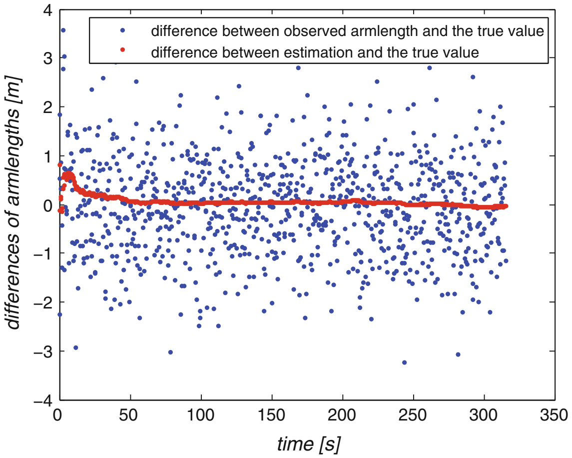

Fig. 3.1 Noise suppression in the armlength measurements

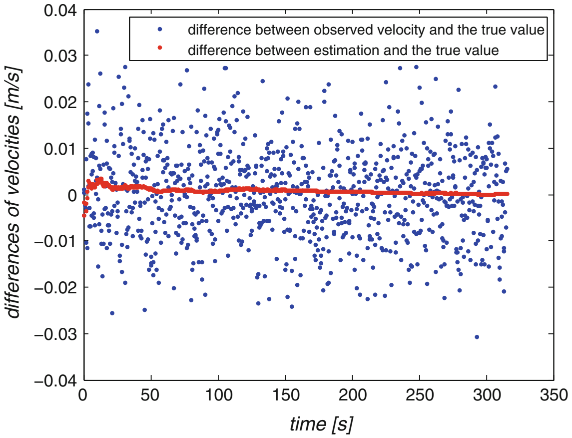

Fig. 3.2 Noise suppression in the Doppler velocity measurements

is weaker than that on the Doppler velocities, which leads to a slower convergence in armlength estimation. What can be done is to take the last filtered state as the new initial state and run the Kalman filter backward in time, since the dynamical model is reversible. This technique is usually called ‘smoothing’.

References

1. R.E. Kalman, A new approach to linear filtering and prediction problems. Trans. ASME J. Basic Eng. **82**(1), 35–45 (1960)
2. D. Simon, *Optimal State Estimation* (Wiley, Hoboken, 2006)
3. G. Heinzel et al., Auxiliary functions of the laser link: ranging, clock noise transfer and data communication. Class. Quantum Gravity **28**, 094008 (2011)
4. B. Hofmann-Wellenhof, H. Lichtenegger, J. Collins, *Global Positioning System: Theory and Practice* (Springer, Wien, 1993)
5. M.S. Grewal, A.P. Andrews, *Kalman Filtering* (Wiley, Hoboken, 2008)

Chapter 4
The Inter-spacecraft Measurements

Abstract The inter-satellite laser communication of LISA provides three types of measurements, (i) the beatnote between the carrier frequencies of the local laser and the remote laser, called the science measurements or the Doppler measurements, which measures the gravitational wave signal, (ii) the beatnotes of the clock side bands modulated onto the laser, which tries to measure the relative frequency drift of the clocks, (iii) the correlation of the pseudo-random code modulated onto the laser, called the ranging measurements, which intends to measure the absolute distance between the spacecraft. These measurements are described and modelled in details in this chapter. The timing errors and the frequency errors of the clocks are also introduced.

4.1 Introduction

Previously, we have designed a Kalman filter for a single link of LISA, where we have assumed Newtonian links (meaning that we calculate the light travelling time between spacecraft purely under Newtonian dynamics) and ignored clock noise. In this chapter, we start to build a Kalman filter for all the laser links of LISA with clock noise in the measurements.

Let us first look at the inter-spacecraft measurements in details. There are altogether six drag-free test masses in LISA constellation, two within each S/C. The distance variations between remote test masses are measured by heterodyne laser interferometry (with laser wavelength $\lambda = 1064\,\text{nm}$) with a designed noise level of 1–10 pm/Hz$^{1/2}$ [1].

Due to the solar system dynamics, the whole LISA constellation cannot be a perfect rigid equilateral triangle. In fact, the arm lengths vary by about one percent [2] annually; the relative longitudinal velocities between S/Cs are minimized to a level below 15 m/s [3]. This variation can cause a Doppler shift in the frequency beatnote of about 15 MHz for a $\lambda = 1064\,\text{nm}$ laser. Just to have some margin, it is designed in LISA that one needs to be able to measure the frequency beatnote at 20 MHz. On the other hand, the 1 pm/Hz$^{1/2}$ requirement for the $\lambda = 1064\,\text{nm}$ laser approximately translates to 1 μcycle/Hz$^{1/2}$ precision. To measure a frequency beatnote at 20 MHz at

Y. Wang, *First-stage LISA Data Processing and Gravitational Wave Data Analysis*,
Springer Theses, DOI 10.1007/978-3-319-26389-2_4

1 μcycle/Hz$^{1/2}$ accuracy requires the timing stability of the sampler in the phasemeter to be better than 50 fs/Hz$^{1/2}$. Such a space-qualified stable clock does not exist. This is really a sorry situation. To solve this problem, we try to measure the clock noise and eliminate it in a post-processing stage. Using about ten percent of the total laser power, one up-converts the master clock frequency to GHz frequencies and modulates it onto the carrier laser as phase modulation sidebands. The clock noise is then measured by the sideband-to-sideband beatnote, which carries identical information as the main beatnote except that the clock jitter is amplified by the up-conversion factor.

As mentioned in previous sections, one other dominating noise is the laser frequency noise. It is to be eliminated by the postprocessing TDI techniques [4–11]. However, TDI techniques require the knowledge of the arm length information to about 1 m [12]. This absolute arm length information is determined by the pseudo-random noise (PRN) phase modulation. The PRN modulation uses about 0.1–1 % of the light power [1, 13–16]. The distance information is revealed by the correlation between the received PRN code and the local copy of the same PRN code. Although the measurement noise of the of ranging signal is below 1 m [1], it has not accounted for the clock noise. Since the distance is determined by comparing the transmission time and the reception time, the distance information is contaminated with the clock noise. The 1 m precision means we can determine the distance plus the relative clock noise very precisely. But we still need to break the degeneracy of the two and to extract the absolute arm length and the relative clock noise information. This is supposed to be addressed by the previously defined pre data processing.

4.2 The Inter-spacecraft Measurements

Now, let us look into these inter-spacecraft measurements. In the middle of Fig. 4.1, the two peaks are the local carrier and the weak received carrier. They form a carrier-to-carrier beatnote, which is usually called the science measurement, denoted by f_{sci}.

$$f_{\text{sci}} = f_{\text{Doppler}} + f_{\text{GW}} + f_{\text{noise}}, \tag{4.1}$$

where f_{Doppler} is the Doppler shift, f_{GW} is the frequency fluctuation induced by GWs, f_{noise} is the noise term, which contains various kinds of noise, such as laser frequency noise, optical path-length noise, clock noise, etc. As mentioned before, f_{Doppler} can be as large as 15 MHz. However, f_{GW} is usually at the μHz level. Among the noise terms, the laser frequency noise is the dominating one. The free-running laser frequency noise is expected to be above MHz/Hz$^{1/2}$ at about 10 mHz. After pre-stabilization, the laser frequency noise is somewhere between 30 and 1000 Hz/Hz$^{1/2}$ at about 10 mHz [1, 17].

On the two sides of Fig. 4.1 are the two clock sidebands. The clock sideband beatnote is given by the following

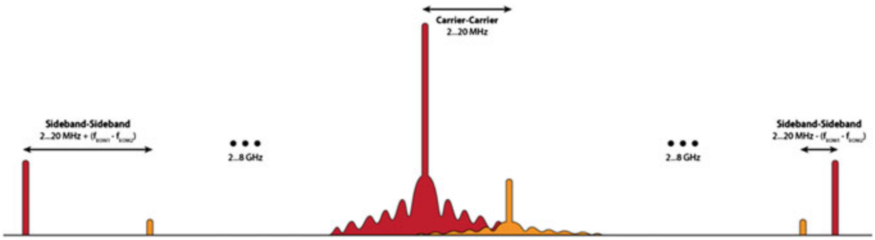

Fig. 4.1 Schematic power spectral density plot of LISA carrier laser beam, clock-sideband modulation and the PRN modulation. *Horizontal direction* denotes frequency and *vertical direction* denotes power. In the *middle*, the two peaks are the two beating carriers. Around the carriers are the PRN modulations. On the *sides* of the figure are the clock sidebands modulation

$$f_{\text{sidebandBN}} = f_{\text{Doppler}} + f_{\text{GW}} + f_{\text{noise}} + m\Delta f_{\text{clock}}, \tag{4.2}$$

where Δf_{clock} is the frequency difference between the local USO and the remote USO, m is an up-conversion factor. Except for the intentionally amplified clock term, the clock sideband beatnote contains the same information as the carrier-to-carrier beatnote does.

The PRN modulations are around the carriers in Fig. 4.1. The two PRN modulations shown in the figure in yellow and in red are orthogonal to each other such that no correlation exists for any delay time. At the local S/C, one correlates the PRN code modulated on the remote laser beam with an exact copy, hence obtaining the delay time between the emission and the reception. This light travel time tells us the arm length information. However, the PRN codes are labelled by their own clocks at the transmitter and the receiver, respectively. Thus, the ranging signal τ_{ranging} also contains the time difference of the two clocks.

$$\tau_{\text{ranging}} = L/c + \Delta T_{\text{clock}} + T_{\text{noise}}, \tag{4.3}$$

where L is the arm length, c is the speed of light, ΔT_{clock} is the clock time difference, T_{noise} denotes the noise in this measurement. The ranging measurement noise T_{noise} is around 3 ns (or 1 m) RMS [1]. However, since the clock is freely drifting all the time, after one year ΔT_{clock} could be quite large. One needs to decouple the bias from the true armlength term to a level better than 3 ns.

4.3 Formulation of the Measurements

In this section, we try to formulate the exact expressions of Eqs. 4.1–4.3. Let us first clarify the notation. The positions of the S/C are denoted by $\vec{x}_i = (x_i, y_i, z_i)^T$, their velocities are denoted by $\vec{v}_i = (v_{xi}, v_{yi}, v_{zi})^T$ in the SSB frame, where $i = 1, 2, 3$ is the S/C index. Each S/C has its own USO. The measurements taken on each S/C are recorded according to their own USO. Let us denote the nominal frequency of the USO in the ith S/C as f_i^{nom} (the design frequency) and denote its actual frequency (the true frequency it runs at) as f_i. The difference

$$\delta f_i = f_i - f_i^{\text{nom}} \tag{4.4}$$

is the frequency jitter of each USO. The USOs are thought to be operating at f_i^{nom}. The actual frequencies f_i are unknown to us. Also, we denote the nominal time of each USO as T_i^{nom} (the readout time of the clock) and the actual clock time (the true time at which the clock reads T_i^{nom}) as T_i. We have

$$T_i^{\text{nom}} = \frac{\phi_i}{2\pi f_i^{\text{nom}}} = \frac{\int f_i(t)\mathrm{d}t}{f_i^{\text{nom}}}, \tag{4.5}$$

$$T_i = \int \mathrm{d}t, \tag{4.6}$$

$$\phi_i = 2\pi \int f_i(t)\mathrm{d}t, \tag{4.7}$$

where ϕ_i denotes the readout phase in the ith S/C. The time difference

$$\begin{aligned}\delta T_i &= T_i^{\text{nom}} - T_i, \\ &= \frac{1}{f_i^{\text{nom}}} \int (f_i - f_i^{\text{nom}})\mathrm{d}t, \\ &= \frac{1}{f_i^{\text{nom}}} \int \delta f_i \mathrm{d}t \end{aligned} \tag{4.8}$$

is the clock jitter of each USO. This leads to

$$\delta \dot{T}_i = \frac{\delta f_i}{f_i^{\text{nom}}}. \tag{4.9}$$

The above two equations mean that the clock jitter (or time jitter) is the accumulative effect of frequency jitters. For the convenience of numerical simulations, we write the discrete version of the above formulae as follows

$$\delta T_i(k) = \frac{1}{f_i^{\text{nom}}} \sum_{a=1}^{k} \delta f_i(a)\Delta t_s + \delta T_i(0), \tag{4.10}$$

$$\begin{aligned}\delta \dot{T}_i(k) &= \frac{\delta T_i(k) - \delta T_i(k-1)}{\Delta t_s} \\ &= \frac{\delta f_i(k)\Delta t_s / f_i^{\text{nom}}}{\Delta t_s} \\ &= \frac{\delta f_i(k)}{f_i^{\text{nom}}}, \end{aligned} \tag{4.11}$$

where k in the parentheses means the value at the kth step or at time $k\Delta t_s$, $\delta T_i(0)$ stands for the initial clock bias.

Now, we are ready to write the measurement equations. Ideally, all the measurements should be formulated within the framework of General Relativity. In the solar system, gravity is relatively weak, so one can expand the relativistic equations in orders of the small parameter v/c and solve it with a perturbation method [18]. However, the full relativistic treatment is computationally too expensive for our testing of Kalman filters. Therefore, we plan to investigate it in future work. Here, we make an approximation that all the inter-spacecraft measurements are instantaneous, meaning that the laser beam takes no time to travel from one S/C to other S/C. As will be explained below, this is a better approximation for the inter-spacecraft measurements than calculating everything in Newtonian theory with a finite speed of light. The whole LISA constellation is trailing the Earth at a speed v_c that is much higher than the relative speed v_r within the constellation. Thus, in Newton's framework with a finite speed of light, the ranging (or armlength) measurements from S/C i to S/C j differ from the ranging measurements from S/C j to S/C i by a length of about Lv_c/c, which is much larger than the true value [18]. The order of magnitude of the true difference between the forward and the backward ranging measurements can be quickly estimated within special relativity framework, where only the relative speed matters. So, the difference in ranging measurements is roughly about Lv_r/c, which is two orders of magnitude smaller than Lv_c/c.

To this point, we try to formulate the ranging measurements. For convenience, we write it in dimensions of length and denote the armlength measurements measured by the laser link from S/C i to S/C j (measured at S/C j) as R_{ij}. Thus, we have

$$R_{ij}(k) = L_{ij}(k) + [\delta T_j(k) - \delta T_i(k)]c + \text{noise}, \tag{4.12}$$

where $L_{ij}(k)$ is the true armlength we want to obtain from the ranging measurements, $[\delta T_j(k) - \delta T_i(k)]c$ is the armlength bias caused by the clock jitters, and 'noise' denotes the effects of other noise sources.

Next, we want to consider Doppler measurements or science measurements. They are phase measurements recorded at the phasemeter. For convenience, we formulate them as frequency measurements, since it is trivial to convert phase measurements to frequency measurements. First, we take into account only the imperfection of the USO and ignore other noises. We denote the true frequency we want to measure as f_{true} and the frequency actually measured as f_{meas}. The USO is thought to be running at f^{nom}. The recorded frequency f_{meas} is compared to it. However, the frequency at which the USO is really running is $f = f^{\text{nom}} + \delta f$. This is what the true frequency f_{true} is actually compared to. Thus, we have the following formula

$$\begin{aligned}\frac{f_{\text{meas}}}{f^{\text{nom}}} &= \frac{f_{\text{true}}}{f} \\ &= \frac{f_{\text{true}}}{f^{\text{nom}} + \delta f}.\end{aligned} \tag{4.13}$$

For a normal USO, $\delta f/f^{\mathrm{nom}}$ is usually a very small number ($<10^{-8}$), therefore the second order in it is smaller than machine accuracy. Thus, we can write the above equation in linear order of $\delta f/f^{\mathrm{nom}}$ for numerical simulation concern without loss of precision:

$$\begin{aligned} f_{\mathrm{meas}} &= \frac{f_{\mathrm{true}}}{1+\delta f/f^{\mathrm{nom}}} \\ &= f_{\mathrm{true}}\left(1-\frac{\delta f}{f^{\mathrm{nom}}}\right). \end{aligned} \tag{4.14}$$

We denote the average carrier frequency (the average laser frequency over certain time) as f^{carrier}, the laser frequency noise as δf^{c} and the unit vector pointing from S/C i to S/C j as $\hat{n}_{ij}$. Let us consider the laser link sent from S/C i to S/C j. When transmitted, the instantaneous carrier frequency is actually $f_i^{\mathrm{carrier}} + \delta f_i^{\mathrm{c}}$. When received at S/C j, this carrier frequency has been Doppler shifted and the GW signals are encoded. Therefore, its frequency can be written as

$$(f_i^{\mathrm{carrier}} + \delta f_i^{\mathrm{c}})\left[1-\frac{(\vec{v}_j-\vec{v}_i)\cdot\hat{n}_{ij}}{c}\right] - f_{ij}^{\mathrm{GW}}. \tag{4.15}$$

This carrier is then beat with the local carrier $f_j^{\mathrm{carrier}} + \delta f_j^{\mathrm{c}}$ of S/C j. The resulting beatnote is the science measurement

$$\begin{aligned} f_{ij}^{\mathrm{sci}}(k) =& \left[f_j^{\mathrm{carrier}} - f_i^{\mathrm{carrier}}\left(1-\frac{(\vec{v}_j-\vec{v}_i)\cdot\hat{n}_{ij}}{c}\right) + f_{ij}^{\mathrm{GW}}(k)\right]\left(1-\frac{\delta f_j(k)}{f_j^{\mathrm{nom}}}\right) \\ &+ \left[\delta f_j^{\mathrm{c}} - \delta f_i^{\mathrm{c}}\left(1-\frac{(\vec{v}_j-\vec{v}_i)\cdot\hat{n}_{ij}}{c}\right)\right]\left(1-\frac{\delta f_j(k)}{f_j^{\mathrm{nom}}}\right) + \text{noise}, \\ =& \left[f_j^{\mathrm{carrier}} - f_i^{\mathrm{carrier}}\left(1-\frac{(\vec{v}_j-\vec{v}_i)\cdot\hat{n}_{ij}}{c}\right) + f_{ij}^{\mathrm{GW}}(k)\right]\left(1-\frac{\delta f_j(k)}{f_j^{\mathrm{nom}}}\right) + \text{noise}, \end{aligned} \tag{4.16}$$

where in the last step we have absorbed the laser frequency noise into the noise term. In practice, the carrier frequencies are adjusted occasionally (controlled by a pre-determined frequency plan) to make sure that the carrier-to-carrier beatnote is within a certain frequency range. Hence, f_i^{carrier} is also a function of time.

Now, let us consider the clock sidebands. At S/C i, the clock frequency $f_i^{\mathrm{nom}} + \delta f_i$ is up-converted by a factor m_i, which is about 40–50, and modulated onto the carrier through an electro optical modulator (EOM). Therefore, we have an upper clock sideband and a lower clock sideband as follows

$$f_i^{\mathrm{USB}} = f_i^{\mathrm{carrier}} + \delta f_i^{\mathrm{c}} + m_i(f_i^{\mathrm{nom}} + \delta f_i), \tag{4.17}$$

$$f_i^{\mathrm{LSB}} = f_i^{\mathrm{carrier}} + \delta f_i^{\mathrm{c}} - m_i(f_i^{\mathrm{nom}} + \delta f_i). \tag{4.18}$$

When received by S/C j, the Doppler effect and GWs are present

$$\left[f_i^{\text{carrier}} + \delta f_i^{\text{c}} \pm m_i(f_i^{\text{nom}} + \delta f_i)\right]\left[1 - \frac{(\vec{v}_j - \vec{v}_i)\cdot \hat{n}_{ij}}{c}\right] - f_{ij}^{\text{GW}}. \tag{4.19}$$

The clock sideband beatnote is obtained by beating this frequency with the local clock sideband

$$\begin{aligned}
f_{ij}^{\text{sidebandBN}}(k) = &\left[f_j^{\text{carrier}} - f_i^{\text{carrier}}\left(1 - \frac{(\vec{v}_j - \vec{v}_i)\cdot \hat{n}_{ij}}{c}\right) + f_{ij}^{\text{GW}}(k)\right]\left(1 - \frac{\delta f_j(k)}{f_j^{\text{nom}}}\right)\\
&+ \left[m_j(f_j^{\text{nom}} + \delta f_j(k)) - m_i(f_i^{\text{nom}} + \delta f_i(k))\left(1 - \frac{(\vec{v}_j - \vec{v}_i)\cdot \hat{n}_{ij}}{c}\right)\right]\\
&\cdot \left(1 - \frac{\delta f_j(k)}{f_j^{\text{nom}}}\right) + \text{noise},\\
= &\left[f_j^{\text{carrier}} - f_i^{\text{carrier}}\left(1 - \frac{(\vec{v}_j - \vec{v}_i)\cdot \hat{n}_{ij}}{c}\right) + f_{ij}^{\text{GW}}(k)\right]\left(1 - \frac{\delta f_j(k)}{f_j^{\text{nom}}}\right)\\
&+ [\alpha_j \delta f_j(k) - \alpha_i \delta f_i(k)] + (m_j f_j^{\text{nom}} - m_i f_i^{\text{nom}}) + m_i f_i^{\text{nom}} \frac{(\vec{v}_j - \vec{v}_i)\cdot \hat{n}_{ij}}{c},\\
&+ \text{noise},
\end{aligned} \tag{4.20}$$

where α_i and α_j are some known constants. Notice that we have neglected some minor terms in the last step. For simulation purposes, we temporarily ignore the constant term $m_j f_j^{\text{nom}} - m_i f_i^{\text{nom}}$ and the small Doppler term $m_i f_i^{\text{nom}}(\vec{v}_j - \vec{v}_i)\cdot \hat{n}_{ij}/c$. Furthermore, we write α_i and α_j as a uniform up-conversion factor m for simplicity. Then, we have the simplified formula

$$\begin{aligned}
f_{ij}^{\text{sidebandBN}}(k) = &\left[f_j^{\text{carrier}} - f_i^{\text{carrier}}\left(1 - \frac{(\vec{v}_j - \vec{v}_i)\cdot \hat{n}_{ij}}{c}\right) + f_{ij}^{\text{GW}}(k)\right]\left(1 - \frac{\delta f_j(k)}{f_j^{\text{nom}}}\right)\\
&+ m(\delta f_j(k) - \delta f_i(k)) + \text{noise}.
\end{aligned} \tag{4.21}$$

Up to now, we have formulated all the inter-spacecraft measurements in Eqs. 4.12, 4.16 and 4.21.

References

1. G. Heinzel et al., Auxiliary functions of the laser link: ranging, clock noise transfer and data communication. Class. Quantum Gravity **28**, 094008 (2011)
2. S.V. Dhurandhar, K. Rajesh Nayak, S. Koshti, J.-Y. Vinet, Fundamentals of the LISA stable flight formation. Class. Quantum Gravity **22**, 481 (2005)
3. Laser Interferometer Space Antenna: sciencecraft description, LISA-SC-DD-0001, NASA Goddard Space Flight Center, http://lisa.gsfc.nasa.gov/Documentation/LISA-SC-DD-0001.pdf

4. T. Massimo, D. Shaddock, J. Sylvestre, J. Armstrong, Implementation of time-delay interferometry for LISA. Phys. Rev. D **67** (2003)
5. J.W. Armstrong et al., Time-delay interferometry for space-based gravitational wave searches. ApJ **527**, 814–826 (1999)
6. N.J. Cornish, R.W. Hellings, The effects of orbital motion on LISA time delay interferometry. Class. Quantum Gravity **20**, 4851 (2003)
7. D.A. Shaddock, B. Ware, R.E. Spero, M. Vallisneri, Postprocessed time-delay interferometry for LISA. Phys. Rev. D **70**, 081101(R) (2004)
8. M. Vallisneri, Synthetic LISA: simulating time delay interferometry in a model LISA. Phys. Rev. D **71**, 022001 (2005)
9. T.A. Prince, M. Tinto, S.L. Larson, J.W. Armstrong, LISA optimal sensitivity. Phys. Rev. D **66**, 122002 (2002)
10. M. Tinto, S.V. Dhurandhar, Time-delay interferometry. Liv. Rev. Relativ. **8**(4) (2005). http://www.livingreviews.org/lrr-2005-4, arXiv:gr-qc/0409034
11. M. Otto, G. Heinzel, K. Danzmann, TDI and clock noise removal for the split interferometry configuration of LISA. Class. Quantum Gravity **29**, 205003 (2012)
12. LISA Frequency Control Study Team 2009, ESA Report No LISA-JPL-TN-823 (in press)
13. J.J. Esteban et al., Optical ranging and data transfer development for LISA. J. Phys.: Conf. Ser. **154**, 012025 (2009)
14. J.J. Esteban et al., Ranging and phase measurement for LISA. J. Phys.: Conf. Ser. **228**, 012045 (2010)
15. S. Barke et al., EOM sideband phase characteristics for the spaceborne gravitational wave detector LISA. Appl. Phys. B **98**(1), 33–39 (2010)
16. A. Sutton, K. McKenzie, B. Ware, D. Saddock, Laser ranging and communication for LISA. Opt. Express **18**, 20759 (2010)
17. D. Shaddock et al., LISA Frequency Control White Paper (2009)
18. B. Chauvineau, T. Regimbau, J.-Y. Vinet, S. Pireaux, Relativistic analysis of the LISA long range optical links. Phys. Rev. D **72**, 122003 (2005)

Chapter 5
Design a Hybrid Extended Kalman Filter for the Entire LISA Constellation

Abstract The hybrid-extended Kalman filter is briefly derived. The three types of inter-spacecraft measurements of LISA are simulated, whose properties are then discussed. The clock errors have been simulated in the measurements, but ignored in the time stamps of the samples. A 24-dimensional state vector is used to describe the system. Accordingly, the measurement equation and dynamic equation are formulated. Then, the hybrid-extend Kalman filter is applied to the simulated data. According to the simulation, the algorithm has significantly improved the ranging accuracy and synchronized the clocks, hence it makes the phasemeter raw measurements usable for time-delay interferometry algorithms.

5.1 Introduction

Previously, we have introduced the basic formulae of Kalman filter and formulated the inter-spacecraft measurements of LISA. In this chapter, we intend to design a Kalman filter for the entire LISA constellation. The basic Kalman filter formulae only apply to discrete and linear systems. Since LISA measurements are not linear and the dynamics of LISA is neither discrete nor linear, we first introduce the so-called hybrid extended Kalman filter, and then try to design such a Kalman filter for LISA.

5.2 The Hybrid Extended Kalman Filter

The hybrid extended Kalman filter [1] is designed for a system with continuous and nonlinear dynamic equations along with nonlinear measurement equations. First, we describe the model of such systems as follows

$$\dot{x} = f(x, t) + w(t) \tag{5.1}$$

$$y_k = h_k(x_k, v_k) \tag{5.2}$$

$$E[w(t)w^T(t+\tau)] = W_c\delta(\tau) \tag{5.3}$$

$$v_k \sim (0, V_k), \tag{5.4}$$

Y. Wang, *First-stage LISA Data Processing and Gravitational Wave Data Analysis*,
Springer Theses, DOI 10.1007/978-3-319-26389-2_5

where both the dynamic function $f(x, t)$ and the measurement function $h_k(x_k)$ are nonlinear, $w(t)$ is the continuous noise. As in previous chapters, $x, f(x, t)$, w, y_k, $h_k(x_k)$, v_k are column vectors. W_c, W_k are covariance matrices. If we discretize the noise with a step size Δt, we have

$$w_k \sim (0, W_k), \tag{5.5}$$

where it can be proven that $W_k = W_c(k\Delta t)/\Delta t$. In order to fit Eqs. 5.1–5.4 into the standard Kalman filter frame, we need to linearize and discretize the formulae and solve the dynamic equation. Eq. 5.1 is expanded to linear order in x_0 as follows

$$\begin{aligned}\dot{x} &\approx f(x_0, t_0) + \left.\frac{\partial f}{\partial x}\right|_{x_0, t_0} (x - x_0) + w(t) \\ &= f(x_0, t_0) + F(x_0, t_0)(x - x_0) + w(t),\end{aligned} \tag{5.6}$$

where we have defined $F(x_0, t_0) \equiv \left.\frac{\partial f}{\partial x}\right|_{x_0, t_0}$, and assumed $\frac{\partial f}{\partial t} \ll 1$. The expectation of this linearized equation (where $\mathrm{E}[w(t)] = 0$ is used) can be solved exactly as follows

$$x(t_2) = e^{F(x_0,t_0)\Delta t} x(t_1) + \left[e^{F(x_0,t_0)\Delta t} - I\right]\left[F^{-1}(x_0, t_0) f(x_0, t_0) - x_0\right], \tag{5.7}$$

where $\Delta t = t_2 - t_1$, and the matrix exponential is defined as

$$e^{F\Delta t} \equiv \sum_{n=0}^{+\infty} \frac{(F\Delta t)^n}{n!}. \tag{5.8}$$

Now, let us switch to the standard Kalman filter notation and denote $x(t_2)$, $x(t_1)$ and $F(x_0, t_0)$ as $\hat{x}_k^-$, $\hat{x}_{k-1}^+$ and F_{k-1}, respectively. Eq. 5.7 can be rewritten as

$$\hat{x}_k^- = e^{F_{k-1}\Delta t} \hat{x}_{k-1}^+ + (e^{F_{k-1}\Delta t} - I)\left[F_{k-1}^{-1} f(x_0, t_0) - x_0\right]. \tag{5.9}$$

Notice that x_0 is a nominal trajectory, around which the Taylor expansion is made. Based on the above solution, the propagation equation of the covariance matrices is obtained

$$P_k^- = e^{F_{k-1}\Delta t} P_{k-1}^+ e^{F_{k-1}^T \Delta t} + W_{k-1}, \tag{5.10}$$

where P^-, P^+ are the a priori and a posteriori covariance matrices as before. Alternatively, Eq. 5.6 can be solved approximately by converting the differential equation to a difference equation. The corresponding formulae are

$$\hat{x}_k^- = (I + F_{k-1}\Delta t)\hat{x}_{k-1}^+ + \left[f(x_0, t_0) - F_{k-1}x_0\right]\Delta t, \tag{5.11}$$

$$P_k^- = (I + F_{k-1}\Delta t)P_{k-1}^+ (I + F_{k-1}\Delta t)^T + W_{k-1}. \tag{5.12}$$

The above two equations can also be obtained from the exact solutions by replacing $e^{F_{k-1}\Delta t}$ with $I + F_{k-1}\Delta t$. The advantage of these formulae is that they are computationally less expensive. On the other hand, they are less accurate. The measurement formula can be linearized similarly

$$y_k = H_k x_k + [h_k(\hat{x}_k^-, 0) - H_k \hat{x}_k^-] + M_k v_k, \tag{5.13}$$

where $H_k \equiv \frac{\partial h_k}{\partial x}\big|_{\hat{x}_k^-}$, $M_k \equiv \frac{\partial h_k}{\partial v}\big|_{\hat{x}_k^-}$. Now, the Kalman filter can be applied without much effort. We summarize the hybrid extended Kalman filter formulae for the model described by Eqs. 5.1–5.4 as follows:

1. Initialize the state vector and the covariance matrix

$$\hat{x}_0^+, P_0^+. \tag{5.14}$$

2. Calculate the a priori estimate $\hat{x}_k^-$ from the a posteriori estimate $\hat{x}_{k-1}^+$ at the previous step, using the dynamic equation

$$\dot{x} = f(x, t). \tag{5.15}$$

Use either of the following two formulae to update the covariance matrix

$$P_k^- = e^{F_{k-1}\Delta t} P_{k-1}^+ e^{F_{k-1}^T \Delta t} + W_{k-1}, \tag{5.16}$$

$$P_k^- = (I + F_{k-1}\Delta t) P_{k-1}^+ (I + F_{k-1}\Delta t)^T + W_{k-1}. \tag{5.17}$$

3. Calculate the Kalman gain

$$K_k = P_k^- H_k^T (H_k P_k^- H_k^T + M_k V_k M_k^T)^{-1}. \tag{5.18}$$

4. Correct the a priori estimate

$$\hat{x}_k^+ = \hat{x}_k^- + K_k[y_k - h_k(\hat{x}_k^-, 0)], \tag{5.19}$$

$$\begin{aligned} P_k^+ &= (I - K_k H_k) P_k^-, \\ &= (I - K_k H_k) P_k^- (I - K_k H_k)^T + K_k V_k K_k^T. \end{aligned} \tag{5.20}$$

5.3 Kalman Filter Model for LISA

In this section, we want to design a hybrid extended Kalman filter for LISA. First, we define a 24-dimensional column state vector

$$x = (\vec{x}_1, \vec{x}_2, \vec{x}_3, \vec{v}_1, \vec{v}_2, \vec{v}_3, \delta T_1, \delta T_2, \delta T_3, \delta f_1, \delta f_2, \delta f_3)^T, \tag{5.21}$$

where $\vec{x}_i = (x_i, y_i, z_i)^T$ are the S/C positions, $\vec{v}_i = (v_{xi}, v_{yi}, v_{zi})^T$ are the S/C velocities, δT_i and δf_i are the clock jitters and frequency jitters, $i = 1, 2, 3$ is the S/C index. Please note the difference between the state vector x_k, the measurements y_k and the position components (x_i, y_i, z_i), since the latter index is the S/C label and can only take three values $1, 2, 3$. For convenience, we rewrite the measurement formulae derived in previous chapters. The ranging measurements from S/C i to S/C j are

$$\begin{aligned} R_{ij} &= L_{ij} + (\delta T_j - \delta T_i)c + n_{ij}^R \\ &= \sqrt{(x_j - x_i)^2 + (y_j - y_i)^2 + (z_j - z_i)^2} + (\delta T_j - \delta T_i) \cdot c + n_{ij}^R, \end{aligned} \tag{5.22}$$

where n_{ij}^R is the ranging measurement noise. The Doppler measurements are denoted as D_{ij},

$$D_{ij} = \left[f_j^{\text{carrier}} - f_i^{\text{carrier}} \left(1 - \frac{(\vec{v}_j - \vec{v}_i) \cdot \hat{n}_{ij}}{c} \right) + f_{ij}^{\text{GW}} \right] \left(1 - \frac{\delta f_j}{f_j^{\text{nom}}} \right) + n_{ij}^D, \tag{5.23}$$

where n_{ij}^D is the Doppler measurement noise. Since the sideband measurements contain the same information as the Doppler measurements, in addition the amplified differential clock jitters, we take the difference. Then, we divide both sides of the equation by the up-conversion factor m and denote it as the clock measurements C_{ij}.

$$C_{ij} = \delta f_j - \delta f_i + n_{ij}^C, \tag{5.24}$$

where n_{ij}^C is the corresponding measurement noise, and the up-conversion factor m has already been absorbed into n_{ij}^C. Altogether, we have 18 measurement formulae, summarized in the 18-dimensional column measurement vector

$$\begin{aligned} y &= h(x, v), \\ &= (R_{31}, D_{31}, C_{31}, R_{21}, D_{21}, C_{21}, R_{12}, D_{12}, C_{12}, \ldots \\ &\quad R_{32}, D_{32}, C_{32}, R_{23}, D_{23}, C_{23}, R_{13}, D_{13}, C_{13})^T, \end{aligned} \tag{5.25}$$

where v is the measurement noise. The 18-by-24 matrix H_k and the 18-by-18 matrix M_k can thus be calculated analytically. We omit the explicit expressions of the 432 components in H_k here. As an example, we show the [1, 1] component of H_k omitting the step index k as follows

$$\begin{aligned} H[1, 1] &= \frac{\partial R_{31}}{\partial x_1} \\ &= \frac{x_1 - x_3}{\sqrt{(x_1 - x_3)^2 + (y_1 - y_3)^2 + (z_1 - z_3)^2}}. \end{aligned} \tag{5.26}$$

As for M_k, if the dependence of the measurements y_k on the noise is linear and without cross coupling, it is simply an identity matrix.

Next, we want to construct the dynamic model for the Kalman filter. Let us consider the solar system dynamics for a single S/C. To Newtonian order the solar system dynamics can be written as

$$\sum_i \frac{GM_i}{r_i^3}\vec{r}_i = \ddot{\vec{x}} \tag{5.27}$$

where $\vec{x}$ is the position of one LISA S/C, $M_i, \vec{x}_i$ are the mass and the coordinates of the ith celestial body (the Sun and the planets) in the solar system, $\vec{r}_i = \vec{x}_i - \vec{x}$ is a vector pointing from that S/C to the ith celestial body, $r_i = |\vec{x}_i - \vec{x}|$. The dynamic equation can be written in a different form

$$\begin{aligned} \frac{\mathrm{d}}{\mathrm{d}t}\begin{bmatrix}\vec{x}\\ \vec{v}\end{bmatrix} &= f(\vec{x}, \vec{v}) \\ &= \begin{bmatrix}\vec{v}\\ \sum_i GM_i(\vec{x}_i - \vec{x})/r_i^3\end{bmatrix}. \end{aligned} \tag{5.28}$$

We denote $\theta = (\vec{x}, \vec{v})^T$, thus

$$F = \frac{\partial f}{\partial \theta} = \begin{bmatrix}\mathbf{O}_3 & \mathbf{I}_3\\ \mathbf{A} & \mathbf{O}_3\end{bmatrix}, \tag{5.29}$$

where $\mathbf{O}_3$ denotes a 3-by-3 zero matrix, $\mathbf{I}_3$ denotes a 3-by-3 identity matrix, and the 3-by-3 matrix $\mathbf{A}$ is defined as follows

$$\mathbf{A} = -\sum_i \frac{GM_i}{r_i^3}\mathbf{I}_3 + \sum_i \frac{3GM_i}{r_i^5}(\vec{x}_i - \vec{x})(\vec{x}_i - \vec{x})^T. \tag{5.30}$$

The dynamic equation for the clock jitters and frequency jitters depends on the specific clock and how well we characterize the clock. A simple dynamic model is shown as follows

$$\frac{\mathrm{d}}{\mathrm{d}t}\begin{bmatrix}\delta T\\ \delta f\end{bmatrix} = \begin{bmatrix}\delta f/f^{\mathrm{nom}}\\ 0\end{bmatrix}, \tag{5.31}$$

where δT, δf denote clock jitters and frequency jitters. For the whole LISA constellation, the dynamic matrix $F = \left.\frac{\partial f}{\partial x}\right|$ is 24-by-24. We omit its explicit expression here, since it can be obtained straightforwardly from the above formulae.

5.4 Simulation Results

We simulated LISA measurements of about 1400 s with a sampling frequency of 3 Hz. Since there are only two independent clock biases out of three, we set one clock bias to be zero, thus defining this clock as reference. The other two initial clock biases are randomly drawn from a Gaussian distribution with a standard deviation of 0.1 s. This would in turn cause a bias of about 4.2×10^7 m in the ranging measurements. The (unknown) initial frequency offset of each USO is randomly drawn from a Gaussian distribution with a standard deviation of 1 Hz. The frequency jitter of each USO has a linear spectral density $(9.2 \times 10^{-6}\text{Hz}/f)\ \text{Hz}/\sqrt{\text{Hz}}$. Additionally, we assume the ranging measurement noise to be white Gaussian with a standard deviation of 1 m. The linear spectral density of the pre-stabilized laser is assumed to be $400\ \text{Hz}/\sqrt{\text{Hz}}$. (The noise of the Doppler measurement is assumed to be white Gaussian with a standard deviation of 1 kHz.) The clock measurement noise is white Gaussian with a standard deviation of 1 Hz.

We show the scatter plots of the measurements R_{ij}, D_{ij}, C_{ij} in Figs. 5.1, 5.2, 5.3 and 5.4. Notice that the average of all the measurements has been removed in the plots for clarity. Fig. 5.1 is a scatter plot of the clock measurements C_{ij}. The frequency drifts within 1400 s are much smaller than the clock measurement noise. Thus, they are buried in the uncorrelated clock measurement noise in the plot. The diagonal histograms show that each clock measurement channel behaves like Gaussian noise during short observation times. The off-diagonal scatter plots are roughly circular scattering clouds, showing that different clock measurement channels are roughly uncorrelated within short times. Unlike clock measurements, scatter plots of Doppler measurements in Fig. 5.2 exhibit elliptical clouds. This is because the Doppler shift whin 1400 s is sizable, which leads to the trend in the plot. The slope of the major axis of the ellipse indicates whether the two Doppler measurement channels are positively correlated or anti-correlated. The real armlength variation is much larger than the ranging measurement noise. Therefore, we see only lines in the off-diagonal plots in Fig. 5.3, which mainly show the armlength changes. The ranging measurement noise is too small compared to the armlength change to be visible in the plot. Fig. 5.4 shows scatter plots of different measurements C_{ij}, D_{ij}, R_{ij}. It is seen from the plot that ranging measurements are correlated with Doppler measurements, but neither of them are correlated with clock measurements.

We then apply our previously designed hybrid extended Kalman filter to these measurements. The progress of the Kalman filter can be characterized by looking at

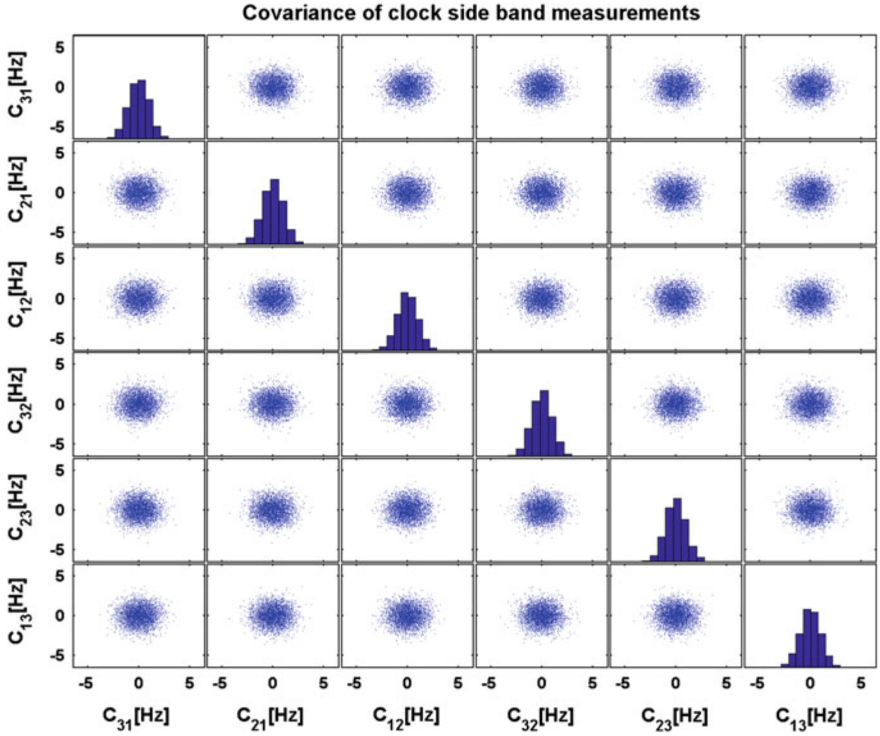

Fig. 5.1 Scatter plot of clock measurements C_{ij}

the uncertainty propagation. Figure 5.5 shows a priori covariance matrices at different steps $k = \{1, 2, 5, 10, 50\}$. The absolute value of each component of the covariance matrix is represented by a color. The color map indicates the magnitude of each component in logarithmic scale. The first covariance matrix P_1^- is diagonal, since we do not assume prior knowledge of the off-diagonal components. As the filter runs, the off-diagonal components emerge automatically from the system model, which can be seen from Fig. 5.5. The initial uncertainties are relatively large. In fact, the initial positions are known only to about 20 km through the deep space network (DSN). The uncertainties are significantly reduced after taking into account the precise inter-spacecraft measurements. However, the uncertainties are not being reduced continuously. Instead, they stay roughly at the same level. This is because there are only 18 measurements at each step, whereas there are 24 variables in the state vector to be determined. There is not enough information to precisely determine every variable in the state vector.

Similar behavior can be observed from the a posteriori covariance matrices in Fig. 5.6, where the uncertainties also roughly stay at the same level. By comparing

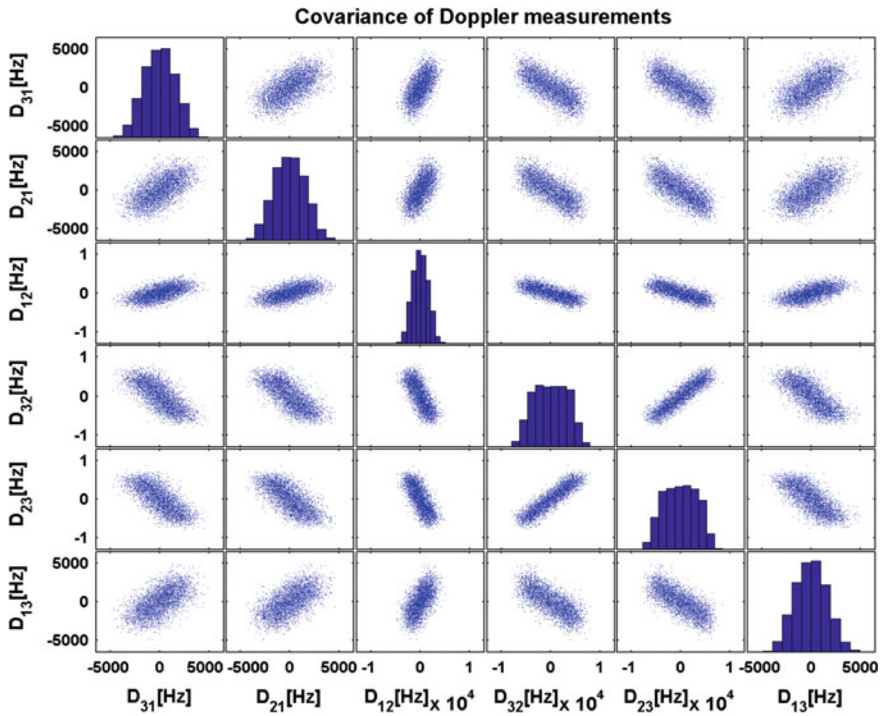

Fig. 5.2 Scatter plot of Doppler measurements D_{ij}. Unlike clock measurements, scatter plots of Doppler measurements exhibit elliptical clouds

Fig. 5.6 with Fig. 5.5, we find that the uncertainties are only slightly reduced from P_k^- to P_k^+ with the help of the measurements y_k. This is again because there are fewer measurements than variables in the state vector. Seemingly, this hybrid extended Kalman filter does not work well. However, our aim is actually to reduce the noise in the measurements. Let us denote the Kalman filter estimate of the measurements y_k as $\hat{y}_k$, which can be calculated from the a posteriori state vector as follows

$$\hat{y}_k = H_k \hat{x}_k^+. \tag{5.32}$$

It is easy to show that the estimation error of y_k can be expressed as $H_k P_k^+ H_k^T$, which is shown in Fig. 5.7. Notice that the color bar shrinks with steps. It is apparent that estimation errors of the measurements are significantly reduced by the hybrid-extended Kalman filter. This is what is expected, since the number of the measurements y_k is now the same as the number of variables $\hat{y}_k$ to be estimated in this case.

Detailed simulation results are shown in Figs. 5.8, 5.9, 5.10. Figure 5.8a shows a comparison of true armlengths, raw arm-length measurements and Kalman filter estimates during a short time. The initial clock bias in the raw arm-length measurements is not included in this figure, otherwise the raw arm-length measurements are

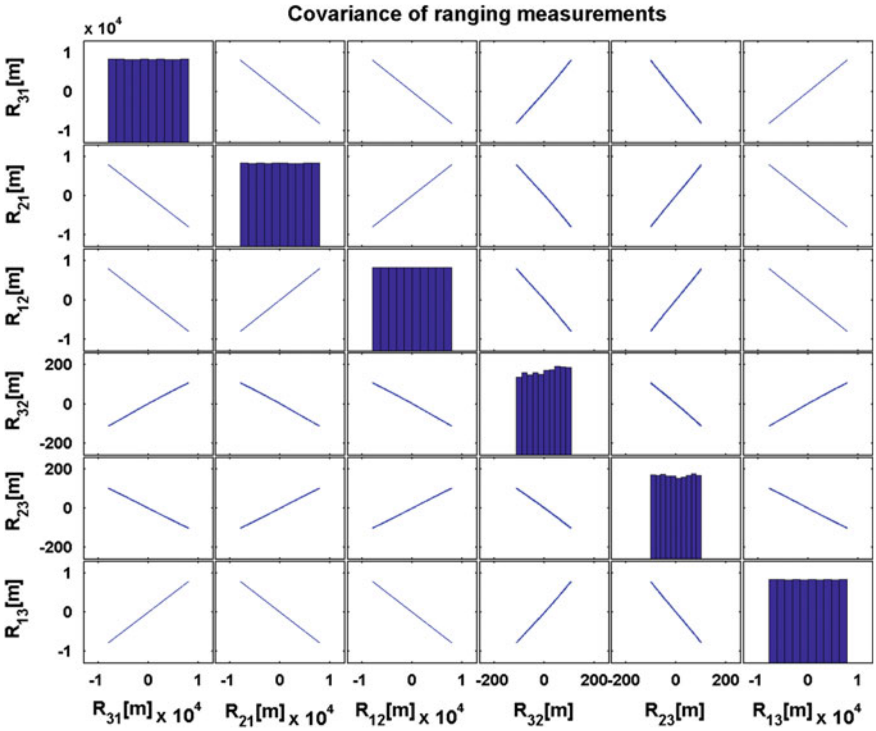

Fig. 5.3 Scatter plot of ranging measurements R_{ij}. The armlength variation is much larger than the ranging measurement noise. Therefore, we see only lines in the off-diagonal plots, which mainly show the armlength changes. The ranging measurement noise is too small compared to the armlength change to be visible in the plot

out of scope of the figure. The armlength variations due to the orbital dynamics are much larger than the residual measurement noise (excluding the initial clock bias). Thus, the three curves appear very close to each other. It still can be seen that the Kalman filter estimates are closer to the true arm-length curve. Fig. 5.8b exhibits histograms of errors of raw armlength measurements and Kalman filter estimates, where the deviations of both raw arm-length measurements (excluding the initial clock bias) and the Kalman filter estimates from the true armlengths are shown. The designed Kalman filter has not only decoupled the arm lengths from the clock biases, but also reduced the measurement noise by more than one order of magnitude to the centimeter level. This precise arm-length knowledge is necessary to allow excellent performance of TDI techniques, which subsequently permits optimal extractions of the science information from the measurement data.

Fig. 5.9a shows typical results of estimates of relative clock jitters and biases, where the blue curve stands for the raw measurements, the green curve exhibits the true time difference between the clock in S/C 1 and S/C 2, the red curve plots the Kalman filter estimates of the clock time differences. It is clear from the figure that

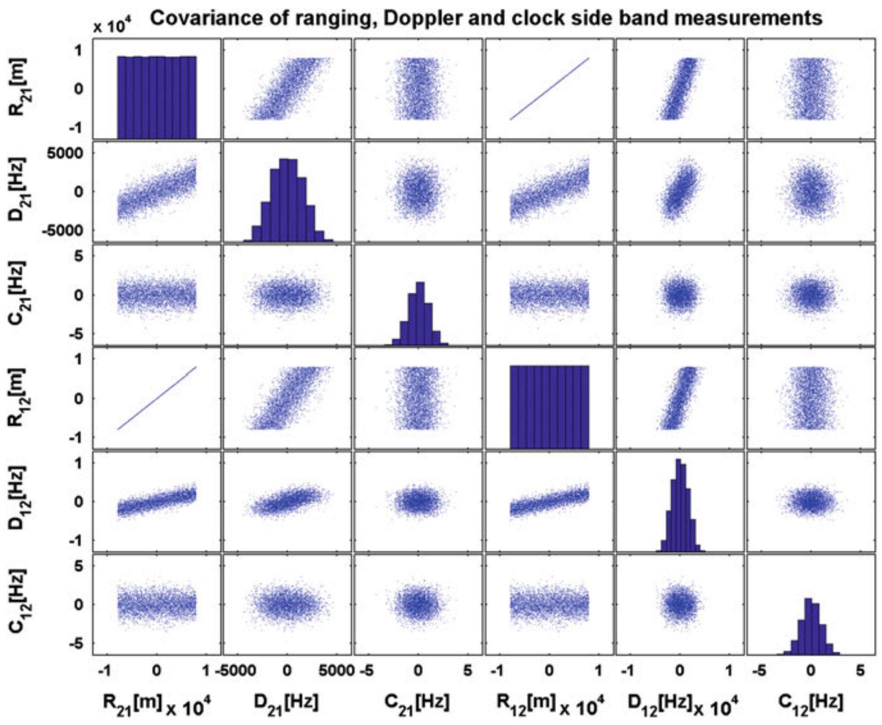

Fig. 5.4 Scatter plot of different measurements C_{ij}, D_{ij}, R_{ij}. Ranging measurements are correlated with Doppler measurements, but neither of them are correlated with clock measurements

the Kalman filter estimates resemble the true values quit well. Fig. 5.9b shows the deviations of the raw measurements and the Kalman filter estimates from the true values in histograms. Notice that the standard deviations in the legend have been converted to equivalent lengths. It is apparent that the designed Kalman filter has reduced the measurement noise by about an order of magnitude. These accurate clock jitter estimates enable us to correct the clock jitters in the postprocessing step. Hence, it potentially allows us to use slightly poorer clocks, yet still achieving the same sensitivity. This would potentially help reduce the cost of the mission.

Fig. 5.10a shows the raw measurements, Kalman filter estimates and the true values of frequency differences between the USO in S/C 1 and the USO in S/C 2. The Kalman filter estimates are so good that they overlap with the true values. Fig. 5.10b exhibits a zoomed-in plot of Fig. 5.10a. The true USO frequency differences and the Kalman filter estimates can clearly be seen in this figure. Fig. 5.10c shows the histograms of the deviations of the raw measurements and the Kalman filter estimates from the true values. With the help of the designed Kalman filter, the measurement

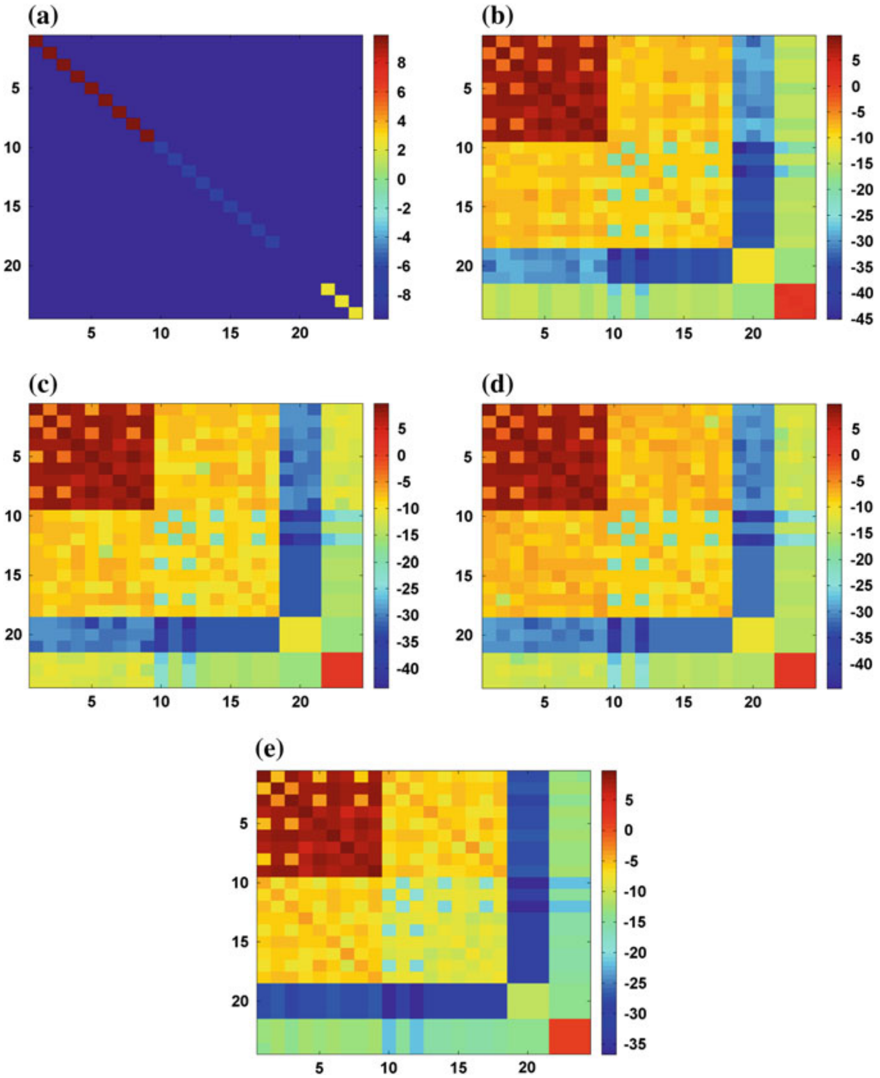

Fig. 5.5 A priori covariance matrices P_k^- at different steps. The absolute value of each component of the covariance matrix is represented by a *color*. The *color map* indicates the magnitude of each component in logarithmic scale $\ln(|P_k^-|)$. **a** P_1^-. **b** P_2^-. **c** P_5^-. **d** P_{10}^-. **e** P_{50}^-

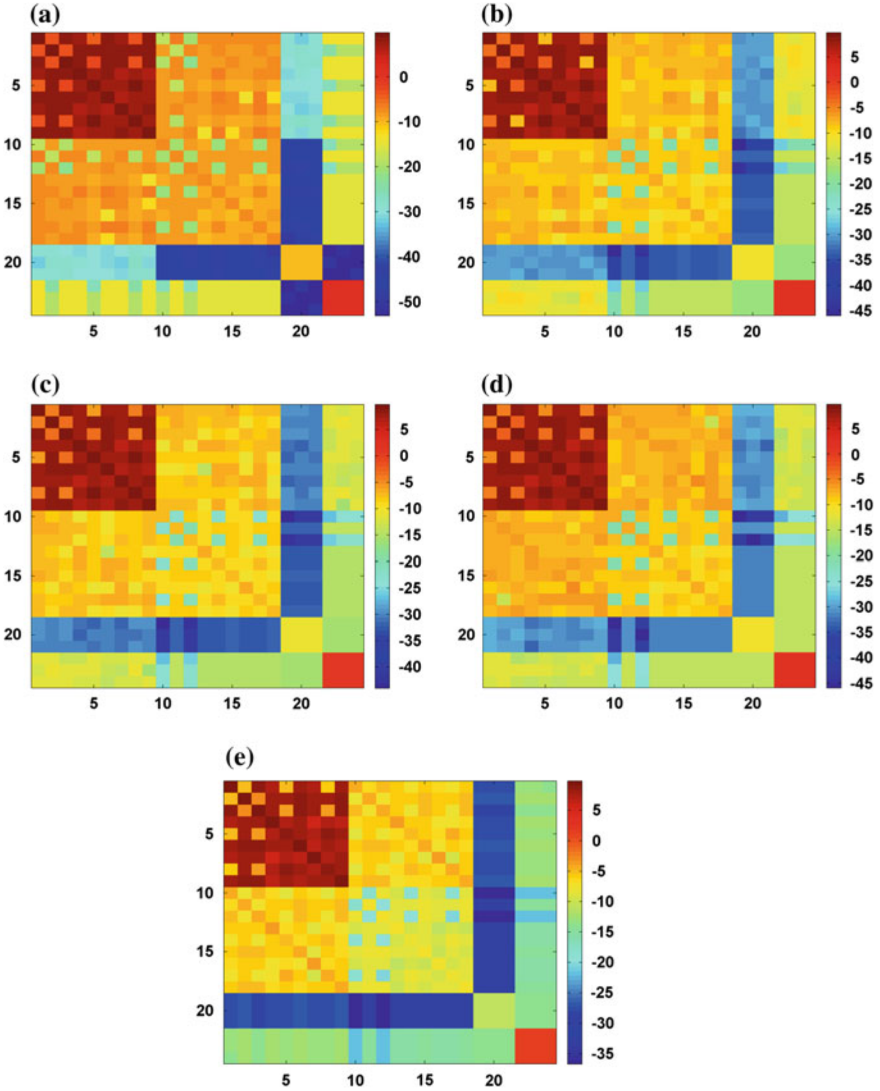

Fig. 5.6 Posteriori matrices P_k^+ at different steps. The absolute value of each component of the covariance matrix is represented by a *color*. The *color map* indicates the magnitude of each component in logarithmic scale **a** P_1^+. **b** P_2^+. **c** P_5^+. **d** P_{10}^+. **e** P_{50}^+

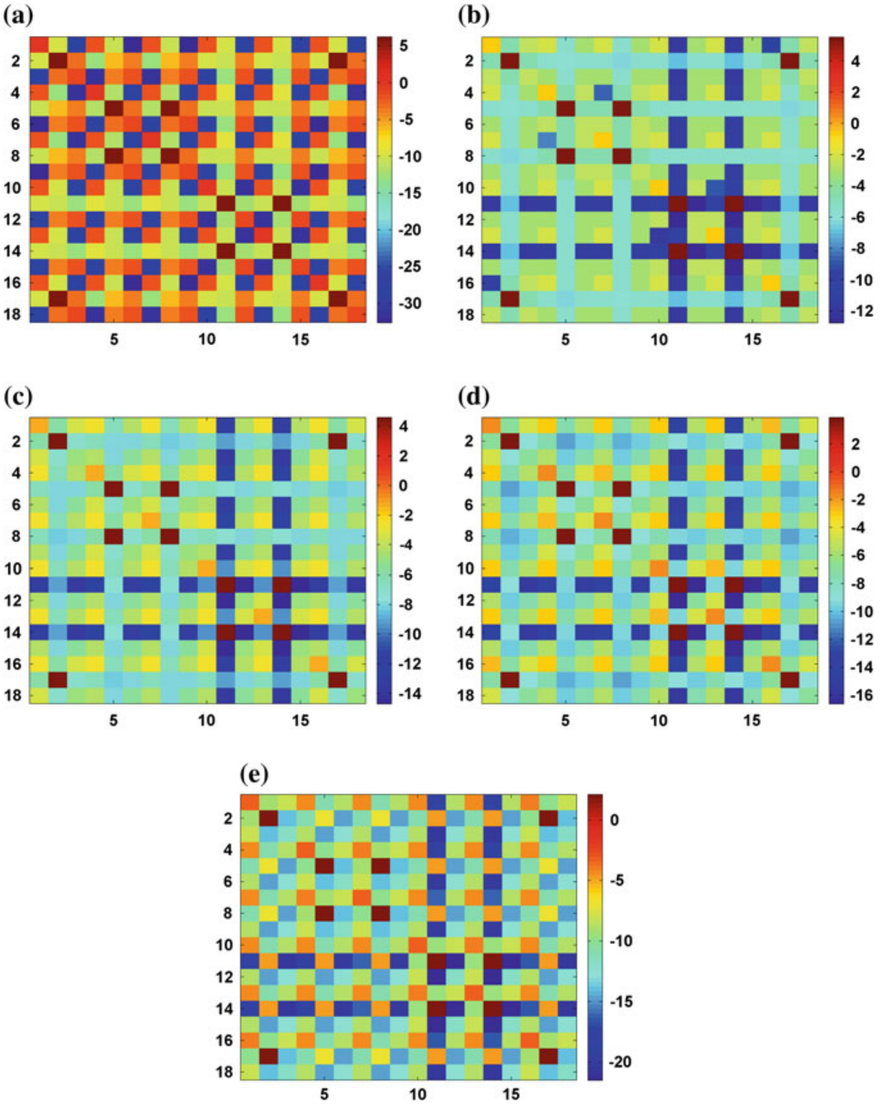

Fig. 5.7 The estimation error of the measurements, $H_k P_k^+ H_k^T$ at different steps. The absolute value of each component is represented by a *color*. The *color map* indicates the magnitude of each component in logarithmic scale **a** Step 1. **b** Step 2. **c** Step 5. **d** Step 10. **e** Step 50

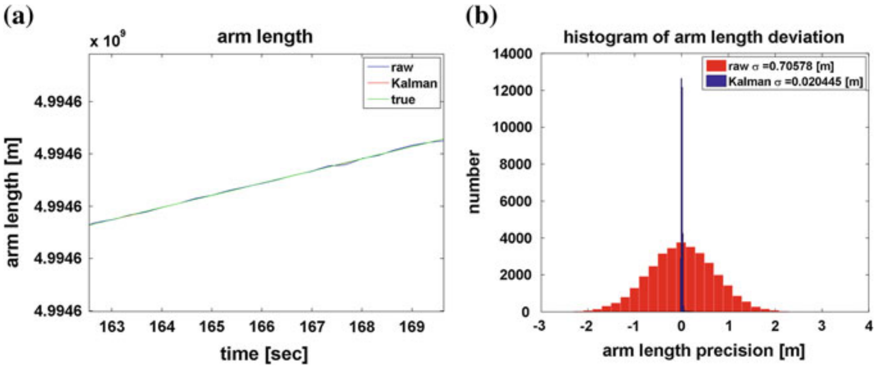

Fig. 5.8 Arm-length plots, **a** shows a comparison of true armlengths, raw arm-length measurements and Kalman filter estimates during short time, **b** exhibits histograms of errors of raw armlength measurements and Kalman filter estimates, where the deviations of both raw arm-length measurements (excluding the initial clock bias) and the Kalman filter estimates from the true armlengths are shown

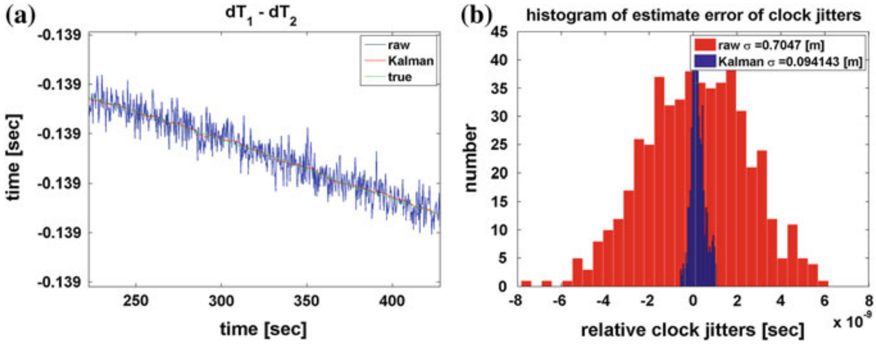

Fig. 5.9 Plots of relative clock jitter and biases, **a** shows typical results of estimates of relative clock jitters and biases, **b** shows the deviations of the raw measurements and the Kalman filter estimates from the true values in histograms. Notice that the standard deviations in the legend have been converted to equivalent lengths

noise has been reduced by 3–4 orders of magnitude. As shown in previous chapters, frequency jitters are directly related to the first differential of the clock drifts. Therefore, such precise estimates of the USO frequency differences will allow a very accurate tracking of the relative clock drifts.

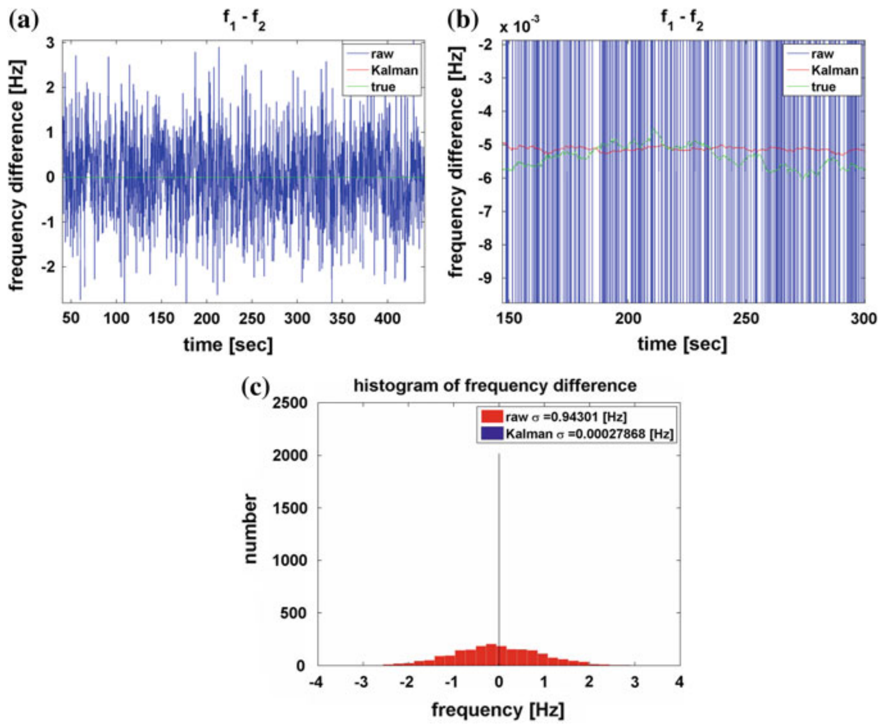

Fig. 5.10 Plots of USO frequency differences, **a** shows the raw measurements, Kalman filter estimates and the true values of frequency differences between the USO in S/C 1 and the USO in S/C 2. The Kalman filter estimates are so good that they overlap with the true values, **b** is a zoomed-in plot of (**a**). The true USO frequency differences and the Kalman filter estimates can clearly be seen in this figure, **c** shows the histograms of the deviations of the raw measurements and the Kalman filter estimates from the true values

5.5 Discussions

We have modeled LISA inter-spacecraft measurements and designed a hybrid-extended Kalman filter to process the raw measurement data. In the designed Kalman filter model, there are 24 variables in the state vector and 18 variables in the measurement vector. Simulations show that our hybrid-extended Kalman filter can well decouple the arm lengths from the clock biases and significantly improve the relative measurements, such as arm lengths, relative clock jitters and relative frequency jitters etc. However, the absolute variables in the state vector cannot be determined accurately. These variables include the absolute positions and velocities of the spacecraft, the absolute clock drifts and the absolute frequency drifts. This is mainly due to the fact that only the differences are measured and the number of measurements is lower than the number of variables in the state vector.

It can be better understood by taking a closer look at the measurement Eqs. 5.22–5.24. In fact, only the relative positions $\sqrt{(x_j - x_i)^2 + (y_j - y_i)^2 + (z_j - z_i)^2}$ and the relative longitudinal velocities $(\vec{v}_j - \vec{v}_i) \cdot \hat{n}_{ij}$ appear in the measurements. Neither absolute positions nor absolute velocities are directly measured. Thus, it is impossible to fully constrain the entire LISA configuration only with these inter-spacecraft measurements. The clock jitters only appear in Eq. 5.22 in the form of $\delta T_j - \delta T_i$, which means the common clock drifts are undetermined. The relative USO frequency jitters $\delta f_j - \delta f_i$ are measured in Eq. 5.24. The absolute USO frequency jitters δf_j appear in Eq. 5.23. However, $\delta f_j / f_j^{\text{nom}}$ is far less than 1, hence Eq. 5.23 can provide only very limited information about δf_j. As a result, the absolute USO frequency jitters δf_j are poorly determined.

5.6 Supplementary A: A Limitation on the Common Clock Drift

As mentioned before, the relative clock drifts can be estimated very accurately, whereas the common clock drift cannot be determined. This would result in errors in the time labels of the measurements. The errors in the time labels will introduce modulations to GW signals, hence they may affect the detection and the parameter estimation of GW signals. In this appendix, we try to estimate this effect and to set a limit on the permissible common clock drifts.

We define a quantity $\sigma_T(\tau)$ to characterize the timing stability

$$\sigma_T(\tau) = \sqrt{\frac{1}{2\tau^2} \langle (\delta T(k+1) - \delta T(k))^2 \rangle}, \tag{5.33}$$

where τ is the nominal time increment between the sample k and the sample $k+1$. Notice that this is different from the Allan variance [2]

$$\begin{aligned} \sigma_A^2(\tau) &= \frac{1}{2} \left\langle \left(\frac{\delta f(k+1)}{f^{\text{nom}}} - \frac{\delta f(k)}{f^{\text{nom}}} \right)^2 \right\rangle \\ &= \frac{1}{2\tau^2} \langle (\delta T(k+2) - 2\delta T(k+1) + \delta T(k))^2 \rangle, \end{aligned} \tag{5.34}$$

which characterizes the frequency stability of the clock.

For a GW signal with frequency f_{GW} and a total observation time T_{obs}, if the mismatch caused by the common clock drift is less than ϵ cycle, the effect on physical data analysis is negligible. Thus, we have a limitation on the common clock drift

$$\sigma_T(\tau) f_{\text{GW}} T_{\text{obs}} < \epsilon. \tag{5.35}$$

For physical data analysis concern, a sampling time of $\tau = 1\,\mathrm{s}$ will suffice. By considering the worst scenario, we take $f_{\mathrm{GW}} = 0.1\,\mathrm{Hz}$, $T_{\mathrm{obs}} = 10^8\,\mathrm{s}$ and $\epsilon = 0.1$, hence the timing stability should satisfy $\sigma_T(1) < 10^{-8}$.

5.7 Supplementary B: A Proof of the Optimality

In the Kalman filter derivation, the Kalman gain K_k is chosen such that the estimation error $\mathrm{tr}(P_k^+)$ in the state vector is minimized. However, in the LISA case we are interested in reducing the noise in the measured variables rather than reducing the uncertainties in the state vector. Hence, the optimal filter in this case should minimize the estimation error in the measurements y_k.

In this appendix, we prove that minimizing the estimation error in the state vector x_k is equivalent to minimizing the estimation error in y_k to the linear order. As shown in previous sections, the estimation error in y_k is $\mathrm{tr}(H_k P_k^+ H_k^T)$ in the linearized model. To minimize the trace of this covariance matrix, we have

$$\begin{aligned}\frac{\partial[\mathrm{tr}(H_k P_k^+ H_k^T)]}{\partial K_k} &= \frac{\partial[\mathrm{tr}(H_k^T H_k P_k^+)]}{\partial K_k} \\ &= \frac{\partial\{\mathrm{tr}[H_k^T H_k (I - K_k H_k) P_k^- (I - K_k H_k)^T + H_k^T H_k K_k V_k K_k]\}}{\partial K_k}. \\ &= 0 \end{aligned} \tag{5.36}$$

To be concise, we omit the step index k and use the subscripts for the component indices.

$$\begin{aligned}&\frac{\partial\{\mathrm{tr}[H^T H (I - KH) P^- (I - KH)^T]\}}{\partial K} \\ &= \frac{\partial\{\mathrm{tr}[H_{ni}^T H_{ij} (I_{jl} - K_{jk} H_{kl}) P_{lm}^- (I - KH)_{mn}^T]\}}{\partial K_{ab}} \\ &= \frac{\partial\{\mathrm{tr}[H_{in} H_{ij} (I_{jl} - K_{jk} H_{kl}) P_{lm}^- (I_{nm} - K_{nc} H_{cm})]\}}{\partial K_{ab}} \\ &= H_{in} H_{ij} (-\delta_{aj} \delta_{bk} H_{kl}) P_{lm}^- (I_{nm} - K_{nc} H_{cm}) + H_{in} H_{ij} (I_{jl} - K_{jk} H_{kl}) P_{lm}^- (-\delta_{an} \delta_{bc} H_{cm}) \\ &= -H_{ai}^T H_{in} (I - KH)_{nm} P_{ml}^{-T} H_{lb}^T - H_{ai}^T H_{ij} (I - KH)_{jl} P_{lm}^- H_{mb}^T \\ &= -2H^T H (I - KH) P^- H^T, \end{aligned} \tag{5.37}$$

where we have adopted Einstein summation convention and used the fact that P^+ is symmetric. Similarly, we have

$$\frac{\partial\{\mathrm{tr}(H^T H K V K)\}}{\partial K} = 2H^T H K V. \tag{5.38}$$

By putting back the step index k, we have

$$\begin{aligned} 0 &= \frac{\partial[\mathrm{tr}(H_k P_k^+ H_k^T)]}{\partial K_k} \\ &= 2H_k^T H_k [K_k V_k - (I - K_k h_k) P_k^- H_k^T]. \end{aligned} \tag{5.39}$$

The Kalman gain is then solved as follows

$$K_k = P_k^- H_k^T (H_k P_k^- H_k^T + V_k)^{-1}, \tag{5.40}$$

which is the same as what we have used.

References

1. D. Simon, *Optimal State Estimation* (Wiley, Hoboken, 2006)
2. D. Allan, Statistics of atomic frequency standards. Proc. IEEE **54**(2), 221–230 (1966)

Chapter 6
Alternative Kalman Filter Models

Abstract In this chapter, three reduced versions of the state vector for LISA have been designed and investigated, in order to alleviate the degeneracy problem, i.e. the number of the measured variables is less than the number of the variables to be determined by the Kalman filter.

6.1 Introduction

In the last chapter, we have designed a hybrid-extended Kalman filter to pre-process LISA raw measurements. The noise in the measurements has been significantly reduced by the filter. The initial clock biases have been decoupled from the arm lengths. However, the state vector cannot be determined well due to the insufficient number of measurements. In this chapter, we will explore alternative Kalman filter models to reduce the ambiguity in the state vector, while using the same measurements. We investigate in detail how different Kalman filter models affect the accuracy of the estimates.

6.2 A Kalman Filter Model with a 23 Dimensional State Vector

As mentioned in the last chapter, the initial clock biases δT_i appear in the measurement equations only in the form of time difference $\delta T_j - \delta T_i$. Therefore, the absolute clock biases δT_i cannot be determined. To eliminate this degeneracy in the Kalman filter model, we replace the three clock bias variables δT_1, δT_2 and δT_3 by two time difference variables $\delta T_1 - \delta T_2$ and $\delta T_2 - \delta T_3$. Hence, the state vector is now a 23-dimensional column vector

$$x = (\vec{x}_1, \vec{x}_2, \vec{x}_3, \vec{v}_1, \vec{v}_2, \vec{v}_3, \delta T_1 - \delta T_2, \delta T_2 - \delta T_3, \delta f_1, \delta f_2, \delta f_3)^T, \tag{6.1}$$

Y. Wang, *First-stage LISA Data Processing and Gravitational Wave Data Analysis*,
Springer Theses, DOI 10.1007/978-3-319-26389-2_6

where $\vec{x}_i = (x_i, y_i, z_i)^T$ are the S/C positions, $\vec{v}_i = (v_{xi}, v_{yi}, v_{zi})^T$ are the S/C velocities, δT_i and δf_i are the clock jitters and frequency jitters, $i = 1, 2, 3$ is the S/C index as before. The third initial clock bias difference $\delta T_1 - \delta T_3$ can be expressed as $(\delta T_1 - \delta T_2) + (\delta T_2 - \delta T_3)$. The dynamic equation for the clock biases can simply be modified as

$$\frac{\mathrm{d}}{\mathrm{d}t}(\delta T_j - \delta T_i) = \frac{\delta f_j}{f_j^{\mathrm{nom}}} - \frac{\delta f_i}{f_i^{\mathrm{nom}}}. \tag{6.2}$$

The dynamic matrix F_k and the observation matrix H_k are then modified accordingly.

We carried out simulations to compare the performance of this Kalman filter model with the performance of the model designed in the previous chapter with a 24-dimensional state vector. The two filters have been run over the same simulated measurement data. Figure 6.1 shows a comparison of the arm length determination between the two Kalman filter models. It can be seen that the performance of the two Kalman filter models is comparable in determining the arm lengths. Both models can successfully decouple the arm lengths from the initial clock biases and reduce the noise in the arm-length roughly by one order of magnitude. Notice that the performance of a Kalman filter depends on the specific noise realization. Therefore, a small difference between the two models in the estimation error is not significant. Figure 6.2 shows histograms of estimation errors in relative clock jitters. Both models are able to reduce the noise in the relative clock jitters roughly by an order. The Kalman filter model with a 23-dimensional state vector performs slightly better. Figure 6.3 shows histograms of estimation errors in relative USO frequency jitters. Both Kalman filter models have greatly reduced the noise in the raw measurements. The performances turn out to be comparable.

All in all, the Kalman filter model with a 23-dimensional state vector designed in this section performs slightly better than the model with a 24-dimensional state

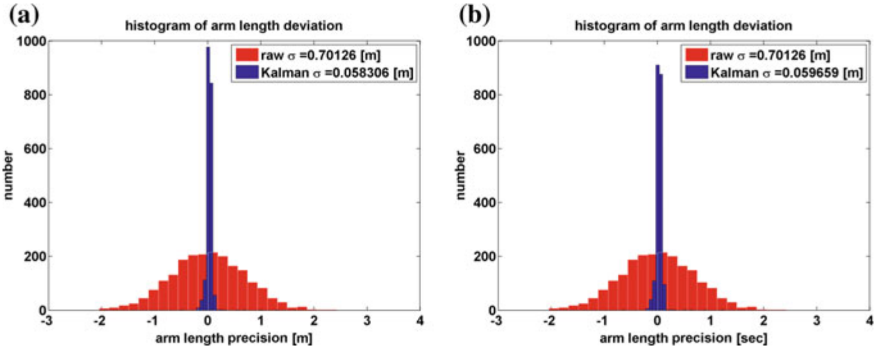

Fig. 6.1 A comparison of the arm length determination, **a** shows histograms of errors in raw arm-length measurements and Kalman filter estimates with a 24-dimensional state vector, **b** shows histograms of errors in raw arm-length measurements and Kalman filter estimates with a 23-dimensional state vector. Notice that the initial clock biases are not included in the raw measurement errors for better vision

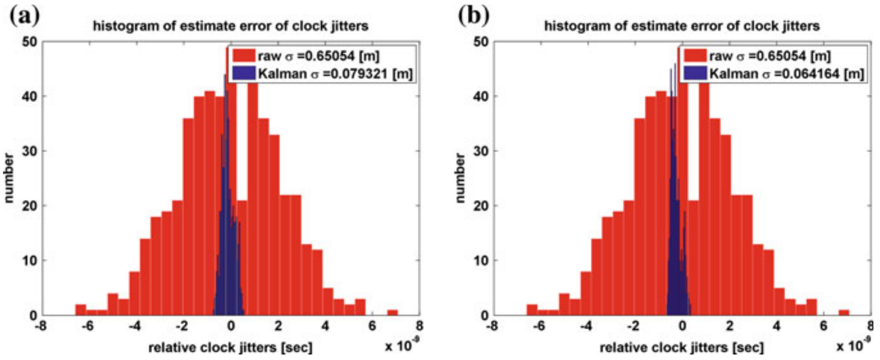

Fig. 6.2 Histograms of estimation errors in relative clock jitters, **a** shows histograms of errors in the raw data and Kalman filter estimates with a 24-dimensional state vector, **b** shows histograms of errors in the raw data and Kalman filter estimates with a 23-dimensional state vector

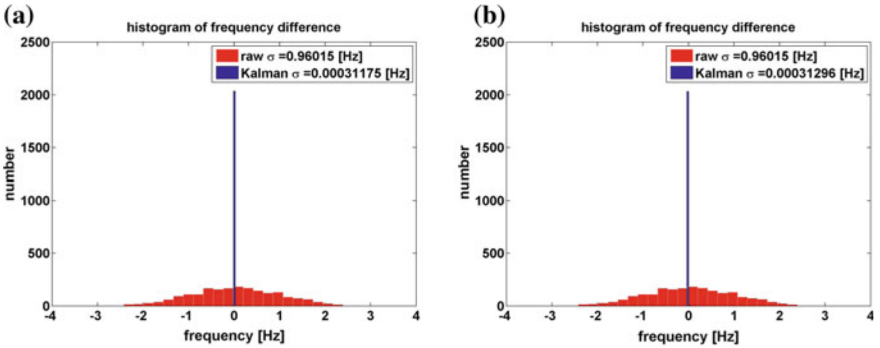

Fig. 6.3 Histograms of estimation errors in relative USO frequency jitters, **a** shows histograms of errors in the raw data and Kalman filter estimates with a 24-dimensional state vector, **b** shows histograms of errors in the raw data and Kalman filter estimates with a 23-dimensional state vector

vector. The reason is that the Kalman filter model with a smaller state vector has reduced the ambiguity in the system model, while retaining the full information on the measurement mechanism.

6.3 A Kalman Filter Model with a 22 Dimensional State Vector

In this section, we try to simplify the state vector further. From the simulation, we know that the absolute frequency jitters cannot be determined accurately. The only information about the absolute frequency jitters comes from the term $1 - \delta f_j / f_j^{\mathrm{nom}}$ of the following measurement equation

$$D_{ij} = \left[f_j^{\text{carrier}} - f_i^{\text{carrier}} \left(1 - \frac{(\vec{v}_j - \vec{v}_i) \cdot \hat{n}_{ij}}{c} \right) + f_{ij}^{\text{GW}} \right] \left(1 - \frac{\delta f_j}{f_j^{\text{nom}}} \right) + n_{ij}^D. \tag{6.3}$$

Usually, $\delta f_j / f_j^{\text{nom}}$ is several orders of magnitude smaller than 1, thus term provides very limited information about the absolute frequency jitters of the USOs. As we mentioned before, this is the reason why the absolute frequency jitters cannot be determined accurately.

We can actually approximate this term by 1 without losing much information. Then, the Doppler measurement equation becomes

$$D_{ij} \doteq \left[f_j^{\text{carrier}} - f_i^{\text{carrier}} \left(1 - \frac{(\vec{v}_j - \vec{v}_i) \cdot \hat{n}_{ij}}{c} \right) + f_{ij}^{\text{GW}} \right] + n_{ij}^D. \tag{6.4}$$

Now, in all the three inter-spacecraft measurement Eqs. 5.22, 6.4 and 5.24 the frequency jitters only appear in the form of frequency difference $\delta f_j - \delta f_i$. Therefore, we can replace the three frequency jitter variables δf_i by two frequency difference $\delta f_1 - \delta f_2$ and $\delta f_2 - \delta f_3$. The state vector is correspondingly reduced to 22 dimensions:

$$x = (\vec{x}_1, \vec{x}_2, \vec{x}_3, \vec{v}_1, \vec{v}_2, \vec{v}_3, \delta T_1 - \delta T_2, \delta T_2 - \delta T_3, \delta f_1 - \delta f_2, \delta f_2 - \delta f_3)^T. \tag{6.5}$$

The dynamic model for the clock jitters and the frequency jitters is approximated as follows

$$\frac{\mathrm{d}}{\mathrm{d}t} \begin{bmatrix} \delta T_j - \delta T_i \\ \delta f_j - \delta f_i \end{bmatrix} = \begin{bmatrix} 2(\delta f_j - \delta f_i)/(f_j^{\text{nom}} + f_i^{\text{nom}}) \\ 0 \end{bmatrix}. \tag{6.6}$$

The main advantages of this Kalman filter model are (i) the reduction of the near degeneracy in the system model, (ii) the reduction of the nonlinearity in the measurement equations. On the other hand, the use of approximate measurement equations could also be disadvantageous at the same time.

We implement this Kalman filter model to process the same simulated measurement data used in the last section. We have set the nominal frequencies of the USOs in different S/C to be identical in the simulation, i.e. $f_j^{\text{nom}} = f_i^{\text{nom}}$. If the nominal frequencies are not identical, the performance of this Kalman filter model would be degraded depending on how different the nominal frequencies are. The simulation results are summarized in Fig. 6.4, where the estimation errors in the arm lengths, clock jitters and USO frequency jitters are shown. Comparing these results with Figs. 6.1, 6.2 and 6.3, we find that the estimation errors of this model in the arm lengths are slight larger than those of the other two Kalman filter models. However, this Kalman filter model performs slightly better than the other two models in determining the clock jitters. Overall, the performances are similar.

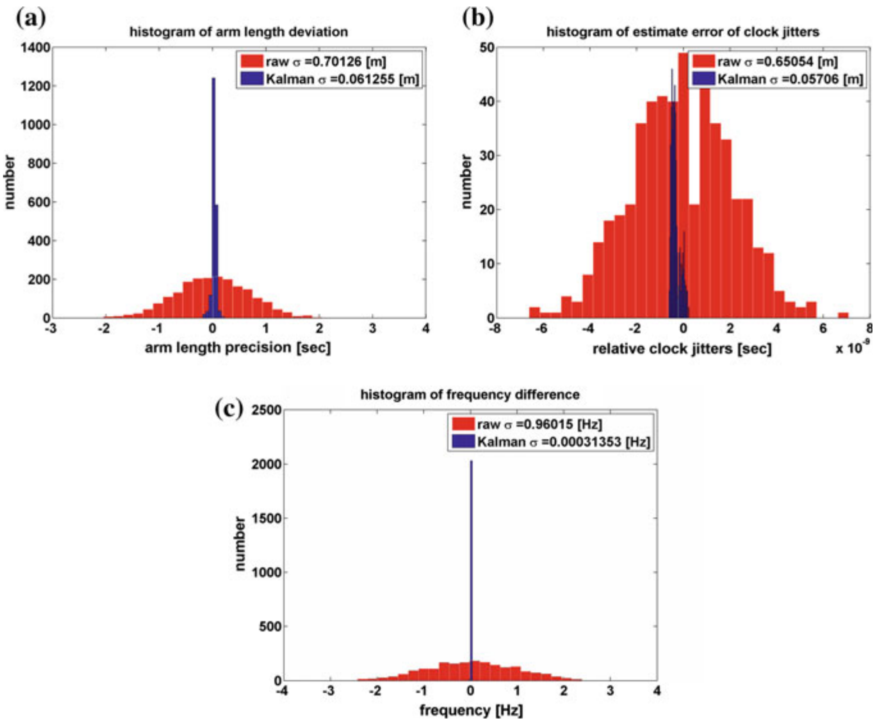

Fig. 6.4 Simulation results of the Kalman filter model with a 22-dimensional state vector, **a** histograms of errors in raw arm-length measurements and Kalman filter estimates, **b** shows histograms of errors in the clock jitters, **c** shows histograms of errors in the USO frequency jitters

6.4 A Simplified Kalman Filter Model with Only Clock Variables

In this section, we show a greatly simplified Kalman filter model only for the USOs. The main benefits from such a model are the simplicity of the linear mathematical model and the efficient implementation. On the other hand, this model is accurate only when the inter-spacecraft laser links are instantaneous, hence not straightforward to be generalized to the full-relativistic treatment with relativistic inter-spacecraft delays. At any rate, in this model we need not to deal with large matrices with hundreds of nonlinear components but only small constant matrices.

Let us first define a 4-dimensional state vector

$$x = \begin{bmatrix} \delta T_1 - \delta T_2 \\ \delta T_2 - \delta T_3 \\ \delta f_1 - \delta f_2 \\ \delta f_2 - \delta f_3 \end{bmatrix} \equiv \begin{bmatrix} x_1 \\ x_2 \\ x_3 \\ x_4 \end{bmatrix}, \tag{6.7}$$

which consists of only the relative clock jitters and the relative USO frequency jitters. The dynamic equations can be simply modeled as

$$\frac{\mathrm{d}}{\mathrm{d}t}\begin{bmatrix} x_1 \\ x_2 \\ x_3 \\ x_4 \end{bmatrix} = \begin{bmatrix} x_3/f^{\mathrm{nom}} \\ x_4/f^{\mathrm{nom}} \\ 0 \\ 0 \end{bmatrix} + \text{noise}, \tag{6.8}$$

where we have assumed the nominal frequencies of the three USOs are identical, i.e. $f_i^{\mathrm{nom}} = f^{\mathrm{nom}}$. Since these dynamic equations are linear, the dynamic matrix is simply

$$F = \frac{\partial f}{\partial x} = \begin{bmatrix} 0 & 0 & 1/f^{\mathrm{nom}} & 0 \\ 0 & 0 & 0 & 1/f^{\mathrm{nom}} \\ 0 & 0 & 0 & 0 \\ 0 & 0 & 0 & 0 \end{bmatrix}. \tag{6.9}$$

Next, let us look into the measurement equations. For instantaneous laser links, the relative clock jitters can be obtain in the following way

$$\delta T_j - \delta T_i = \frac{1}{2c}(R_{ij} - R_{ji} - n_{ij}^R + n_{ji}^R), \tag{6.10}$$

where the ranging measurements R_{ij} are given in Eq. 5.22. The relative USO frequency jitters are indirectly inferred by the modified clock measurements, see Eq. 5.24. As mentioned before, the Doppler measurements (see Eq. 5.23) contain little information on the frequency jitters, hence for this Kalman filter model with only clock variables they are nearly irrelevant. Therefore, the measurement equations are simplified to the following linear form

$$y = \begin{bmatrix} \delta T_1 - \delta T_2 \\ \delta T_2 - \delta T_3 \\ \delta T_3 - \delta T_1 \\ \delta f_1 - \delta f_2 \\ \delta f_2 - \delta f_3 \\ \delta f_3 - \delta f_1 \end{bmatrix} + \text{noise} = \begin{bmatrix} x_1 \\ x_2 \\ -x_1 - x_2 \\ x_3 \\ x_4 \\ -x_3 - x_4 \end{bmatrix} + \text{noise}, \tag{6.11}$$

which leads to a constant measurement matrix

$$H = \frac{\partial y}{\partial x} = \begin{bmatrix} 1 & 0 & 0 & 0 \\ 0 & 1 & 0 & 0 \\ -1 & -1 & 0 & 0 \\ 0 & 0 & 1 & 0 \\ 0 & 0 & 0 & 1 \\ 0 & 0 & -1 & -1 \end{bmatrix}. \tag{6.12}$$

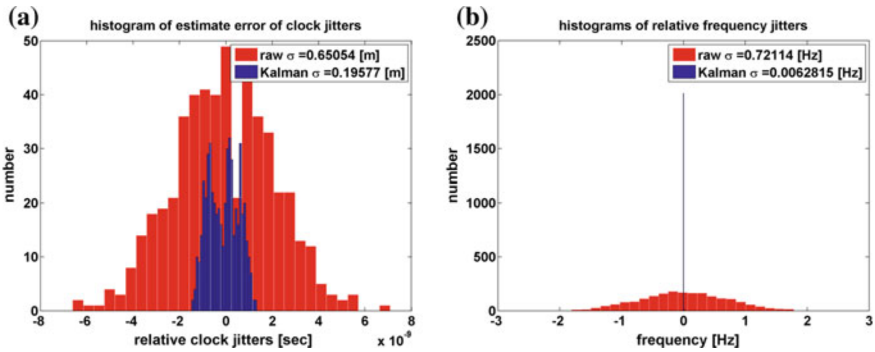

Fig. 6.5 Simulation results of the simplified Kalman filter model with only clock variables, **a** shows histograms of errors in the relative clock jitters, **b** shows histograms of errors in the relative USO frequency jitters

We implement the above simplified Kalman filter model to process the same simulated measurement data used in previous sections. The simulation results are shown in Fig. 6.5. It can be seen that in the considered case the simplified Kalman filter has significantly reduced the noise in the relative clock jitters and greatly reduced the noise in the relative USO frequency jitters. Comparing these results with Figs. 6.2, 6.3 and 6.4, the performance of this simplified Kalman filter is a few times worse than other Kalman filter models in determining the relative clock jitters and about ten times worse in determining the relative USO frequency jitters.

6.5 Summary

In this chapter, we have designed and tested several alternative Kalman filter models. The Kalman filter models with 24-dimensional, 23-dimensional and 22-dimensional state vectors are comparable in reducing the measurement noise. The greatly simplified Kalman filter model with only clock variables performs a few times worse than the other filters as expected. All the filter models have successfully and significantly reduced the measurement noise. Each Kalman filter model has its own advantages and disadvantages. One should select the proper one for the specific case.

Chapter 7
Broken Laser Links and Robustness

Abstract This chapter investigates the effects of broken laser links of LISA. Different combinations of broken laser links have been simulated and studied via a sequential Kalman filter. As a special case, eLISA configuration can be viewed as the standard LISA with two broken laser links in the same arm. Simulation shows that the arm-length determination and clock synchronization algorithm works well for eLISA. In addition, the square-root Kalman filter has been introduced and implemented in this chapter to reduce the condition number of the large matrices in the filter, hence making the algorithm more robust.

7.1 Introduction

In previous chapters, we have described LISA inter-spacecraft measurements and designed several hybrid-extended Kalman filter models to process the raw measurements of the classic LISA configuration. Simulations showed that the designed filters are able to reduce the measurement noise significantly, hence precisely determining the arm lengths and the relative clock drifts.

In this chapter, we will look into two issues. (i) The Kalman filter models designed in previous chapters assume all the six laser links of the classic LISA concept are functioning properly all the time. However, in case of improper performances of some laser links, what could we do? The improper performances during some certain time period refer to much more noisy measurements than required or even a breakdown of some laser link. Although these situations are unexpected to happen in practice, a successful treatment of this issue will significantly increase the robustness of the whole LISA project. The solution will also be directly applicable to eLISA by assuming two laser links of the classic LISA to be broken. (The arm length difference is inconsequential.) (ii) The dynamic range of the simulation is very large. For example,

Y. Wang, *First-stage LISA Data Processing and Gravitational Wave Data Analysis*,
Springer Theses, DOI 10.1007/978-3-319-26389-2_7

the distance from the S/C to the sun is 1.5×10^{11} m, which is 13 orders of magnitude larger than the arm length accuracy we finally reach via data processing. Moreover, Kalman filters usually rely on propagating of different covariance matrices, which essentially square the dynamic range. For the LISA problem, there are many variables that differ from each other by many orders of magnitude. Unfortunately, there is no way to rescale all the variables to have them with comparable values, since there are four types of variables (i.e. positions, velocities, time, and frequency), but only two physical dimensions (i.e. [m] and [s]). Therefore, the four types of variables are essentially dependent. Rescaling one type of variables would rescale other types of variables accordingly, leaving the dynamic range unchanged. The large difference in orders of magnitude between different components of the covariance matrices results in large condition numbers, which cause numerical instabilities and errors. Therefore, it is important to reduce the condition number. We try to address these problems to enhance the robustness of the algorithms via the square root Kalman filter formulation.

7.2 Sequential Kalman Filtering

7.2.1 Sequential Kalman Filter Formulation

By its name, the sequential Kalman filter [1] proposes to process the measurement data one after another. It requires the covariance matrix of the measurement noise to be diagonal, which we denote as

$$V_k = \mathrm{diag}(V_{1k}, V_{2k}, \ldots). \tag{7.1}$$

When this requirement is satisfied, the set of measurements y_k at step k are essentially independent. Hence, we can view each datum y_{ik} in y_k as a single measurement. The measurement equation then becomes

$$y_{ik} = H_{ik} x_k + v_{ik}. \tag{7.2}$$

By replacing the standard measurement equation with this single-datum measurement equation, we obtain the so-called sequential Kalman filter, which only processes one measurement at a step. One other advantage of the sequential Kalman filter is that this formulation requires no matrix inversion in the calculation. Moreover, this formulation easily accommodates individual measurements that are corrupt or broken.

We summarize the sequential Kalman filter formulations as follows:

1. Initialize the state vector and the covariance matrix

$$\hat{x}_0^+,\, P_0^+. \tag{7.3}$$

2. Calculate the a priori estimate $\hat{x}_k^-$ from the a posteriori estimate $\hat{x}_{k-1}^+$ at the previous step, using the dynamic equation

$$\dot{x} = f(x, t). \tag{7.4}$$

Use either of the following two formulae to update the covariance matrix

$$P_k^- = e^{F_{k-1}\Delta t} P_{k-1}^+ e^{F_{k-1}^T \Delta t} + W_{k-1}, \tag{7.5}$$

$$P_k^- = (I + F_{k-1}\Delta t) P_{k-1}^+ (I + F_{k-1}\Delta t)^T + W_{k-1}. \tag{7.6}$$

3. Initialize the posteriori state vector and the covariance matrix as

$$\hat{x}_{0k}^+ = \hat{x}_k^- \tag{7.7}$$

$$P_{0k}^+ = P_k^- \tag{7.8}$$

4. Process each measurement datum y_{ik} $(i = 1, 2, \ldots, l)$ one after another at the step k

$$K_{ik} = \frac{P_{i-1,k}^+ H_{ik}^T}{H_{ik} P_{i-1,k}^+ H_{ik}^T + V_{ik}} \tag{7.9}$$

$$\hat{x}_{ik}^+ = \hat{x}_{i-1,k}^+ + K_{ik}[y_{ik} - h_{ik}(\hat{x}_{i-1,k}^+)] \tag{7.10}$$

$$P_{ik}^+ = (I - K_{ik} H_{ik}) P_{i-1,k}^+ \tag{7.11}$$

5. Set the posteriori state vector and covariance matrix after processing a set of measurements y_k as

$$\hat{x}_k^+ = \hat{x}_{lk}^+ \tag{7.12}$$

$$P_k^+ = P_{lk}^+ \tag{7.13}$$

7.2.2 *Classic LISA with Broken Links, eLISA-like Configuration, and GRACE-like Configuration*

In this section, we apply the sequential Kalman filter described in the last section to the classic LISA with broken laser links. As special cases, eLISA-like configuration (i.e. with only two arms, or four laser links) and GRACE-like configuration (i.e. with only one arm, or two laser links) are also considered. In the simulation, the standard LISA arm length is used for these two special configurations. That is why they are referred to as eLISA-like and GRACE-like. Still, the simulation results could justify the principles and show potentials of the designed algorithms for these two missions. At any rate, we will see how the missing links would affect the Kalman filter estimates. The inter-spacecraft measurements for each laser link are similar to that used in previous chapters. The difference is that we sometimes only use parts of the laser links in this section instead of all the six laser links. For clarity, all the histograms of estimation errors in this section are for the laser link from S/C 2 to S/C 1, namely (a) the relative clock jitters $\delta T_1 - \delta T_2$, (b) the arm length L_{21}, and (c) the relative frequency jitters $\delta f_1 - \delta f_2$.

First, we apply the sequential Kalman filter to the standard LISA, with all the six laser links working properly. The simulation results are shown in Fig. 7.1. For comparison, the estimation errors of the hybrid-extended Kalman filter applying to the

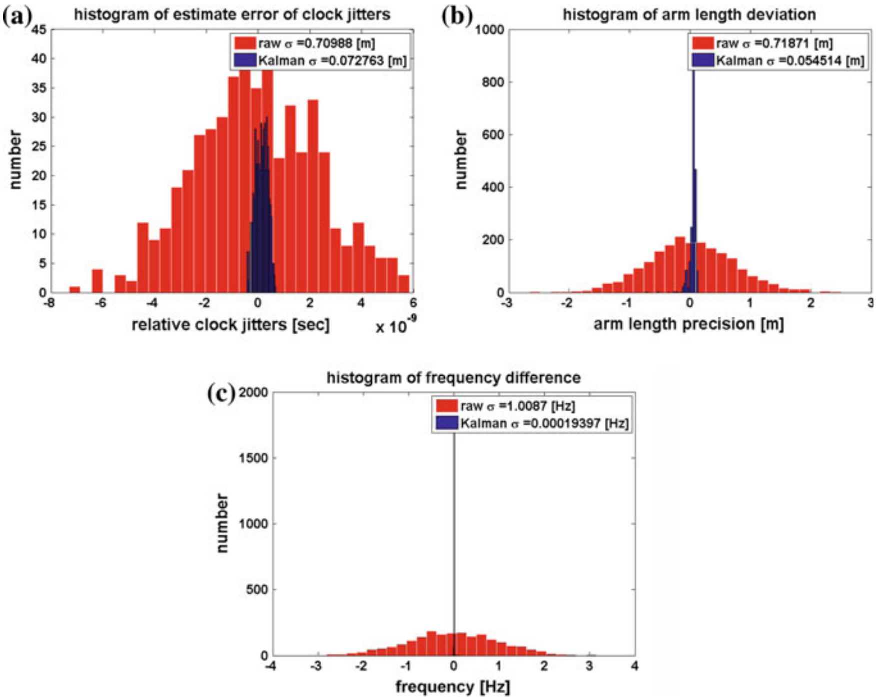

Fig. 7.1 Histograms of sequential Kalman filter estimation errors in **a** relative clock jitters, **b** arm lengths, and **c** relative frequency jitters for the laser link from S/C 2 to S/C 1, given that all laser links are working properly

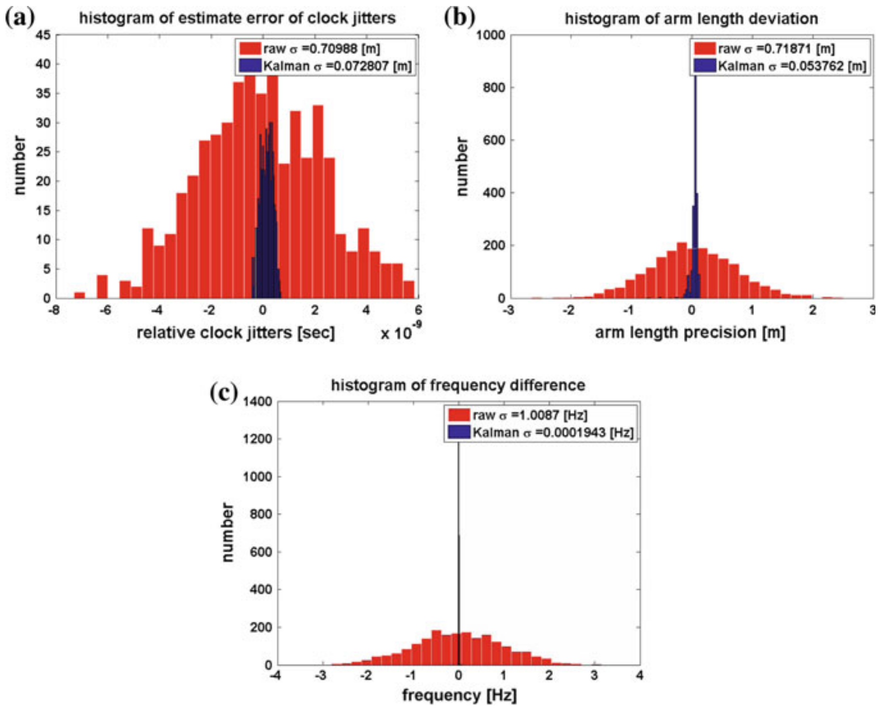

Fig. 7.2 Histograms of hybrid-extended Kalman filter estimation errors in **a** relative clock jitters, **b** arm lengths, and **c** relative frequency jitters for the laser link from S/C 2 to S/C 1, given that all laser links are working properly

same measurement data are shown in Fig. 7.2. Apparently, both algorithms have accurately estimated the relative clock jitters, the arm lengths and the relative frequency jitters. In this case, the performances of the two algorithms are very similar. On one hand, the hybrid-extended Kalman filter is able to deal with the cross-correlations between the noise of different measurements, which has been ignored by the sequential Kalman filter. On the other hand, the sequential Kalman filter algorithm has avoided the matrix inversion, which helps increase numerical accuracies, especially when the condition number of the matrix is large.

Next, we consider the situation when one laser link of LISA is broken or too noisy to be used. This can be classified into two cases: how a broken laser link affects the estimates of the inter-spacecraft measurements in a different arm, and how a broken laser link affects the estimates of the inter-spacecraft measurements in the same arm. The simulation results for these two cases are shown in Figs. 7.3 and 7.4, respectively. From Fig. 7.3 we see that a single missing laser link in a different arm hardly affects

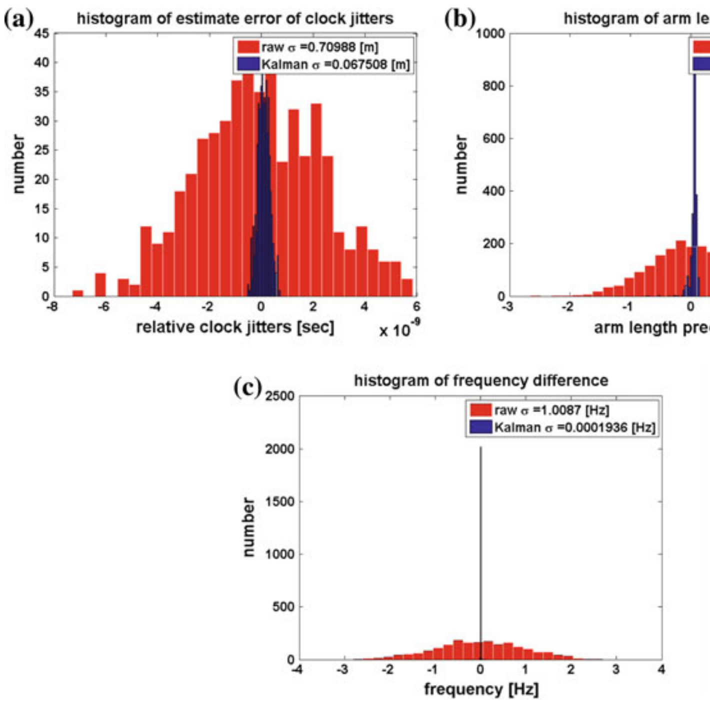

Fig. 7.3 Histograms of sequential Kalman filter estimation errors in **a** relative clock jitters, **b** arm lengths, and **c** relative frequency jitters for the laser link from S/C 2 to S/C 1, when the laser link from S/C 3 to S/C 2 is broken

the estimates of the inter-spacecraft measurements. However, Fig. 7.4 tells us that a missing laser link in the same arm significantly affects the estimates of the relative clock jitters and the arm lengths. The estimation errors in the clock jitters are about 25 percent larger, and the estimation errors in the arm lengths about twice larger. This is reasonable, since the laser link in the same arm directly measures the quantities to be estimated.

In principle, the situation when two laser links are shut down can be classified into four cases: (i) the two broken laser links are in one arm, which is different from the arm to be estimated, (ii) the two broken laser links are in two different arms, while neither arm is the one to be estimated, (iii) the two broken laser links are in two different arms, one of which is the arm to be estimated, and (iv) the two broken laser links are in one arm, which is the arm to be estimated. The last case is not interesting, since we need to estimate the arm length (or the delay time) for the TDI techniques, which requires there is a laser link in the same arm in the first place.

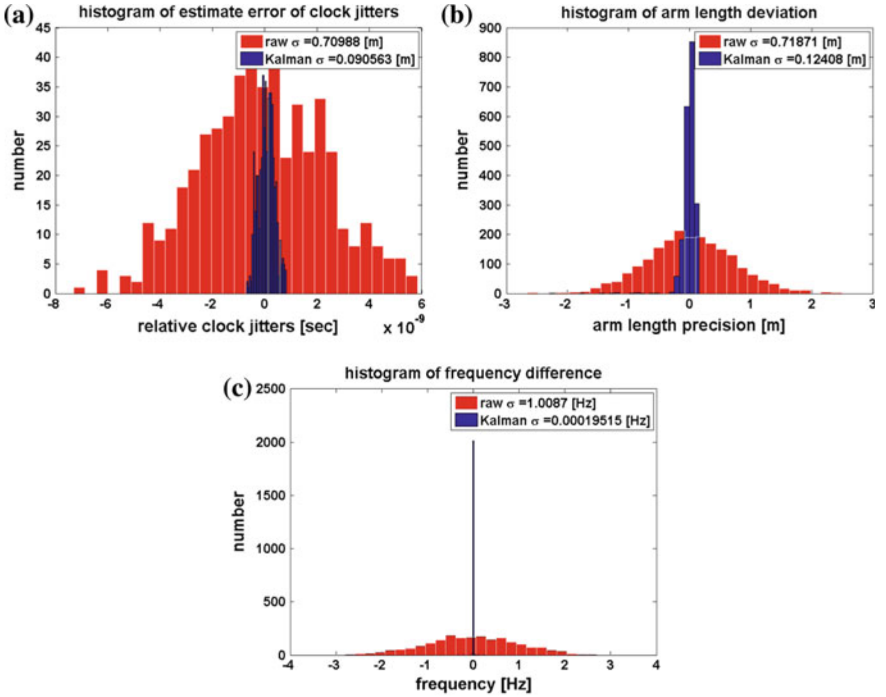

Fig. 7.4 Histograms of sequential Kalman filter estimation errors in **a** relative clock jitters, **b** arm lengths, and **c** relative frequency jitters for the laser link from S/C 2 to S/C 1, when the laser link from S/C 1 to S/C 2 is broken

The simulation results for the first three cases are respectively shown in Figs. 7.5, 7.6 and 7.7. Among them, Fig. 7.5 shows the estimation errors for the eLISA-like configuration, where the arm between S/C 2 and S/C 3 is missing. Compared to Fig. 7.1, we find that the relative clock jitter estimates for the eLISA-like configuration is slightly better, while the arm length estimates for the eLISA-like configuration is slightly worse. Overall, the two performs similarly. This implies the designed Kalman filter algorithms can also help estimate inter-spacecraft quantities for eLISA.

In the case (ii), when the two broken laser links are in two different arms, the designed Kalman filter still works well, as shown in Fig. 7.6. However, the estimates of all the three quantities (the relative clock jitters, the arm lengths and the relative frequency jitters) are slightly worse than the estimates for the eLISA-like configuration. In the case (iii), when a second broken link is in the arm we want to estimate for, it turns out that the relative clock jitters and the arm length cannot be estimated well. Actually, the large estimation errors in Fig. 7.7 result from the degeneracy between the relative clock jitters and the arm length in the ranging measurements, when there is not enough information to decouple them. Compared to Fig. 7.4, which also has a broken laser link in the arm to be estimated, we see the second missing laser link in

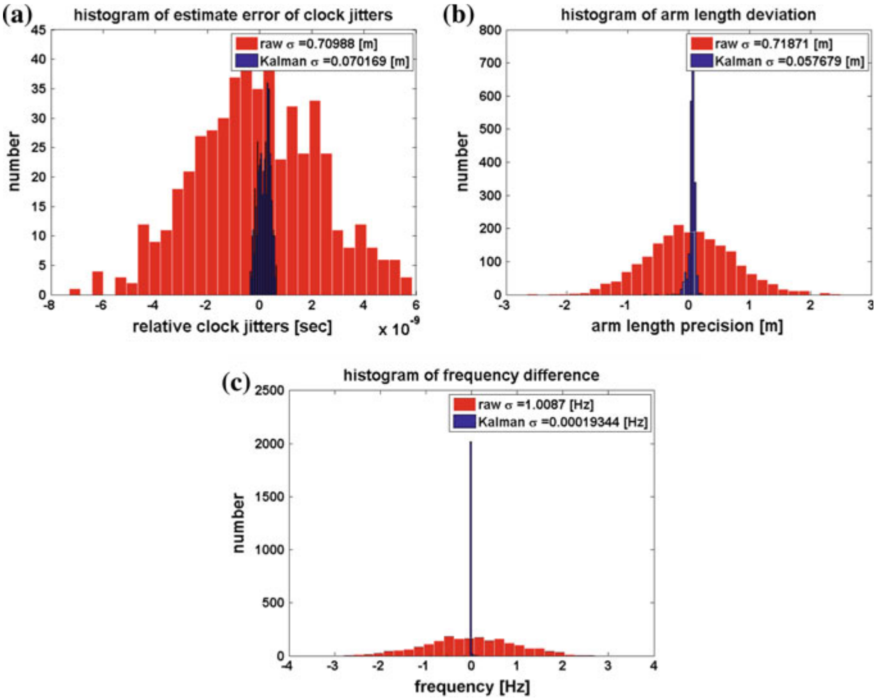

Fig. 7.5 Histograms of sequential Kalman filter estimation errors in **a** relative clock jitters, **b** arm lengths, and **c** relative frequency jitters for the laser link from S/C 2 to S/C 1, given that the arm between S/C 2 and S/C 3 (i.e. the laser link from S/C 3 to S/C 2 and the laser link from S/C 2 to S/C 3) is broken, which is the eLISA-like configuration

this case is crucial. It contains the information to decouple the arm lengths from the relative clock jitters.

The situation when three laser links are broken is not interesting, since LISA-like missions require at least four laser links to perform TDI algorithms to achieve the designed sensitivities. In the end of this section, we consider the case when there is only one arm, which resembles the GRACE mission in some aspects. We will see whether the designed algorithms could help the GRACE-like configuration. We simulate this special case by shutting down all the four laser links in the other two arms and only using the measurements from one arm. The simulation results are shown in Fig. 7.8. It turns out that the designed sequential Kalman filter algorithms work well in this case.

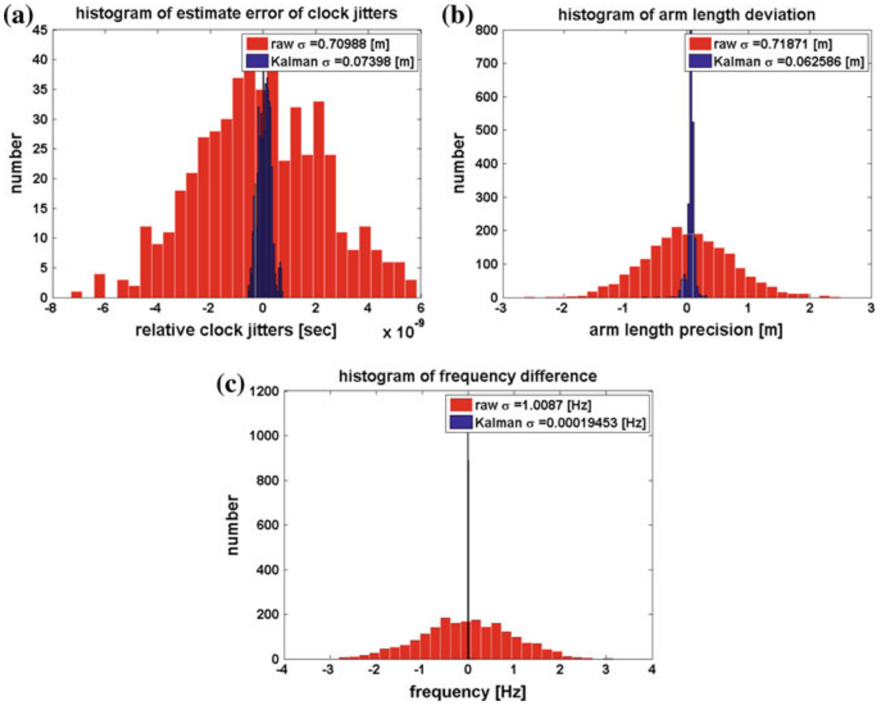

Fig. 7.6 Histograms of sequential Kalman filter estimation errors in **a** relative clock jitters, **b** arm lengths, and **c** relative frequency jitters for the laser link from S/C 2 to S/C 1, when both the laser link from S/C 3 to S/C 2 and the laser link from S/C 1 to S/C 3 are broken

7.3 Square-Root Sequential Kalman Filtering

7.3.1 *Square Root Kalman Filter Formulation*

As mentioned before, square-root Kalman filters [1–3] aim to increase the numeric stability and the robustness of the algorithms. In this section, we briefly describe the derivation of the square-root sequential Kalman filter formulae following [1]. (An error in the formulation in [1] has been corrected here.)

We first define the square roots S_k^+ and S_k^- of the covariance matrices P_k^+ and P_k^- by the relation

$$P_k^+ = S_k^+ (S_k^+)^T, \tag{7.14}$$

$$P_k^- = S_k^- (S_k^-)^T. \tag{7.15}$$

This is possible because P_k^+ and P_k^- are symmetric positive-definite matrices, allowing a Cholesky decomposition. Then, the propagation formula

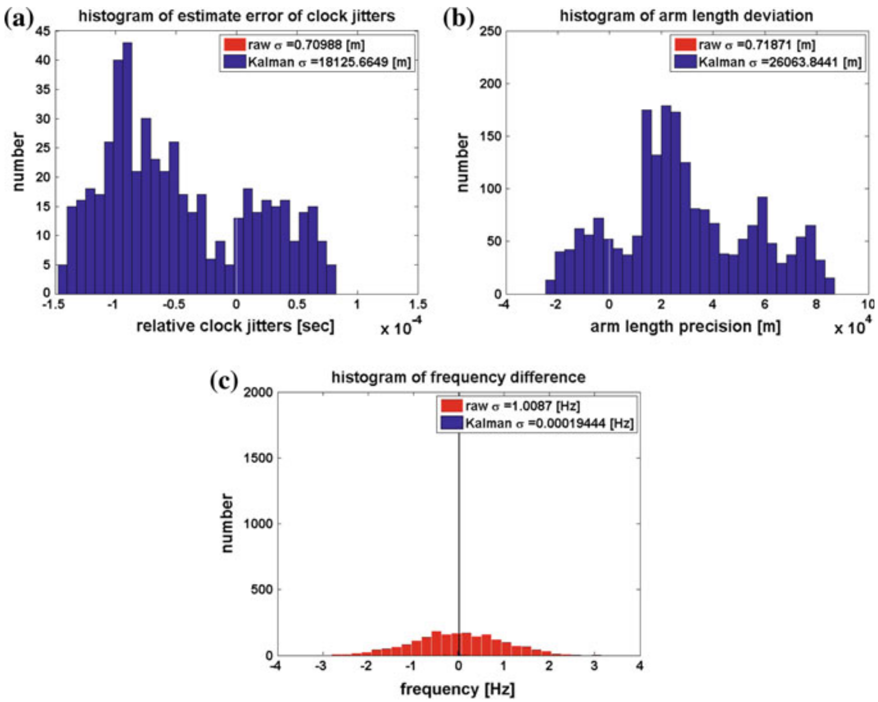

Fig. 7.7 Histograms of sequential Kalman filter estimation errors in **a** relative clock jitters, **b** arm lengths, and **c** relative frequency jitters for the laser link from S/C 2 to S/C 1, when both the laser link from S/C 3 to S/C 2 and the laser link from S/C 1 to S/C 2 are broken

$$P_k^- = e^{F_{k-1}\Delta t} P_{k-1}^+ e^{F_{k-1}^T \Delta t} + W_{k-1} \tag{7.16}$$

can be rewritten as

$$S_k^- (S_k^-)^T = e^{F_{k-1}\Delta t} S_{k-1}^+ (S_{k-1}^+)^T e^{F_{k-1}^T \Delta t} + W_{k-1}^{1/2} W_{k-1}^{T/2}. \tag{7.17}$$

The above formula can be summarized in matrix form

$$\begin{aligned} & [S_k^- \; 0] \begin{bmatrix} (S_k^-)^T \\ 0 \end{bmatrix} \\ &= \left[e^{F_{k-1}\Delta t} S_{k-1}^+ \;\; W_{k-1}^{1/2} \right] \begin{bmatrix} (S_{k-1}^+)^T e^{F_{k-1}^T \Delta t} \\ W_{k-1}^{T/2} \end{bmatrix} \\ &= \left[e^{F_{k-1}\Delta t} S_{k-1}^+ \;\; W_{k-1}^{1/2} \right] Q^T Q \begin{bmatrix} (S_{k-1}^+)^T e^{F_{k-1}^T \Delta t} \\ W_{k-1}^{T/2} \end{bmatrix}, \end{aligned} \tag{7.18}$$

where we have assumed Q to be a unitary matrix, satisfying $Q^T Q = I$. Therefore, if we can find a unitary matrix Q, which fulfils the following requirement

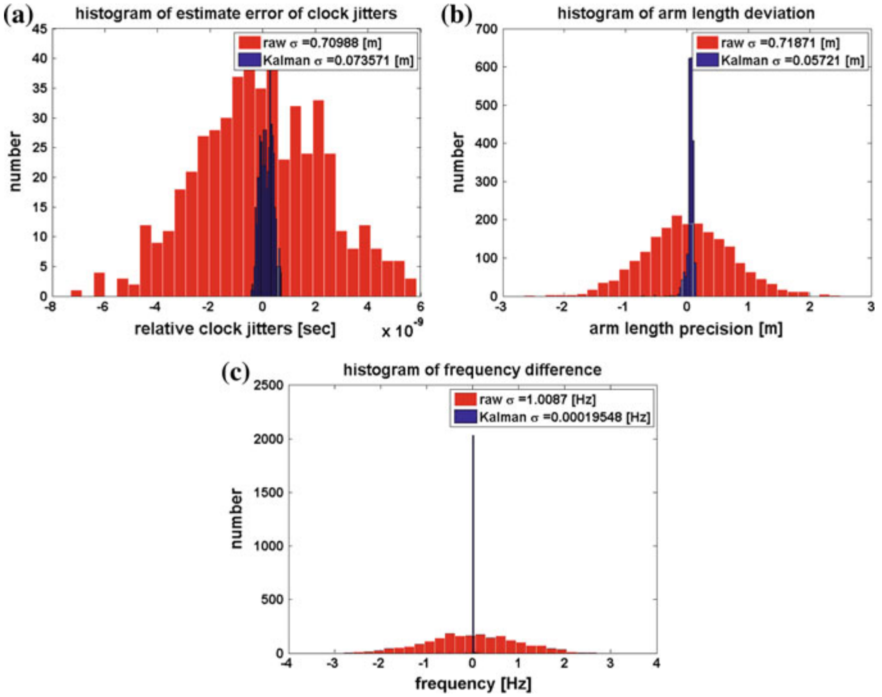

Fig. 7.8 Histograms of sequential Kalman filter estimation errors in **a** relative clock jitters, **b** arm lengths, and **c** relative frequency jitters for the laser link from S/C 2 to S/C 1, when only the arm between S/C 1 and S/C 2 is working properly. This resembles the GRACE configuration

$$Q\begin{bmatrix}(S_{k-1}^{+})^{T}e^{F_{k-1}^{T}\Delta t}\\ W_{k-1}^{T/2}\end{bmatrix}=\begin{bmatrix}R\\ 0\end{bmatrix}, \tag{7.19}$$

it is straightforward to show that $R^T R = P_k^-$. Thus, we can let $(S_k^-)^T = R$. The above equation is then rewritten as

$$\begin{bmatrix}(S_{k-1}^{+})^{T}e^{F_{k-1}^{T}\Delta t}\\ W_{k-1}^{T/2}\end{bmatrix}=Q^{T}\begin{bmatrix}(S_{k}^{-})^{T}\\ 0\end{bmatrix}. \tag{7.20}$$

Hence, we can calculate S_k^- from S_{k-1}^+ by implementing a QR decomposition of the matrix on the left hand side of the above equation. The Modified Gram-Schmidt algorithm will be used to achieve a better numerical stability of the QR decomposition in the simulation.

We define the square root of P_{ik}^+ as S_{ik}^+, i.e.

$$P_{ik}^{+} = S_{ik}^{+}(S_{ik}^{+})^{T}. \tag{7.21}$$

Now, the task is to calculate S^+_{ik} from $S^+_{i-1,k}$. When this relation is derived, we have closed the square root Kalman filter propagation loop. First, we rewrite the Kalman gain in Eq. 7.9 as

$$K_{ik} = a_i S^+_{i-1.k} \phi_i, \tag{7.22}$$

where we have defined

$$\phi_i \equiv S^{+T}_{i-1,k} H^T_{ik}, \tag{7.23}$$

$$a_i \equiv \frac{1}{\phi_i^T \phi_i + V_{ik}}. \tag{7.24}$$

Equation 7.11 then becomes

$$\begin{aligned} S^+_{ik}(S^+_{ik})^T &= \left(I - a_i S^+_{i-1.k} \phi_i H_{ik}\right) S^+_{i-1,k} (S^+_{i-1,k})^T \\ &= S^+_{i-1,k}(I - a_i \phi_i \phi_i^T)(S^+_{i-1,k})^T. \end{aligned} \tag{7.25}$$

Letting

$$I - a_i \phi_i \phi_i^T = (I - a_i \gamma_i \phi_i \phi_i^T)^2, \tag{7.26}$$

it is straightforward to solve the above equation

$$\gamma_i = \frac{1}{1 \pm \sqrt{a_i V_{ik}}}. \tag{7.27}$$

Hence, we obtain the propagation formula

$$S^+_{ik} = S^+_{i-1,k}(I - a_i \gamma_i \phi_i \phi_i^T). \tag{7.28}$$

All the key formulae of the square root Kalman filter have been derived up to here. We summarize the square root Kalman filter algorithm as follows:

1. Initialize the state vector, the covariance matrix and its square root matrix

$$\hat{x}^+_0, P^+_0 = S^+_0 (S^+_0)^T. \tag{7.29}$$

2. Calculate the a priori estimate $\hat{x}^-_k$ from the a posteriori estimate $\hat{x}^+_{k-1}$ at the previous step, using the dynamic equation

$$\dot{x} = f(x, t). \tag{7.30}$$

Obtain S^-_k by implementing a QR decomposition of the following matrix via the modified Gram-Schmidt algorithm.

$$\begin{bmatrix} (S_{k-1}^{+})^T e^{F_{k-1}^T \Delta t} \\ W_{k-1}^{T/2} \end{bmatrix}. \tag{7.31}$$

3. Initialize the posteriori state vector and the square root of the covariance matrix as

$$\hat{x}_{0k}^{+} = \hat{x}_k^{-} \tag{7.32}$$

$$S_{0k}^{+} = S_k^{-} \tag{7.33}$$

4. Process each measurement datum y_{ik} ($i = 1, 2, \ldots, l$) one after another at the step k to calculate the Kalman gain, Kalman estimates and the square root of the posteriori covariance matrix

$$\phi_i = S_{i-1,k}^{+T} H_{ik}^T \tag{7.34}$$

$$a_i = \frac{1}{\phi_i^T \phi_i + V_{ik}} \tag{7.35}$$

$$\gamma_i = \frac{1}{1 \pm \sqrt{a_i V_{ik}}} \tag{7.36}$$

$$K_{ik} = a_i S_{i-1,k}^{+} \phi_i \tag{7.37}$$

$$S_{ik}^{+} = S_{i-1,k}^{+} (I - a_i \gamma_i \phi_i \phi_i^T) \tag{7.38}$$

$$\hat{x}_{ik}^{+} = \hat{x}_{i-1,k}^{+} + K_{ik}(y_{ik} - H_{ik} \hat{x}_{i-1,k}^{+}) \tag{7.39}$$

5. Set the posteriori state vector and the square root of the covariance matrix after processing a set of measurements y_k as

$$\hat{x}_k^{+} = \hat{x}_{lk}^{+} \tag{7.40}$$

$$S_k^{+} = S_{lk}^{+} \tag{7.41}$$

7.3.2 Simulation Results

We applied the derived square-root sequential Kalman filter formulations to the standard LISA configuration. The condition number of the matrices have been reduced from about 10^{20}–10^{10}, thus making the algorithms numerically more stable and more accurate. The simulation results are shown in Fig. 7.9. Compared to previous results, we find that the square-root sequential Kalman filter provides slightly better estimates. This improvement is purely numerical, since mathematically the square-root sequential formulation is equivalent to the sequential Kalman filter formulation. The square-root sequential filter can also be directly applied to LISA with broken laser links. As expected, the simulation results are similar to that given by the sequential Kalman filter in the previous section. For brevity, we omit the results.

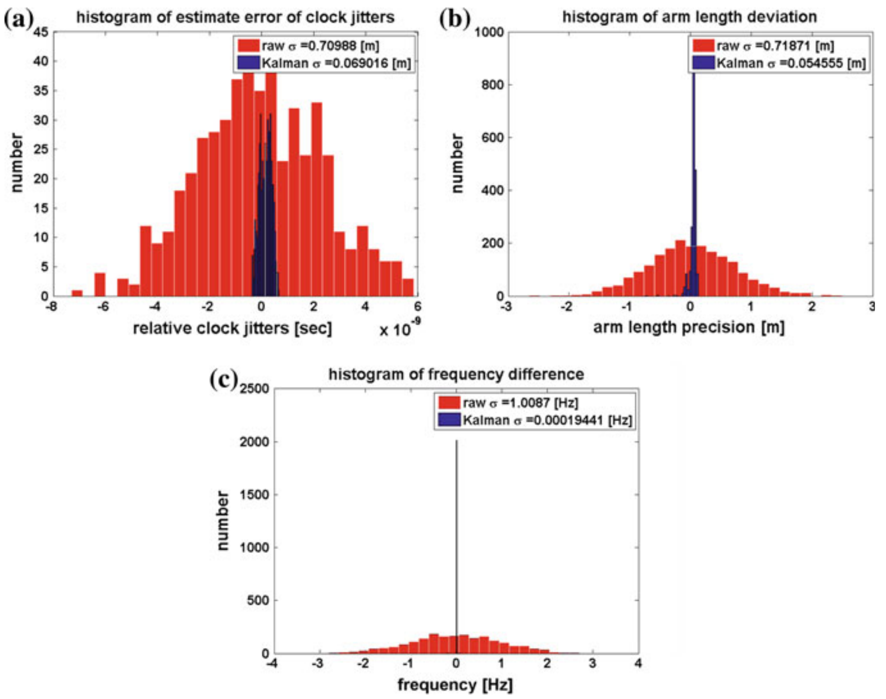

Fig. 7.9 Histograms of square-root sequential Kalman filter estimation errors in **a** relative clock jitters, **b** arm lengths, and **c** relative frequency jitters for the laser link from S/C 2 to S/C 1, with all laser links working properly

7.4 Summary

We have derived the formulations of the sequential Kalman filter and the square-root sequential Kalman filter. The designed filters were then applied to the standard LISA. Both filters are able to estimate the inter-spacecraft quantities accurately. The square-root sequential Kalman filter has greatly reduced the condition number of the matrices, hence achieving better numerically stability and better accuracy. LISA with several different possible combinations of broken laser links has been investigated with the sequential filter. Simulations have shown that a single broken laser link will not affect the estimates of the inter-spacecraft quantities. When there are more than two broken laser links, the estimates of the inter-spacecraft quantities are greatly jeopardized only if one the broken laser link is in the arm we want to estimate the inter-spacecraft quantities for. The designed sequential Kalman filter has successfully processed the measurement data for the eLISA-like configuration. It also showed greatly potential in the application to the GRACE-like configuration.

References

1. *Optimal State Estimation* (John Wiley and Sons, Inc., New Jersey, 2006)
2. A. Andrews, A square root formulation of the Kalman covariance equations. AIAA Journal **6**, 1165–1166 (1968)
3. P. Kaminski et al., Discrete square root filtering: a survey of current techniques. IEEE Trans. Autom. Control **16**(6), 727–736 (1971)

Chapter 8
Optimal Filtering for LISA with Effective System Models

Abstract Two effective dynamic models have been designed and studied in this chapter. These effective dynamic models employ smaller state vector and simplified dynamic functions, hence they are numerically more efficient and more robust. The degeneracy in the previous Kalman filter model can be eliminated by these effective models. The posterior measurements have been used via a RTS smoother and a modified iterative smoother to improve the estimates of the algorithms. Simulation shows that the posterior measurements can further reduce the estimation errors significantly.

8.1 Introduction

We have designed and implemented several Kalman filter models to process the raw data for LISA. Most of the designed models use physical parameters, such as the positions and the velocities of the S/C, in the state vector to characterize the motion of the LISA constellation. The advantage of using these physical parameters is that they automatically fit into the physical laws, hence we can directly use Newton's equations or relativistic equations as the dynamic equations to evolve the state vector of the Kalman filter. However, LISA inter-spacecraft measurements contain only relative quantities, such as the arm lengths, relative tangential velocities, relative clock jitters and relative frequency jitters. Therefore, the number of variables in the state vector is larger than the number of measurements, the physical variables in the state vector cannot be fully determined, and the measurement equations are very nonlinear. All of these add up complexities and numerical inaccuracies to the Kalman filter.

In this chapter, we explore two effective models with phenomenological parameters to deal with these issues. The effective models try to use variables that are directly measured, thus reducing the nonlinearities in the measurement equations and increasing the numerical accuracies of the Kalman filter algorithms. The number of variables in the state vector of these effective models is also significantly smaller. The matrices in these filter models are better conditioned. It turns out that the effective models are simpler and more efficient.

Y. Wang, *First-stage LISA Data Processing and Gravitational Wave Data Analysis*,
Springer Theses, DOI 10.1007/978-3-319-26389-2_8

Previously, the designed algorithms calculate best linear estimates of the inter-spacecraft quantities based only on prior measurements. Therefore, those algorithms could be run on board. In reality, the LISA pre-processing stage is expected to be carried out on the ground. The raw measurements can be analyzed off-line or at least with some latency. This allows to use the measurements posterior to the time of the estimates, which could potentially improve the estimates. In this chapter, we use a Kalman filter formulation similar to that of the so-called RTS smoother [1, 2] to calculate the best linear estimates based on measurements both prior to and posterior to the time of the estimates. Simulation results show that the use of the extra measurements can significantly improve the accuracy of the estimates.

8.2 A Periodic System Model

If each S/C of LISA would follow a Kepler orbit, the variations of the arm lengths of LISA were strictly periodic. Even for relativistic orbits under consideration of all the planets in the solar system, the variations of the arm lengths are also nearly periodic. Using the Kepler orbital setup in the paper [3], the annual evolutions of the LISA arm lengths are shown in Fig. 8.1a. The arm-length variations resemble sinusoidal functions within 6 months. In the subsequent half year, the arm length variation remains a roughly sinusoidal shape, but with a different amplitude. By optimizing the inclination angle between the ecliptic plane and the LISA constellation plane [4], the arm-length variations can be further reduced, and we obtain the arm-length variations shown in Fig. 8.1b. These arm-length variations are similar to a sinusoidal function with a period of one year. In either cases, we can phenomenologically model the arm-length evolutions as follows

$$L(t) = \bar{L} + A \sin(\omega t), \tag{8.1}$$

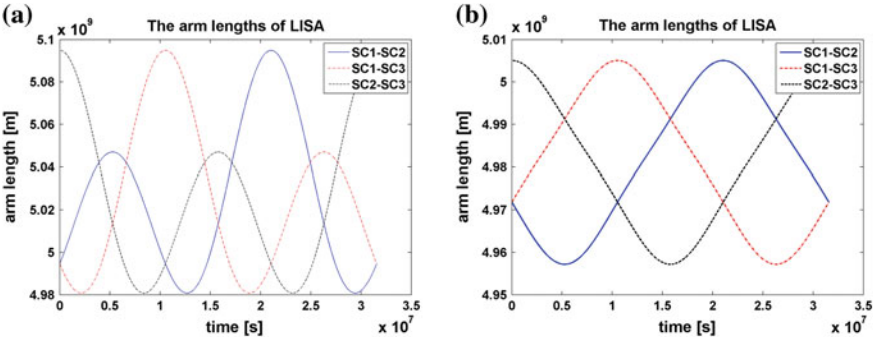

Fig. 8.1 The annual arm-length variations of the LISA constellation for Kepler orbits, **a** has fixed the inclination angle between the ecliptic plane and the constellation plane of LISA as 60°, **b** has varied and optimized this inclination angle to minimize the annual arm-length variations

where $\bar{L}$ is the average arm length, and ω is angular frequency with either a half-year period or a one-year period. If we define the arm length change as below

$$\Delta L(t) \equiv L(t) - \bar{L} = A\sin(\omega t), \tag{8.2}$$

the dynamic equation of the arm length change is the same as that of a simple harmonic oscillation

$$\frac{\mathrm{d}^2 \Delta L}{\mathrm{d}t^2} + \omega^2 \Delta L = 0. \tag{8.3}$$

A Kalman filter based on this simple periodic dynamic model can thus be designed. We define a 11-dimensional state vector as follows

$$x = (\Delta L_{21}, v_{21}, \Delta L_{32}, v_{32}, \Delta L_{13}, v_{13}, \delta T_1 - \delta T_2, \delta T_2 - \delta T_3, \delta f_1, \delta f_2, \delta f_3)^T. \tag{8.4}$$

The dynamic equations for the arm-length variations and the relative tangential velocities can be obtained from Eq. 8.3 by rewriting it as first order differential equations

$$\frac{\mathrm{d}}{\mathrm{d}t}\begin{bmatrix}\Delta L \\ v\end{bmatrix} = \begin{bmatrix}0 & 1 \\ -\omega^2 & 0\end{bmatrix}\begin{bmatrix}\Delta L \\ v\end{bmatrix} + \text{noise}. \tag{8.5}$$

The dynamic equations for the clock variables are given as follows

$$\frac{\mathrm{d}}{\mathrm{d}t}\begin{bmatrix}\delta T_1 - \delta T_2 \\ \delta T_2 - \delta T_3 \\ \delta f_1 \\ \delta f_2 \\ \delta f_3\end{bmatrix} = \begin{bmatrix}0 & 0 & 1/f_1^{\text{nom}} & -1/f_2^{\text{nom}} & 0 \\ 0 & 0 & 0 & 1/f_2^{\text{nom}} & -1/f_3^{\text{nom}} \\ 0 & 0 & 0 & 0 & 0 \\ 0 & 0 & 0 & 0 & 0 \\ 0 & 0 & 0 & 0 & 0\end{bmatrix}\begin{bmatrix}\delta T_1 - \delta T_2 \\ \delta T_2 - \delta T_3 \\ \delta f_1 \\ \delta f_2 \\ \delta f_3\end{bmatrix} + \text{noise}. \tag{8.6}$$

In order to make the system model fit better into the Kalman filter frame, we subtract the average arm length from the ranging measurements, thus obtaining the following observation vector

$$\begin{aligned} y' = (&R_{31} - \bar{L}, D_{31}, C_{31}, R_{21} - \bar{L}, D_{21}, C_{21}, R_{12} - \bar{L}, D_{12}, C_{12}, \ldots \\ &R_{32} - \bar{L}, D_{32}, C_{32}, R_{23} - \bar{L}, D_{23}, C_{23}, R_{13} - \bar{L}, D_{13}, C_{13})^T, \end{aligned} \tag{8.7}$$

where the inter-spacecraft measurements are

$$R_{ij} = L_{ij} + (\delta T_j - \delta T_i)c + n_{ij}^R, \tag{8.8}$$

$$D_{ij} = \left[f_j^{\text{carrier}} - f_i^{\text{carrier}} \left(1 - \frac{v_{ij}}{c}\right) + f_{ij}^{\text{GW}} \right] \left(1 - \frac{\delta f_j}{f_j^{\text{nom}}}\right) + n_{ij}^{D}, \tag{8.9}$$

$$C_{ij} = \delta f_j - \delta f_i + n_{ij}^{C}. \tag{8.10}$$

The Measurement matrix $H_k' = \left.\frac{\partial h_k'}{\partial x}\right|_{\hat{x}_k^-}$ is 18-by-11. We explicitly give its first three rows below

$$\left[\begin{matrix} 0\ldots0\ 1 & 0 & c\ c & 0 & 0\ \ 0 \\ 0\ldots0\ 0 & \frac{f_3^{\text{carrier}}}{c}\left(1 - \frac{\delta f_1}{f_1^{\text{nom}}}\right) & 0\ 0 & \frac{f_3^{\text{carrier}} - f_1^{\text{carrier}}}{f_1^{\text{nom}}} - \frac{f_3^{\text{carrier}} v_{31}}{f_1^{\text{nom}} c} & 0\ \ 0 \\ 0\ldots0\ 0 & 0 & 0\ 0 & 1 & 0\ {-1} \end{matrix}\right]_{\hat{x}_k^-},$$

where we have omitted the step index k in the components of the matrix. Notice that the dynamic matrix F_k for this model is a constant matrix, and most components of the measurement matrix H_k' are constant. The nonlinearity of the Kalman filter model has been significantly reduced. Also, the number of the variables in the state vector is 11, which is less than the number of measured quantities 18. Except for the absolute

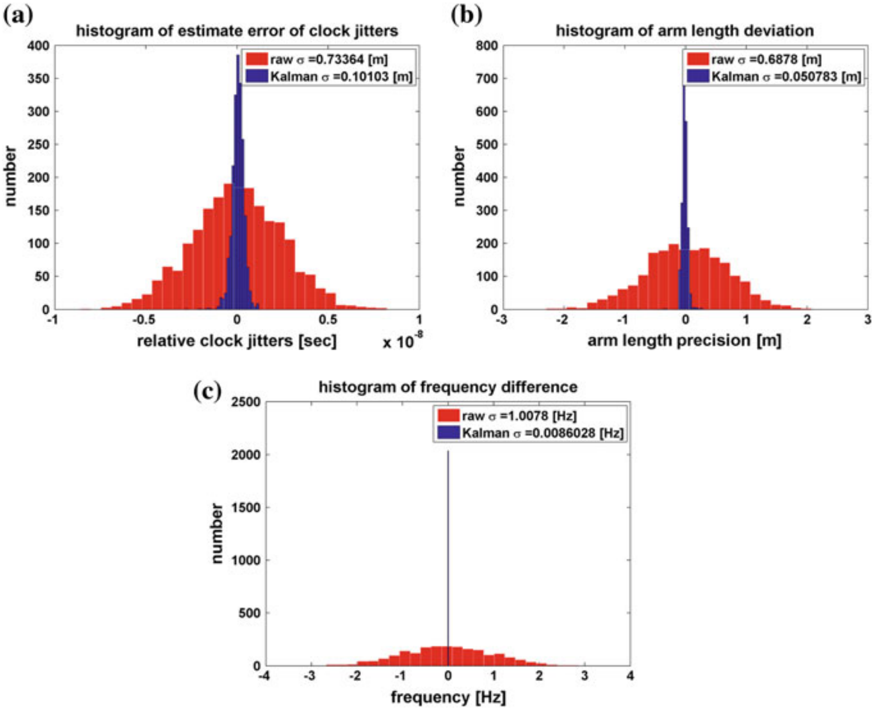

Fig. 8.2 Histograms of the estimation errors of a hybrid-extended Kalman filter with a periodic system model in **a** relative clock jitters, **b** arm lengths, and **c** relative frequency jitters for the laser link from S/C 2 to S/C 1

frequency jitters, all other variables in the state vector are directly constrained by the measurements, hence in principle they can be determined by the Kalman filter.

We design a hybrid-extended Kalman filter based on the model described above to process simulated LISA measurement data. The estimation errors in the relative clock jitters, arm lengths and the relative frequency jitters are plotted in Fig. 8.2. With this phenomenological periodic model, the designed Kalman filter has successfully estimated these three kinds of inter-spacecraft quantities. We also find that the designed Kalman filter model is not sensitive to the actual orbits of the LISA constellation. With either angular velocities $\omega = 2\pi$ rad/year or $\omega = 4\pi$ rad/year and with either LISA orbits shown in Fig. 8.1a, b, the performance of the designed Kalman filter turns out to be similar in terms of estimation errors.

8.3 An Effective System Model

In this section, we try to design an other effective system model, whose errors can be accessed analytically. This form of system model is expected to be directly applicable to relativistic LISA orbits. The arm lengths of LISA are smooth, slowly varying and (nearly) periodic functions of time, no matter whether they are calculated in the non-relativistic or relativistic framework. The smooth arm-length functions of time can be decomposed into harmonics

$$L(t) = \bar{L} + \sum_{n=1}^{\infty} A_n \sin(n\omega t + \phi_n), \tag{8.11}$$

where $\bar{L}$ is the average arm length, and A_1 is the lowest order arm-length variation, whose value is about $\bar{L}/100$ according to the orbit design of LISA.

The arm-length function can be expanded in polynomials around any time t_0

$$\begin{aligned} L(t) = \bar{L} &+ \sum_{n=1}^{\infty} A_n \sin(n\omega t_0 + \phi_n) + \sum_{n=1}^{\infty} A_n \cos(n\omega t_0 + \phi_n)(n\omega \Delta t) \\ &- \frac{1}{2}\sum_{n=1}^{\infty} A_n \sin(n\omega t_0 + \phi_n)(n\omega \Delta t)^2 + O[\Delta t^3], \end{aligned} \tag{8.12}$$

where $\Delta t \equiv t - t_0$. For elliptical Kepler orbits, A_n decays exponentially with n. For relativistic orbits, A_n also decays much faster than linearly, which leads to $(n+1)A_{n+1} \ll nA_n$. For a short time $\Delta t = 1000$ s, we estimate the contribution of each order as follows

$$A_1 \omega \Delta t \sim 10^4 \text{ m}, \tag{8.13}$$

$$\frac{1}{2} A_1 (\omega \Delta t)^2 \sim 1 \text{ m}, \tag{8.14}$$

$$\frac{1}{6}A_1(\omega\Delta t)^3 \sim 10^{-4}\,\mathrm{m}. \tag{8.15}$$

As a consequence, if we want to design a Kalman filter to process 1000 s LISA measurement data, the following polynomial model characterize the LISA arm lengths to 0.1 mm accuracy.

$$L(t) = \bar{L} + \sum_{n=1}^{\infty} A_n \sin(n\omega t_0 + \phi_n) + v\Delta t + \frac{1}{2}a\Delta t^2 + O[\Delta t^3], \tag{8.16}$$

where v and a are phenomenological variables.

According to the above phenomenological model, we define a 14-dimensional state vector in the Kalman filter as follow

$$x = (L_{21}, v_{21}, a_{21}, L_{32}, v_{32}, a_{32}, L_{13}, v_{13}, a_{13}, \delta T_1 - \delta T_2, \delta T_2 - \delta T_3, \delta f_1, \delta f_2, \delta f_3)^T. \tag{8.17}$$

The dynamic model for the arm-length phenomenological variables is simply as follows

$$\frac{\mathrm{d}}{\mathrm{d}t}\begin{bmatrix} L \\ v \\ a \end{bmatrix} = \begin{bmatrix} 0 & 1 & 0 \\ 0 & 0 & 1 \\ 0 & 0 & 0 \end{bmatrix}\begin{bmatrix} L \\ v \\ a \end{bmatrix} + \text{noise}. \tag{8.18}$$

The dynamics for the clock variables are the same as Eq. 8.6.

The measurement matrix $H_k = \frac{\partial h_k}{\partial x}\Big|_{\hat{x}_k^-}$ is 18-by-14 and a bit different from that in the last section, we therefore again explicitly write its first three rows as below

$$\begin{bmatrix} 0\ldots0 & 1 & 0 & 0 & c & c & 0 & 0 & 0 \\ 0\ldots0 & 0 & \frac{f_3^{\mathrm{carrier}}}{c}\left(1 - \frac{\delta f_1}{f_1^{\mathrm{nom}}}\right) & 0 & 0 & 0 & \frac{f_3^{\mathrm{carrier}} - f_1^{\mathrm{carrier}}}{f_1^{\mathrm{nom}}} - \frac{f_3^{\mathrm{carrier}} v_{31}}{f_1^{\mathrm{nom}} c} & 0 & 0 \\ 0\ldots0 & 0 & 0 & 0 & 0 & 0 & 1 & 0 & -1 \end{bmatrix}_{\hat{x}_k^-},$$

where we have omitted the step index k in the matrix components.

We design a hybrid-extended Kalman filter with the phenomenological polynomial system model described above to process the simulated LISA measurement data. The results of the simulation are summarized in Fig. 8.3. Comparing these estimation errors with that given in the last section, we find that the overall performance of this phenomenological polynomial model is slightly better. Since this model is directly applicable to relativistic cases, we expect it to outperform the periodic model in general.

Usually, the trace of the posteriori matrix tells how large the overall estimation error is. The trace of the posteriori matrix at each Kalman filter step is shown in Fig. 8.4a, where we see that the overall estimation error is not improving much

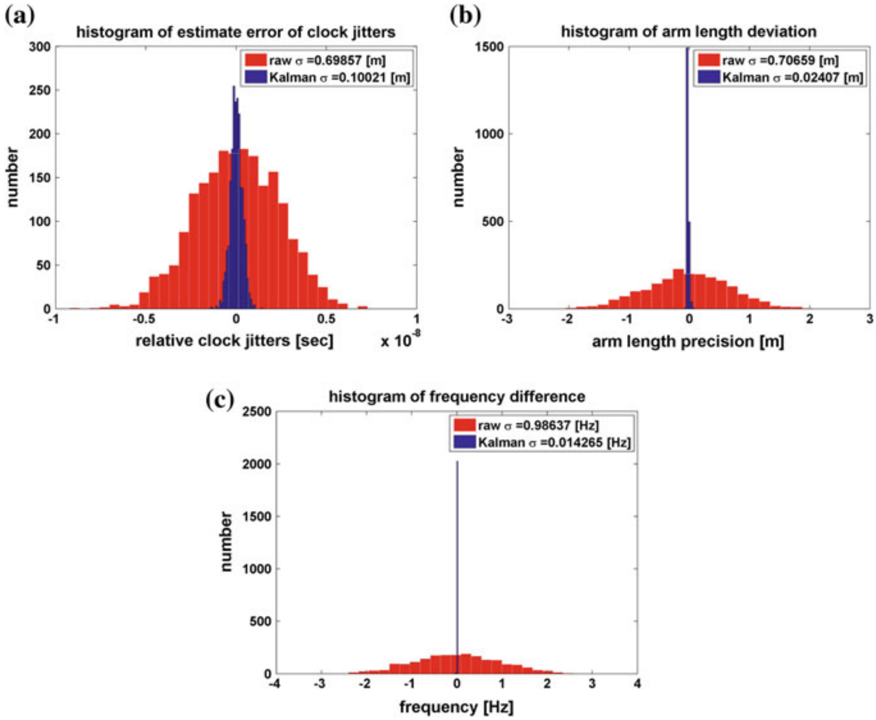

Fig. 8.3 Histograms of the estimation errors of a hybrid-extended Kalman filter with a phenomenological polynomial system model in **a** relative clock jitters, **b** arm lengths, and **c** relative frequency jitters for the laser link from S/C 2 to S/C 1

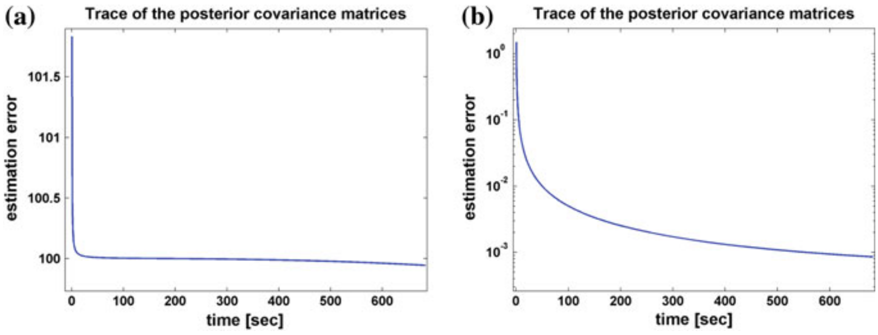

Fig. 8.4 **a** The trace of the posteriori matrices. **b** The trace of the posterior matrices excluding frequency jitters

with time. After the first few steps, the overall estimation error roughly stays at the same level. This is because the absolute frequency jitters δf_i cannot be determined well. As explained in previous chapters, the measurements contain very limited information about the absolute frequency jitters. Figure 8.4b shows the trace of the posteriori matrices excluding the frequency jitters. If we use the relative frequency jitters $\delta f_1 - \delta f_2$ and $\delta f_2 - \delta f_3$ in the state vector instead of the absolute frequency jitters δf, the trace of the full posteriori matrix behaves similar to Fig. 8.4b. We see that the overall estimation error is significantly decaying with time. During the 700 s shown in the figure, the estimation error is reduced by more than three orders of magnitude. Since the Kalman filter calculate the best linear estimates of the state vector based on the measurements prior to the time of the estimates, the estimates at a later time actually use more measurements. Therefore, the estimates at a later time are much more accurate.

The pre-processing stage of LISA data is expected to be done on the earth. Thus, we can estimate the state vector also using the measurements posterior to it. This can potentially further reduce the estimation errors. In the next section, we will describe the algorithms and apply them to LISA measurements.

8.4 Improving the Estimates by Using Posterior Measurements

There are several existing algorithms that generate the best estimates based on a fixed amount of data [2]. These algorithms are usually referred to as optimal smoothers. The so-call RTS smoother [1, 2] is an efficient algorithm among them. In the following, we directly describe a similar iterative algorithm without going through the lengthy derivation.

1. Initialize the state vector and the covariance matrix

$$\hat{x}^+_{1,0},\ P^+_{1,0}, \tag{8.19}$$

   where in $\hat{x}_{a,k}$ and $P_{a,k}$ the index a stands for the ath iteration, and k is the normal step index.
2. Calculate the a priori estimate $\hat{x}^-_{a,k}$ from the a posteriori estimate $\hat{x}^+_{a,k-1}$ at the previous step, using the dynamic equation

$$\dot{x} = f(x, t). \tag{8.20}$$

   Use either of the following two formulae to update the covariance matrix

$$P^-_{a,k} = e^{F_{a,k-1}\Delta t} P^+_{a,k-1} e^{F^T_{a,k-1}\Delta t} + W_{a,k-1}, \tag{8.21}$$

$$P^-_{a,k} = (I + F_{a,k-1}\Delta t) P^+_{a,k-1} (I + F_{a,k-1}\Delta t)^T + W_{a,k-1}, \tag{8.22}$$

   where $F_{a,k-1} \equiv \left.\frac{\partial f}{\partial x}\right|_{x^+_{a,k-1}}$.

3. Calculate the Kalman gain

$$K_{a,k} = P_{a,k}^{-} H_{a,k}^{T} (H_{a,k} P_{a,k}^{-} H_{a,k}^{T} + M_{a,k} V_k M_{a,k}^{T})^{-1}, \tag{8.23}$$

where $H_{a,k} \equiv \left.\frac{\partial h_k}{\partial x}\right|_{\hat{x}_{a,k}^{-}}$, $M_{a,k} \equiv \left.\frac{\partial h_k}{\partial v}\right|_{\hat{x}_{a,k}^{-}}$.

4. Correct the a priori estimate

$$\hat{x}_{a,k}^{+} = \hat{x}_{a,k}^{-} + K_{a,k}[y_k - h_k(\hat{x}_{a,k}^{-}, 0)], \tag{8.24}$$

$$\begin{aligned} P_{a,k}^{+} &= (I - K_{a,k} H_{a,k}) P_{a,k}^{-}, \\ &= (I - K_{a,k} H_{a,k}) P_{a,k}^{-} (I - K_{a,k} H_{a,k})^{T} + K_{a,k} V_k K_{a,k}^{T}. \end{aligned} \tag{8.25}$$

5. Let $a \to a + 1$, initialize the new iteration backwards as the following

$$\hat{x}_{a,N} = \hat{x}_{a-1,N}^{+} \tag{8.26}$$

$$P_{a,N} = P_{a-1,N}^{+} \tag{8.27}$$

6. Filter the posteriori estimates obtained in the last iteration backwards for $k = N - 1, N - 2, \ldots, 0$

$$K_{a,k} = P_{a-1,k}^{+} F_{a-1,k}^{T} (P_{a-1,k+1}^{-})^{-1} \tag{8.28}$$

$$P_{a,k} = P_{a-1,k}^{+} - K_{a-1,k} (P_{a-1,k+1}^{-} - P_{a,k+1}) K_{a-1,k}^{T} \tag{8.29}$$

$$\hat{x}_{a,k} = \hat{x}_{a-1,k}^{+} + K_{a-1,k} (\hat{x}_{a,k+1} - \hat{x}_{a-1,k+1}^{-}) \tag{8.30}$$

7. Let $a \to a + 1$, initialize the new iteration as follows

$$\hat{x}_{a,0}^{+} = \hat{x}_{a-1,0}, \tag{8.31}$$

$$P_{a,0}^{+} = P_{a-1,0}, \tag{8.32}$$

and repeat the calculations from step 2.

We want to elaborate a few points about the above algorithm: (i) The first iteration of the algorithm is the same as a hybrid-extended Kalman filter algorithm, where each posteriori estimate is obtained based on the measurements prior to it. (ii) The first two iterations together are similar to a nonlinear version of the RTS smoother, where the posteriori estimates are obtained based on measurements both prior to and posterior to them. (iii) When the dynamic equations or the measurement equations are nonlinear, additional iterations from the third on help increase the estimation accuracy. This is because we need to expand the nonlinear dynamic equations or the nonlinear measurement equations around some estimate of the state vector. New iterations calculate the expansions around better estimates, hence the nonlinear functions are better approximated. (iv) From the third iteration on, the measurements are used more than once. Effectively, we are using more measurements than we have.

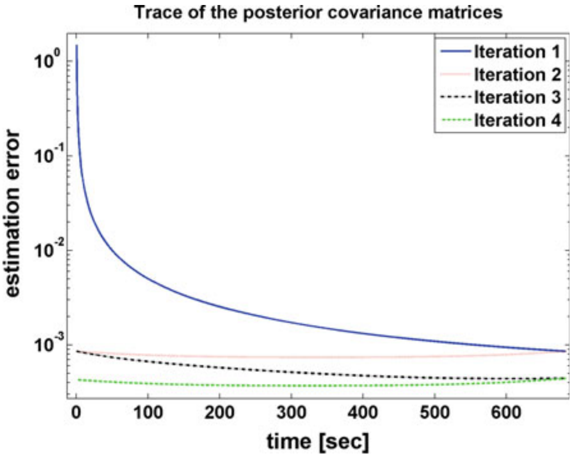

Fig. 8.5 The trace of the posteriori matrices as a function of time in each iteration

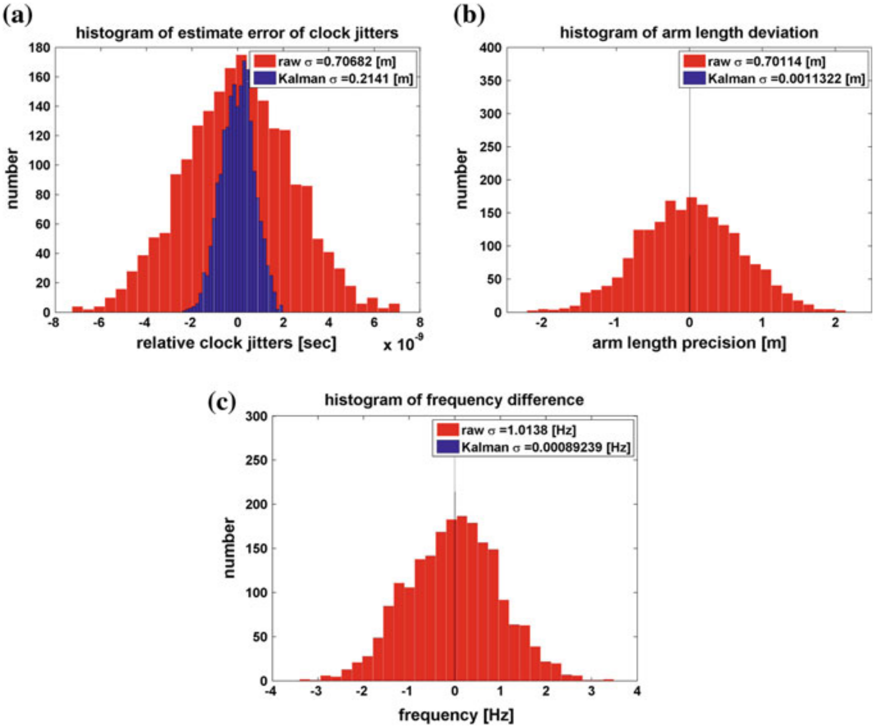

Fig. 8.6 Histograms of the posteriori estimation errors after two iterations in **a** relative clock jitters, **b** arm lengths, and **c** relative frequency jitters for the laser link from S/C 2 to S/C 1

As a result, the posteriori covariance matrices (the uncertainty of the estimates) are underestimated from the third iteration on. (v) The uncertainty of the dynamic equation is characterized by $W_{a,k}$, which is tunable. We can start with slightly larger $W_{1,k}$ in the first iteration to increase the robustness of the algorithm, and use smaller $W_{a,k}$ in the subsequent iterations, when we can expand the dynamic equations around better estimates. (vi) It is not recommended to go beyond the fourth iteration, unless the measurements or the dynamic equations are strongly nonlinear.

We implement the designed algorithm to process simulated LISA measurement data up to the fourth iteration. The trace of the posteriori matrices in each iteration is plotted in Fig. 8.5. Similar as before, we have excluded the absolute frequency jitters from the trace. The second iteration has significantly improved the overall estimation accuracy and brought the estimates at all time to a similar precision. The third and the fourth iterations have further reduced the trace of the posteriori matrices. As we explained above, the uncertainties of the estimates after the third iteration are underestimated, therefore the improvements in the third and the fourth iterations are not that large. This is mainly because the dynamic equations are linear and the measurement equations in the polynomial phenomenological variables are almost linear. So the linear expansion of the dynamic

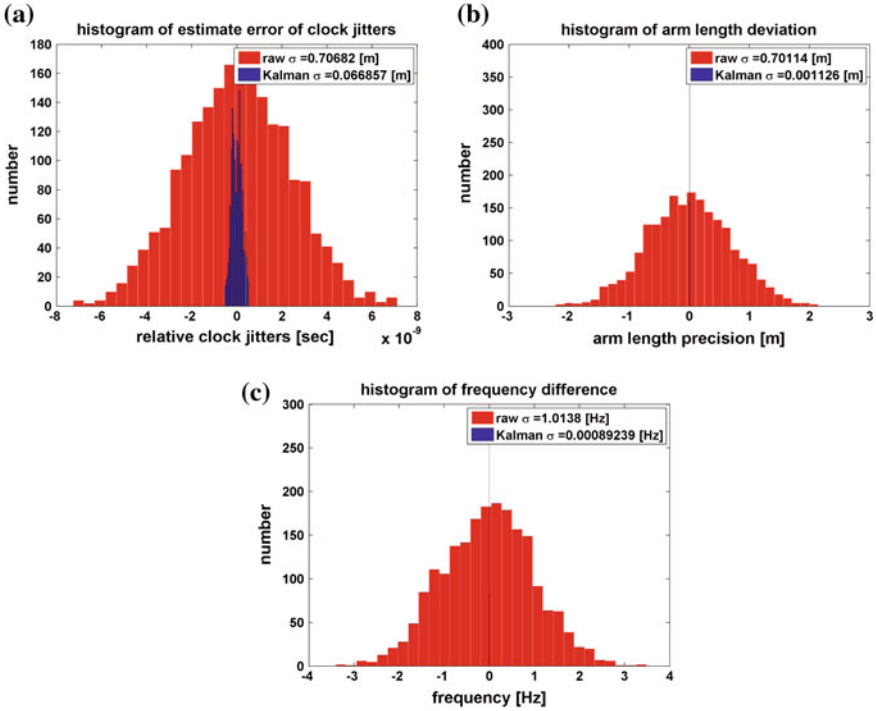

Fig. 8.7 Histograms of the posteriori estimation errors after four iterations in **a** relative clock jitters, **b** arm lengths, and **c** relative frequency jitters for the laser link from S/C 2 to S/C 1

equations is the same around any state estimates, and that of the measurement equations only weakly depends on the location of the expansion. Figures 8.6 and 8.7 respectively show histograms of posteriori estimation errors after two iterations and after four iterations. Comparing the two figures, we see that the estimates of the relative clock jitters have been significantly improved by the third and the fourth iterations, while the estimates of the arm lengths and the relative frequency jitters almost remain the same. Comparing Fig. 8.7 with previous results, we find that the iterative algorithm designed in this section significantly outperforms other algorithms. The uncertainty in the relative clock jitters can be reduced by this algorithm by an order of magnitude. The arm length uncertainty is reduced to millimeter level. However, due to the approximate dynamics, the estimate in the arm lengths sometimes has a bias about 1–2 cm. Still, the arm-length estimates are much more accurate than before and sufficiently accurate for TDI algorithms. The relative frequency jitters are estimated to the sub-mHz level, which are also more accurate than the results in the previous sections. All in all, the designed iterative algorithm has successfully enhanced the robustness and improved the estimation accuracy of the inter-spacecraft quantities.

References

1. H.E. Rauch, F. Tung, C.T. Striebel, Maximum likelihood estimates of linear dynamic systems. AIAA J. **3**(8), 1445–1450 (1965)
2. D. Simon, *Optimal State Estimation* (Wiley, Hoboken, 2006)
3. S.V. Dhurandhar, K.R. Nayak, S. Koshti, J.-Y. Vinet, Fundamentals of the LISA stable flight formation. Class. Quantum Gravity **22**, 481 (2005)
4. K.R. Nayak, S. Koshti, S.V. Dhurandhar, J.-Y. Vinet, On the minimum flexing of LISA's arms. Class. Quantum Gravity **23**, 1763–1778 (2006)

Chapter 9
Clock Noise and Disordered Measurements

Abstract In this chapter, we have studied different types of clock noise including the realistic clock noise measured in the lab (which is several orders of magnitude more noisy than the current best space-qualified clocks). Simulation indicates that the clock noise can significantly affect the performance of the filter algorithms. More sophisticated dynamic models have been designed for the clock noise, which are then incorporated in the filter algorithms. The filter algorithm with the sophisticated model turns out to work well in the presence of stronger and more complicated clock noise. In addition, the effects of the clock noise on the sampling time stamps have been simulated and investigated. It turns out that the errors in the time stamps can introduce biases in the estimates of the arm lengths and the clock errors. We have invented a hybrid interpolated filter to solve this problem. Simulation shows that in the presence of complicated strong clock noise, in both the measurements and the sampling time stamps, the filter algorithms designed in this thesis can still accurately determine the inter-spacecraft distances and synchronize the clocks. This work has two main implications: (i) it bridges the gap between the phasemeter raw data and the well-studied time-delay interferometry algorithms and the astrophysical data analysis algorithms, hence contributing to the readiness and maturity of the (e)LISA-like missions, (ii) it demonstrates the possibility of using less expensive clocks, hence it can potentially reduce the cost of the (e)LISA-like missions.

9.1 Introduction

So far, we have designed several Kalman filter algorithms, including the hybrid-extended Kalman filter, the sequential Kalman filter and the square-root sequential Kalman filter, to process LISA measurement data. In addition, we designed an iterative algorithm that is similar to the RTS smoother. For the standard LISA configuration, we have investigated several Kalman filter models, including the models with 24-dimensional, 23-dimensional and 22-dimensional state vectors, and a simplified model which separates and only deal with the clock jitters and the frequency jitters. We have also considered several possible combinations of broken laser links in the

Y. Wang, *First-stage LISA Data Processing and Gravitational Wave Data Analysis*,
Springer Theses, DOI 10.1007/978-3-319-26389-2_9

LISA constellation, along with the eLISA-like configuration and the GRACE-like configuration.

In the case of physical system model, all the hundreds of components in the large matrices H_k and F_k have been calculated analytically. Many control parameters are investigated and carefully tuned. These allow the designed algorithms to accurately estimate the arm lengths, the relative clock jitters and the relative frequency jitters. We have designed two phenomenological system models, where the measurement matrix H_k and the dynamic matrix F_k are greatly simplified. The iterative algorithm has significantly improved the estimates of the inter-spacecraft quantities. For the arm lengths, we have been able to estimate the quantities of about 5×10^9 m to an accuracy of centimeters or even millimeters, which is 11 or 12 orders of magnitude in difference.

We have assumed and used clock jitters and frequency jitters that follow power-law PSDs, which exactly obeys the clock dynamic model we have used in the Kalman filter model. In reality, the clocks usually have more complicated PSDs, that follow different clock dynamic models. In this chapter, we will investigate how different types of clock noise, including the clock noise directly measured in the lab, would affect the Kalman filter estimates, and how the discrepancy between the clock dynamic model used in the Kalman filter algorithms and the real clock dynamic model would affect the performance of the designed algorithms.

As mentioned in previous chapters, although we have included the clock noise in the measurements, we have made the approximation that the recording time of the measurements is perfect, meaning that all the measurements taken in the same Kalman filter step are assumed to be measured at the same time, and the sampling rate is uniform. In other words, we have neglected part of the clock noise. In face, this is usually required by the Kalman filter formulations. In this chapter, we will take into account this effect, simulate it and analyze it. We will simulate the measurements that are recorded according to their own imperfect clocks. The measurements are taken non-uniformly with unknown record time. The Kalman filter formulations do not fit it in this case. We will investigate how and whether the previously designed algorithms work and design new algorithms to analyze the data.

9.2 Clock Noise with Power a Law Decay LSD

9.2.1 *Frequency Noise with a* $1/\nu$ *Slope*

We have been using frequency jitters with a linear spectral density (LSD) that follows a $1/\nu$ slope. Here, we denote ν as the Fourier frequency to make a distinction from the clock jitters δf. This $1/\nu$-slope LSD is a good and simple approximation, since we find the LSDs of many measured frequency jitters of USOs have a slope close to $1/\nu$. This kind of frequency jitters can be described by the following simple model

$$\dot{\delta f}(t) = n(t), \tag{9.1}$$

where $n(t)$ is a white-Gaussian noise process. Thus, the LSD of the frequency jitters is

$$\sqrt{S_{\delta f}(\nu)} = \frac{\sqrt{S_n(\nu)}}{2\pi\nu}, \tag{9.2}$$

where the PSD of the white-Gaussian noise $S_n(\nu)$ is a constant at all Fourier frequency ν. From the relation $\dot{\delta T} = \delta f/f^{\mathrm{nom}}$, we know that the LSD of the clock jitters has a slope of $1/\nu^2$

$$\sqrt{S_{\delta T}(\nu)} = \frac{\sqrt{S_n(\nu)}}{(2\pi\nu)^2 f^{\mathrm{nom}}}, \tag{9.3}$$

where f^{nom} is the nominal frequency of the USO.

The clock model we have been using in the Kalman filter is the following

$$\frac{\mathrm{d}}{\mathrm{d}t}\begin{bmatrix}\delta T\\ \delta f\end{bmatrix} = \begin{bmatrix}\delta f/f^{\mathrm{nom}}\\ 0\end{bmatrix} + \begin{bmatrix}n_1\\ n_2\end{bmatrix}, \tag{9.4}$$

where n_1, n_2 are uncorrelated white-Gaussian noise processes. By converting the above two first-order differential equations into a single second-order differential equation

$$\ddot{\delta T} = \dot{n}_1 + n_2/f^{\mathrm{nom}}, \tag{9.5}$$

the LSD of the clock jitters for this Kalman filter model is

$$\sqrt{S_{\delta T}(\nu)} = \left[\frac{S_{n_1}(\nu)}{(2\pi\nu)^2} + \frac{S_{n_2}(\nu)}{(f^{\mathrm{nom}})^2(2\pi\nu)^4}\right]^{1/2}. \tag{9.6}$$

When $S_{n_1}(\nu)$ is much smaller than $S_{n_2}(\nu)$, the above LSD approximates a $1/\nu^2$ slope. However, S_{n_1} cannot be arbitrarily small in numerical simulation, since n_1 is at least at the numerical precision level of the first-order different equation it appeared in. As shown in previous chapters, this system model works well for frequency jitters with a $1/\nu$ slope.

9.2.2 Clock Noise LSD with a Higher-Order Decay

We can generalize the system model described in the previous subsection to higher-order differential equations, which can be converted to a set of first-order equations

$$\frac{\mathrm{d}}{\mathrm{d}t}\begin{bmatrix} x \\ x_1 \\ \vdots \\ \vdots \\ x_N \end{bmatrix} = \begin{bmatrix} x_1 \\ \vdots \\ \vdots \\ x_N \\ 0 \end{bmatrix} + \begin{bmatrix} n_1 \\ \vdots \\ \vdots \\ n_N \\ n_{N+1} \end{bmatrix}, \tag{9.7}$$

where n_k are uncorrelated white Gaussian noise, $(k = 1, \ldots, N+1)$. By eliminating x_k, we obtain

$$x^{(N+1)} = \sum_{k=1}^{N+1} n_k^{(N+1-k)}, \tag{9.8}$$

where $x^{(N)}$ denotes the nth derivative of x, and $x^{(0)} = x$. It is straightforward to calculate the LSD of x from the above formulae

$$\sqrt{S_x(\nu)} = \left[\sum_{k=1}^{N+1} \frac{S_{n_k}(\nu)}{(2\pi\nu)^{2k}}\right]^{1/2} . \tag{9.9}$$

When the noise processes n_k, $(k = 1, \ldots, N)$ are negligible compared to n_{N+1}, x approximately has a LSD as

$$\sqrt{S_x(\nu)} \approx \frac{\sqrt{S_{n_{N+1}}(\nu)}}{(2\pi\nu)^k}. \tag{9.10}$$

9.3 Measure and Characterize Laboratory Clock Noise

9.3.1 Measured Clock Noise

The clock noise is a key ingredient for the inter-spacecraft measurements and the LISA project, thus it is important to measure and analyze realistic clock noise. We try to characterize the clock noise by measuring the beat-note of two USOs. The schematic plot is shown in Fig. 9.1, where two analog signals respectively from two USOs are mixed, and then low-pass filtered. The beat-note signal is digitized by an analog-to-digital converter (ADC) and recorded.

Instead of using high-quality space-qualified USOs, we first measure the clock noise of low-quality cheap oscillators. Some realistic features of the clock noise would appear from the measurements. By using these realistic clock noise measurements in the LISA data pre-processing simulation, we will be able to see how the realistic clock noise would affect the ranging accuracy and the time labels of LISA raw measurements. Consequently, we can tell whether the realistic clock noise would

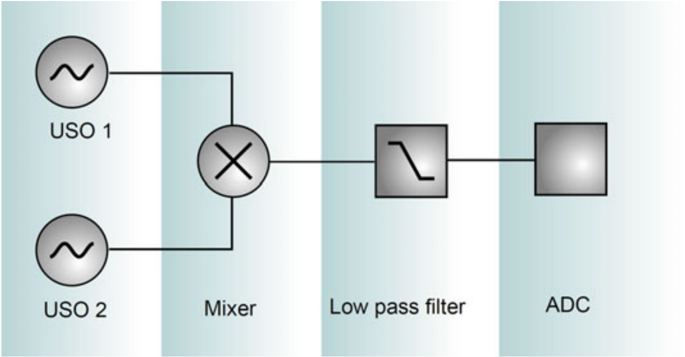

Fig. 9.1 A schematic diagram of measuring the clock noise

affect the extraction of the astrophysical information from LISA data. The requirements on the performance of LISA USOs can then be set. If we can still achieve sufficient ranging accuracy and precisely calibrate LISA raw measurements with these clock noise measurements, it would permit using less precise clocks instead of high-quality USOs in the LISA projects. This will both greatly reduce the budget and increase the robustness of the LISA project.

We designed breadboard circuits to measure the beat-note of two oscillators, as shown in Fig. 9.2a. The sampling rate of the ADC is 20 kHz. The nominal frequency of the two oscillators is $f^{\mathrm{nom}} = 20\,\mathrm{MHz}$. The signals from the two oscillators are

$$s_i \propto \cos[2\pi(f^{\mathrm{nom}} + \delta f_i)t + \Phi_i], \tag{9.11}$$

where $i = 1, 2$ is the oscillator label, δf_i denotes the frequency jitters of the oscillators, and Φ_i are the initial phases. After the mixer and the low-pass filter, the measured signal can be formulated as

$$s \propto \cos[2\pi(\delta f_1 - \delta f_2)t + (\Phi_1 - \Phi_2)]. \tag{9.12}$$

When the frequency jitters δf_1 and δf_2 are independent, the measured frequency jitters $\delta f_1 - \delta f_2$ is statistically $\sqrt{2}$-times as large as the frequency jitters of a single oscillator. The time-frequency plot of the measured frequency jitters is shown in Fig. 9.2b, where the strongest signal at about 450 Hz is the beat-note of the two oscillators. Other weak harmonics in the plot are due to the imperfection of the sinusoidal signal. In order to extract the frequency jitters and calculate the its linear spectral density (LSD), we first get rid of the DC component of the measured raw data by a high-pass filter. The time of the ascendant crosses of the filtered data with the x-axis t_k is then interpolated and calculated. The instantaneous period of the measured signal is the difference between two successive cross time $t_{k+1} - t_k$. The instantaneous frequency jitters are the inverses of the instantaneous periods, which is plotted in Fig. 9.2c. Notice that the recording time of these instantaneous frequency

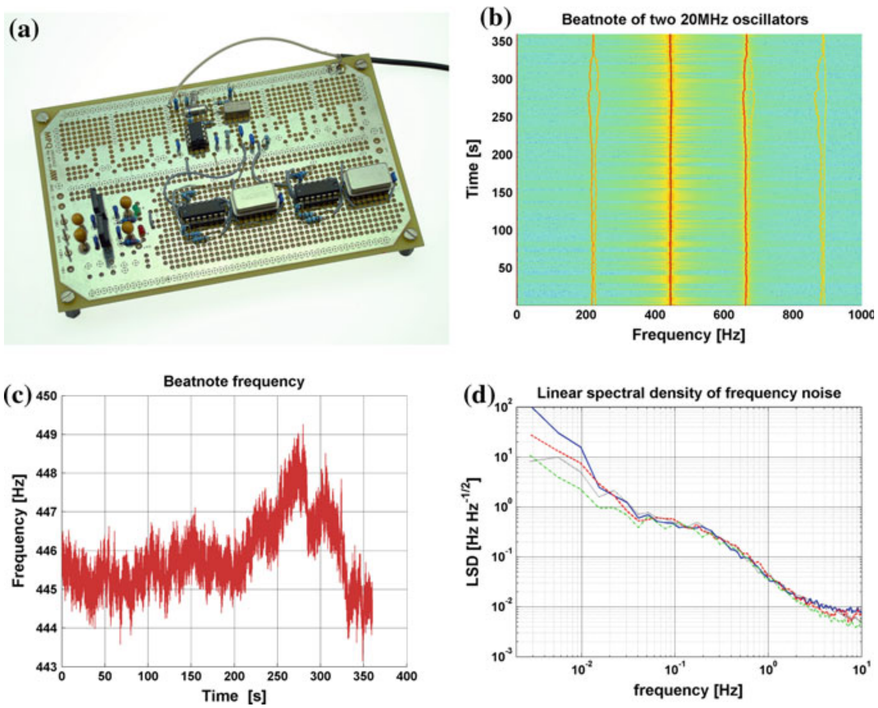

Fig. 9.2 Clock noise measurements. **a** The designed breadboard circuits that measure the clock noise. **b** The time-frequency plane of the measured beat-notes between the two oscillators. **c** The frequency difference between the two oscillators as a function of time. **d** The LSDs of the beat-note frequency noise measured at four different time periods

jitters is uneven. Also, the uneven sampling frequencies of these frequency jitters are quite high. Therefore, we low-pass filter these frequency jitters, average the jitters over short time, and down-sample the averaged frequency jitters. The LSD of the frequency jitters is calculated based on these down-sampled data. In Fig. 9.2d, the LSDs of the frequency jitters during four different time periods are shown. From the figure, we see that the frequency jitters of the oscillators we used are actually several orders of magnitude more noisy than the best space-qualified USOs.

9.3.2 Characterizing and Modelling the Clock Noise

Usually, a stationary noise process can be modelled by a high order differential equation

$$x^{(N+1)} + \sum_{j=0}^{N} a_j x^{(N-j)} = \sum_{k=0}^{M} b_k u^{(M-k)}, \qquad (9.13)$$

where N and M are two positive integers, a_j, b_k are real coefficients, $x(t)$ is the noise process, and $u(t)$ is a white-Gaussian noise process. This model is also called the autoregressive-moving-average (ARMA) model in the time series analysis. In the Fourier domain, the relation between $\tilde{x}(\nu)$ and $\tilde{u}(\nu)$ is

$$\begin{aligned}\tilde{x}(\nu) &= \frac{\sum_{k=0}^{M} b_k (i2\pi\nu)^{M-k}}{(i2\pi\nu)^{N+1} + \sum_{j=0}^{N} a_j (i2\pi\nu)^{N-j}} \tilde{u}(\nu), \\ &= \frac{b_0 \prod_{k=1}^{M} (i2\pi\nu - z_k)}{\prod_{j=1}^{N+1} (i2\pi\nu - p_j)} \tilde{u}(\nu), \end{aligned} \tag{9.14}$$

where z_k are zeros, and p_j are poles of the transfer function. Since the coefficients a_j and b_k are real, the zeros z_k and the poles p_j are either real or forming a complex pair (e.g. when z_k is complex, there exists one other zero $z_{k'}$ that satisfies $z_{k'} = z_k^*$), respectively. Therefore, the LSD of the noise process $x(t)$ is

$$\begin{aligned}\sqrt{S_x(\nu)} &= \left| \frac{\sum_{k=0}^{M} b_k (i2\pi\nu)^{M-k}}{(i2\pi\nu)^{N+1} + \sum_{j=0}^{N} a_j (i2\pi\nu)^{N-j}} \right| \sqrt{S_u(\nu)}, \\ &= \left| \frac{b_0 \prod_{k=1}^{M} (i2\pi\nu - z_k)}{\prod_{j=1}^{N+1} (i2\pi\nu - p_j)} \right| \sqrt{S_u(\nu)}, \end{aligned} \tag{9.15}$$

where $|\ldots|$ denotes the absolute value. Notice that, by definition, the PSD $S_u(\nu)$ of a white-Gaussian noise process is constant at all frequencies.

Given a measured LSD of the phase noise or the frequency jitters, we want to fit it to the model described by Eq. 9.13, while minimizing the fitting error. In other words, we need to calculate the coefficients a_j, b_k or the zeros z_k, poles p_j and b_0. For a given $\sqrt{S_x(\nu)}$, there is degeneracy between b_0 and $\sqrt{S_u(\nu)}$. Thus, we require $\sqrt{S_u(\nu)} = 1$ to avoid the ambiguity. By requiring the total power of the noise process $x(t)$ to be finite, we have $M \leq N$. Therefore, the measured LSD can be reexpressed as

$$\begin{aligned}\sqrt{S_x(\nu)} &= \left| \frac{b_0 \prod_{k=1}^{M} (i2\pi\nu - z_k)}{\prod_{j=1}^{N+1} (i2\pi\nu - p_j)} \right|, \\ &= \left| \sum_{j=1}^{N+1} \frac{r_j}{i2\pi\nu - p_j} \right|, \end{aligned} \tag{9.16}$$

where r_j are the residues. When the phase of the LSD is known, we denote the complex LSD with phase evolutions as $L_x(\nu)$, which is

$$L_x(\nu) = \frac{b_0 \prod_{k=1}^{M} (i2\pi\nu - z_k)}{\prod_{j=1}^{N+1} (i2\pi\nu - p_j)} = \sum_{j=1}^{N+1} \frac{r_j}{i2\pi\nu - p_j}. \tag{9.17}$$

For a measured $L_x(\nu)$, the residues r_j and the poles p_j can be calculated, using the iterative vector fitting method invented in the paper [1]. Here, we only explain the main idea of the algorithm. By inserting the initial guess of the poles $\bar{p}_m$ into the above equation, we can rewrite it as

$$\frac{\prod_{j=1}^{N+1}(i2\pi\nu - p_j)}{\prod_{m=1}^{N+1}(i2\pi\nu - \bar{p}_m)} L_x(\nu) = \frac{b_0 \prod_{k=1}^{M}(i2\pi\nu - z_k)}{\prod_{m=1}^{N+1}(i2\pi\nu - \bar{p}_m)}. \tag{9.18}$$

The above equation can be expressed in the residues and poles form

$$\left(\sum_{j=1}^{N+1} \frac{\bar{r}_j}{i2\pi\nu - \bar{p}_j} + 1\right) L_x(\nu) = \sum_{j=1}^{N+1} \frac{r_j}{i2\pi\nu - \bar{p}_j}. \tag{9.19}$$

This equation is linear in its unknown residues $\bar{r}_j$ and r_j, hence the residues can easily be calculated by minimizing the square error or the weighted square error. Once the residues are known, the zeros $\bar{z}_j$ of the left hand side of the above equation can also be calculated. Notice that the zeros of the left hand side of the above equation are poles of $L_x(\nu)$. The zeros of $\sum_{j=1}^{N+1} \frac{\bar{r}_j}{i2\pi\nu - \bar{p}_j} + 1$ are just the eigenvalues of the following matrix

$$H = \begin{bmatrix} \bar{p}_1 - \bar{r}_1 & -\bar{r}_2 & \dots & -\bar{r}_{N+1} \\ -\bar{r}_1 & \bar{p}_2 - \bar{r}_2 & \dots & -\bar{r}_{N+1} \\ \vdots & \vdots & \ddots & \vdots \\ -\bar{r}_1 & -\bar{r}_2 & \dots & \bar{p}_{N+1} - \bar{r}_{N+1} \end{bmatrix}. \tag{9.20}$$

A brief proof is shown in the Sect. 9.5. Then, we set the new poles $\bar{p}_j$ as the calculated $\bar{z}_j$ and repeat the whole calculation until the square error is sufficiently small. The estimates of the residues r_j and the poles p_j are obtained after the convergence.

Usually, the phase of the LSD is not known or even defined. The above method does not work in this case. One can use the software LISO [2] designed by Gerhard Heinzel to fit the LSD without phase. Instead of an iterative deterministic algorithm, LISO uses a combination of stochastic optimization algorithms to fit the LSD without phase by minimizing the square error in the amplitude of the LSD. It starts with an initial run of the Particle Swarm Optimization (PSO) [3, 4] algorithm, followed by an iterated combination of Nelder–Mead Simplex [5] and Levenberg–Marquardt algorithms [6] to polish the solution obtained from the PSO algorithm.

Alternatively, one could use the algorithm described in the papers [7, 8] to fit the LSD without phase to zero-pole models. I separately derived a similar algorithm to accomplish the same task, which fits the LSD without phase iteratively. Instead of fitting the LSD $|L_x(\nu)|$ without phase, we first fit the PSD $S_x(\nu) = L_x(\nu)\, L_x^*(\nu)$, which is

$$S_x(\nu) = \frac{|b_0|^2 \prod_{k=1}^{M}(i2\pi\nu - z_k)(i2\pi\nu - z_k)^*}{\prod_{j=1}^{N+1}(i2\pi\nu - p_j)(i2\pi\nu - p_j)^*}. \tag{9.21}$$

For real poles p_j, we have the following

$$(i2\pi\nu - p_j)(i2\pi\nu - p_j)^* = (2\pi\nu)^2 + p_j^2. \tag{9.22}$$

For a complex pole p_j and its complex conjugate pole $p_{j'} = p_j^*$, we have the following

$$\begin{aligned}
&(i2\pi\nu - p_j)(i2\pi\nu - p_j)^*(i2\pi\nu - p_{j'})(i2\pi\nu - p_{j'})^* \\
&\quad = (i2\pi\nu - p_j)(-i2\pi\nu - p_j^*)(i2\pi\nu - p_j^*)(-i2\pi\nu - p_j) \\
&\quad = \left[(2\pi\nu)^2 + p_j^2\right]\left[(2\pi\nu)^2 + (p_{j'}^2)\right].
\end{aligned} \tag{9.23}$$

The same principle applies to the zeros. Therefore, the PSD can be reorganized as

$$S_x(\nu) = \frac{|b_0|^2 \prod_{k=1}^{M}\left[(2\pi\nu)^2 - Z_k\right]}{\prod_{j=1}^{N+1}\left[(2\pi\nu)^2 - P_j\right]} = \sum_{j=1}^{N+1} \frac{R_j}{(2\pi\nu)^2 - P_j}, \tag{9.24}$$

where we have defined the modified zeros $Z_k \equiv -z_k^2$ and the modified poles $P_j \equiv -p_j^2$, and R_j denote the modified residues. We can fit the modified poles and residues in an iterative way. Starting from some initial guess of the modified poles $\bar{P}_j$, we can fit for the unknown modified residues R_j and $\bar{R}_j$ from the equation below

$$\left[\sum_{j=1}^{N+1} \frac{\bar{R}_j}{(2\pi\nu)^2 - \bar{P}_j} + 1\right] S_x(\nu) = \sum_{j=1}^{N+1} \frac{R_j}{(2\pi\nu)^2 - \bar{P}_j}. \tag{9.25}$$

The modified poles $\bar{R}_j$ in the next iteration are then set as the modified zeros $\bar{Z}_j$ of the left hand side of the above equation in the current iteration. After convergence (i.e. the fitting error is sufficiently small), we obtain the estimates of P_j and R_j. The zeros and poles of $L_x(\nu)$ can be calculated from the modified poles and the modified residues.

9.3.3 *Generating Clock Noise with Given LSD*

Using the methods described in the last subsection, we can fit the measured LSD of the clock noise and obtain the coefficients of Eq. 9.13. Thus, we have the model for the clock noise

$$x^{(N+1)} + \sum_{j=0}^{N} a_j x^{(N-j)} = \sum_{k=0}^{N} b_k u^{(N-k)}, \tag{9.26}$$

where we have changed the upper index of the summation on the right hand side to N so that the total energy of the noise process $x(t)$ is finite. Notice that some of the coefficients a_j and b_k can be zero. The amount of the measured clock noise data is limited. It is useful to simulate clock noise with the same LSD. Then, we will be able to generate clock noise series with arbitrarily long time and to study how different noise realizations affect the measurements and the data pre-processing algorithms.

However, generating clock noise from the high-order differential equation model is not a trivial task. A direct clock noise generation from this model will cause numerical instabilities. Therefore, we first rewrite this equation as a set of first order differential equations as follows

$$\frac{\mathrm{d}}{\mathrm{d}t}\begin{bmatrix} x \\ x_1 \\ \vdots \\ x_{N-1} \\ x_N \end{bmatrix} = \begin{bmatrix} 0 & 1 & & & \\ & 0 & 1 & & \\ & & \ddots & \ddots & \\ & & & 0 & 1 \\ d_0 & d_1 & \dots & d_{N-1} & d_N \end{bmatrix} \begin{bmatrix} x \\ x_1 \\ \vdots \\ x_{N-1} \\ x_N \end{bmatrix} + \begin{bmatrix} c_1 \\ c_2 \\ \vdots \\ c_N \\ c_{N+1} \end{bmatrix} u, \tag{9.27}$$

where the new coefficients d_k and c_j are calculated from the old coefficients

$$d_k = -a_{N-k} \quad (k = 0, \dots, N) \tag{9.28}$$

$$c_{j+1} = b_j - \sum_{m=1}^{j} a_{j-m} c_m \quad (j = 0, \dots, N). \tag{9.29}$$

The proof of the equivalence of this set of first-order differential equations to the high-order differential equation is given in Sect. 9.6. Equation 9.27 is continuous in time. To simulate the noise, one needs to discretize it. However, a naive direct discretization will likely cause instability and divergence. Therefore, we try to analytically solve it and propagate the state from time t_{k-1} to t_k.

To be brief, we rewrite Eq. 9.27 as the following compact form

$$\dot{\mathbf{x}} = \mathbf{D}\mathbf{x} + \mathbf{c}u, \tag{9.30}$$

where $\mathbf{x}$ is a column state vector, $\mathbf{c}$ a constant column vector, and $\mathbf{D}$ is a constant matrix. A direct integration of the above vector differential equation from time t_{k-1} to t_k gives

$$\begin{aligned}\mathbf{x}_k &= e^{\mathbf{D}\Delta t}\mathbf{x}_{k-1} + e^{\mathbf{D}\Delta t}\int\limits_{t_{k-1}}^{t_k} e^{\mathbf{D}(t_{k-1}-t)}u(t)\mathrm{d}t\,\mathbf{c},\\ &= e^{\mathbf{D}\Delta t}\mathbf{x}_{k-1} + e^{\mathbf{D}\Delta t}\int\limits_{0}^{\Delta t} e^{-\mathbf{D}t}u(t+t_{k-1})\mathrm{d}t\,\mathbf{c},\end{aligned} \tag{9.31}$$

where $\mathbf{x}_k = \mathbf{x}(t_k)$, and we have denoted the sampling time $\Delta t = t_k - t_{k-1}$. In the end, when we have generated the noise process $x(t_k)$ (the scalar noise) according to the given LSD, its total power should be finite, which should also be guaranteed by the LSD itself. In the sampling process, the sampling time should be chosen such that the component of $x(t)$ with frequencies higher than the Nyquist frequency $1/2\Delta t$ is negligible, to avoid aliasing. Meanwhile, $u(t)$ is a white-Gaussian noise process, which has power contributions from all frequencies. Therefore, the calculated matrix **D** and the column vector **c** should have the property to suppress the high-frequency components of $u(t)$ to some negligible level. Hence, in Eq. 9.31 the variation of $u(t)$ during time between t_{k-1} and t_k is less important. We take it out of the integral and obtain the approximate solution

$$\begin{aligned}\mathbf{x}_k &\approx e^{\mathbf{D}\Delta t}\mathbf{x}_{k-1} + e^{\mathbf{D}\Delta t}\int\limits_{0}^{\Delta t} e^{-\mathbf{D}t}\mathrm{d}t\,\mathbf{c}u(t_{k-1}),\\ &= e^{\mathbf{D}\Delta t}\,\mathbf{x}_{k-1} + \left(e^{\mathbf{D}\Delta t} - \mathbf{I}\right)\mathbf{D}^{-1}\mathbf{c}\,u_{k-1},\end{aligned} \tag{9.32}$$

where we have denoted $u_{k-1} = u(t_{k-1})$, and **I** is a unit matrix. This discrete form of the noise propagation equation is numerically stable, hence it can be used to generate the clock noise. Figure 9.3 shows the LSDs of the measured frequency jitters, the

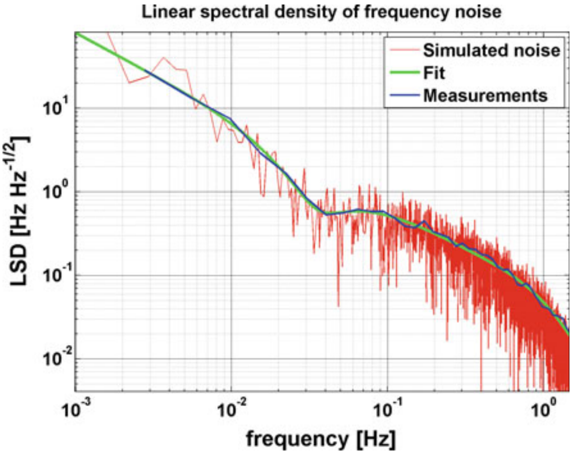

Fig. 9.3 The LSDs of the measured frequency noise, the fitted noise model and the simulated frequency noise

fitted noise model with six poles and the simulated frequency noise with the method described in this subsection. The three curves agree with each other well.

9.3.4 Kalman Filters for the Clock Noise

In this subsection, we will test how different clock noise would affect the Kalman filter estimates and how different clock noise model can amend it. For test and simplicity concern, we will adopt the simplified measurement model used in the last section but one of Chap. 6. The simplified measurements are in the following form

$$y = \begin{bmatrix} \delta T_1 - \delta T_2 \\ \delta T_2 - \delta T_3 \\ \delta T_3 - \delta T_1 \\ \delta f_1 - \delta f_2 \\ \delta f_2 - \delta f_3 \\ \delta f_3 - \delta f_1 \end{bmatrix} + \text{noise}. \tag{9.33}$$

Instead of using simulated frequency jitters with $1/f$-slope, we directly use the measured clock noise in this section, which is several orders of magnitude more noisy than the best space-qualified USOs. Notice that the clock noise is what we want to predict and estimate. Beside the measured clock noise, there are simulated ranging measurement noise and clock side-band measurement noise in the raw data. We first use the simplified Kalman filter model in the last section but one of Chap. 6 to process the measurement data. The simulation results are shown in Fig. 9.4. It is clear that the simplified Kalman filter model cannot estimate the relative clock jitters and the relative frequency jitters accurately. This is due to the oversimplified dynamic model, which includes only clock jitters and frequency jitters.

We extend the model for the clock to three variables, including the derivative of the frequency jitters δa. Therefore, we have the following dynamic model for a single clock

$$\frac{\mathrm{d}}{\mathrm{d}t} \begin{bmatrix} \delta T \\ \delta f \\ \delta a \end{bmatrix} = \begin{bmatrix} \delta f / f^{\text{nom}} \\ \delta a \\ 0 \end{bmatrix} + \begin{bmatrix} n_1 \\ n_2 \\ n_3 \end{bmatrix}, \tag{9.34}$$

where can be converted to a single three-order differential equation

$$\dddot{\delta T} = \ddot{n}_1 + (\dot{n}_2 + n_3)/f^{\text{nom}}. \tag{9.35}$$

For uncorrelated noise processes $n_1(t),\ n_2(t),\ n_3(t)$, the LSD of the clock jitters are as follows

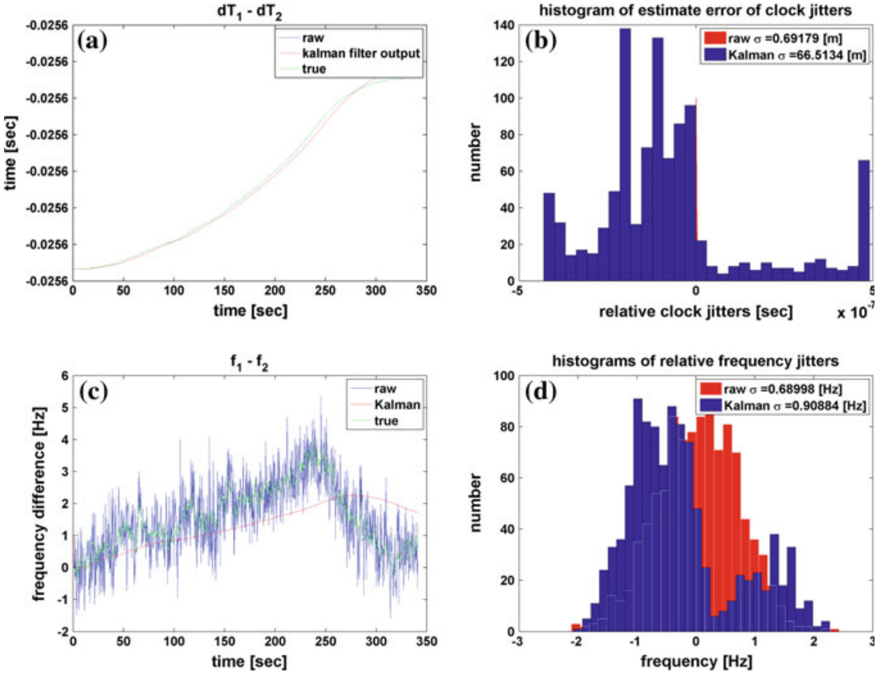

Fig. 9.4 Using the simplified Kalman filter model with only clock variables, designed in a previous chapter, to process the clock noise measured in the laboratory. **a** Relative clock jitters as time series. **b** Histograms of measurement noise on relative clock jitters and Kalman filter estimate errors. **c** Relative frequency jitters as time series. **d** Histograms of measurement noise on relative frequency jitters and Kalman filter estimate errors

$$\sqrt{S_{\delta T}(\nu)} = \left[\frac{S_{n_1}(\nu)}{(2\pi\nu)^2} + \frac{S_{n_2}(\nu)}{(f^{\text{nom}})^2(2\pi\nu)^4} + \frac{S_{n_3}(\nu)}{(f^{\text{nom}})^2(2\pi\nu)^6} \right]^{1/2}. \tag{9.36}$$

By adjusting the expected relative strengths of the noise $n_1(t)$, $n_2(t)$, $n_3(t)$, this model can approximate more complicated noise processes than the model we used in the previous simplified Kalman filter. We design a Kalman filter based on this clock model to process the same measured clock noise. The simulation results are shown in Fig. 9.5. The estimation errors based on this extended clock model are greatly reduced comparing to the performance of the previous clock model. The Kalman filter estimates have significantly improved the knowledge of the relative frequency jitters. However, the estimates of the relative clock jitters are still not satisfying.

We can try to add another parameter to the clock model in a similar way, hence we have the following model

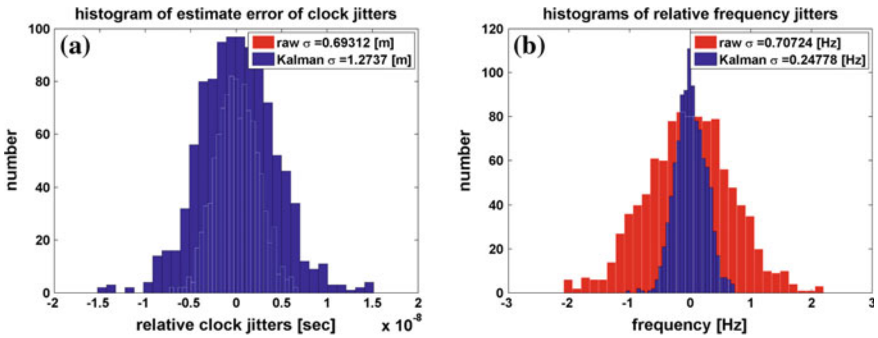

Fig. 9.5 Using the Kalman filter model based on the clock model with an additional frequency-derivative parameter to process the clock noise measured in the laboratory. **a** Histograms of measurement noise on relative clock jitters and Kalman filter estimate errors. **b** Histograms of measurement noise on relative frequency jitters and Kalman filter estimate errors

$$\frac{\mathrm{d}}{\mathrm{d}t}\begin{bmatrix}\delta T\\ \delta f\\ \delta a\\ \delta b\end{bmatrix}=\begin{bmatrix}\delta f/f^{\mathrm{nom}}\\ \delta a\\ \delta b\\ 0\end{bmatrix}+\begin{bmatrix}n_1\\ n_2\\ n_3\\ n_4\end{bmatrix}. \tag{9.37}$$

The performance of this dynamic model in the Kalman filter is summarized in Fig. 9.6. We see that this additional parameter does not improve the estimates of the relative clock jitters and the relative frequency jitters. Therefore, it is not advisable to add more parameters to the model in the same way.

We need turn to more sophisticated clock models. We fit the LSD of the measured clock noise with a three-poles model using the algorithms we described previously. Then, the model is converted to three first-order differential equations as follows

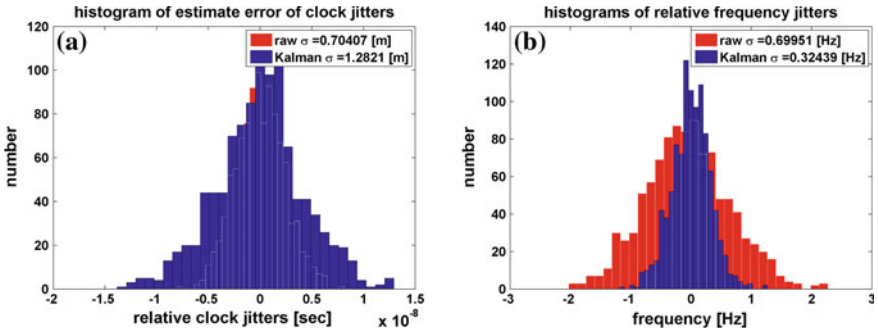

Fig. 9.6 Using the Kalman filter model based on the clock model with two additional frequency-derivative parameters to process the clock noise measured in the laboratory. **a** Histograms of measurement noise on relative clock jitters and Kalman filter estimate errors. **b** Histograms of measurement noise on relative frequency jitters and Kalman filter estimate errors

$$\frac{\mathrm{d}}{\mathrm{d}t}\begin{bmatrix}\delta T\\ \delta f\\ \delta a\end{bmatrix}=\begin{bmatrix}0 & 1/f^{\text{nom}} & 0\\ 0 & 0 & 1\\ d_0 & d_1 & d_2\end{bmatrix}\begin{bmatrix}\delta T\\ \delta f\\ \delta a\end{bmatrix}+\begin{bmatrix}c_1\\ c_2\\ c_3\end{bmatrix}u, \tag{9.38}$$

where d_j and c_j are constant coefficients, and u is a white-Gaussian noise process. We use Eq. 9.32 to discretize these equations. A Kalman filter based on this new clock model is then designed and used to process the simplified measurements. Figure 9.7 shows the estimation errors of the relative clock jitters and relative frequency jitters. This fitted clock model works much better than previous models and has successfully improved the accuracy of the clock-jitter measurements and the frequency-jitter measurements.

In a similar way, we can fit the measured LSD of the clock noise with a four-pole model. The discrete dynamic equations for the clock noise can then be constructed. We design a Kalman filter model based on these equations to process the measurement data. The results are plotted in Fig. 9.8. This model has also successfully suppressed the errors in the estimates of the relative clock jitters and the relative frequency jitters. However, comparing with the performance of the three-pole model, the extra pole does not help much. We have also tested with six-pole and seven-pole models, which led to instabilities of the Kalman filter. The reason is that those more complex models use more variables in the state vector, but among them, only the relative clock jitters and the relative frequency jitters are observed. Sophisticated noise models with much more unobserved variables than observed variables are usually numerically unstable. Therefore, it is important to design simple models that characterize the main features of the dynamics.

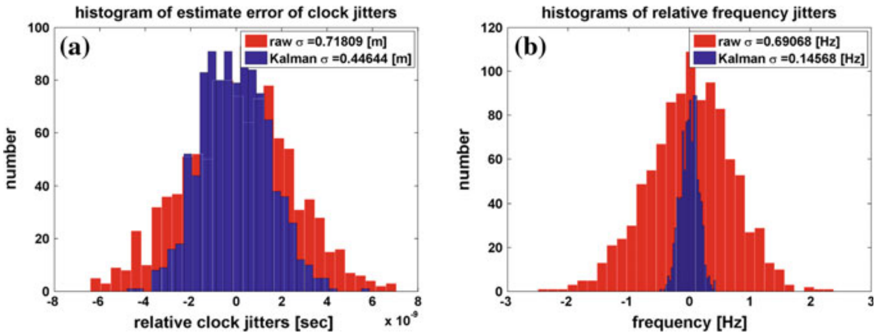

Fig. 9.7 Using the Kalman filter model based on the fitted clock model with three poles to process the clock noise measured in the laboratory. **a** Histograms of measurement noise on relative clock jitters and Kalman filter estimate errors. **b** Histograms of measurement noise on relative frequency jitters and Kalman filter estimate errors

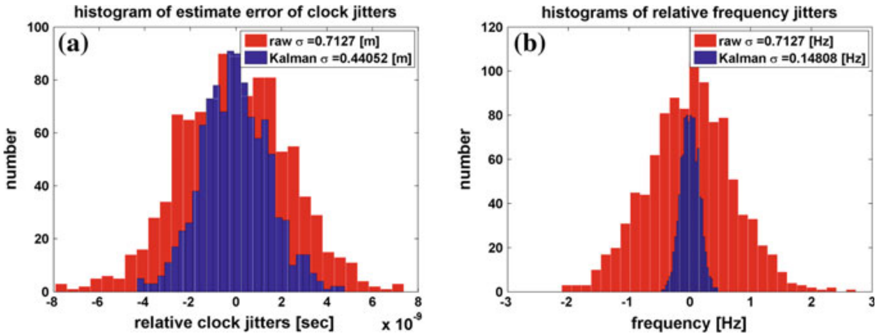

Fig. 9.8 Using the Kalman filter model based on the fitted clock model with four poles to process the clock noise measured in the laboratory. **a** Histograms of measurement noise on relative clock jitters and Kalman filter estimate errors. **b** Histograms of measurement noise on relative frequency jitters and Kalman filter estimate errors

9.3.5 Iterative Kalman Filter with a Fitted Clock Noise Model

We have designed and tested several clock noise models in simplified circumstances where we apply Kalman filters with only clock variables to simplified LISA measurements with real clock jitters measured in the laboratory. Among them, the fitted clock models with three poles and four poles are significantly better than other models. In this subsection, we try to process all the inter-spacecraft measurements of LISA with measured clock jitters in the laboratory and simulated measurement noise. We replace the clock model of the previously designed iterative Kalman filter with the fitted clock model with three poles, therefore, we have the following 15-dimensional state vector

$$\begin{aligned} x = (&L_{21}, v_{21}, a_{21}, L_{32}, v_{32}, a_{32}, L_{13}, v_{13}, a_{13}, \delta T_1 - \delta T_2, \delta f_1 - \delta f_2, \delta a_1 - \delta a_2, \\ &\delta T_2 - \delta T_3, \delta f_2 - \delta f_3, \delta a_2 - \delta a_3)^T . \end{aligned} \tag{9.39}$$

The dynamics of L_{ij}, v_{ij}, a_{ij} are designed in the previous chapter. We use this iterative Kalman filter with the fitted clock model to process standard LISA measurements with clock noise measured from the laboratory. The simulation results are plotted in Fig. 9.9. Even with clocks several orders of magnitude more noisy than the best space-qualified USOs, the designed iterative Kalman filter and the clock models have still determined the armlengths, the relative clock jitters and the frequency jitters precisely. This kind of accurate information will help better extract the astrophysical information from the LISA data. Our designed algorithms also potentially permit to use low-standard clocks in the LISA project, while still achieving the designed science goal.

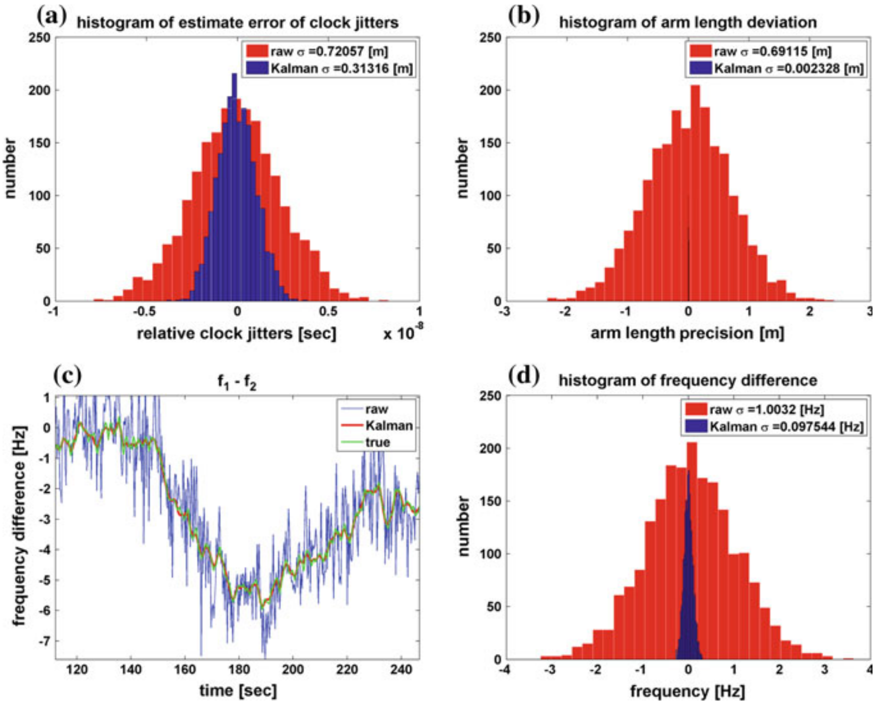

Fig. 9.9 Using the iterative Kalman filter model with fitted three-pole clock model to process the standard LISA measurements with clock noise measured in the laboratory. **a** Histograms of measurement noise on relative clock jitters and Kalman filter estimate errors. **b** Histograms of the estimation errors in the armlengths. **c** Relative frequency jitters as time series. **d** Histograms of the estimation errors in the relative frequency jitters

9.4 Disordered LISA Measurements

Clock noise (i.e. the USO noise) has its effects on the LISA measurements in two ways. On the one hand, the USOs serve as the time reference and the frequency reference of the measurements, hence the clock noise enters directly into the ranging measurements, the Doppler measurements (i.e. the main science measurements) and the clock side-band measurements. On the other hand, the USOs are driving the ADCs on board, controlling the sampling time. Therefore, the clock noise also affects the time stamps of LISA measurements. We have been dealing with the first kind of effects of the clock noise in different circumstances successfully. However, the second kind of effects has been neglected so far. In this section, we will investigate the second kind of effects of the clock noise.

9.4.1 Effects of the Clock Noise on the Time Stamps

Ideally, the three USOs (i.e. clocks) of LISA constellation are infinitely accurate and perfectly synchronized to each other. In this case, the ideal time stamps of LISA measurements are plotted in Fig. 9.10a, where all the measurements are sampled uniformly at the nominal sampling frequency (we use 3 Hz as an example), and the data measured in different spacecraft are recorded at the same UTC time. However, in practice, the clocks of LISA are jittering all the time and are unsynchronized. Figure 9.10b shows the actual recording time of the measurements taken in different spacecraft with exaggerated clock noise. We see that the measurements at different spacecraft are not recorded at the same time. Even the measurements recorded in the same spacecraft are not sampled perfectly uniformly. Furthermore, the actual recording time of these measurements are unknown to us, since the absolute clock jitters and frequency jitters are impossible to measure. We only get the nominal time stamps of the measurements which look like Fig. 9.10a.

To study this effect, we first need to simulate it. According to the LSD of the clock noise, we can simulate the clock jitters and the frequency jitters of each clock at a sampling frequency much higher than the actual sampling frequency 3 Hz of the down-link of LISA. From the clock jitters, the true recording time of the measurements at each SC can be calculated, such as the true recording time shown in Fig. 9.10. The inter-spacecraft measurements are calculated at the true recording time. In the calculation, the positions and the velocities of the SC can be obtained at arbitrary time according to the dynamics. The clock jitters and the frequency jitters are filtered by a low-pass filter with a corner frequency much higher than the nominal sampling frequency 3 Hz. Then, these jitters can also be interpolated to arbitrary time. In the end, we have several time series of measurements from each SC sampled according to its own clock.

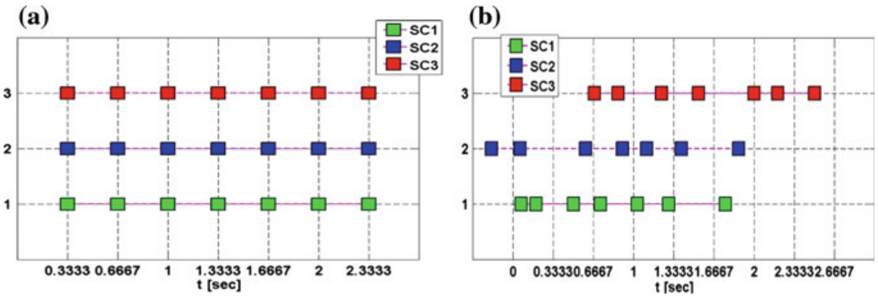

Fig. 9.10 The time stamps of LISA measurements with nominal sampling frequency at 3 Hz. The *vertical axis* indicates the spacecraft index. **a** The time stamps with perfectly stable clocks that are also ideally synchronized to each other. **b** The exaggerated plot of time stamps with unstable and unsynchronized clocks

9.4.2 *Performances of the Designed Algorithms*

In this subsection, we will apply the previously designed algorithms to simulated LISA measurements with unknown jittering time stamps, and investigate how the jittering time stamps will influence the performances of the algorithms. Firstly, we generate frequency jitters whose LSD has a $1/\nu$-slope, and the corresponding clock jitters. We simulate LISA measurements with unknown jittering time stamps calculated from these frequency jitters and clock jitters. We apply the hybrid-extended Kalman filter with the 24-dimensional state vector to the simulated data. The results are shown in Fig. 9.11. Although, the estimates of the relative frequency jitters are still accurate, the estimates of the relative clock jitters and the arm lengths are significantly biased. This is partly because the measurements are already biased by the unknown jittering time stamps. We also apply the previously designed Kalman filter with effective system models to similar simulated LISA measurements with a different noise realization. The results are summarized in Fig. 9.12. Similarly, we observe that the unknown jittering time stamps have led to biases in the relative clock

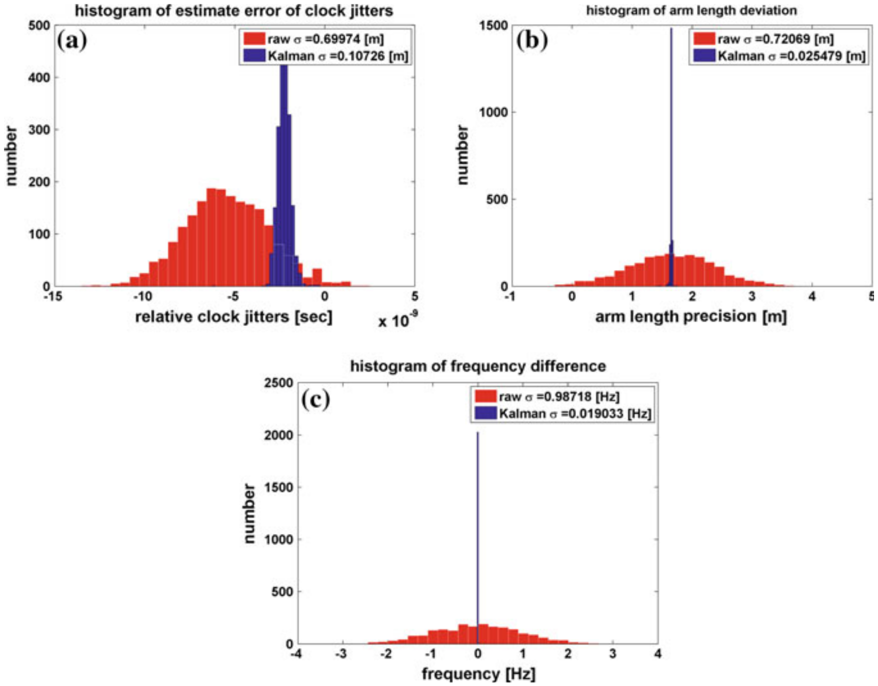

Fig. 9.11 Application of the hybrid-extended Kalman filter with the 24-dimensional state vector to simulated LISA measurements with unknown jittering time stamps. **a** Histograms of estimation errors of relative clock jitters. **b** Histograms of estimation errors of arm lengths. **c** Histograms of estimation errors of relative frequency jitters

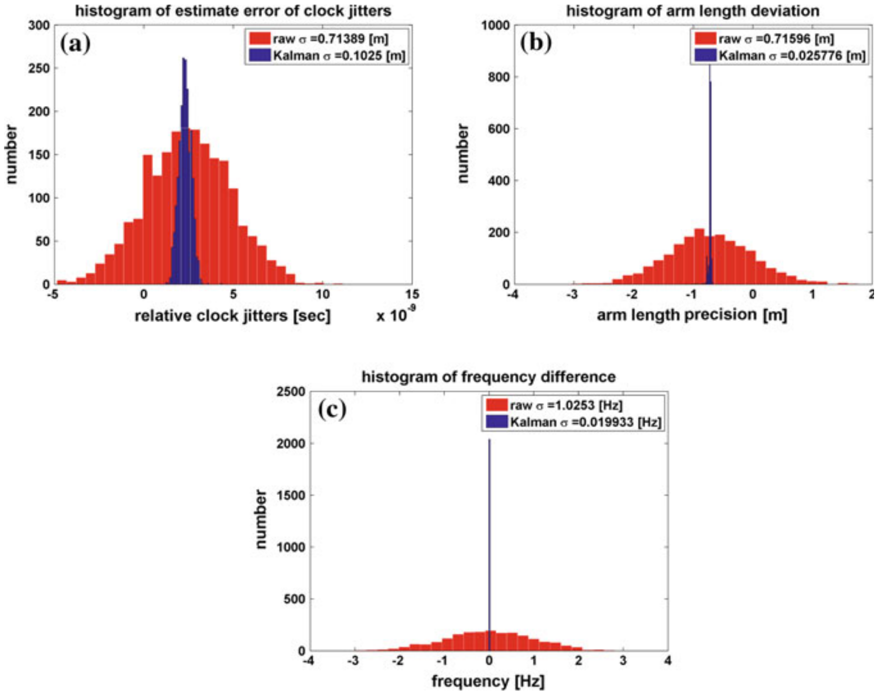

Fig. 9.12 Application of the Kalman filter with the effective system dynamics to simulated LISA measurements with unknown jittering time stamps. **a** Histograms of estimation errors of relative clock jitters. **b** Histograms of estimation errors of arm lengths. **c** Histograms of estimation errors of relative frequency jitters

jitters and the arm lengths, which cannot be corrected by the designed Kalman filter the effective system models.

We also use stronger and more complicated clock noise to test other designed algorithms. We generate clock noise that has a LSD 40-times weaker than the measured clock noise in the last section. Notice that this clock noise is still much stronger than the $1/\nu$-slope frequency noise. LISA measurements with unknown jittering time stamps are simulated based on this clock noise. We then apply the iterative Kalman filter with fitted three-pole clock models to the simulated LISA measurements. The results are shown in Fig. 9.13. Similarly, the estimates of the relative clock jitters and the arm lengths are significantly biased. However, the influences of the jittering time stamps on the relative frequency jitters are not apparent.

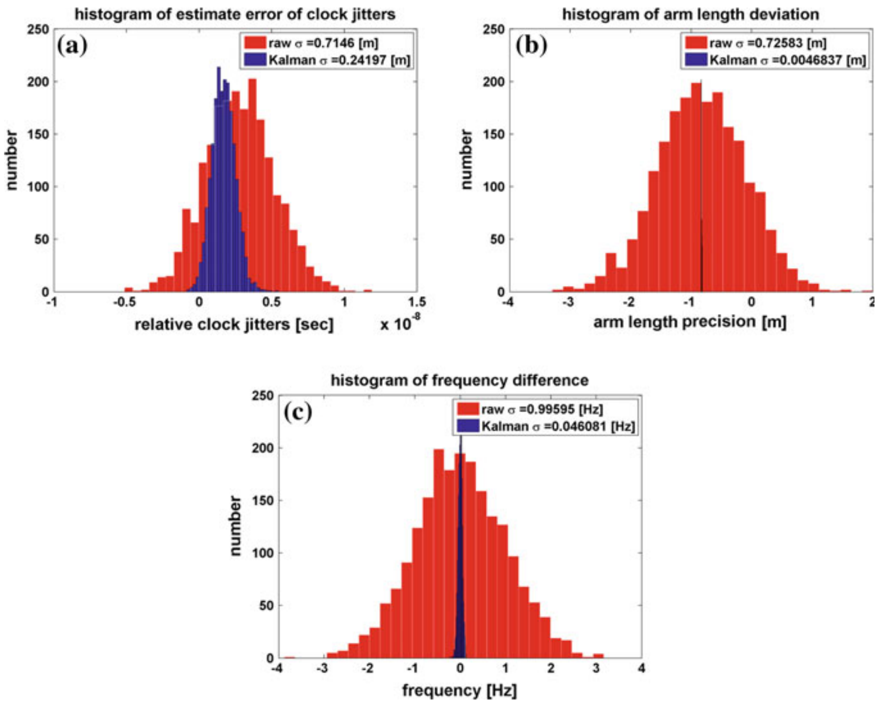

Fig. 9.13 Application of the iterative Kalman filter with fitted three-pole clock models to simulated LISA measurements with unknown jittering time stamps. **a** Histograms of estimation errors of relative clock jitters. **b** Histograms of estimation errors of arm lengths. **c** Histograms of estimation errors of relative frequency jitters

9.4.3 Properties of the Jittering Time Stamps

We denote the time span of LISA measurements, to be processed by the designed Kalman filter-like algorithms, as T_{obs}, which is usually of the order of 1000 s. The initial time biases of the clock in the ith SC at the beginning of this time span are denoted by ΔT_i. The instantaneous clock biases excluding the initial clock biases are denoted by δT_i. The relation between the true time t_{UTC} and the nominal time t_i of the ith clock is given by

$$t_{\text{UTC}} = t_i + \Delta T_i + \delta T_i(t_{\text{UTC}}). \tag{9.40}$$

Notice that the initial clock bias ΔT_i can be as large as a fraction of a second, while the instantaneous clock bias δT_i within the time span is several orders of magnitude smaller (e.g. $\delta T_i < 10^{-6}$ s). Also notice that all the measurements and related quantities are ‘uniformly’ sampled in the nominal time t_i. Therefore, we expand the instantaneous clock biases in a Taylor series

$$\begin{aligned}\delta T_i(t_{\mathrm{UTC}}) &= \delta T_i(t_i + \Delta T_i + \delta T_i)\\ &= \delta T_i(t_i + \Delta T_i) + \delta\dot{T}_i(t_i + \Delta T_i)\delta T_i + O(\delta T_i^2).\end{aligned} \tag{9.41}$$

To make an order of magnitude estimation, we assume the PSD of the instantaneous clock biases to be $S_{\delta T} \approx A/\nu^4$, where ν is the Fourier frequency, and A is an amplitude. The standard deviation of the instantaneous clock bias can then be estimated

$$\sqrt{\mathrm{E}[\delta T_i^2]} = \sqrt{2\int_{1/T_{\mathrm{obs}}}^{\infty} S_{\delta T}(\nu)\mathrm{d}\nu} \approx \sqrt{\frac{2}{3}AT_{\mathrm{obs}}^3}. \tag{9.42}$$

The magnitude of the derivative of the instantaneous clock bias is

$$\begin{aligned}\delta\dot{T}_i \sim \sqrt{\mathrm{E}[\delta\dot{T}_i^{\,2}]} &= \sqrt{2\int_{1/T_{\mathrm{obs}}}^{\infty} 4\pi^2\nu^2 S_{\delta T}(\nu)\mathrm{d}\nu}\\ &\approx \sqrt{8\pi^2 A T_{\mathrm{obs}}} \approx \sqrt{\frac{12\pi^2}{T_{\mathrm{obs}}^2}}\sqrt{\mathrm{E}[\delta T_i^2]} \le 10^{-8}.\end{aligned} \tag{9.43}$$

Hence, we make the following approximation

$$\delta T_i(t_i + \Delta T_i + \delta T_i) \approx \delta T_i(t_i + \Delta T_i) + \text{noise}, \tag{9.44}$$

where the noise term is several orders of magnitude smaller than δT_i. Similarly, we can justify the following

$$L_{ij}(t_j + \Delta T_j + \delta T_j) \approx L_{ij}(t_j + \Delta T_j) + \text{noise}, \tag{9.45}$$
$$v_{ij}(t_j + \Delta T_j + \delta T_j) \approx v_{ij}(t_j + \Delta T_j) + \text{noise}, \tag{9.46}$$
$$\delta f_i(t_i + \Delta T_i + \delta T_i) \approx \delta f_i(t_i + \Delta T_i) + \text{noise}, \tag{9.47}$$

where L_{ij} and v_{ij} respectively denote the arm length and the relative tangential velocity between SC i and SC j measured at SC j. By choosing the time span T_{obs} properly, we can approximately treat the inter-spacecraft measurements as uniformly sampled at the cost of introducing extra noise. This is almost the best we could do, since the absolute values of δT_i are impossible to be recovered from the inter-spacecraft measurements. In principle, the differential clock bias $(\delta T_i - \delta T_j)/2$ can be estimated, while the common clock bias $(\delta T_i + \delta T_j)/2$ cannot be. For independent instantaneous clock biases δT_i and δT_j, the differential clock bias and the common clock bias are comparable. Therefore, adding the correction of the differential clock bias to the nominal sampling time stamps does not help much.

However, the initial clock biases ΔT_i are much larger, hence they cannot simply be treated as noise. Since the initial clock biases differ from each other, the quantities measured at different SC are not sampled at the same time. The approximate model of the inter-spacecraft measurements does not directly fit into the designed algorithms. Before running any Kalman filter-like algorithms, the relative initial clock biases can be roughly estimated as

$$\begin{aligned}\Delta T_j - \Delta T_i &= \frac{R_{ij} - R_{ji}}{2c} - \frac{L_{ij} - L_{ji}}{2c} + \text{noise}\\ &\approx \frac{R_{ij} - R_{ji}}{2c},\end{aligned} \tag{9.48}$$

where we have neglected the second term on the right hand side, which is small even in the full relativistic treatment

$$\frac{L_{ij} - L_{ji}}{2c} \sim \frac{v_{ij}}{c}\frac{L_{ij}}{2c} \sim 10^{-7}\ \text{s}. \tag{9.49}$$

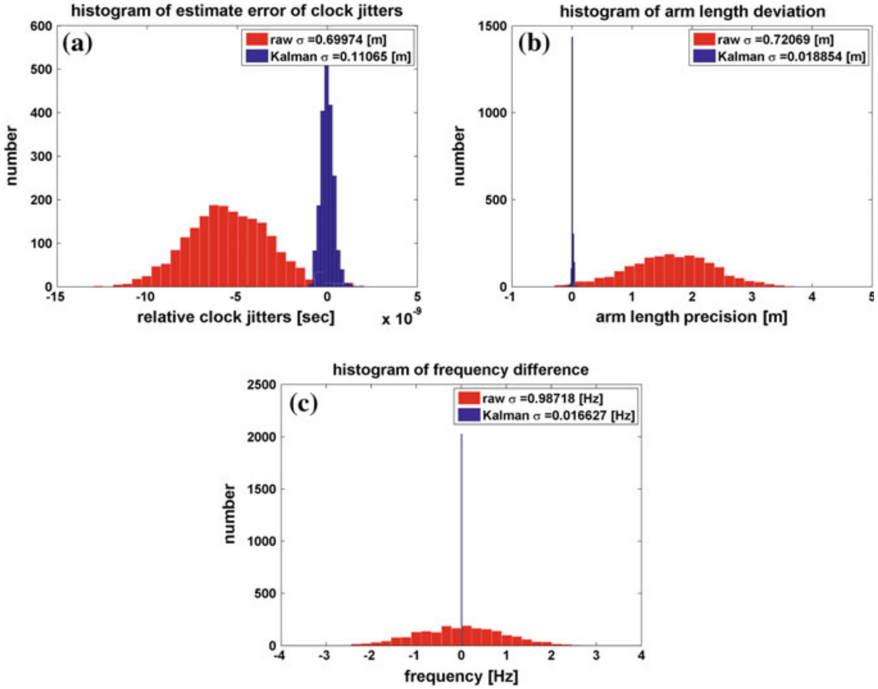

Fig. 9.14 Application of the interpolated hybrid-extended Kalman filter with the 24-dimensional state vector to simulated LISA measurements with unknown jittering time stamps. **a** Histograms of estimation errors of relative clock jitters. **b** Histograms of estimation errors of arm lengths. **c** Histograms of estimation errors of relative frequency jitters

Notice that, although this term can be neglected in the time stamps by introducing extra noise, it cannot be neglected in the ranging measurements. It is clear that this term can cause ~30 m error in the arm length estimates.

9.4.4 Hybrid Interpolated Filters

With the help of the rough estimates of $\Delta T_1 - \Delta T_2$ and $\Delta T_2 - \Delta T_3$, we can sort the inter-spacecraft measurements from all the three SC in sequence. We run the sequential Kalman filter previously designed to process the LISA measurements in sequence. The measurements that recorded at the same time (at the same SC) are processed together in one step. Ideally, this modified sequential Kalman filter would work, since the data fit into its frame. However, for the ultra-precise multi-scale problem we consider here, this modified filter turns out to be numerically unstable. Therefore, we need to design new algorithms.

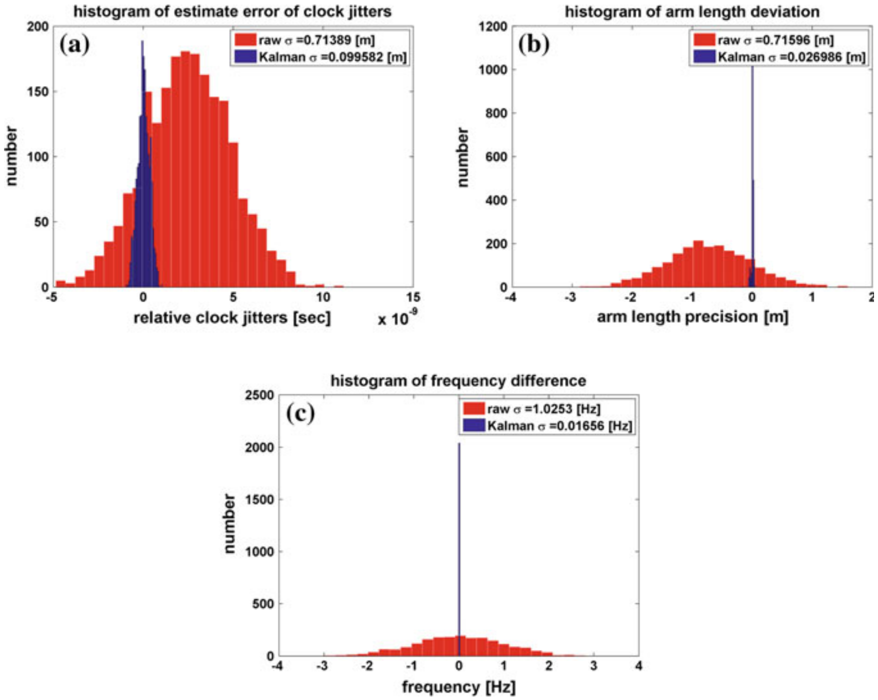

Fig. 9.15 Application of the interpolated Kalman filter with the effective system model to simulated LISA measurements with unknown jittering time stamps. **a** Histograms of estimation errors of relative clock jitters. **b** Histograms of estimation errors of arm lengths. **c** Histograms of estimation errors of relative frequency jitters

Instead of a single Kalman filter, we propose to design three similar but separate filters respectively to estimate the quantities measured in one SC at its own recording time. For instance, one filter is to estimate the arm lengths L_{21} and L_{31} observed by SC 1 recorded at the approximate time $t_1 + \Delta T_1$. We first design a low-order (e.g. three-order) low-pass digital filter to polish the measurements recorded at the other two SC. The filter is run forward and then backward in order to have zero-phase distortion. The corner frequency of the filter is set above 1 Hz. These measurements are then interpolated to the recording time $t_1 + \Delta T_1$ of SC 1, using Lagrange fractional-delay filters [9–11], based on the rough estimates of the relative initial clock biases $\Delta T_1 - \Delta T_2$ and $\Delta T_2 - \Delta T_3$. We run the hybrid-extended Kalman filter to process these interpolated measurements. The estimates of the quantities measured at SC 1 are obtained, whose estimation errors are plotted in Fig. 9.14. Comparing with Fig. 9.11, we see that the biases caused by the unknown jittering time stamps have been corrected by this hybrid interpolated filter. Similarly, we apply the Kalman filter with the effective system models to the interpolated measurements. The results are shown in Fig. 9.15. The estimates of the interpolated filter have also corrected the

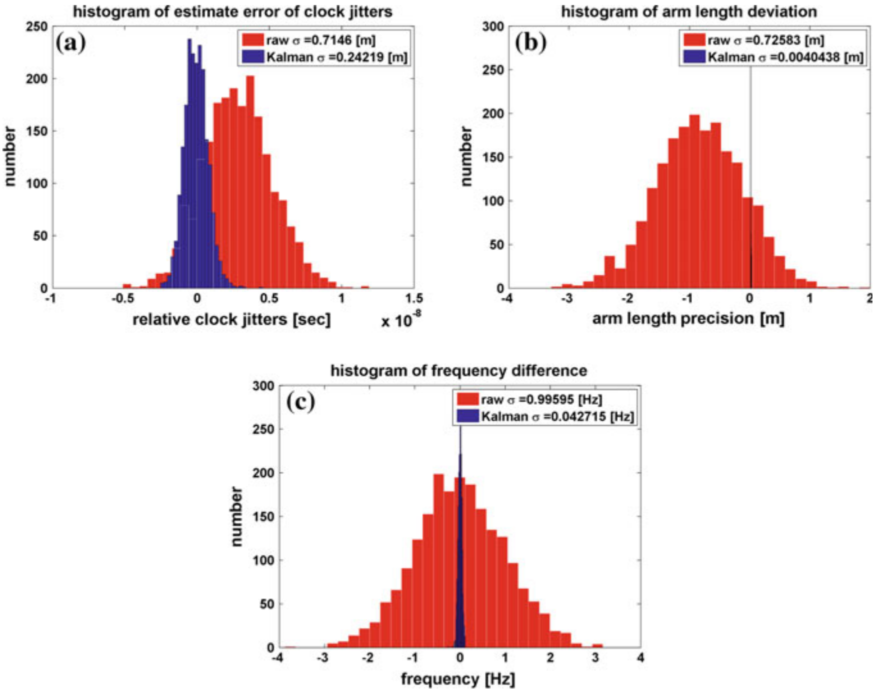

Fig. 9.16 Application of the interpolated iterative Kalman filter with the fitted three-pole clock model to simulated LISA measurements with unknown jittering time stamps. **a** Histograms of estimation errors of relative clock jitters. **b** Histograms of estimation errors of arm lengths. **c** Histograms of estimation errors of relative frequency jitters

big biases in the measurements. Notice that the frequency jitters in these two cases have a $1/\nu$-slope LSD.

For the clock noise that has a similar LSD as the measured clock noise (but 40-times weaker), we apply the iterative Kalman filter with the fitted three-pole clock model to the interpolated LISA measurements. The simulation results are shown in Fig. 9.16. Even for this stronger and more complicated clock noise, the hybrid interpolated algorithm has also successfully estimate the relative clock jitters, the arm lengths and the relative frequency jitters, while eliminating the big biases in the measurements, comparing with Fig. 9.13. However, the hybrid interpolated algorithms does not apply to arbitrarily strong clock noise. For the measured original clock noise from the laboratory, the hybrid interpolated algorithms sometimes become unstable. As long as one uses slightly better clocks, the newly designed algorithms work properly.

9.5 Supplementary A: Calculation of the Zeros from the Residues and Poles

Here, we want to prove that the zeros of $\sum_{j=1}^{N+1} \frac{\bar{r}_j}{i2\pi\nu - \bar{p}_j} + 1$ are the eigenvalues of the following matrix

$$H = \begin{bmatrix} \bar{p}_1 - \bar{r}_1 & -\bar{r}_2 & \dots & -\bar{r}_{N+1} \\ -\bar{r}_1 & \bar{p}_2 - \bar{r}_2 & \dots & -\bar{r}_{N+1} \\ \vdots & \vdots & \ddots & \vdots \\ -\bar{r}_1 & -\bar{r}_2 & \dots & \bar{p}_{N+1} - \bar{r}_{N+1} \end{bmatrix}. \tag{9.50}$$

The eigenvalues of the matrix H are the roots of the determinant $|\lambda I - H|$, hence we have the following

$$\begin{aligned} 0 &= |\lambda I - H|, \\ &= \begin{vmatrix} \lambda - \bar{p}_1 + \bar{r}_1 & \bar{r}_2 & \dots & \bar{r}_{N+1} \\ \bar{r}_1 & \lambda - \bar{p}_2 + \bar{r}_2 & \dots & \bar{r}_{N+1} \\ \vdots & \vdots & \ddots & \vdots \\ \bar{r}_1 & \bar{r}_2 & \dots & \lambda - \bar{p}_{N+1} + \bar{r}_{N+1} \end{vmatrix}, \\ &= \begin{vmatrix} \lambda - \bar{p}_1 + \bar{r}_1 & \bar{r}_2 & \dots & \bar{r}_{N+1} \\ \bar{p}_1 - \lambda & \lambda - \bar{p}_2 & \dots & 0 \\ \vdots & \ddots & \ddots & \vdots \\ 0 & \dots & \bar{p}_N - \lambda & \lambda - \bar{p}_{N+1} \end{vmatrix}, \\ &= (\lambda - \bar{p}_1 + \bar{r}_1) \prod_{j=2}^{N+1} (\lambda - \bar{p}_j) + \sum_{j=2}^{N+1} (-1)^{j-1} \bar{r}_j \prod_{k=1}^{j-1} (\bar{p}_k - \lambda) \prod_{m=j+1}^{N+1} (\lambda - \bar{p}_m), \end{aligned}$$

$$= \prod_{k=1}^{N+1}(\lambda - \bar{p}_k)\left[\sum_{j=1}^{N+1}\frac{\bar{r}_j}{\lambda - \bar{p}_j} + 1\right],$$
$$= \prod_{j=1}^{N+1}(\lambda - \bar{z}_j). \tag{9.51}$$

Hence, the eigenvalues λ_j are identical to the zeros $\bar{z}_j$.

9.6 Supplementary B: A Proof of the Clock Model

In this supplementary, we show a way of decomposing the following high-order differential equation into a set of first-order differential equations.

$$x^{(N+1)} + \sum_{j=0}^{N} a_j x^{(N-j)} = \sum_{k=0}^{N} b_k u^{(N-k)}. \tag{9.52}$$

Notice that there are in total $2(N+1)$ coefficients a_j and b_k. We assume the above equation can be decomposed into the following form

$$\frac{\mathrm{d}}{\mathrm{d}t}\begin{bmatrix} x \\ x_1 \\ \vdots \\ x_{N-1} \\ x_N \end{bmatrix} = \begin{bmatrix} 0 & 1 & & & \\ & 0 & 1 & & \\ & & \ddots & \ddots & \\ & & & 0 & 1 \\ d_0 & d_1 & \dots & d_{N-1} & d_N \end{bmatrix}\begin{bmatrix} x \\ x_1 \\ \vdots \\ x_{N-1} \\ x_N \end{bmatrix} + \begin{bmatrix} c_1 \\ c_2 \\ \vdots \\ c_N \\ c_{N+1} \end{bmatrix} u, \tag{9.53}$$

where c_j and d_k are unknown coefficients to be determined. Notice that there are $2(N+1)$ unknown coefficients in total. In principle, these unknowns can be completely determined from the coefficients of the high-order differential equation. For $k = 1, \dots, N$, it is easy to obtain the following

$$x_k = x^{(k)} - \sum_{j=1}^{k} c_j u^{(k-j)}. \tag{9.54}$$

Therefore, the set of first-order differential equations is equivalent to

$$x^{(N+1)} - \sum_{k=0}^{N} d_k x^{(k)} = \sum_{j=0}^{N} c_{j+1} u^{(N-j)} - \sum_{k=1}^{N}\sum_{l=1}^{k} d_k c_l u^{(k-l)}. \tag{9.55}$$

For the last term of the above equation, we define the following new summation indices

$$
\begin{aligned}
j &= N - k + l \in [1, N],\\
m &= l \in [1, j].
\end{aligned}
\tag{9.56}
$$

It can be proved that

$$
\sum_{k=1}^{N}\sum_{l=1}^{k} d_k c_l u^{(k-l)} = \sum_{j=1}^{N}\sum_{m=1}^{j} d_{N+m-j} c_m u^{(N-j)}. \tag{9.57}
$$

By inserting the above equation into Eq. 9.55, we have

$$
x^{(N+1)} - \sum_{k=0}^{N} d_k x^{(k)} = \sum_{j=0}^{N}\left(c_{j+1} - \sum_{m=1}^{j} d_{N+m-j} c_m\right) u^{(N-j)}. \tag{9.58}
$$

Compare with Eq. 9.52, we can solve the unknown coefficients

$$
d_k = -a_{N-k} \quad (k = 0, \ldots, N) \tag{9.59}
$$

$$
c_{j+1} = b_j - \sum_{m=1}^{j} a_{j-m} c_m \quad (j = 0, \ldots, N). \tag{9.60}
$$

References

1. B. Gustavsen, A. Semlyen, Rational approximation of frequency domain responses by vector fitting. IEEE Trans. Power Deliv. **14**(3), 1052–1061 (1999)
2. G. Heinzel, Electronic Noise in Interferometers, in *Gravitational Wave Detection II, Proceedings of the 2nd TAMA International Workshop on Gravitational Wave Detection*, Tokyo, 19–22 Oct 1999, ed. by S. Kawamura, N. Mio (Universal Academy Press, Tokyo, 1999)
3. J. Kennedy, R.C. Eberhart, Proc. IEEE Int. Conf. Neural Netw. **4**, 1942 (1995). http://ieeexplore.ieee.org
4. Y. Wang, S.D. Mohanty, Phys. Rev. D **81**, 063002 (2010). arXiv:gr-qc/1001.0923
5. D.M. Olssona, L.S. Nelson, The Nelder–Mead simplex procedure for function minimization. Technometrics **17**(1), 45–51 (1975)
6. J.J. Moré, *The Levenberg–Marquardt Algorithm: Implementation and Theory*, Numerical analysis (Springer, Berlin, 1978)
7. L. De Tommasi, B. Gustavsen, T. Dhaene, Accurate macromodeling based on tabulated magnitude frequency responses, Signal propagation on interconnects (2008)
8. L. De Tommasi, B. Gustavsen, T. Dhaene, Robust transfer function identification via an enhanced magnitude vector fitting algorithm. IET Control Theory Appl. **4**(7), 1169–1178 (2010)
9. T.I. Laakso et al., Splitting the unit delay. IEEE Signal Process. Mag. **13**(1), 30–60 (1996)
10. V. Valimaki, A. Haghparast, Fractional delay filter design based on truncated Lagrange interpolation. IEEE Signal Process. Lett. **4**(11), 816–819 (2007)
11. D.A. Shaddock, B. Ware, R.E. Spero, M. Vallisneri, Postprocessed time-delay interferometry for LISA. Phys. Rev. D **70**, 081101(R) (2004)

Chapter 10
Octahedron Configuration for a Displacement Noise-Canceling Gravitational Wave Detector in Space

Abstract We study for the first time a three-dimensional octahedron constellation for a space-based gravitational wave detector, which we call the octahedral gravitational observatory (OGO). With six spacecraft the constellation is able to remove laser frequency noise and acceleration disturbances from the gravitational wave signal without needing LISA-like drag-free control, thereby simplifying the payloads and placing less stringent demands on the thrusters. We generalize LISA's time-delay interferometry to displacement noise free interferometry (DFI) by deriving a set of generators for those combinations of the data streams that cancel laser and acceleration noise. However, the three-dimensional configuration makes orbit selection complicated. So far, only a halo orbit near the Lagrangian point L1 has been found to be stable enough, and this allows only short arms up to 1400 km. We derive the sensitivity curve of OGO with this arm length, resulting in a peak sensitivity of about 2×10^{-23} Hz $^{-1/2}$ near 100 Hz. We compare this version of OGO to the present generation of ground-based detectors and to some future detectors. We also investigate the scientific potentials of such a detector, which include observing gravitational waves from compact binary coalescences, the stochastic background, and pulsars as well as the possibility to test alternative theories of gravity. We find a mediocre performance level for this short arm length detector, between those of initial and advanced ground-based detectors. Thus, actually building a space-based detector of this specific configuration does not seem very efficient. However, when alternative orbits that allow for longer detector arms can be found, a detector with much improved science output could be constructed using the octahedron configuration and DFI solutions demonstrated in this chapter. Also, since the sensitivity of a DFI detector is limited mainly by shot noise, we discuss how the overall sensitivity could be improved by using advanced technologies that reduce this particular noise source.

10.1 Introduction

The search for gravitational waves (GWs) has been carried out for more than a decade by ground-based detectors. Currently, the LIGO and Virgo detectors are being upgraded using advanced technologies [1, 2]. The ground-based detectors are

Y. Wang, *First-stage LISA Data Processing and Gravitational Wave Data Analysis*,
Springer Theses, DOI 10.1007/978-3-319-26389-2_10

sensitive in quite a broad band from about 10 Hz to a few kHz. In this band possible GW sources include stellar-mass compact coalescing binaries [3], asymmetric core collapse of evolved heavy stars [4], neutron stars with a nonzero ellipticity [5] and, probably, a stochastic GW background from the early Universe or from a network of cosmic strings [6, 7].

In addition, the launch of a space-based GW observatory is expected in the next decade, such as the classic LISA mission concept [8] (or its recent modification known as evolved LISA (eLISA)/NGO [9]), and DECIGO [10]. LISA has become a mission concept for any heliocentric drag-free configuration that uses laser interferometry for detecting GWs. The most likely first GW observatory in space will be the eLISA mission, which has an arm length of 10^9 m and two arms, with one "mother" and two "daughter" spacecraft exchanging laser light in a V-shaped configuration to sense the variation of the metric due to passing GWs.

The eLISA mission aims at mHz frequencies, targeting other sources than ground-based detectors, most importantly supermassive black hole binaries. In a more ambitious concept, DECIGO is supposed to consist of a set of four smaller triangles (12 spacecraft in total) in a common orbit, leading to a very good sensitivity in the intermediate frequency region between LISA and advanced LIGO (aLIGO).

Here we want to present a concept for another space-based project with quite a different configuration from what has been considered before. The concept was inspired by a three-dimensional interferometer configuration in the form of an octahedron, first suggested in Ref. [11] for a ground-based detector, based on two Mach–Zehnder interferometers.

The main advantage of this setup is the cancellation of timing, laser frequency and displacement noise by combining multiple measurement channels. We have transformed this detector into a space-borne observatory by placing one LISA-like spacecraft (but with four telescopes and a single test mass) in each of the six corners of the octahedron, as shown in Fig. 10.1. Therefore, we call this project the *Octahedral Gravitational Observatory* (OGO).

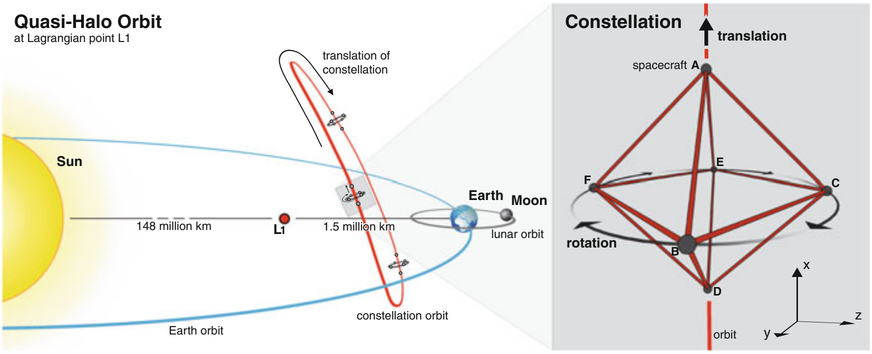

Fig. 10.1 *Left* Graphical representation of the proposed halo orbit around L1. *Right* OGO's spacecraft constellation along the halo orbit, with a radius of 1000 km and spacecraft separation of $L = \sqrt{2}\,r \approx 1400$ km. [Image by S. Barke]

Before going into the mathematical details of displacement-noise free interferometry (DFI), we first consider possible orbits for a three-dimensional octahedron constellation in Sect. 10.2. As we will find later on, the best sensitivities of an OGO-like detector are expected at very long arm lengths. However, the most realistic orbits we found that can sustain the three-dimensional configuration with stable distances between adjacent spacecraft for a sufficiently long time are so-called “halo” and “quasihalo” orbits around the Lagrange point L1 in the Sun-Earth system.

These orbits are rather close to Earth, making a mission potentially cheaper in terms of fuel and communication, and corrections to maintain the formation seem to be reasonably low. On the other hand, a constellation radius of only 1000 km can be supported, corresponding to a spacecraft-to-spacecraft arm length of approximately 1400 km.

We will discuss this as the standard configuration proposal for OGO in the following, but ultimately we still aim at using much longer arm lengths. As a candidate, we will also discuss OGO orbits with 2×10^9 m arm lengths in Sect. 10.2. However, such orbits might have significantly varying separations and would require further study of the DFI technique in such circumstances.

The octahedron configuration gives us 24 laser links, each corresponding to a science measurement channel of the distance (photon flight-time) variation between the test masses on adjacent spacecraft. The main idea is to use a sophisticated algorithm called *displacement-noise free interferometry* (DFI, [11–13]), which proceeds beyond conventional Time-Delay Interferometry techniques (TDI, [14, 15]), and in the right circumstances can improve upon them.

It can cancel both timing noise and acceleration noise when there are more measurements than noise sources. In three dimensions, the minimum number of spacecraft for DFI is 6, which we therefore use for OGO: this gives $6 - 1$ relative timing (clock) noise sources and $3 \times 6 = 18$ components of the acceleration noise, so that $24 > 5 + 18$ and the DFI requirement is fulfilled. On the one hand, this required number of links increases the complexity of the detector. On the other hand, it provides some redundancy in the number of shot-noise-only configurations, which could be very useful if one or several links between spacecraft are interrupted.

After applying DFI, we assume that the dominant remaining noise will be shot noise. For the case of an equal-arm-length three-dimensional constellation, we analytically find a set of generators for the measurement channel combinations that cancel simultaneously all timing and acceleration noise. We assume that all deviations from the equal-arm configuration are small and can be absorbed into a low-frequency part of the acceleration noise. We describe the procedure of building DFI combinations in Sect. 10.3. This will also allow us to quantify the redundancy inherent in the six-spacecraft configuration. The technical details of the derivation can be found in Sect. 10.7.

In Sect. 10.4, we compute the response functions of the octahedron DFI configuration and derive the sensitivity curve of the detector. We assume the conservative 1400 km arm length, a laser power of 10 W and a telescope diameter of 1 m, while identical strain sensitivity is achievable for smaller telescopes and higher power.

Unfortunately, those combinations that cancel acceleration and timing noise also suppress the GW signal at low frequencies. This effect shows up as a rather steep slope $\sim f^2$ in the response function.

We present sensitivity curves for single DFI combinations and find that there are in principle 12 such noise-uncorrelated combinations (corresponding to the number of independent links) with similar sensitivity, leading to an improved network sensitivity of the full OGO detector. We find that the best sensitivity is achieved around 78 Hz, in a range similar to that of ground-based detectors. The network sensitivity of OGO is better than that of initial LIGO at this frequency, but becomes better than that of aLIGO only below 10 Hz. The details of these calculations are presented in Sect. 10.4.2.

At this point, in Sect. 10.4.3, we briefly revisit the alternative orbits with a longer arm length, which would result in a sensitivity closer to the frequency band of interest for LISA and DECIGO. For this variant of OGO, we assume LISA-like noise contributions (but without spacecraft jitter) and compare the sensitivity of an octahedron detector using DFI with one using TDI, thus directly comparing the effects of these measurement techniques.

Actually, we find that the 2×10^9 m arm length is close to the point of equal sensitivity of DFI and TDI detectors in the limit of vanishing jitter. This implies that DFI would be preferred for even longer arm lengths, but might already become competitive at moderate arm lengths if part of the jitter couples into the displacement noise in such a way that it can also be canceled.

A major advantage of the OGO concept lies in its rather moderate requirement on acceleration noise, as detailed in Sect. 10.4.4. For other detectors, this limits the overall performance, but in this concept it gets canceled out by the DFI combinations. Assuming some improvements in subdominant noise sources, our final sensitivity thus depends only on the shot-noise level in each link.

Hence, we can improve the detector performance over all frequencies by reducing solely the shot noise. This could be achieved, for example, by increasing the power of each laser, by introducing cavities (similar to DECIGO), or with nonclassical (squeezed) states of light. We briefly discuss these possibilities in Sect. 10.4.5.

In Sect. 10.5, we discuss the scientific potentials OGO would have even using the conservative short-arm-length orbits. First, as a main target, the detection rates for inspiraling binaries are higher than for initial LIGO, but fall short of aLIGO expectations. However, joint detections with OGO and aLIGO could yield some events with greatly improved angular resolution. Second, due to the large number of measurement channels, OGO is good for probing the stochastic background. Furthermore, the three-dimensional configuration allows us to test alternative theories of gravity by searching for additional GW polarization modes. In addition, we briefly consider other source types such as pulsars, intermediate mass ($10^2 < M/M_\odot < 10^4$) black hole (IMBH) binaries and supernovae.

Finally, in Sect. 10.6, we summarize the description and abilities of the Octahedral Gravitational Observatory and mention additional hypothetical improvements. In this article, we use geometric units, $c = G = 1$, unless stated otherwise.

10.2 Orbits

The realization of an octahedral constellation of spacecraft depends on the existence of suitable orbits. Driving factors, apart from separation stability, are assumed to be (i) fuel costs in terms of velocity Δv necessary to deploy and maintain the constellation of six spacecraft, and (ii) a short constellation-to-Earth distance, required for a communication link with sufficient bandwidth to send data back to Earth. As described in the introduction, OGO features a three-dimensional satellite constellation. Therefore, using heliocentric orbits with a semimajor axis $a = 1\,\text{AU}$ similar to LISA would cause a significant drift of radially separated spacecraft and is in our opinion not feasible.

However, in the last decades orbits in the nonlinear regime of Sun/Earth-Moon libration points L1 and L2 have been exploited, which can be reached relatively cheaply in terms of fuel [16]. A circular constellation can be deployed on a torus around a halo L1 orbit. The radius is limited by the amount of thrust needed for keeping the orbit stable. A realistic Δv for orbit maintenance allows a nominal constellation radius of $r = 1000\,\text{km}$ [17]. We assume the spacecraft B, C, E and F in Fig. 10.1 to be placed on such a torus, whereby the out-of-plane spacecraft A and D will head and trail on the inner halo. The octahedron formation then has a base length $L = \sqrt{2}\,r \approx 1400\,\text{km}$. The halo and quasihalo orbits have an orbital period of roughly 180 days and the whole constellation rotates around the A–D line.

We already note at this point that a longer baseline would significantly improve the detector strain sensitivity. Therefore, we also propose an alternative configuration with an approximate average side length of $2 \times 10^9\,\text{m}$, where spacecraft A and D are placed on a small halo or Lissajous orbit around L1 and L2, respectively. The remaining spacecraft are arranged evenly on a (very) large halo orbit around either L1 or L2. However, simulations using natural reference trajectories showed that this formation is slightly asymmetric and that the variations in the arm lengths (and therefore in the angles between the links) are quite large. Nevertheless, we will revisit this alternative in Sect. 10.4.3 and do a rough estimation of its sensitivity. To warrant a full scientific study of such a long-arm-length detector would first require a more detailed study of these orbits.

Hence, we assume the 1400 km constellation to be a more realistic baseline, especially since the similarity of the spacecraft orbits is advantageous for the formation deployment, because large (and expensive) propulsion modules for each satellite are not required as proposed in the LISA/NGO mission [18, 19]. The $2 \times 10^9\,\text{m}$ formation will be stressed only to show the improvement of the detector sensitivity with longer arms.

Formation flight in the vicinity of Lagrange points L1 and L2 is still an ongoing research topic [20]. Detailed (numerical) simulations have to be performed to validate these orbit options and to figure out appropriate orbit and formation control strategies. In particular the suppression of constellation deformations using non-natural orbits with correction maneuvers and required Δv and fuel consumption needs to be investigated. Remaining deformations and resizing of the constellation will likely require a beam or telescope steering mechanism on the spacecraft.

In addition, the formation will have a varying Sun-incidence angle, leading to further issues for power supply, thermal shielding and blinding of interferometer arms. These points need to be targeted at a later stage of the OGO concept development as well as the effect of unequal arms on the DFI scheme.

10.3 Measurements and Noise-Canceling Combinations

In this section we will show how to combine the available measurement channels of the OGO detector to cancel laser and acceleration noise.

Each spacecraft of OGO is located at a corner of the octahedron, as shown in Fig. 10.1, and it exchanges laser light with four adjacent spacecraft. We consider interference between the beam emitted by spacecraft I and received by spacecraft J with the local beam in J, where $I, J = \{\mathrm{A, B, C, D, E, F}\}$ refer to the labels in Fig. 10.1. For the sake of simplicity, we assume a rigid and nonrotating constellation. In other words, all arm lengths in terms of light travel time are equal, constant in time and independent of the direction in which the light is exchanged between two spacecraft. This is analogous to the first generation TDI assumptions [14]. If the expected deviations from the equal arm configuration are small, then they can be absorbed into the low-frequency part of the acceleration noise. This imposes some restrictions on the orbits and on the orbit correction maneuvers. We also want to note that the overall breathing of the constellation (scaling of the arm length) is not important if the breathing time scale is significantly larger than the time required for the DFI formation, which is usually true. All calculations below are valid if we take the arm length at the instance of DFI formation, which is the value that affects the sensitivity of the detector.

The measurement of the fractional frequency change for each link is then given by

$$s_{IJ}^{\mathrm{tot}} = h_{IJ} + b_{IJ} + \mathcal{D}p_I - p_J + \mathcal{D}\left(\vec{a}_I \cdot \hat{n}_{IJ}\right) - \left(\vec{a}_J \cdot \hat{n}_{IJ}\right), \tag{10.1}$$

where we have neglected the factors to convert displacement noise to optical frequency shifts. Here, we have the following:

1. h_{IJ} is the influence of gravitational waves on the link $I \rightarrow J$.
2. b_{IJ} is the shot noise (and other similar noise sources at the photo detector and phase meter of spacecraft J) along the link $I \rightarrow J$.
3. p_I is the laser noise of spacecraft I.
4. $\vec{a}_I$ is the acceleration noise of spacecraft I.
5. $\hat{n}_{IJ} = (\vec{x}_J - \vec{x}_I)/L$ is the unit vector along the arm $I \rightarrow J$ (with length L). Hence, the scalar product $\vec{a}_I \cdot \hat{n}_{IJ}$ is the acceleration noise of spacecraft I projected onto the arm characterized by the unit vector $\hat{n}_{IJ}$.

This is similar to TDI considerations, but in addition to canceling the laser noise p_I, we also want to eliminate the influence of the acceleration noise, that is all terms containing a_I. Following Ref. [14], we have introduced a delay operator $\mathcal{D}$, which acts as

$$\mathcal{D}y(t) = y(t - L). \tag{10.2}$$

Note that we use a coordinate frame associated with the center of the octahedron, as depicted in Fig. 10.1.

The basic idea is to find combinations of the individual measurements (Eq. 10.1) which are free of acceleration noise $\vec{a}_I$ and laser noise p_I. In other words, we want to find solutions to the following equation:

$$\sum_{\text{all } IJ \text{ links}} q_{IJ}\, s_{IJ} = 0. \tag{10.3}$$

In Eq. (10.3), q_{IJ} denotes an unknown function of delays $\mathcal{D}$ and s_{IJ} contains only the noise we want to cancel:

$$\begin{aligned} s_{IJ} &\equiv s_{IJ}^{\text{tot}}(b_{IJ} = h_{IJ} = 0) \\ &= \mathcal{D}p_I - p_J + \mathcal{D}\left(\vec{a}_I \cdot \hat{n}_{IJ}\right) - \left(\vec{a}_J \cdot \hat{n}_{IJ}\right). \end{aligned} \tag{10.4}$$

If a given q_{IJ} is a solution, then $f(\mathcal{D})q_{IJ}$ is also a solution, where $f(\mathcal{D})$ is a polynomial function (of arbitrary order) of delays. The general method for finding generators of the solutions for this equation is described in Ref. [14] and we will follow it closely.

Before we proceed to a general solution for Eq. (10.3), we can check that the solution corresponding to Mach–Zehnder interferometers suggested in Ref. [11] also satisfies Eq. (10.3):

$$\begin{aligned} Y_1 = {} & [(s_{CD} + \mathcal{D}s_{AC}) - (s_{CA} + \mathcal{D}s_{DC}) + (s_{FD} + \mathcal{D}s_{AF}) \\ & - (s_{FA} + \mathcal{D}s_{DF})] - [(s_{BD} + \mathcal{D}s_{AB}) - (s_{BA} + \mathcal{D}s_{DB}) \\ & + (s_{ED} + \mathcal{D}s_{AE}) - (s_{EA} + \mathcal{D}s_{DE})]. \end{aligned} \tag{10.5a}$$

Using the symmetries of an octahedron, we can write down two other solutions:

$$\begin{aligned} Y_2 = {} & [(s_{CE} + \mathcal{D}s_{BC}) - (s_{CB} + \mathcal{D}s_{EC}) + (s_{FE} + \mathcal{D}s_{BF}) \\ & - (s_{FB} + \mathcal{D}s_{EF})] - [(s_{AE} + \mathcal{D}s_{BA}) - (s_{AB} + \mathcal{D}s_{EA}) \\ & + (s_{DE} + \mathcal{D}s_{BD}) - (s_{DB} + \mathcal{D}s_{ED})], \end{aligned} \tag{10.5b}$$

$$\begin{aligned} Y_3 = {} & [(s_{DF} + \mathcal{D}s_{CD}) - (s_{DC} + \mathcal{D}s_{FD}) + (s_{AF} + \mathcal{D}s_{CA}) \\ & - (s_{AC} + \mathcal{D}s_{FA})] - [((s_{EF} + \mathcal{D}s_{CE}) - (s_{EC} + \mathcal{D}s_{FE}) \\ & + (s_{BF} + \mathcal{D}s_{CB}) - (s_{BC} + \mathcal{D}s_{FB})]. \end{aligned} \tag{10.5c}$$

We can represent these solutions as 24-tuples of coefficients for the delay functions q_{IJ}:

$$\begin{aligned} q_1 = \{&1, 1, -1, -1, -1, -1, 1, 1, -\mathcal{D}, \mathcal{D}, 0, 0, -\mathcal{D}, \mathcal{D}, 0, 0, \\ &\mathcal{D}, -\mathcal{D}, 0, 0, \mathcal{D}, -\mathcal{D}, 0, 0\}, \end{aligned} \tag{10.6a}$$

$$\begin{aligned} q_2 = \{&-\mathcal{D}, \mathcal{D}, 0, 0, -\mathcal{D}, \mathcal{D}, 0, 0, 1, 1, -1, -1, -1, -1, 1, 1, \\ &0, 0, \mathcal{D}, -\mathcal{D}, 0, 0, \mathcal{D}, -\mathcal{D}\}, \end{aligned} \tag{10.6b}$$

$$\begin{aligned} q_3 = \{&0, 0, \mathcal{D}, -\mathcal{D}, 0, 0, \mathcal{D}, -\mathcal{D}, 0, 0, -\mathcal{D}, \mathcal{D}, 0, 0, -\mathcal{D}, \mathcal{D}, \\ &-1, -1, 1, 1, 1, 1, -1, -1\}. \end{aligned} \tag{10.6c}$$

The order used in the 24-tuples is {*BA*, *EA*, *CA*, *FA*, *BD*, *ED*, *CD*, *FD*, *AB*, *DB*, *CB*, *FB*, *AE*, *DE*, *CE*, *FE*, *AC*, *DC*, *BC*, *EC*, *AF*, *DF*, *BF*, *EF*}, so that, for example, the first entry in q_1 represents the s_{BA} coefficient in the Y_1 equation.

These particular solutions illustrate that not all links are used in producing a DFI stream. Multiple zeros in the equations for q_1, q_2, q_3 above indicate those links which do not contribute to the final result, and each time we use only 16 links. We will come back to the issue of "lost links" when we discuss the network sensitivity.

In the following, we will find generators of all solutions. The first step is to use Gaussian elimination (without division by delay operators) in Eq. (10.3), and as a result, we end up with a single (master) equation which we need to solve:

$$\begin{aligned} 0 = {} & (\mathcal{D}-1)^2 q_{BC} + (\mathcal{D}-1)\mathcal{D}q_{CE} + (1-\mathcal{D})(\mathcal{D}-1)\mathcal{D}q_{DB} \\ & + (\mathcal{D}-1)((1-\mathcal{D})\mathcal{D}-1)q_{DC} \\ & + (\mathcal{D}-1)q_{DF} + (\mathcal{D}-1)q_{EF}. \end{aligned} \tag{10.7}$$

In the next step, we want to find the so-called "reduced generators" of Eq. (10.7), which correspond to the reduced set $(q_{BC}, q_{CE}, q_{DB}, q_{DC}, q_{DF}, q_{EF})$. For this we need to compute the Gröbner basis [21], a set generating the polynomial ideals q_{IJ}. Roughly speaking, the Gröbner basis is comparable to the greatest common divisor of q_{IJ}. Following the procedure from Ref. [14], we obtain seven generators:

$$\begin{aligned} S_1 = \{&0, \mathcal{D}^2+\mathcal{D}, 0, -\mathcal{D}-\mathcal{D}^2, 1-\mathcal{D}, \mathcal{D}^2+1, -1+\mathcal{D}, -1-\mathcal{D}^2, \\ &\mathcal{D}-\mathcal{D}^2, 0, -\mathcal{D}, \mathcal{D}^2, -\mathcal{D}^2-1, -\mathcal{D}-1, 1, 1+\mathcal{D}+\mathcal{D}^2, \\ &-\mathcal{D}+\mathcal{D}^2, 0, \mathcal{D}, -\mathcal{D}^2, \mathcal{D}^2+1, 1+\mathcal{D}, -1, -\mathcal{D}-\mathcal{D}^2-1\}, \end{aligned} \tag{10.8a}$$

$$\begin{aligned} S_2 = \{&\mathcal{D}+1, \mathcal{D}+1, -\mathcal{D}-1, -\mathcal{D}-1, -1+\mathcal{D}, \mathcal{D}-1, 1-\mathcal{D}, 1-\mathcal{D}, \\ &-2\mathcal{D}, 0, \mathcal{D}, \mathcal{D}, -2\mathcal{D}, 0, \mathcal{D}, \mathcal{D}, 2\mathcal{D}, 0, -\mathcal{D}, -\mathcal{D}, 2\mathcal{D}, 0, -\mathcal{D}, -\mathcal{D}\}, \end{aligned} \tag{10.8b}$$

$$\begin{aligned} S_3 = \{&0, \mathcal{D}, -\mathcal{D}, 0, -1, \mathcal{D}-1, 1-\mathcal{D}, 1, 1-\mathcal{D}, 1, -1+\mathcal{D}, -1, -\mathcal{D}, \\ &0, \mathcal{D}, 0, \mathcal{D}, 0, 0, -\mathcal{D}, \mathcal{D}-1, -1, 1, -\mathcal{D}+1\}, \end{aligned} \tag{10.8c}$$

$$\begin{aligned} S_4 = \{&\mathcal{D}, -\mathcal{D} + \mathcal{D}^2, \mathcal{D}, -\mathcal{D} - \mathcal{D}^2, 2, -2\mathcal{D} + \mathcal{D}^2 + 2, -2 + 2\mathcal{D}, \\ &-2 - \mathcal{D}^2, 2\mathcal{D} - 2 - \mathcal{D}^2, -2, 2 - 2\mathcal{D}, 2 + \mathcal{D}^2, \mathcal{D} - \mathcal{D}^2, \\ &-\mathcal{D}, -\mathcal{D}, \mathcal{D} + \mathcal{D}^2, -2\mathcal{D} + \mathcal{D}^2, 0, 0, 2\mathcal{D} - \mathcal{D}^2, -\mathcal{D} + \mathcal{D}^2 + 2, \\ &2 + \mathcal{D}, -2 - \mathcal{D}, \mathcal{D} - \mathcal{D}^2 - 2\}, \end{aligned} \tag{10.8d}$$

$$\begin{aligned} S_5 = \{&0, \mathcal{D}^2 + \mathcal{D}, -\mathcal{D}^2, -\mathcal{D}, 1 - \mathcal{D}, \mathcal{D}^2 + 1, \mathcal{D} - \mathcal{D}^2 - 1, -1, \\ &\mathcal{D} - \mathcal{D}^2, 0, -\mathcal{D} + \mathcal{D}^2, 0, -1 - \mathcal{D}^2, -\mathcal{D} - 1, 1 + \mathcal{D}^2, 1 + \mathcal{D}, \\ &\mathcal{D}^2, \mathcal{D}, 0, -\mathcal{D}^2 - \mathcal{D}, -\mathcal{D} + \mathcal{D}^2 + 1, 1, \mathcal{D} - 1, -1 - \mathcal{D}^2\}, \end{aligned} \tag{10.8e}$$

$$\begin{aligned} S_6 = \{&\mathcal{D} + 2 + \mathcal{D}^2, \mathcal{D} + \mathcal{D}^3 + 2, -\mathcal{D} + \mathcal{D}^2 - 2, -\mathcal{D} - 2 - 2\mathcal{D}^2 - \mathcal{D}^3, \\ &-2 + 2\mathcal{D}, 2\mathcal{D} - \mathcal{D}^2 + \mathcal{D}^3 - 2, -2\mathcal{D} + 2\mathcal{D}^2 + 2, 2 - 2\mathcal{D} - \mathcal{D}^2 - \mathcal{D}^3, \\ &\mathcal{D}^2 - 4\mathcal{D} - \mathcal{D}^3, 0, 2\mathcal{D} - 2\mathcal{D}^2, 2\mathcal{D} + \mathcal{D}^2 + \mathcal{D}^3, -3\mathcal{D} - \mathcal{D}^3, \mathcal{D} - \mathcal{D}^2, \\ &\mathcal{D} - \mathcal{D}^2, 2\mathcal{D}^2 + \mathcal{D} + \mathcal{D}^3, -\mathcal{D}^2 + 2\mathcal{D} + \mathcal{D}^3, -2\mathcal{D}, 0, \mathcal{D}^2 - \mathcal{D}^3, \\ &5\mathcal{D} + \mathcal{D}^3, \mathcal{D} + \mathcal{D}^2, -3\mathcal{D} - \mathcal{D}^2, -3\mathcal{D} - \mathcal{D}^3\}, \end{aligned} \tag{10.8f}$$

$$\begin{aligned} S_7 = \{&1, 1 + \mathcal{D}, -1, -1 - \mathcal{D}, 0, \mathcal{D}, 0, -\mathcal{D}, -\mathcal{D}, 0, 0, \mathcal{D}, -1 - \mathcal{D}, -1, \\ &1, 1 + \mathcal{D}, \mathcal{D}, 0, 0, -\mathcal{D}, 1 + \mathcal{D}, 1, -1, -1 - \mathcal{D}\}. \end{aligned} \tag{10.8g}$$

As before, these operators have to be applied to s_{IJ}, using the same ordering as given above. All other solutions can be constructed from these generators. A detailed derivation of expressions (10.8a)–(10.8g) is given in Sect. 10.7.

Before we proceed, let us make several remarks. The generators found here are not unique, just like in the case of TDI [14]. The set of generators does not necessarily form a minimal set, and we can only guarantee that the found set of generators gives us a module of syzygies and can be used to generate other solutions. The combinations S_1 to S_7 applied on 24 raw measurements s_{IJ}^{tot} eliminate both laser and displacement noise while mostly preserving the gravitational wave signal. Note that again in those expressions we do not use all links—for example, if the link *BA* is lost due to some reasons, we still can use S_1, S_3, S_5 to produce DFI streams.

10.4 Response Functions and Sensitivity

In the previous section we have found generators that produce data streams free of acceleration and laser noise. Now we need to apply these combinations to the shot noise and to the GW signal to compute the corresponding response functions.

10.4.1 Shot Noise Level and Noise Transfer Function

We will assume that the shot noise is independent (uncorrelated) in each link and equal in power spectral density, based on identical laser sources and telescopes on each spacecraft. We denote the power spectral density of the shot noise by $\widetilde{S}_{\rm sn}$. A lengthy but straightforward computation shows that the spectral noise $\widetilde{S}_{{\rm n},i}$ corresponding to the seven combinations S_i, $i = 1, \ldots, 7$ from Eqs. (10.8a)–(10.8g) is given by

$$\widetilde{S}_{\rm n,1} = 16\,\widetilde{S}_{\rm sn}\,\epsilon^2\,(9 + 2\cos 2\epsilon + 3\cos 4\epsilon), \tag{10.9a}$$

$$\widetilde{S}_{\rm n,2} = 160\,\widetilde{S}_{\rm sn}\,\epsilon^2\,, \tag{10.9b}$$

$$\widetilde{S}_{\rm n,3} = 48\,\widetilde{S}_{\rm sn}\,\epsilon^2\,(2 - \cos 2\epsilon)\,, \tag{10.9c}$$

$$\widetilde{S}_{\rm n,4} = 16\,\widetilde{S}_{\rm sn}\,\epsilon^2\,(24 - 13\cos 2\epsilon + 6\cos 4\epsilon), \tag{10.9d}$$

$$\widetilde{S}_{\rm n,5} = 16\,\widetilde{S}_{\rm sn}\,\epsilon^2(\,9 - 2\cos 2\epsilon + 3\cos 4\epsilon), \tag{10.9e}$$

$$\widetilde{S}_{\rm n,6} = 16\,\widetilde{S}_{\rm sn}\,\epsilon^2\,(45 - 6\cos 2\epsilon + 17\cos 4\epsilon), \tag{10.9f}$$

$$\widetilde{S}_{\rm n,7} = 48\,\widetilde{S}_{\rm sn}\,\epsilon^2\,(2 + \cos 2\epsilon)\,, \tag{10.9g}$$

where $\epsilon \equiv \omega L/2$, with the GW frequency ω. In the low frequency limit ($\epsilon \ll 1$), the noise $\widetilde{S}_{{\rm n},i}$ for each combination S_i is proportional to ϵ^2.

Let us now compute the shot noise in a single link. We consider for OGO a configuration with LISA-like receiver-transponder links and the following parameters: spacecraft separation $L = 1414\,$km, laser wavelength $\lambda = 532\,$nm, laser power $P = 10\,$W and telescope diameter $D = 1\,$m. For this arm length and telescope size, almost all of the laser power from the remote spacecraft is received by the local spacecraft. Hence, the shot-noise calculation for OGO is different from the LISA case, where an overwhelming fraction of the laser beam misses the telescope [19].

For a Michelson interferometer, the sensitivity to shot noise is usually expressed as [22]

$$\sqrt{\widetilde{S}_h(f)} = \frac{1}{2L}\sqrt{\frac{\hbar c \lambda}{\pi P}}[1/\sqrt{\rm Hz}], \tag{10.10}$$

where we have temporarily restored the speed of light c and the reduced Planck constant $\hbar$. Notice that the effect of the GW transfer function is not included here yet. For a single link $I \rightarrow J$ of OGO as opposed to a full two-arm Michelson with dual links, $\sqrt{\widetilde{S}_{h,IJ}}$ is a factor of 4 larger. However, our design allows the following two improvements: (i) Since there is a local laser in J with power similar to the received laser power from I, the power at the beam splitter is actually $2P$, giving an improvement of $1/\sqrt{2}$. This is also different from LISA, where due to the longer arm length the received power is much smaller than the local laser power. (ii) If we assume that the arm length is stable enough to operate at the dark fringe, then we gain another factor of $1/\sqrt{2}$.

So, we arrive at the following shot-noise-only sensitivity for a single link:

$$\sqrt{\widetilde{S}_{h,IJ}(f)} = \frac{1}{L}\sqrt{\frac{\hbar c \lambda}{\pi P}} \quad [1/\sqrt{\mathrm{Hz}}]. \tag{10.11}$$

As mentioned before, almost all of the laser power from the remote spacecraft can be received by the telescope with a radius 0.5 m for OGO. Alternatively, if we want to use a smaller telescope, we could increase the transmitted laser power to achieve the same sensitivity as the standard OGO design (with a 10 W transmitted laser power and a 0.5 m telescope radius). As a rough estimate, we assume the laser beam to be Gaussian

$$E(x, y, z) = \frac{1}{w(z)}\sqrt{\frac{2P_0}{\pi}} \exp\left[-ikz + i\eta(z) - \frac{x^2+y^2}{w^2(z)} - i\frac{k(x^2+y^2)}{2R(z)}\right], \tag{10.12}$$

where $\eta(z)$ is the Gouy phase shift, $R(z)$ is the radius of curvature of the wavefront, and $w(z)$ is the radius at which the magnetic field decays to e^{-1} of the central value. Therefore, the intensity of the beam is

$$I(x, y, z) = |E(x, y, z)|^2 = \frac{2P_0}{\pi w^2(z)} \exp\left[-\frac{2(x^2+y^2)}{w^2(z)}\right], \tag{10.13}$$

which satisfies

$$\int\int I(x, y, z)\mathrm{d}x\mathrm{d}y = P_0. \tag{10.14}$$

Along the propagation direction z-axis, we have

$$w(z) = w_0\sqrt{1 + \left(\frac{z}{z_R}\right)^2}, \tag{10.15}$$

where w_0 is the beam waist, z_R is the so-called Rayleigh range

$$z_R = \frac{\pi w_0^2}{\lambda}, \tag{10.16}$$

where λ is the wavelength. We put the transmission telescope at the waist of the laser beam and assume the reception telescope is roughly at the axial center of the beam. By calculating the received laser power at the remote spacecraft, we can calculate the sensitivity level. The relative sensitivities for different combinations of transmitted laser powers and telescope radii are shown in Fig. 10.2, where the sensitivity of the standard OGO design (with a 10 W transmitted laser power and a 0.5 m telescope radius) is normalized to unity. From the figure, we see that the same sensitivity can

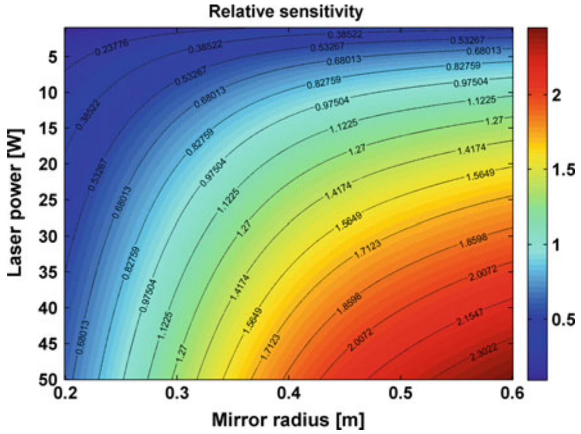

Fig. 10.2 The relative sensitivities for different combinations of transmitted laser powers and telescope radii

roughly be achieved by a transmitted laser power 15 W and a telescope with a radius 0.4 m.

10.4.2 GW Signal Transfer Function and Sensitivity

Next, we will compute the detector response to a gravitational wave signal. We assume a GW source located in the direction $\hat{n} = -\hat{k} = (\sin\theta\cos\phi, \sin\theta\sin\phi, \cos\theta)$ as seen from the detector frame. We choose unit vectors

$$\hat{u} = \begin{bmatrix} \cos\theta\cos\phi \\ \cos\theta\sin\phi \\ -\sin\theta \end{bmatrix}, \qquad \hat{v} = \begin{bmatrix} \sin\phi \\ -\cos\phi \\ 0 \end{bmatrix} \tag{10.17}$$

orthogonal to $\hat{k}$ pointing tangentially along the θ and ϕ coordinate lines to form a polarization basis. This basis can be described by polarization tensors $\mathbf{e}_+$ and $\mathbf{e}_\times$, given by

$$\mathbf{e}_+ \equiv \hat{u}\otimes\hat{u} - \hat{v}\otimes\hat{v}, \quad \mathbf{e}_\times \equiv \hat{u}\otimes\hat{v} + \hat{v}\otimes\hat{u}. \tag{10.18}$$

The single arm fractional frequency response to a GW is [23]

$$h_{IJ} = \frac{H_{IJ}(t - \hat{k}\cdot\vec{x}_I - L) - H_{IJ}(t - \hat{k}\cdot\vec{x}_J)}{2\left(1 - \hat{k}\cdot\hat{n}_{IJ}\right)}, \tag{10.19}$$

where $\vec{x}_I$ is the position vector of the Ith spacecraft, L the (constant) distance between two spacecraft and

$$H_{IJ}(t) \equiv h_+(t)\,\xi_+(\hat{u}, \hat{v}, \hat{n}_{IJ}) + h_\times(t)\,\xi_\times(\hat{u}, \hat{v}, \hat{n}_{IJ}). \tag{10.20}$$

Here $h_{+,\times}(t)$ are two GW polarizations in the basis (10.18) and

$$\xi_+(\hat{u}, \hat{v}, \hat{n}_{IJ}) \equiv \hat{n}_{IJ}^{\mathsf{T}} \mathbf{e}_+ \hat{n}_{IJ} = \left(\hat{u} \cdot \hat{n}_{IJ}\right)^2 - \left(\hat{v} \cdot \hat{n}_{IJ}\right)^2, \tag{10.21}$$

$$\xi_\times(\hat{u}, \hat{v}, \hat{n}_{IJ}) \equiv \hat{n}_{IJ}^{\mathsf{T}} \mathbf{e}_\times \hat{n}_{IJ} = 2\left(\hat{u} \cdot \hat{n}_{IJ}\right)\left(\hat{v} \cdot \hat{n}_{IJ}\right). \tag{10.22}$$

In order to find the arm response for arbitrary incident GWs, we can compute the single arm response to a monochromatic GW with Eq. (10.19) and then deduce the following general response in the frequency domain,

$$\begin{aligned} h_{IJ}(f) = {} & \epsilon\, \mathrm{sinc}\left[\epsilon(1 - \hat{k} \cdot \hat{n}_{IJ})\right] \mathrm{e}^{-\mathrm{i}\epsilon[\hat{k}\cdot(\vec{x}_I + \vec{x}_J)/L+1]} \\ & \times \left[\xi_+(\hat{n}_{IJ}) h_+(f) + \xi_\times(\hat{n}_{IJ}) h_\times(f)\right], \end{aligned} \tag{10.23}$$

where we used the normalized sinc function, conventionally used in signal processing: $\mathrm{sinc}(x) := \sin(\pi x)/(\pi x)$.

Hence, the transfer function for a GW signal is

$$\mathcal{T}^{\mathrm{GW}}_{IJ+,\times}(f) = \epsilon\, \mathrm{sinc}\left[\epsilon(1 - \hat{k} \cdot \hat{n}_{IJ})\right] \times\ \mathrm{e}^{-\mathrm{i}\epsilon[\hat{k}\cdot(\vec{x}_I + \vec{x}_J)/L+1]} \xi_{+,\times}(\hat{n}_{IJ}). \tag{10.24}$$

For the sake of simplicity, we will from now on assume that the GW has "+" polarization only. This simplification will not affect our qualitative end result. Substituting the transfer function for a single arm response into the above 7 generators [Eqs. (10.8a)–(10.8g)], we can get the transfer function $\mathcal{T}_i^{\mathrm{GW}}$ for each combination. The final expressions are very lengthy and not needed here explicitly.

Having obtained the transfer function, we can compute the sensitivity for each combination $i = 1, \ldots, 7$ as

$$\sqrt{\widetilde{S}_{h,i}} = \sqrt{\frac{\widetilde{S}_{\mathrm{n},i}}{\langle(\mathcal{T}_i^{\mathrm{GW}})^2\rangle}}, \tag{10.25}$$

where the triangular brackets imply averaging over polarization and source sky location.

We expect up to 12 independent round trip measurements, corresponding to the number of back-and-forth links between spacecraft. It is out of the scope of this work to explicitly find all noise-uncorrelated combinations (similar to the optimal channels A, E, T in the case of LISA [14]). However, if we assume approximately equal sensitivity for each combination (which is almost the case for the combinations $S_1, \ldots, S_7$), we expect an improvement in the sensitivity of the whole network by a factor $1/\sqrt{12}$.

Therefore, we simply approximate the network sensitivity of the full detector as $\sqrt{\widetilde{S}_{h,\mathrm{net}}} = \sqrt{\widetilde{S}_{h,5}/12}$. Note that the potential loss of some links would imply that not all generators can be formed. We can lose up to 6 links and still be able to form a DFI stream (but probably only one). The number of lost links (and which links are lost exactly) will affect the network sensitivity. In our estimations below we deal with the idealized situation and assume that no links are lost.

We plot the sensitivity curves for individual combinations and the network sensitivity in Fig. 10.3. For comparison we also show the design sensitivity curves of initial LIGO (S6 science run [24]) and advanced LIGO (high laser power configuration with zero detuning of the signal recycling mirror [25]). Indeed one can see that the sensitivities of the individual OGO configurations are similar to each other and close to initial LIGO. The network sensitivity of OGO lies between LIGO and aLIGO sensitivities. OGO as expected outperforms aLIGO below 10 Hz, where the seismic noise on the ground becomes strongly dominant.

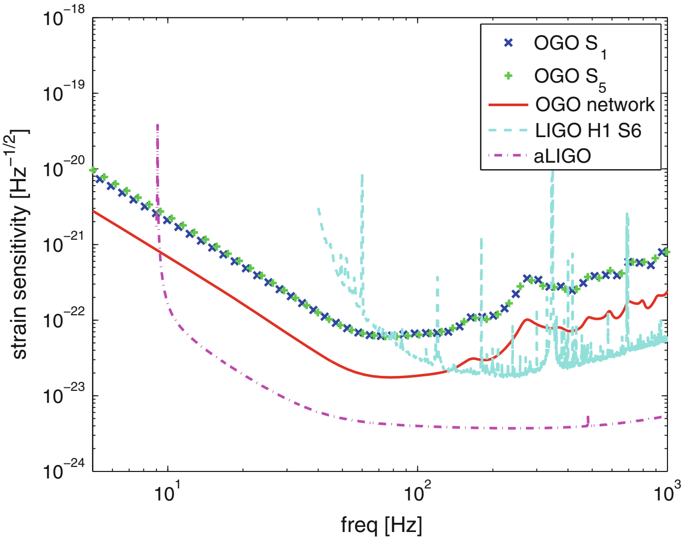

Fig. 10.3 Sensitivities for two single DFI combinations (S_1, *blue crosses* and S_5, *green plus signs*) of OGO (with $L \approx 1400$ km) and for the full OGO network sensitivity (scaled from S_5, *red solid line*). For comparison, the *dashed lines* show sensitivities for initial LIGO (H1 during science run S6, from Ref. [24], *cyan dashed line*) and aLIGO (design sensitivity for high-power, zero detuning configuration, from Ref. [25], *magenta dash-dotted line*) (color figure online)

10.4.3 General Performance of the DFI Scheme

Having derived the full sensitivity curve of the OGO mission design with $L \approx 1400\,\mathrm{km}$ as an exemplary implementation of the three-dimensional DFI scheme in space, let us take a step back and analyze the general performance of a DFI-enabled detector. These features are also what led us to consider the octahedron configuration in the first place.

Specifically, let us look in more detail at the low frequency asymptotic behavior of the transfer functions and sensitivity curves. We consider a LISA-like configuration with two laser noise free combinations: an unequal arm Michelson (TDI-X) and a Sagnac combination (TDI-α). Let us assume for a moment that the only noise source is shot noise, which at low frequencies ($\epsilon \ll 1$) scales as $\sqrt{\widetilde{S}_{\mathrm{n},X}} \sim \epsilon^2$ and $\sqrt{\widetilde{S}_{\mathrm{n},\alpha}} \sim \epsilon^1$ for those two combinations, respectively.

The GW transfer function, for both TDI combinations, scales as $\mathcal{T}_\alpha, \mathcal{T}_X \sim \epsilon^2$; therefore, the sensitivity curves scale as $\sqrt{\widetilde{S}_{h,\alpha}} \sim \sqrt{\widetilde{S}_{\mathrm{n},\alpha}}/\mathcal{T}_\alpha \sim \epsilon^{-1}$ for TDI-α and $\sqrt{\widetilde{S}_{h,X}} \sim \sqrt{\widetilde{S}_{\mathrm{n},X}}/\mathcal{T}_X \sim \epsilon^0$ for TDI-X. We see that a LISA-like TDI-X-combination has a *flat* shot-noise spectrum at low frequencies, corresponding to a flat total detector sensitivity if all other dominant noise sources can be canceled—which looks extremely attractive.

Thus, a naive analysis suggests that the acceleration and laser noise free combinations for an octahedron detector could yield a flat sensitivity curve at low frequencies. Checking this preliminary result with a more careful analysis was the main motivation for the research presented in this article.

In fact, as we have seen in Sect. 10.4.2, the full derivation delivers transfer functions that, in leading order of ϵ, go as $\mathcal{T}_{1,2,\ldots,7} \sim \epsilon^3$. This implies that the sensitivity for laser and acceleration noise free combinations behaves as $\sqrt{\widetilde{S}_{h,1,2,\ldots,7}/\mathcal{T}_{1,2,\ldots,7}} \sim \epsilon^{-2}$, which is similar to the behavior of acceleration noise. In other words, the combinations eliminating the acceleration noise also cancel a significant part of the GW signal at low frequencies.

In fact, we find that a standard LISA-like TDI-enabled detector of the same arm length and optical configuration as OGO could achieve a similar low-frequency sensitivity (at few to tens of Hz) with an acceleration noise requirement of only $\sim 10^{-12}\,\mathrm{m/s^2}\,\sqrt{\mathrm{Hz}}$. This assumes negligible spacecraft jitter and that no other noise sources (phase-meter noise, sideband noise, thermal noise) limit the sensitivity, which at this frequency band would behave differently than in the LISA band. In fact, the GOCE mission [26] has already demonstrated such acceleration noise levels at mHz frequencies [27], and therefore this seems a rather modest requirement at OGO frequencies. We therefore see that such a short-arm-length OGO would actually only be a more complicated alternative to other feasible mission designs.

In addition, it is hard to see from just the comparison with ground-based detectors in Fig. 10.3 how exactly the DFI method itself influences the final noise curve of OGO, and how much of its shape is instead determined by the geometrical and technical parameters of the mission concept (arm length, laser power, telescope size). Also, the secondary technological noise sources of a space mission in the comparatively high-frequency band of this exemplary OGO implementation are somewhat different from more well-studied missions like LISA and DECIGO.

Therefore, to disentangle these effects, we will now tentatively study a different version of OGO based on the alternative orbit with an average arm length of 2×10^9 m, as mentioned in Sect. 10.2. It requires further study to determine whether a stable octahedron constellation and the DFI scheme are possible on such an orbit, but assuming they are, we can compute its sensitivity as before.

In Fig. 10.4, we then compare this longer-baseline DFI detector with another detector with the same geometry and optical components, but without the DFI technique, using instead conventional TDI measurements. Here, we are in a similar frequency range as LISA and therefore assume similar values for the acceleration noise of 3×10^{-15} m/s^2 $\sqrt{\text{Hz}}$ [19] and secondary noise sources (phase meter, thermal noise, etc.; see Sect. 10.4.4).

However, there is another noise source, spacecraft jitter, which is considered subdominant for LISA, but might become relevant for both the TDI and DFI versions of the 2×10^9 m OGO-like detector. Jitter corresponds to the rotational degrees of freedom between spacecraft, and its coupling into measurement noise is not fully understood. We have therefore computed both sensitivities without any jitter. It seems

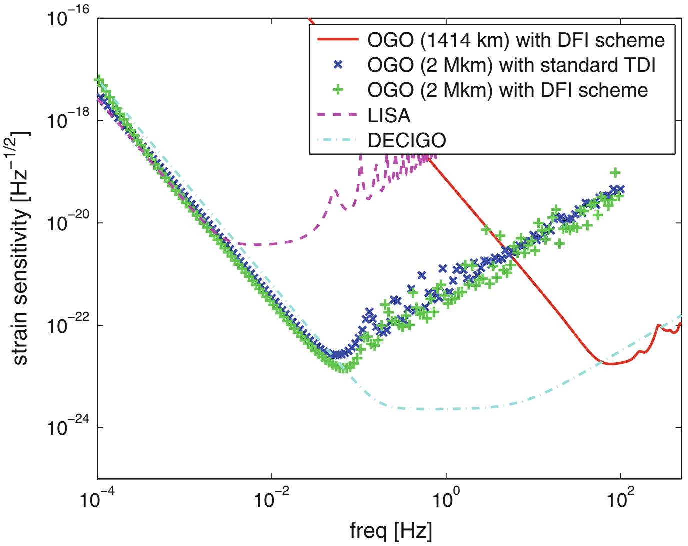

Fig. 10.4 Network sensitivities, scaled from S_5, of standard OGO (with DFI, arm length 1414 km, *red solid line*) compared to an OGO-like detector with spacecraft separation of 2×10^9 m, with either full DFI scheme (*blue crosses*) or standard TDI only (*green plus signs*). Also shown for comparison are (classic) LISA (5×10^9 m, network sensitivity, *magenta dashed line*, from Ref. [28]) and DECIGO (using the fitting formula Eq. (20) from Ref. [29], *cyan dash-dotted line*) (color figure online)

possible that at least the part of jitter that couples linearly into displacement noise could also be canceled by DFI, or that an extension of DFI (e.g. more links) could take better care of this, and therefore that the full OGO with DFI would look more favorable compared to the TDI version when nonvanishing jitter is taken into account.

Generally, as one goes for longer arm lengths, the DFI scheme will perform better in comparison to the TDI scheme. At the high-frequency end of the sensitivity curves, both schemes are limited by shot noise and the respective GW transfer functions. Since the shot-noise level does not depend on the arm length, it remains the same for all relevant frequencies. Therefore, as the arm length increases, the high-frequency part of the sensitivity curves moves to the low-frequency regime in parallel (i.e. the corner frequency of the transfer function is proportional to $1/L$). This is the same for both schemes.

On the other hand, in the low-frequency regime of the sensitivity curves the two schemes perform very differently. For TDI, the low-frequency behavior is limited by acceleration noise, while for DFI this part is again limited by shot noise and the GW transfer function. When the arm length increases, the low-frequency part of the sensitivity curve in the TDI scheme moves to lower frequencies in proportion to $1/\sqrt{L}$; while for DFI, it moves in proportion to $1/L$.

Graphically, when the arm length increases, the high-frequency parts of the sensitivity curves in both schemes move toward the lower-frequency regime in parallel, while the low-frequency part of the sensitivity curve for DFI moves faster than for TDI.

Under the assumptions given above, we find that an arm length of $2 \times 10^9\,\mathrm{m}$ is close to the transition point where the sensitivities of TDI and DFI are almost equal, as shown in Fig. 10.4. At even longer arm lengths, employing DFI would become clearly advantageous.

Of course, these considerations show that a longer-baseline detector with good sensitivity in the standard space-based detector frequency band of interest would make a scientifically much more interesting case than the default short-arm OGO which we presented first. However, as no study on the required orbits has been done so far, we consider such a detector variant to be highly hypothetical and not worthy of a detailed study of technological feasibility and scientific potential yet. Instead, for the remainder of this paper, we concentrate again on the conservative 1400 km version of OGO. Although the sensitivity curve in Fig. 10.3 already demonstrates its limited potential, we will attempt to neutrally assess its advantages, limitations and scientific reach.

10.4.4 Technological Feasibility

Employing DFI requires a large number of spacecraft but on the other hand allows us to relax many of the very strict technological requirements of other space-based GW detector proposals such as (e)LISA and DECIGO. Specifically, the clock noise is canceled by design, so there is no need for a complicated clock tone transfer chain [30].

Furthermore, OGO does not require a drag-free technology, and the configuration has to be stabilized only as much as required for the equal arm length assumption to hold. This strongly reduces the requirements on the spacecraft thrusters. Also, for the end mirrors, which have to be mounted on the same monolithic structure for all four laser links per spacecraft, it is not required that they are freefalling. Instead, they can be fixed to the spacecraft.

Still, to reach the shot-noise-only limited sensitivity shown in Fig. 10.3, the secondary noise contributions from all components of the measurement system must be significantly below the shot-noise level. Considering a shot-noise level of about $2 \times 10^{-17}\,\mathrm{m}/\sqrt{\mathrm{Hz}}$—which is in agreement with the value derived earlier for the 1400 km version of OGO—this might be challenging.

When actively controlling the spacecraft position and hence stabilizing the distance and relative velocity between the spacecraft, we will be able to lower the heterodyne frequency of the laser beat notes drastically. Where LISA will have a beat note frequency in the tens of MHz, with OGO's short arm length we could be speaking of kHz or less and might even consider a homodyne detection scheme as in LIGO. This might in the end enable us to build a phase meter capable of detecting relative distance fluctuations with a sensitivity of $10^{-17}\,\mathrm{m}/\sqrt{\mathrm{Hz}}$ or below as required by OGO.

As mentioned before, temperature noise might be a relevant noise source for OGO: The relative distance fluctuations on the optical benches due to temperature fluctuations and the test mass thermal noise must be significantly reduced in comparison to LISA. But even though the LISA constellation is set in an environment which is naturally more temperature stable, stabilization should be easier for the higher-frequency OGO measurement band. A requirement of $10^{-17}\,\mathrm{m}/\sqrt{\mathrm{Hz}}$ could be reached by actively stabilizing the temperature down to values of $1\,\mathrm{nK}/\sqrt{\mathrm{Hz}}$ at the corner frequency.

Assuming future technological progress, optimization of the optical bench layout could also contribute to mitigating this constraint, as could the invention of thermally more stable materials for the optical bench. Most likely, this challenge can be solved only with a combination of the mentioned approaches.

The same is true for the optical path length stability of the telescopes. We estimate the required pointing stability to be roughly similar to the LISA mission requirements.

10.4.5 Shot-Noise Reduction

Assuming the requirements from the previous section can be met, the timing and acceleration noise free combinations of the OGO detector are dominated by shot noise, and any means of reducing the shot noise will lead to a sensitivity improvement over all frequencies. In this subsection, we discuss possible ways to achieve such a reduction.

The most obvious solution is to increase laser power, with an achievable sensitivity improvement that scales with $\sqrt{P}$. However, the available laser power is limited by the power supplies available on a spacecraft. Stronger lasers are also heavier and take more place, making the launch of the mission more difficult. Therefore, there is a limit to simply increasing laser power, and we want to shortly discuss more advanced methods of shot-noise reduction.

One such hypothetical possibility is to build cavities along the links between spacecraft, similar to the DECIGO design [10]. The shot noise would be decreased due to an increase of the effective power stored in the cavity. Effectively, this also results in an increase of the arm length. Note, however, that the sensitivity of OGO with cavities cannot simply be computed by inserting effective power and arm length into our previously derived equations. Instead, a rederivation of the full transfer function along the lines of Ref. [31] is necessary.

Alternatively, squeezed light [32] is a way to directly reduce the quantum measurement noise, which has already been demonstrated in ground-based detectors [33, 34]. However, squeezing in a space-based detector is challenging in many aspects due to the very sensitive procedure and would require further development.

10.5 Scientific Perspectives

In this section, we will discuss the science case for our octahedral GW detector (with an arm length of 1400 km) by considering the most important potential astrophysical sources in its band of sensitivity. Using the full network sensitivity, as derived above, the best performance of OGO is at 78 Hz, between the best achieved performance of initial LIGO during its S6 science run and the anticipated sensitivity for advanced LIGO. OGO outperforms the advanced ground-based detectors below 10 Hz, where the seismic noise strongly dominates. In this analysis, we will therefore consider sources emitting GWs with frequencies between 1 Hz and 1 kHz, concentrating on the low end of this range.

Basically, those are the same sources as for ground-based detectors, which include compact binaries coalescences (CBCs), asymmetric single neutron stars (continuous waves, CWs), binaries containing intermediate-mass black holes (IMBHs), burst sources (unmodeled short-duration transient signals), and a cosmological stochastic background.

We will go briefly through each class of sources and consider perspectives of their detection. As was to be expected from the sensitivity curve in Fig. 10.3, in most categories OGO performs better than initial ground-based detectors, but does not even reach the potential of the advanced generation currently under commissioning.

Therefore, this section should be understood not as an endorsement of actually building and flying an OGO-like mission, but just as an assessment of its (limited, but existing) potentials. This demonstrates that an octahedral GW detector employing DFI in space is in principle capable of scientifically interesting observations, even though improving its performance to actually surpass existing detectors or more mature mission proposals still remains a subject of further study.

In addition, we put a special focus on areas where OGO's design offers some specific advantages. These include the triangulation of CBCs through joint detection with ground-based detectors as well as searching for a stochastic GW background and for additional GW modes.

Note that the hypothetical 2×10^9 m variant of OGO (see Sects. 10.2 and 10.4.3) would have a very different target population of astrophysical sources due to its sensitivity shift to lower frequencies. Such a detector would still be sensitive to CBCs, IMBHs, and stochastic backgrounds, probably much more so. But instead of high-frequency sources like CW pulsars and supernova bursts, it would start targeting supermassive black holes, investigating the merging history of galaxies over cosmological scales.

However, as this detector concept relies on an orbit hypothesis not studied in any detail, we do not consider it mature enough to warrant a study of potential detection rates in any detail, and we therefore only refer to established reviews of the astrophysical potential in the frequency band of LISA and DECIGO, e.g. Ref. [35].

10.5.1 Coalescing Compact Binaries

Heavy stars in binary systems will end up as compact objects (such as NSs or BHs) inspiralling around each other, losing orbital energy and angular momentum through gravitational radiation. Depending on the proximity of the source and the detector's sensitivity, we could detect GWs from such a system a few seconds up to a day before the merger and the formation of a single spinning object. These CBCs are expected to be the strongest sources of GWs in the frequency band of current GW detectors.

To estimate the event rates for various binary systems, we will follow the calculations outlined in Ref. [3]. To compare with predictions for initial and advanced LIGO (presented in Ref. [3]), we also use only the inspiral part of the coalescence to estimate the *horizon distance* (the maximum distance to which we can observe a given system with a given signal-to-noise ratio (SNR)). We use here the same detection threshold on signal-to-noise ratio, a SNR of $\rho = 8$, as in Ref. [3] and consider the same fiducial binary systems: NS-NS (with $1.4\,\mathrm{M}_\odot$ each), BH-NS (BH mass $10\,\mathrm{M}_\odot$, NS with $1.4\,\mathrm{M}_\odot$), and BH-BH ($10\,\mathrm{M}_\odot$ each).

For a binary of given masses, the sky-averaged horizon distance is given by

$$D_h = \frac{4\sqrt{5}\,G^{\frac{5}{6}}\,\mu^{\frac{1}{2}}\,M^{\frac{1}{3}}}{\sqrt{96}\,\pi^{\frac{2}{3}}\,c^{\frac{3}{2}}\,\rho}\sqrt{\int_{f_{\min}}^{f_{\mathrm{ISCO}}} \frac{f^{-\frac{7}{3}}}{\tilde{S}_{\mathrm{h}}(f)}\,\mathrm{d}f}. \tag{10.26}$$

Here, $M = M_1 + M_2$ is the total mass and $\mu = M_1 M_2 / M$ is the reduced mass of the system. We have used a lower cutoff of $f_{\min} = 1\,\mathrm{Hz}$, and at the upper end the frequency of the innermost stable circular orbit is $f_{\mathrm{ISCO}} = c^3/(6^{3/2}\pi\,G\,M)$ Hz, which conventionally is taken as the end of the inspiral.

Now, for any given type of binary (as characterized by the component masses), we obtain the observed event rate (per year) using $\dot{N} = R \cdot N_{\rm G}$, where we have adopted the approximation for the number of galaxies inside the visible volume from Eq. (5) of Ref. [3]:

$$N_{\rm G} = \frac{4}{3}\pi \left(\frac{D_{\rm h}}{\rm Mpc}\right)^3 (2.26)^{-3} \cdot 0.0116, \tag{10.27}$$

and the intrinsic coalescence rates R per Milky-Way-type galaxy are given in Table 2 of Ref. [3].

A single DFI combination S_i has annual rates similar to initial LIGO, and the results for the network sensitivity of full OGO are summarized in Table 10.1. For each binary, we give three numbers following the uncertainties in the intrinsic event rate (“pessimistic”, “realistic”, “optimistic”) as introduced in Ref. [3].

From this, we see that OGO achieves detection rates an order of magnitude better than initial LIGO. But we still expect to have only one event in about three years of observation assuming “realistic” intrinsic coalescence rates. The sensitivity of aLIGO is much better than for OGO above 10 Hz, and the absence of seismic noise does not help OGO much because the absolute sensitivities below 10 Hz are quite poor and only a very small fraction of SNR is contributed from the lower frequencies. This is the reason why OGO cannot compete directly with aLIGO in terms of total CBC detection rates, which are about two orders of magnitude lower.

However, OGO does present an interesting scientific opportunity when run in parallel with aLIGO. If OGO indeed detects a few events over its mission lifetime, as the realistic predictions allow, it can give a very large improvement to the sky localization of these sources. Parameter estimation by aLIGO alone typically cannot localize signals enough for efficient electromagnetic follow-up identification. However, in a joint detection by OGO and aLIGO, triangulation over the long baseline between space-based OGO and ground-based aLIGO would yield a fantastic angular resolution. As signals found by OGO are very likely to be picked up by aLIGO as well, such joint detections indeed seem promising. Additionally, the three-dimensional configuration and independent channels of OGO potentially allow a more accurate parameter estimation than a network of two or three simple L-shaped interferometers could achieve.

Table 10.1 Estimated yearly detection rates for CBC events, given in triplets of the form (lower limit, realistic value, upper limit) as defined in Ref. [3]

	NS-NS	NS-BH	BH-BH
OGO	(0.002, 0.2, 2.2)	(0.001, 0.06, 2.0)	(0.003, 0.1, 9)
LIGO	(2e-4, 0.02, 0.2)	(7e-5, 0.004, 0.1)	(2e-4, 0.007, 0.5)
aLIGO	(0.4, 40, 400)	(0.2, 10, 300)	(0.4, 20, 1000)

10.5.2 Stochastic Background

There are mainly two kinds of stochastic GW backgrounds [6, 7]: The first is the astrophysical background (sometimes also called astrophysical foreground), arising from unresolved astrophysical sources such as compact binaries [36] and core-collapse supernovae [37]. It provides important statistical information about distribution of the sources and their parameters. The second is the cosmological background which was generated by various mechanisms in the early Universe [38–40]. It carries unique information about the very beginning of the Universe ($\sim 10^{-28}$ s). Thus, the detection of the GW stochastic background is of great interest.

Currently, there are two ways to detect the stochastic GW background. One of them [41] takes advantage of the null stream (e.g. the Sagnac combination of LISA). By definition, the null stream is insensitive to gravitational radiation, while it suffers from the same noise sources as the normal data stream. A comparison of the energy contained in the null stream and the normal data stream allows us to determine whether the GW stochastic background is present or not. The other way of detection is by cross-correlation [6, 42] of measurements taken by different detectors. In our language, this uses the GW background signal measured by one channel as the template for the other channel. In this sense, the cross-correlation can be viewed as matched filtering. Both ways require redundancy, i.e. more than one channel observing the same GW signal with independent noise.

Luckily, the octahedron detector has plenty of redundancy, which potentially allows precise background detection. There are in total 12 dual-way laser links between spacecraft, forming 8 LISA-like triangular constellations. Any pair of two such LISA-like triangles that does not share common links can be used as an independent correlation. There are 16 such pairs within the octahedron detector. Within each pair, we can correlate the orthogonal TDI variables A, E and T (as they are denoted in LISA [14]). Altogether, there are $16 \times 3^2 = 144$ cross-correlations.

And we have yet more information encoded by the detector, which we can access by considering that any two connected links form a Michelson interferometer, thus providing a Michelson-TDI variable. Any two of these variables that do not share common links can be correlated. There are in total 36 such variables, forming 450 cross-correlations, from which we can construct the optimal total sensitivity.

Furthermore, each of these is sensitive to a different direction on the sky. So the octahedron detector has the potential to detect anisotropy of the stochastic background. However, describing an approach for the detection of anisotropy is beyond the scope of this feasibility study.

Instead, we will present here only an order of magnitude estimation of the total cross-correlation SNR. Usually, it can be expressed as

$$\mathrm{SNR} = \frac{3H_0^2}{10\pi^2}\sqrt{T_{\mathrm{obs}}}\left[2\sum_{k,l}\int_0^\infty \mathrm{d}f\,\frac{\gamma_{kl}^2(f)\,\Omega_{\mathrm{gw}}^2(f)}{f^6\widetilde{S}_{\mathrm{h},k}(f)\widetilde{S}_{\mathrm{h},l}(f)}\right]^{\frac{1}{2}}, \tag{10.28}$$

where $T_{\rm obs}$ is the observation time, $\Omega_{\rm gw}$ is the fractional energy-density of the Universe in a GW background, H_0 the *Hubble constant*, and $\widetilde{S}_{{\rm h},k}(f)$ is the effective sensitivity of the kth channel. $\gamma_{kl}(f)$ denotes the *overlap reduction function* between the kth and lth channels, introduced by Flanagan [43].

$$\gamma_{kl}(f) = \frac{5}{8\pi} \sum_{p=+,\times} \int {\rm d}\hat{\Omega}\, {\rm e}^{2\pi {\rm i} f \hat{\Omega}\cdot\Delta\mathbf{x}/c} F_k^p(\hat{\Omega}) F_l^p(\hat{\Omega}), \tag{10.29}$$

where $F_k^p(\hat{\Omega})$ is the antenna pattern function. As mentioned in the previous section, there might be 12 independent DFI solutions. These DFI solutions can form $12 \times 11/2 = 66$ cross-correlations. According to Ref. [6], we know $\gamma_{kl}^2(f)$ varies between 0 and 1. As a rough estimate, we approximate $\sum_{k,l} \gamma_{kl}^2(f) \sim 10$; hence, we get the following result for OGO:

$$\mathrm{SNR} = 2.57 \left(\frac{H_0}{72\, \frac{\rm km\, s^{-1}}{\rm Mpc}} \right)^2 \left(\frac{\Omega_{\rm gw}}{10^{-9}} \right) \left(\frac{T_{\rm obs}}{10\,{\rm yr}} \right)^{\frac{1}{2}}. \tag{10.30}$$

Initial LIGO has set an upper limit of 6.9×10^{-6} on $\Omega_{\rm gw}$ [44], and aLIGO will be able to detect the stochastic background at the 1×10^{-9} level [44]. Hence, our naive estimate of OGO's sensitivity to the GW stochastic background is similar to that of aLIGO. Actually, an optimal combination of all the previously-mentioned possible cross-correlations would potentially result in an even better detection ability for OGO.

10.5.3 Testing Alternative Theories of Gravity

In this section we will consider OGO's ability to test predictions of General Relativity against alternative theories. In particular, we will estimate the sensitivity of the proposed detector to all six polarization modes that could be present in (alternative) metric theories of gravitation [45]. We refer to Ref. [46] for a discussion on polarization states, and Refs. [47, 48] for reviews on alternative theories of gravity. The six possible polarizations are (i) two transverse-traceless (tensorial) polarizations usually denoted as $\mathbf{e}_+$ and $\mathbf{e}_\times$, (ii) two scalar modes called breathing (or common) $\mathbf{e}_b$ and longitudinal $\mathbf{e}_l$ and (iii) two vectorial modes $\mathbf{e}_x$ and $\mathbf{e}_y$, which are given explicitly in the following

$$\mathbf{e}_+ = \hat{u} \otimes \hat{u} - \hat{v} \otimes \hat{v}, \tag{10.31a}$$

$$\mathbf{e}_\times = \hat{u} \otimes \hat{v} + \hat{v} \otimes \hat{u}, \tag{10.31b}$$

$$\mathbf{e}_b = \hat{u} \otimes \hat{u} + \hat{v} \otimes \hat{v}, \tag{10.31c}$$

$$\mathbf{e}_l = \hat{k} \otimes \hat{k}, \tag{10.31d}$$

$$\mathbf{e}_x = \hat{u} \otimes \hat{k} + \hat{k} \otimes \hat{u}, \tag{10.31e}$$

$$\mathbf{e}_y = \hat{v} \otimes \hat{k} + \hat{k} \otimes \hat{v}. \tag{10.31f}$$

The corresponding antenna pattern functions for a single arm along (1, 0, 0) direction are given as follows

$$\xi_+ = \cos^2\theta\cos^2\phi - \sin^2\phi, \tag{10.32a}$$

$$\xi_\times = \cos\theta\sin 2\phi, \tag{10.32b}$$

$$\xi_b = \cos^2\theta\cos^2\phi + \sin^2\phi, \tag{10.32c}$$

$$\xi_l = \sin^2\theta\cos^2\phi, \tag{10.32d}$$

$$\xi_x = -\sin 2\theta\cos^2\phi, \tag{10.32e}$$

$$\xi_y = -\sin\theta\sin 2\phi, \tag{10.32f}$$

which are plotted in Fig. 10.5.

As a comparison, the antenna pattern functions for a Michelson interferometer with two arms along (1, 0, 0) and (0, 1, 0) directions are given as follows

$$\xi_+ = (\cos^2\theta + 1)\cos 2\phi, \tag{10.33a}$$

$$\xi_\times = 2\cos\theta\sin 2\phi, \tag{10.33b}$$

$$\xi_b = -\sin^2\theta\cos 2\phi, \tag{10.33c}$$

$$\xi_l = \sin^2\theta\cos 2\phi, \tag{10.33d}$$

$$\xi_x = -\sin 2\theta\cos 2\phi, \tag{10.33e}$$

$$\xi_y = -2\sin\theta\sin 2\phi, \tag{10.33f}$$

which are plotted in Fig. 10.6.

We have followed the procedure for computing the sensitivity of OGO, as outlined above, for the four modes not present in General Relativity, and we compare those sensitivities to the results for the +, × modes as presented in Fig. 10.3. The generalization of the transfer function used in this paper (Eq. 10.24) for other polarization modes is given in Ref. [49].

We have found that all seven generators show similar sensitivity for each mode. OGO is not sensitive to the common (breathing) mode, which is not surprising as it can be attributed to a common displacement noise, which we have removed by our procedure. The sensitivity to the second (longitudinal) scalar mode scales as ϵ^{-4} at low frequencies and is much worse than the sensitivity to the +, × polarizations below 200 Hz. However, OGO is more sensitive to the longitudinal mode (by about an order of magnitude) above 500 Hz. The sensitivity of OGO to vectorial modes is overall similar to the +, × modes: it is by factor few less sensitive to vectorial modes below 200 Hz and by similar factors more sensitive above 300 Hz. These sensitivities are shown in Fig. 10.7.

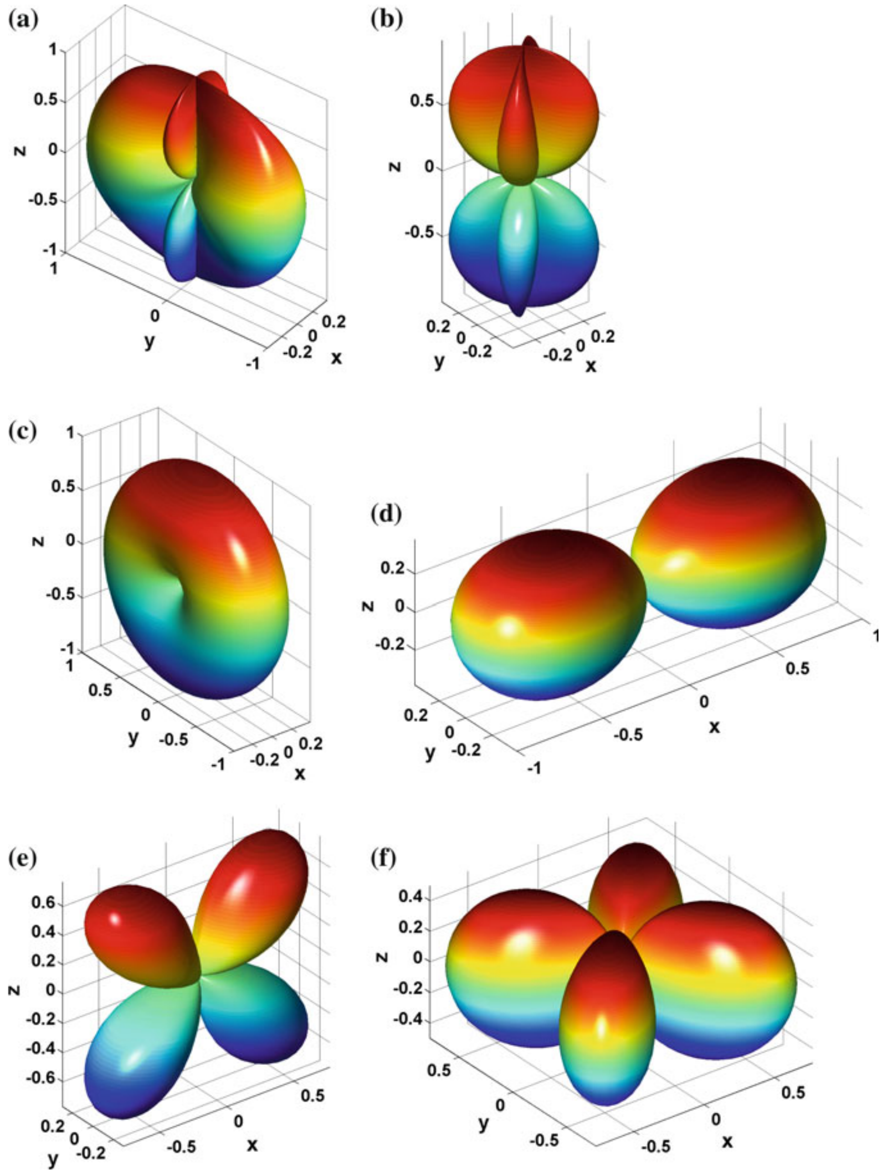

Fig. 10.5 Antenna pattern functions for a single arm along (1, 0, 0) direction. **a** + mode. **b** × mode. **c** Breathing mode. **d** Longitudinal mode. **e** Vector-x mode. **f** Vector-y mode

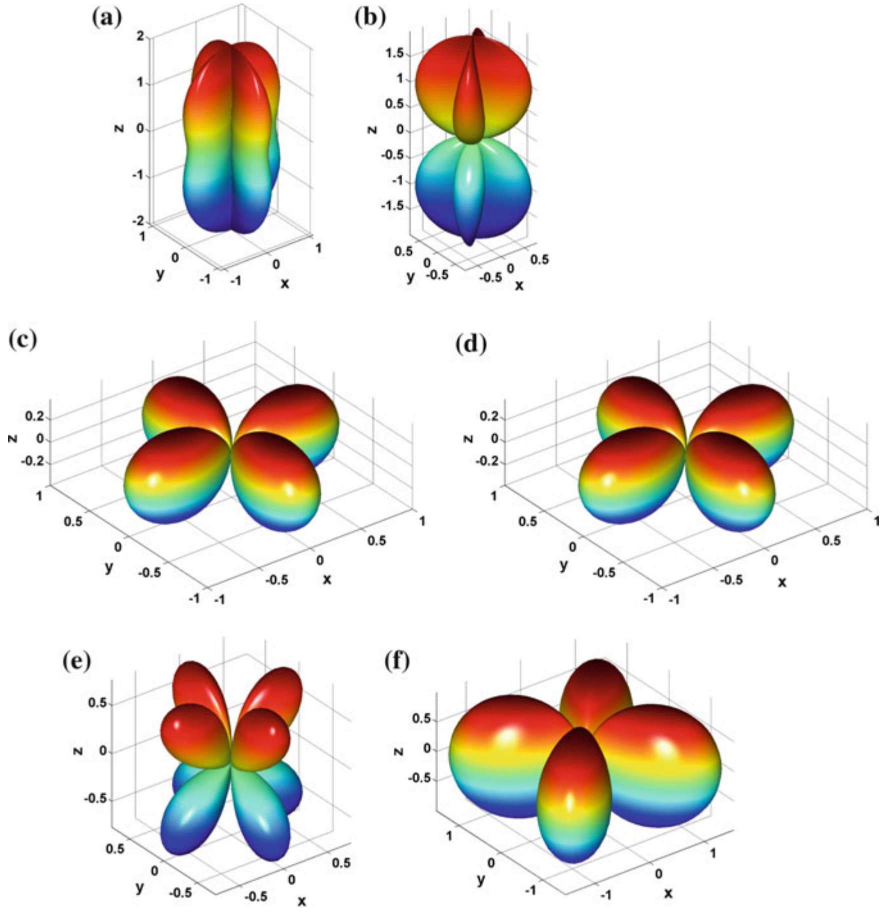

Fig. 10.6 Antenna pattern functions for a Michelson interferometer. **a** + mode. **b** × mode. **c** Breathing mode. **d** Longitudinal mode. **e** Vector-x mode. **f** Vector-y mode

10.5.4 Pulsars—Continuous Waves

CWs are expected from spinning neutron stars with nonaxisymmetric deformations. Spinning NSs are already observed as radio and gamma-ray pulsars. Since CW emission is powered by the spindown of the pulsar, the strongest emitters are the pulsars with high spindowns, which usually are young pulsars at rather high frequencies. Note that the standard emission model [50] predicts a gravitational wave frequency $f_{\mathrm{gw}} = 2f$, while alternative models like free precession [51] and r-modes [52] also allow emission at $f_{\mathrm{gw}} = f$ and $f_{\mathrm{gw}} = \frac{4}{3}f$, where f is the NS spin frequency.

OGO has better sensitivity than initial LIGO below 133 Hz, has its best sensitivity around 78 Hz, and is better than aLIGO below 9 Hz. This actually fits well with

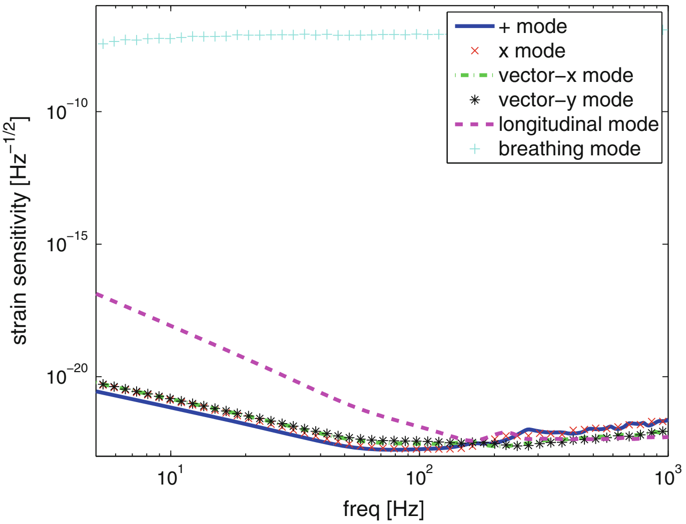

Fig. 10.7 Relative sensitivity of the full OGO network (scaled from S5 combination) to alternative polarizations: + mode (*blue solid line*), x mode (*red crosses*), vector-x mode (*green dash-dotted line*), vector-y mode (*black stars*), longitudinal mode (*magenta dashed line*), and breathing mode (*cyan plus signs*) (color figure online)

the current radio census of the galactic pulsar population, as given by the ATNF catalog [53]. As shown in Fig. 10.8, the bulk of the population is below ∼10 Hz, and also contains many low-frequency pulsars with decent spindown values, even including a few down to ∼0.1 Hz.

We estimate the abilities of OGO to detect CW emission from known pulsars following the procedure outlined in Ref. [54] for analysis of the Vela pulsar. The GW strain for a source at distance D is given as

$$h_0 = \frac{4\pi^2 G I_{zz} \epsilon f^2}{c^4 D}, \tag{10.34}$$

where ϵ is the ellipticity of the neutron star and we assume a canonical momentum of inertia $I_{zz} = 10^{38}\,\mathrm{kg\,m^2}$. After an observation time T_{obs}, we could detect a strain amplitude

$$h_0 = \Theta\sqrt{\frac{S_{\mathrm{h}}}{T_{\mathrm{obs}}}}. \tag{10.35}$$

The statistical factor is $\Theta \approx 11.4$ for a fully coherent targeted search with the canonical values of 1 and 10 % for false alarm and false dismissal probabilities, respectively [55]. We find that, for the Vela pulsar (at a distance of 290 pc and a frequency of $f_{\mathrm{Vela,gw}} = 2 \cdot 11.19\,\mathrm{Hz}$), with $T_{\mathrm{obs}} = 30$ days of observation, we could probe ellipticities as low as $\epsilon \sim 5 \times 10^{-4}$ with the network OGO configuration. Sev-

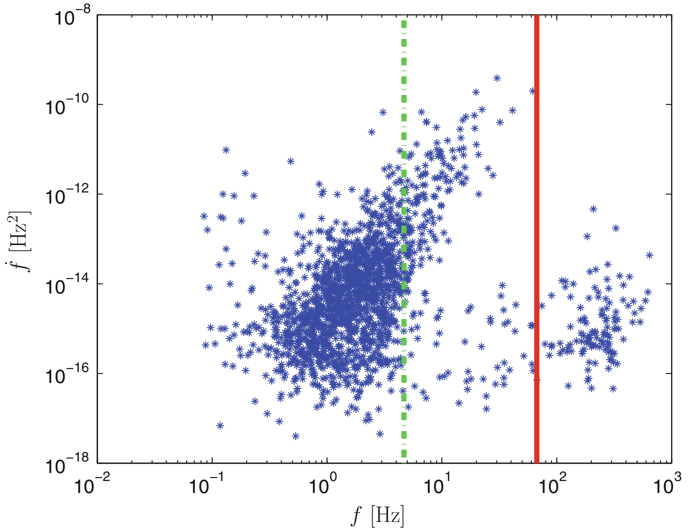

Fig. 10.8 Population of currently known pulsars in the frequency-spindown plain (f-$\dot{f}$). OGO could beat initial LIGO *left* of the *red solid line* and Advanced LIGO *left* of the *green dashed line*. Data for this plot were taken from Ref. [53] on March 2, 2012. [Image by D. Keitel] (color figure online)

eral known low-frequency pulsars outside the aLIGO band would also be promising objectives for OGO targeted searches.

All-sky searches for unknown pulsars with OGO would focus on the low-frequency range not accessible to aLIGO with a search setup comparable to current Einstein@Home LIGO searches [56]. As seen above, the sensitivity estimate factors into a search setup related part $\Theta/\sqrt{T_{\mathrm{obs}}}$ and the sensitivity $\sqrt{S_{\mathrm{h}}}$. Therefore, scaling a search with parameters identical to the Einstein@Home S5 runs to OGO's best sensitivity at 76 Hz would reach a sensitivity of $h_0 \approx 3 \times 10^{-25}$. This would, for example, correspond to a neutron star ellipticity of $\epsilon \sim 4.9 \times 10^{-5}$ at a distance of 1 kpc. Since the computational cost of such searches scales with f^2, low-frequency searches are actually much more efficient and would allow very deep searches of the OGO data, further increasing the competitiveness. Note, however, that for low-frequency pulsars the ellipticities required to achieve detectable GW signals can be very high, possibly mostly in the unphysical regime. On the other hand, for "transient CW"-type signals [57], low-frequency pulsars might be the strongest emitters, even with realistic ellipticities.

10.5.5 Other Sources

Many (indirect) observational evidences exist for stellar mass BHs, which are the end stages of heavy star evolution, as well as for supermassive BHs, the result of accretion and galactic mergers throughout the cosmic evolution, in galactic nuclei. On the other hand, there is no convincing evidence so far for a BH of an intermediate mass in the range of 10^2–$10^4\,M_\odot$. These IMBHs might, however, still exist in dense stellar clusters [58, 59]. Moreover, stellar clusters could be formed as large, gravitationally bound groups, and collision of two clusters would produce inspiralling binaries of IMBHs [60, 61].

The ISCO frequency of the second orbital harmonic for a $300\,M_\odot$-$300\,M_\odot$ system is about 7 Hz, which is outside the sensitivity range of aLIGO. Still, those sources could show up through the higher harmonics (the systems are expected to have non-negligible eccentricity) and through the merger and ring-down gravitational radiation [62–64]. The ground-based LIGO and VIRGO detectors have already carried out a first search for IMBH signals in the $100\,M_\odot$ to $450\,M_\odot$ mass range [65].

With its better low-frequency sensitivity, OGO can be expected to detect a GW signal from the inspiral of a $300\,M_\odot$–$300\,M_\odot$ system in a quasicircular orbit up to a distance of approximately 245 Mpc, again using Eq. (10.26). This gives the potential for discovery of such systems and for estimating their physical parameters.

As for other advanced detectors, unmodeled searches (as opposed to the matched-filter CBC and CW searches; see Ref. [66] for a LIGO example) of OGO data have the potential for detecting many other types of gravitational wave sources, including, but not limited to, supernovae and cosmic string cusps. However, as in the case for IMBHs, the quantitative predictions are hard to produce due to uncertainties in the models.

10.6 Summary and Outlook

In this paper, we have presented for the first time a three-dimensional gravitational wave detector in space, called the Octahedral Gravitational wave Observatory (OGO). The detector concept employs displacement-noise free interferometry (DFI), which is able to cancel some of the dominant noise sources of conventional GW detectors. Adopting the octahedron shape introduced in Ref. [11], we put spacecraft in each corner of the octahedron. We considered a LISA-like receiver-transponder configuration and found multiple combinations of measurement channels, which allow us to cancel both laser frequency and acceleration noise. This new three-dimensional result generalizes the Mach–Zehnder interferometer considered in Ref. [11].

We have identified a possible halolike orbit around the Lagrange point L1 in the Sun-Earth system that would allow the octahedron constellation to be stable enough. However, this orbit limits the detector to an arm length of $\approx$1400 km.

Much better sensitivity and a richer astrophysical potential are expected for longer arm lengths. Therefore, we also looked for alternative orbits and found a possible alternative allowing for $\approx 2 \times 10^9$ m arms, but is not clear yet if this would be stable enough. Future studies are required to relax the equal-arm-length assumption of our DFI solutions, or to determine a stable, long-arm-length constellation.

Next, we have computed the sensitivity of OGO-like detectors—and have shown that the noise-cancelling combinations also cancel a large fraction of the GW signal at low frequencies. The sensitivity curve therefore has a characteristic slope of f^{-2} at the low-frequency end.

However, the beauty of this detector is that it is limited by a single noise source at all frequencies: shot noise. Thus, any reduction of shot noise alone would improve the overall sensitivity. This could, in principle, be achieved with DECIGO-like cavities, squeezing or other advanced technologies. Also, OGO does not require drag-free technology and has moderate requirements on other components so that it could be realized with technology already developed for LISA Pathfinder and eLISA.

When comparing a DFI-enabled OGO with a detector of similar design, but with standard TDI, we find that at $\approx$1400 km, the same sensitivity could be reached by a TDI detector with very modest acceleration noise requirements.

However, at longer arm lengths DFI becomes more advantageous, reaching the same sensitivity as TDI under LISA requirements but without drag-free technology and clock transfer, at $\approx 2 \times 10^9$ m. Such a DFI detector would have its best frequency range between LISA and DECIGO, with peak sensitivity better than LISA and approaching DECIGO without the latter mission concept's tight acceleration noise requirements and with no need for cavities.

Finally, we have assessed the scientific potentials of OGO, concentrating on the less promising, but more mature short-arm-length version. We estimated the event rates for coalescing binaries, finding that OGO is better than initial LIGO, but does not reach the level of advanced LIGO. Any binary detected with both OGO and aLIGO could be localized in the sky with very high accuracy.

Also, the three-dimensional satellite constellation and number of independent links makes OGO an interesting mission for detection of the stochastic GW background or hypothetical additional GW polarizations. Further astrophysically interesting sources such as low-frequency pulsars and IMBH binaries also lie within the sensitive band of OGO, but again the sensitivity does not reach that of aLIGO.

However, we point out that the improvement in the low-frequency sensitivity with increasing arm length happens faster for DFI as compared to the standard TDI. Therefore, searching for stable three-dimensional (octahedron) long-baseline orbits could lead to an astrophysically much more interesting mission.

Regarding possible improvements of the presented setup, there are several possibilities to extend and improve the first-order DFI scheme presented here. One more spacecraft could be added in the middle, increasing the number of usable links. Breaking the symmetry of the octahedron could modify the steep response function at low frequencies. This should be an interesting topic for future investigations.

In principle, the low-frequency behavior of OGO-like detectors could also be improved by more advanced DFI techniques such as introducing artificial time delays [67, 68]. This would result in a three-part power law less steep than the shape derived in Sect. 10.4.2. On the other hand, this would also introduce a new source of time delay noise. Therefore, such a modification requires careful investigation.

10.7 Supplementary A: Details on Calculating the Displacement and Laser Noise Free Combinations

Here we will give details on building the displacement (acceleration) and laser noise free configurations. The derivations closely follow the method outlined in [14]. We want to find the generators solving Eq. (10.7), so called reduced generators because they correspond to the reduced set $(q_{BC}, q_{CE}, q_{DB}, q_{DC}, q_{DF}, q_{EF})$. We start with building the ideal Z:

$$Z = \begin{cases} f_1 = (\mathcal{D}-1)^2 \\ f_2 = (\mathcal{D}-1)\mathcal{D} \\ f_3 = (1-\mathcal{D})(\mathcal{D}-1) \\ f_4 = (\mathcal{D}-1)((1-\mathcal{D})\mathcal{D}-1) \\ f_5 = \mathcal{D}-1 \\ f_6 = \mathcal{D}-1 \end{cases} . \tag{10.36}$$

The corresponding Gröbner basis to this ideal is:

$$\mathcal{G} = \{g_1 = \mathcal{D}-1\}. \tag{10.37}$$

The connection between f_i and g_j is defined by two transformation matrices

$$d = \begin{pmatrix} \mathcal{D}-1 \\ \mathcal{D} \\ 1-\mathcal{D} \\ (1-\mathcal{D})\mathcal{D}-1 \\ 1 \\ 1 \end{pmatrix} \tag{10.38}$$

and c with (at least) two possible solutions

$$c^{(1)} = (0\ 0\ 0\ 0\ 1\ 0) \text{ or } c^{(2)} = (0\ 0\ 0\ 0\ 0\ 1)\,. \tag{10.39}$$

The resulting basis is not unique and not necessarily independent. The first 6 reduced generators are given by the row vectors of the matrix $A^{(1)} = a_i^{(1)} = I - d \times c^{(1)}$:

$$a_1^{(1)} = \{1, 0, 0, 0, 0, 1-\mathcal{D}\}\,, \tag{10.40a}$$

$$a_2^{(1)} = \{0, 1, 0, 0, 0, -\mathcal{D}\}\,, \tag{10.40b}$$

$$a_3^{(1)} = \{0, 0, 1, 0, 0, (\mathcal{D}-1)\mathcal{D}\}\,, \tag{10.40c}$$

$$a_4^{(1)} = \{0, 0, 0, 1, 0, 1+(\mathcal{D}-1)\mathcal{D}\}\,, \tag{10.40d}$$

$$a_5^{(1)} = \{0, 0, 0, 0, 1, -1\}\,, \tag{10.40e}$$

$$a_6^{(1)} = \{0, 0, 0, 0, 0, 0\}\,. \tag{10.40f}$$

These reduced generators correspond directly to values for $(q_{BC}, q_{CE}, q_{DB}, q_{DC}, q_{DF}, q_{EF})$. As the Gröbner basis contains only one element, we cannot form other generator from S-polynomial.

We can form 6 other generators using $c^{(2)}$ instead of $c^{(1)}$. After applying those generators we have the following acceleration-free combinations:

$$\begin{aligned} a_1^{(1)}s^n &= 2(p_B - p_C + p_E - p_F + \mathcal{D}(-p_A + p_B - p_D + p_E \\ &\quad + (p_B - p_C + p_E - p_F)q_{BA})), \end{aligned} \tag{10.41a}$$

$$\begin{aligned} a_2^{(1)}s^n &= -2\mathcal{D}(p_A + p_D + p_C(-1 + q_{BA}) + p_F(-1 + q_{BA}) \\ &\quad - (p_B + p_E)q_{BA}), \end{aligned} \tag{10.41b}$$

$$\begin{aligned} a_3^{(1)}s^n &= 2\mathcal{D}((1 + \mathcal{D})p_A + p_D - p_E - \mathcal{D}(p_C - p_D + p_F) \\ &\quad + p_B(-1 + q_{BA}) - (p_C - p_E + p_F)q_{BA}), \end{aligned} \tag{10.41c}$$

$$\begin{aligned} a_4^{(1)}s^n &= 2(p_B - p_C + p_E + \mathcal{D}^2(p_A - p_C + p_D - p_F) \\ &\quad - p_F + \mathcal{D}(p_B - p_C + p_E - p_F)q_{BA}), \end{aligned} \tag{10.41d}$$

$$\begin{aligned} a_5^{(1)}s^n &= 2\mathcal{D}(p_A + p_D + p_B(-1 + q_{BA}) + p_E(-1 + q_{BA}) \\ &\quad - (p_C + p_F)q_{BA}), \end{aligned} \tag{10.41e}$$

$$a_6^{(1)}s^n = 2\mathcal{D}(p_B - p_C + p_E - p_F)q_{BA}, \tag{10.41f}$$

where s^n_{IJ} are given by Eq. (10.4). Note that we have a free (polynomial) function of delay q_{BA} which we can choose arbitrary. We will omit subscripts BA and use $q \equiv q_{BA}$. The arbitrariness of this function implies that terms which contain q and terms free of q are two independent sets of generators. We will keep q until we obtain laser noise free combinations, and then split each generator in two. After some analysis only two out of six acceleration free generators are independent, so we can rewrite them as

$$s_1 = y_{12} + \mathcal{D}(y_{13} + qy_{12}), \tag{10.42a}$$

$$s_3 = -y_{13} + \mathcal{D}(y_{12} - y_{13}) + qy_{12}, \tag{10.42b}$$

$$s_4 = y_{12} + \mathcal{D}qy_{12} + \mathcal{D}^2(y_{12} - y_{13}), \tag{10.42c}$$

$$s_2 + s_5 = y_{12} - 2y_{13}, \tag{10.42d}$$

$$s_2 - s_5 = (2q - 1)y_{12}, \tag{10.42e}$$

$$s_6 = qy_{12}, \tag{10.42f}$$

where

$$\begin{aligned} s_1 &= \frac{a_1^{(1)}s^n}{2}, s_2 = -\frac{\mathcal{D}^{-1}(a_2^{(1)}s^n)}{2}, s_3 = \frac{\mathcal{D}^{-1}(a_3^{(1)}s^n)}{2} \\ s_4 &= \frac{a_4^{(1)}s^n}{2}, s_5 = \frac{\mathcal{D}^{-1}(a_5^{(1)}s^n)}{2}, s_6 = \frac{\mathcal{D}^{-1}(a_6^{(1)}s^n)}{2} \end{aligned} \tag{10.43}$$

and

$$y_{12} = p_B + p_E - p_C - p_F, \; y_{13} = p_B + p_E - p_A - p_D \,. \tag{10.44}$$

We have introduced the inverse delay operator, $\mathcal{D}^{-1}$, for mathematical convenience, which obeys $\mathcal{D}\mathcal{D}^{-1} = I$. One can easily get rid of it by applying the delay operator on both sides. The final result will not contain the operator $\mathcal{D}^{-1}$. Next we use Eqs. (10.42d) and (10.42e) to express y_{12}, y_{13} and eliminate them from the other equations. The resulting combinations that eliminate both acceleration and laser noise are

$$(1-2q)s_1 + (-1-2\mathcal{D}q)s_2 + (1+\mathcal{D})s_5 \tag{10.45a}$$

$$(1-2q)s_3 + \mathcal{D}(q-1)s_2 + (-1+2q+q\mathcal{D})s_5 \tag{10.45b}$$

$$(1-2q)s_4 - (1+\mathcal{D}q)(s_2-s_5) - \mathcal{D}^2((1-q)s_2 - qs_5) \tag{10.45c}$$

$$(1-2q)s_6 - q(s_2-s_5). \tag{10.45d}$$

Out of these solutions we obtain seven independent generators which we have rewritten in the final form similar to the Y-equations from Sect. 10.3. They are explicitly given by Eqs. (10.8a)–(10.8g).

References

1. G.M. Harry, LIGO Scientific Collaboration, Advanced LIGO: the next generation of gravitational wave detectors. Class. Quantum Gravity **27**, 084006 (2010)
2. The Virgo Collaboration, Advanced Virgo baseline design, VIRC027AC09 (2009). https://tds.ego-gw.it/itf/tds/file.php?callFile=VIR-0027A-09.pdf
3. J. Abadie et al., [LIGO Scientific and Virgo Collaborations], Predictions for the rates of compact binary coalescences observable by ground-based gravitational-wave detectors. Class. Quantum Gravity **27**, 173001 (2010). arXiv:1003.2480
4. C.L. Fryer, K.C.B. New, Gravitational waves from gravitational collapse. Living Rev. Relat. **14**, 1 (2011). http://www.livingreviews.org/lrr-2011-1
5. B. Owen, Probing neutron stars with gravitational waves, LIGO-T0900053 (2009). arXiv:0903.2603
6. B. Allen, J.D. Romano, Detecting a stochastic background of gravitational radiation: sensitivities. Phys. Rev. D **59**, 102001 (1999). arXiv:gr-qc/9710117
7. M. Maggiore, Gravitational wave experiments and early universe cosmology. Phys. Rep. **331**, 283 (2000). arXiv:gr-qc/9909001
8. K. Danzmann, The LISA Study Team, LISA - an ESA cornerstone mission for the detection and observation of gravitational waves. Adv. Space Res. **32**, 12331242 (2003)
9. P. Amaro-Seoane et al., eLISA: astrophysics and cosmology in the millihertz regime. GW Notes **6**, 4–110 (2013). arXiv:1201.3621
10. M. Ando et al., DECIGO and DECIGO pathfinder. Class. Quantum Gravity **27**, 084010 (2010)
11. Y. Chen et al., Interferometers for displacement-noise-free gravitational-wave detection. Phys. Rev. Lett. **97**, 151103 (2006). arXiv:gr-qc/0603054
12. S. Kawamura, Y. Chen, Displacement-noise-free gravitational-wave detection. Phys. Rev. Lett. **93**, 211103 (2004). arXiv:gr-qc/0405093
13. Y. Chen, S. Kawamura, Displacement- and timing-noise free gravitational-wave detection. Phys. Rev. Lett. **96**, 231102 (2006). arXiv:gr-qc/0504108

14. M. Tinto, S.V. Dhurandhar, Time-delay interferometry. Living Rev. Relat. **8**, 4 (2005). arXiv:gr-qc/0409034, http://www.livingreviews.org/lrr-2005-4
15. M. Otto, G. Heinzel, K. Danzmann, TDI and clock noise removal for the split interferometry configuration of LISA. Class. Quantum Gravity **29**, 205003 (2012)
16. G. Gomez, A. Jorba, J. Masdemont, C. Simo, Study of the transfer from the Earth to a halo orbit around the equilibrium point L1. Celest. Mech. Dyn. Astron. **56**(4), 541–562 (1993)
17. K.C. Howell, B.T. Barden, Trajectory design and stationkeeping for multiple spacecraft in formation near the Sun-Earth L1 point, in *Proceedings of the 50th International Astronautical Federation Congress*, IAF/IAA Paper 99-A707 (1999)
18. NGO science working team, NGO assessment study report (Yellow book) ESA/SRE(2011)19
19. LISA International Science Team 2011, LISA assessment study report (Yellow Book) (European Space Agency) ESA/SRE(2011) 3. http://sci.esa.int/science-e/www/object/index.cfm?fobjectid=48364
20. D. Folta, Formation flying design and applications in weak stability boundary regions. Ann. N. Y. Acad. Sci. **1017**, 95–111 (2004)
21. B. Buchberger, Ein algorithmisches Kriterium für die Lösbarkeit eines algebraischen Gleichungssystems. Aequationes mathematicae **4**, 374–383 (1970)
22. M. Maggiore, Theory and experiments, *Gravitational Waves*, vol. 1 (Oxford University Press, Oxford, 2008)
23. F.B. Estabrook, H.D. Wahlquist, Response of Doppler spacecraft tracking to gravitational radiation. Gen. Relat. Gravity **6**, 439 (1975)
24. J. Abadie et al., [LIGO and Virgo Collaborations], Sensitivity to gravitational waves from compact binary coalescences achieved during LIGO's fifth and Virgo's first science run, LIGO-T0900499-v19 (2010). arXiv:1003.2481
25. D. Shoemaker et al., Advanced LIGO anticipated sensitivity curves, LIGO-T0900288-v3 (2010). https://dcc.ligo.org/LIGO-T0900288-v3/public
26. M.R. Drinkwater et al., GOCE: ESA's first earth explorer core mission. Space Sci. Rev. **108**(1), 419–432 (2003)
27. G. Sechi et al., In-flight results from the drag-free and attitude control of GOCE satellite, in *Preprints of the 18th IFAC World Congress*, Milano, pp. 733–740 (2011)
28. S.L. Larson, W.A. Hiscock, R.W. Hellings, Sensitivity curves for spaceborne gravitational wave interferometers. Phys. Rev. D **62**, 062001 (2000). arXiv:gr-qc/9909080
29. K. Yagi, Scientific potential of DECIGO pathfinder and testing GR with space-borne gravitational wave interferometers. Int. J. Mod. Phys. D **22**, 1341013 (2013). arXiv:1302.2388
30. S. Barke et al., EOM sideband phase characteristics for the spaceborne gravitational wave detector LISA. Appl. Phys. B **98**(1), 33–39 (2010)
31. M. Rakhmanov, Response of LIGO to gravitational waves at high frequencies and in the vicinity of the FSR (37.5 kHz), LIGO-T060237-00-D (2005). https://dcc.ligo.org/T060237-x0/public
32. R. Schnabel, N. Mavalvala, D.E. McClell, P.K. Lam, Quantum metrology for gravitational wave astronomy. Nat. Commun. **1**, 121 (2010)
33. Nat. Phys. A gravitational wave observatory operating beyond the quantum shot-noise limit: squeezed light in application. **7**, 962 (2011). arXiv:1109.2295
34. A. Khalaidovski, H. Vahlbruch, N. Lastzka, C. Graf, H. Luck, K. Danzmann, H. Grote, R. Schnabel, Status of the GEO 600 squeezed-light laser. J. Phys. Conf. Ser. **363**, 012013 (2012). arXiv:1112.0198
35. B.S. Sathyaprakash, B.F. Schutz, Physics, astrophysics and cosmology with gravitational waves. Living Rev. Relat. **12**, 2 (2009). arXiv:0903.0338, http://www.livingreviews.org/lrr-2009-2
36. A.J. Farmer, E.S. Phinney, The gravitational wave background from cosmological compact binaries. Mon. Not. R. Astron. Soc. **346**, 1197 (2003). arXiv:astro-ph/0304393
37. V. Ferrari, S. Matarrese, R. Schneider, Mon. Not. R. Astron. Soc. **303**, 247 (1999). arXiv:astro-ph/9804259
38. R. Brustein, M. Gasperini, M. Giovannini, G. Veneziano, Relic gravitational waves from string cosmology. Phys. Lett. B **361**, 45 (1995). arXiv:hep-th/9507017

39. M.S. Turner, Detectability of inflation produced gravitational waves. Phys. Rev. D **55**, 435 (1997). arXiv:astro-ph/9607066
40. K.N. Ananda, C.Clarkson, D. Wands, The cosmological gravitational wave background from primordial density perturbations. Phys. Rev. D **75**, 123518 (2007). arXiv:gr-qc/0612013
41. C.J. Hogan, P.L. Bender, Estimating stochastic gravitational wave backgrounds with Sagnac calibration. Phys. Rev. D **64**, 062002 (2001). arXiv:astro-ph/0104266
42. N. Seto, Correlation analysis of stochastic gravitational wave background around 0.1-1 Hz. Phys. Rev. D **73**, 063001 (2006). arXiv:gr-qc/0510067
43. E.E. Flanagan, The Sensitivity of the laser interferometer gravitational wave observatory (LIGO) to a stochastic background, and its dependence on the detector orientations. Phys. Rev. D **48**, 2389 (1993). arXiv:astro-ph/9305029
44. B.P. Abbott et al., LIGO Scientific and VIRGO Collaborations, An upper limit on the stochastic gravitational-wave background of cosmological origin, Nature **460**, 990 (2009). arXiv:0910.5772
45. M. Hohmann, Propagation of gravitational waves in multimetric gravity. Phys. Rev. D **85**, 084024 (2012). arXiv:1105.2555
46. D.M. Eardley, D.L. Lee, A.P. Lightman, Gravitational-wave observations as a tool for testing relativistic gravity. Phys. Rev. D **8**, 3308 (1973)
47. C.M. Will, The confrontation between general relativity and experiment. Living Rev. Relat. **9**, 3 (2006). arXiv:gr-qc/0510072, http://www.livingreviews.org/lrr-2009-2
48. J.R. Gair, M. Vallisneri, S.L. Larson, J.G. Baker, Testing general relativity with low-frequency, space-based gravitational-wave detectors. Living Rev. Relat. **16**, 7 (2013). arXiv:1212.5575, http://www.livingreviews.org/lrr-2013-7
49. S.J. Chamberlin, X. Siemens, Stochastic backgrounds in alternative theories of gravity: overlap reduction functions for pulsar timing arrays. Phys. Rev. D **85**, 082001 (2012). arXiv:1111.5661
50. P. Jaranowski, A. Krolak, B.F. Schutz, Data analysis of gravitational - wave signals from spinning neutron stars. 1. The signal and its detection. Phys. Rev. D **58**, 063001 (1998). arXiv:gr-qc/9804014
51. D.I. Jones, N. Andersson, Gravitational waves from freely precessing neutron stars. Mon. Not. R. Astron. Soc. **331**, 203 (2002). arXiv:gr-qc/0106094
52. N. Andersson, K.D. Kokkotas, N. Stergioulas, On the relevance of the r mode instability for accreting neutron stars and white dwarfs. Astrophys. J. **516**, 307 (1999). arXiv:astro-ph/9806089
53. R.N. Manchester, G.B. Hobbs, A. Teoh, M. Hobbs, The Australia Telescope National Facility pulsar catalogue. Astron. J. **129**, 1993 (2005). arXiv:astro-ph/0412641
54. J. Abadie et al., [LIGO Scientific and Virgo Collaborations], Beating the spin-down limit on gravitational wave emission from the Vela pulsar. Astrophys. J. **737**, 93 (2011). arXiv:1104.2712
55. B. Abbott et al., [LIGO Scientific Collaboration], Setting upper limits on the strength of periodic gravitational waves using the first science data from the GEO 600 and LIGO detectors. Phys. Rev. D **69**, 082004 (2004). arXiv:gr-qc/0308050
56. J. Aasi et al., [The LIGO Scientific and the Virgo Collaboration], Einstein@Home all-sky search for periodic gravitational waves in LIGO S5 data. Phys. Rev. D **87**, 042001 (2013). arXiv:1207.7176
57. R. Prix, S. Giampanis, C. Messenger, Search method for long-duration gravitational-wave transients from neutron stars. Phys. Rev. D **84**, 023007 (2011). arXiv:1104.1704
58. M.C. Miller, E.J.M. Colbert, Intermediate - mass black holes. Int. J. Mod. Phys. D **13**, 1 (2004). arXiv:astro-ph/0308402
59. M. Pasquato, Croatian Black Hole School 2010 lecture notes on IMBHs in GCs, arXiv:1008.4477
60. P. Amaro-Seoane, M. Freitag, Intermediate-mass black holes in colliding clusters: implications for lower-frequency gravitational-wave astronomy. Astrophys. J. **653**, L53 (2006). arXiv:astro-ph/0610478

61. P. Amaro-Seoane, M.C. Miller, M. Freitag, Gravitational waves from eccentric intermediate-mass black hole binaries. Astrophys. J. **692**, L50 (2009). arXiv:0901.0604
62. J.M. Fregeau, S.L. Larson, M.C. Miller, R.W. O'Shaughnessy, F.A. Rasio, Observing IMBH-IMBH binary coalescences via gravitational radiation. Astrophys. J. **646**, L135 (2006). arXiv:astro-ph/0605732
63. I. Mandel, D.A. Brown, J.R. Gair, M.C. Miller, Rates and characteristics of intermediate-mass-ratio inspirals detectable by advanced LIGO. Astrophys. J. **681**, 1431 (2008). arXiv:0705.0285
64. K. Yagi, Gravitational wave observations of galactic intermediate-mass black hole binaries with DECIGO path finder. Class. Quantum Gravity **29**, 075005 (2012). arXiv:1202.3512
65. J. Abadie et al., [LIGO Scientific and Virgo Collaborations], Search for gravitational waves from intermediate mass binary black holes. Phys. Rev. D **85**, 102004 (2012). arXiv:1201.5999
66. J. Abadie et al., [LIGO Scientific and Virgo Collaborations], All-sky search for gravitational-wave bursts in the second joint LIGO-Virgo run. Phys. Rev. D **85**, 122007 (2012). arXiv:1202.2788
67. K. Somiya, K. Goda, Y. Chen, E.E. Mikhailov, Isolation of gravitational waves from displacement noise and utility of a time-delay device. J. Phys. Conf. Ser. **66**, 012053 (2007) arXiv:gr-qc/0610117
68. K. Somiya, Y. Chen, K. Goda, E.E. Mikhailov, Utility investigation of artificial time delay in displacement-noise-free interferometers. Phys. Rev. D **76**, 022002 (2007)

Chapter 11
EMRI Data Analysis with a Phenomenological Waveform

Abstract Extreme mass ratio inspirals (EMRIs) (capture and inspiral of a compact stellar mass object into a Massive Black Hole (MBH)) are among the most interesting objects for the gravitational wave astronomy. It is a very challenging task to detect those sources with the accurate estimation parameters of binaries primarily due to a large number of the secondary maxima on the likelihood surface. Search algorithms based on the matched filtering require computation of the gravitational waveform hundreds of thousands of times, which is currently not feasible with the most accurate (faithful) models of EMRIs. Here we propose to use a phenomenological template family which covers a large range of EMRIs parameter space. We use these phenomenological templates to detect the signal in the simulated data and then, assuming a particular EMRI model, estimate the physical parameters of the binary. We have separated the detection problem, which is done in a model-independent way, from the parameter estimation. For the latter one, we need to adopt the model for inspiral in order to map phenomenological parameters onto the physical parameters characterizing EMRIs.

11.1 Introduction

Stellar compact objects like a black hole, neutron star or white dwarf in the cusp surrounding the massive black hole (MBH) in the galactic nuclei could be deployed on a very eccentric orbit due to N-body interaction. Such an object could either plunge (directly or after few orbits) into MBH or form an EMRI: inspiralling compact object on originally very eccentric orbit which shrinks and circularizes due to loss of the energy and angular orbital momentum through gravitational radiation. The compact object spends $\sim 10^{5-6}$ orbits in the very strong field of a MBH before it plunges, all this orbital evolution will be encoded in the phase of emitted gravitational waves (GWs). Space based GW observatories, like LISA or similar planned missions, will observe those sources few years before the plunge. By fitting precisely the GW phase one can extract extremely accurate parameters of a binary system [1] (like mass and spin of MBH M, a, mass of a small object m, inclination of the orbital plane (to the

Y. Wang, *First-stage LISA Data Processing and Gravitational Wave Data Analysis*,
Springer Theses, DOI 10.1007/978-3-319-26389-2_11

spin of MBH), orbital eccentricity and semi-latus rectum (ι_0, e_0, p_0) at some fiducial moment of time t_0, location of the source on the sky (θ, ϕ) and more).

Precise tracking of the GW phase implies that we can also test the nature of the central massive object. The general belief is that it should be a MBH with surrounding spacetime described by a Kerr solution. The nature of the spacetime affects the orbital evolution of the compact object which in turn could be extracted from the GW phase. Kerr spacetime is described by only two parameters: black hole's mass and spin, as stated by a "no-hair" theorem. The spacetime could be decomposed in the multipole moments of a central massive object, and, for Kerr BH, all moments depend only on M, a: $M_l + iS_l = (ia)^l M$, where M_l and S_l are mass and current moments. Here $S_1 = J$ is the spin of MBH and $a = J/M$ is the usual Kerr spin parameter. We could measure three first moments (mass, spin and quadrupole moment) [2], and check the "Kerrness" of a spacetime. In general, the deviations from Kerr could come in several ways: (i) it is Kerr BH but there is an additional perturber (gas disk, another MBH) (ii) it is not Kerr BH but some other object satisfying GR (boson star, gravastar), (iii) there are deviations from GR. For discussion on the topics we refer the reader to [3–5] and references therein.

Modeling orbital evolution even within GR is not yet fully complete. Large mass ratio allows us to consider a small compact object as a perturbation on the Kerr background spacetime, and treat the problem perturbatively in orders of the mass ratio. In zero order approximation the compact object moves on a geodesic orbit, however, as soon as we assign the mass to it, it creates its own gravitational field interacting with the background and this system emits gravitational radiation. The force resulting from the interaction of the self field with the background is called self force, and the motion of the compact object could be seen as the forced geodesic motion. Alternative interpretation is that the motion is governed by a geodesic motion but in the perturbed spacetime. Calculation of the self force is a complicated task which is accomplished for the orbits around Schwarzschild BH only [6, 7], the Kerr spacetime is underway. There are also questions concerning the calculation of the orbital evolution under the self force: the self force depends on the past history of the compact object (which is usually assumed to be a geodesic in the background spacetime). To compute the motion under the self force one can use the osculating elements approach [8], or self-consistent approach of direct integration of the regularized equations [9]. For more details on this subject we refer to [10].

All in all, the modeling of the orbital evolution and the GW signal is a complex task which requires significant theoretical and computational developments. The latter prevents us currently from using the state-of-art GW models of EMRIs in our data analysis explorations. In majority of the cases the phenomenological model suggested in [1], so called "analytic kludge" (AK), is used. It is based on Post-Newtonian expressions and puts together all relevant physics of EMRIs. However, this model has restrictions in the number of harmonics and in their strength, and any search algorithm which relies on its specific harmonic content will not work for a more realistic model of GW signal. The main motivation of this work is to create the phenomenological search template family which would fit a very large range of EMRI-like signals. The typical EMRI signal consists of a set of harmonics of three (slowly evolving) orbital frequencies, and we will use it as a basis of our template. The phenomenological template consists of N_h harmonics with constant amplitude and slowly evolving phase which we decompose in a Taylor series. Truncation of the Taylor series and the assumption about constant amplitude set restrictions on the duration over which the phenomenological template can fit an EMRI signal. The amplitude of EMRI's harmonics changes due to shrinking of the orbit (overall amplitude increases), circularization of the orbit (power is shifted to lower harmonics) and slight change in the inclination of the orbit to the spin of MBH. Using more terms in the Taylor series helps to track phase of the EMRI signal for longer time (which is more important than accurate description of the amplitude). Finally, we decide on the number of harmonics to use in the template (and their indices) based on the analysis of the harmonic structure of the Numerical Kludge (NK) model [11] of EMRI in different parts of the parameter space. The restriction that the phenomenological waveform (PW) is valid only for a limited period of time is very weak since we can fit the signal piecewise, as long as the accumulated signal-to-noise ratio (SNR) over that time is significant to claim presence of the signal. In this work we consider only those parts of the EMRI signal where the orbital frequencies are not decreasing which is true over almost all time of the inspiral and breaks quite close to the plunge. However, this is not really necessary since we did not restrict the values of frequency derivatives to positive values during the search.

The PW family is quite generic and does not depend on the orbital evolution, or, in other words, the orbital evolution of the binary is encoded in the Taylor coefficients of phase of each harmonic. This allows us to detect an EMRI signal in a model independent way. Once the harmonics of the signal are recovered we can analyze them using a specific EMRI model to recover physical parameters of the system. It is at this point we need the orbital evolution with high accuracy, which involves computation of the self-force and tests of possible deviations from the "Kerrness".

After constructing the phenomenological waveform we perform blind searches on the simulated data without noise (to avoid stochastic errors in the parameter estimation) and with the noise. We have used the NK waveform (as described in [11]) as a model of our signal and the orbital evolution according to [12]. We have also used Markov chain Monte-Carlo (MCMC) search with phenomenological waveforms on the simulated three month of data. This search has provided us with multiple local maxima in the likelihood which we gathered and analyzed in a similar way as described in [13]. We associate local maxima in the likelihood with partial detections of the signal and construct the time–frequency map of the detected (patchy) harmonics of the source. The next step is to assume the model for the orbital evolution and, by matching the found time–frequency tracks to the harmonics of the signal, estimate parameters of the binary system. We have used the same model for the orbital evolution as in the simulated data sets and recovered physical parameters with precision better than few percent.

The chapter is organized as follows. In the next Section we will give a brief overview of available models for GWs from EMRIs. In Sect. 11.3, we introduce PW family in details. We describe MCMC search with PWs in Sect. 11.4. Analysis of

MCMC results and mapping to the physical parameters are done in the Sect. 11.5. Finally we conclude with a summary Sect. 11.6.

11.2 Review of EMRI Waveforms

As was already mentioned in the Introduction, accurate computation of the GWs from EMRIs and the orbital evolution is a complex and computationally intensive task. The most promising approach probably is the coupled integration of the compact object dynamics and GW emission taken in [9]. Alternatively, one could have a separate evolution of the orbital motion using self force computed across various geodesic orbits and employ osculating elements approach [8, 14]. The waveform at infinity could be obtained from the Teukolsky equations [15] in time or in frequency domain [16, 17].

The above methods are computationally expensive and several approximations were suggested. Less accurate but still quite reliable are Numerical Kludge (NK) waveforms: original NK [11] and extended/improved NK called "Chimera" [18, 19]. Those methods combine accurate prescription for the orbital evolution with approximate (Post-Newtonian) waveform generation formalism.

The less precise model, which captures all relevant physics of EMRIs (orbital precession, three orbital frequencies) was suggested in [1], so called Analytic Kludge waveform. These waveforms are very fast to generate, and even though they cannot be used for searching for actual GW signals, they are used to develop data analysis algorithms and to evaluate their performance [1, 2, 20].

In this work, we used NK waveform. In the original paper [11], the waveform was generated in the time domain, we have reimplemented it in the frequency domain following suggestions of S. Drasco who did it first (private communications). Let us give a brief explanation of this procedure. We start with an initial geodesic characterized by initial position and three other constants of motion which could be chosen to be either energy (E), axial orbital angular momentum (L_z) and Carter constant (Q) or eccentricity, semi-latus rectum and inclination [11]. These three constants could be used to compute three fundamental frequencies of the orbital motion: f_r, f_θ, f_ϕ. The geodesic motion is periodic in those three frequencies and therefore any function of the orbital coordinates can be decomposed into Fourier series. That is exactly what we do: for a given geodesic we decompose the waveform into Fourier series of harmonics of the fundamental frequencies. We truncate the series when adding extra harmonics does not change the signal by more that 0.1 % in the overlap. Under the self-force the motion is not geodesic anymore, however it can still be accurately described as slow drift from one geodesic to another. In oscillating element approach, we evolve three constants defining initial position of the compact object (due to conservative part of the self-force) as well as $\{E, L_z, Q\}$ or equivalently $\{f_r, f_\theta, f_\phi\}$ [8, 14]. We evolve $\{E, L_z, Q\}$ according to PN expressions suggested in [12], and, like in the original NK paper we dropped evolution of the initial positions. This does not affect our search results, since PW is model independent, however we have to use the same model (as in the simulated data) for mapping the phenomenological parameters onto the physical parameters of the binary. Mismatch in the models would result in the undesirable bias. So we have computed the evolution of the fundamental frequencies, then we have calculated the amplitudes of the harmonics at discrete (sparse) moments of time with consequent interpolation in between. We have computed the phase of each harmonic as a numerical integral of time dependent frequencies. It takes about a few minutes on 2.80 GHz single core CPU to generate 3-month long template which is definitely too slow for the data analysis purposes.

Finally we want to avoid using in this work the Analytic Kludge model, because it predicts somewhat simplified (detectable) harmonic content of the waveform. The NK waveforms for generic orbits were compared against waveforms based on the Teukolsky equation and they show quite good agreement. We believe that NK deviates from the true EMRI signal in the phase but not so much in the number and strength of harmonics. Therefore we use NK model as a representation of the EMRI signal throughout this paper.

11.3 EMRI Phenomenological Waveform Family

There are several algorithms which have been proven to be successful in detecting EMRIs in the simulated LISA data [13, 20, 21]. However, those algorithms partially utilize the features of AK waveform which was used in the simulation of the data and in the data analysis. As explained in Sect. 11.2, we want to avoid it by building a generic phenomenological template family.

11.3.1 Phenomenological Waveform in the Source Frame

The model we want to propose is based on the following assumptions about GW signals from EMRIs:

1. The orbital motion can be effectively described by six slowly changing quantities. Explicitly, three time-dependent initial phases are governed by the conservative part of the self force; three fundamental time-dependent frequencies are governed by the radiative part of the self force.
2. The waveform is represented by harmonics of three frequencies (phenomenologically, these frequencies are the summation of the fundamental orbital frequencies and the evolution of the initial phases) with slowly changing intrinsic amplitude:

$$
\begin{aligned}
h(t) &= \sum_{l,m,n} h_{lmn}(t) \\
&= \mathrm{Re}\left(\sum_{l,m,n} A_{lmn}(t) e^{i\Phi_{lmn}(t)} \right) \\
&= \mathrm{Re}\left(\sum_{l,m,n} A_{lmn}(t) e^{i(l\Phi_r + m\Phi_\theta + n\Phi_\varphi)} \right), \qquad (11.1)
\end{aligned}
$$

where Φ_r, Φ_θ, Φ_φ are the phase evolutions corresponding to the three fundamental motions. Here we omitted the tensorial spatial indices for simplicity.

The first assumption basically expresses that the motion is described by a slow drift from one geodesic to another. The initial phases correspond to the initial position of a compact object on a given geodesic and the orbital frequencies are functions of the energy, azimuthal component of the orbital momentum and Carter constant. The slow drift ensures that phases Φ_{lmn} are slowly varying functions of time.

Figure 11.1 shows the time–frequency plot of a typical EMRI signal. There are 30 clearly separated frequency tracks in the noiseless plot, which display the dominant harmonics. It can also be seen that the frequencies of harmonics are smooth and vary slowly. It is generally true that both amplitude and the phase are slowly varying functions of time, thus we can safely make the Taylor expansion:

$$
\begin{aligned}
\Phi_r(t) &= \Phi_r(t_0) + \omega_r(t_0)(t - t_0) + \frac{1}{2}\dot{\omega}_r(t - t_0)^2 + \ldots \\
&= \Phi_r(t_0) + 2\pi f_r(t_0)(t - t_0) + \pi\dot{f}_r(t - t_0)^2 + \cdots, \qquad (11.2)
\end{aligned}
$$

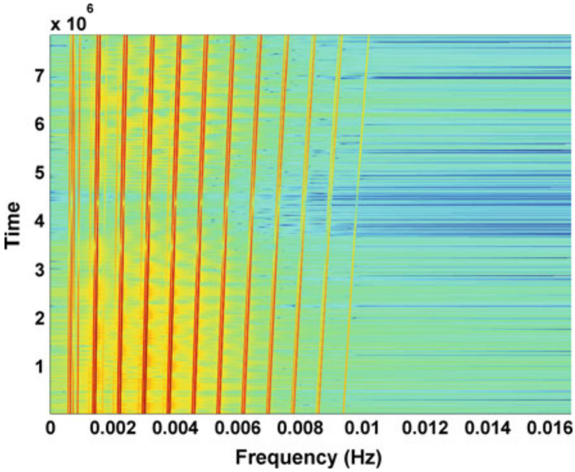

Fig. 11.1 The time–frequency plot of a typical EMRI signal without noise. There are 30 dominant harmonics in total

$$\begin{aligned}
\Phi_\theta(t) &= \Phi_\theta(t_0) + \omega_\theta(t_0)(t-t_0) + \frac{1}{2}\dot{\omega}_\theta(t-t_0)^2 + \cdots \\
&= \Phi_\theta(t_0) + 2\pi f_\theta(t_0)(t-t_0) + \pi \dot{f}_\theta(t-t_0)^2 + \cdots\,, \qquad (11.3)\\
\Phi_\varphi(t) &= \Phi_\varphi(t_0) + \omega_\varphi(t_0)(t-t_0) + \frac{1}{2}\dot{\omega}_\varphi(t-t_0)^2 + \cdots \\
&= \Phi_\varphi(t_0) + 2\pi f_\varphi(t_0)(t-t_0) + \pi \dot{f}_\varphi(t-t_0)^2 + \cdots\,, \qquad (11.4)\\
A_{lmn}(t) &= A_{lmn}(t_0) + \dot{A}_{lmn}(t_0)(t-t_0) + \cdots \qquad (11.5)
\end{aligned}$$

Since the amplitudes A_{lmn} are even smoother than the phase over extended period of time, and because the detection techniques are more sensitive to mismatch in the phase than in the amplitude, we can neglect the time evolution in the amplitudes and treat all of them as constant. It is a very good assumption over three months of the simulated data which we analyze in this paper. As for the phase expansion, we calculate the so-called fitting factor (FF) for the different orders of polynomial approximations of the phase to check the fidelity of the PW. Numerical results show that the Taylor expansion for three months data, up to $\ddot{f}$ order, gives the FF around 0.9, and up to $\dddot{f}$ order the FF is larger than 0.999. So it is sufficient to expand the phase to $\dddot{f}$ order. This is the phenomenological waveform family which we propose to analyze an EMRI signal. To summarize, the phenomenological waveform is a summation of individual harmonics with constant (or linear) amplitudes and polynomial (in time) phases.

11.3.2 From the Source Frame to the LISA Frame

First we will express the GW wavefrom in the solar system barycenter frame and then translate it to the frame attached to LISA (or a LISA-like space based observatory). In the source frame, an arbitrary gravitational wave (GW) signal in the TT gauge can be written in the following form:

$$\mathbf{h}(t) = h_+^S(t)\mathbf{e}_+ + h_\times^S(t)\mathbf{e}_\times, \qquad (11.6)$$

where the superscript ‘S’ denotes the source frame. Since the LISA constellation is orbiting the sun, it is convenient to express the GW signal in the solar system barycenter (SSB) frame.

$$\begin{aligned}
\mathbf{h}(t) &= h_+(t)\boldsymbol{\epsilon}_+ + h_\times(t)\boldsymbol{\epsilon}_\times, \qquad (11.7)\\
\boldsymbol{\epsilon}_+ &= \hat{\theta}^S \otimes \hat{\theta}^S - \hat{\phi}^S \otimes \hat{\phi}^S \qquad (11.8)\\
\boldsymbol{\epsilon}_\times &= \hat{\theta}^S \otimes \hat{\phi}^S + \hat{\phi}^S \otimes \hat{\theta}^S, \qquad (11.9)
\end{aligned}$$

where (θ^S, ϕ^S) denotes the direction of the GW source in the SSB frame, $\hat{\theta}^S$, $\hat{\phi}^S$ are the unit vectors along longitudinal and latitudinal directions. The principal polarization vectors attached to the solar system barycenter frame, $\hat{\theta}^S$, $\hat{\phi}^S$ are connected to the principal polarization vectors in the source frame via rotation angle ψ (since they lie in the same plane orthogonal to the GW propagation direction). The polarization components h_+ and $h_\times$ are transformed under this rotation according to

$$h_+ = h_+^S \cos(2\psi) + h_\times^S \sin(2\psi) \tag{11.10}$$

$$h_\times = -h_+^S \sin(2\psi) + h_\times^S \cos(2\psi). \tag{11.11}$$

Now we will add LISA response. LISA measures the Doppler shift of the inter-spacecraft lasers induced by a gravitational wave. The single-link full response to this frequency shift can be derived with the help of three Killing vectors [22]. However, this single-link signal is orders of magnitude smaller than the dominating laser frequency noise. Thus, we need to use the so-called Time-Delay-Interferometry (TDI) variables [23], which cancel the laser noise through the recombination of the artificially delayed single-link signals. In the low frequency limit, the two orthogonal TDI (noise independent) variables of Michelson type can be expressed as [24, 25]

$$\begin{aligned} h_I(t) &= [\delta L_1(t) - \delta L_2(t)]/L \\ &= \mathbf{h}(\zeta) : \boldsymbol{D}_I \qquad (11.12) \\ h_{II}(t) &= \frac{1}{\sqrt{3}}[\delta L_1(t) + \delta L_2(t) - 2\delta L_3(t)]/L \\ &= \mathbf{h}(\zeta) : \boldsymbol{D}_{II} \qquad (11.13) \end{aligned}$$

where L stands for the average arm length. The retarded time $\zeta(t) = t - \hat{k} \cdot \mathbf{x}/c$ defines the wavefront, where $\hat{k}$ is the GW propagation direction. The two detector tensors are defined as $\boldsymbol{D}_I \equiv \frac{1}{2}(\hat{n}_1 \otimes \hat{n}_1 - \hat{n}_2 \otimes \hat{n}_2), \boldsymbol{D}_{II} \equiv \frac{1}{2\sqrt{3}}(\hat{n}_1 \otimes \hat{n}_1 + \hat{n}_2 \otimes \hat{n}_2 - 2\hat{n}_3 \otimes \hat{n}_3)$, where $\hat{n}_1, \hat{n}_2, \hat{n}_3$ denote the unit vectors along each arm of LISA. Here we assume LISA-like setup which has six links (three arms). Even though the EMRI signal could reach quite high frequencies and require full response, we adopt the low-frequency approximation for our exercises. This does not restrict ability of our analysis as long as the simulated signal and the search template use the same response function.

11.3.3 Data Analysis with Phenomenological Waveform

We start with a brief overview of our notations and basics of data analysis. We denote the Fourier transform of a time series $a(t)$ by $\tilde{a}(f)$ and adopt the following convention

$$\tilde{a}(f) = \int a(t) e^{i2\pi ft} dt. \tag{11.14}$$

We assume that the detector is characterized by a Gaussian, stationary noise $n(t)$ and its two-sided noise power spectral density is defined as $\overline{\tilde{n}^*(f')\tilde{n}(f)} = S_n(f)\delta(f - f')$, where the over bar denotes the ensemble average. With this power spectral density, it is conventional to define an inner product of two time series $a(t), b(t)$ as follows

$$< a|b >= \int_{-\infty}^{\infty} \frac{\tilde{a}^*(f)\tilde{b}(f)}{S_n(f)} df. \tag{11.15}$$

The signal-to-noise ratio is defined as

$$SNR^2 \equiv < h|h >= \int_{-\infty}^{\infty} \frac{|\tilde{h}(f)|^2}{S_n(f)} df, \tag{11.16}$$

where h is the GW signal. Let us denote the probability of a gravitational wave signal $h(\boldsymbol{\theta})$ being present in the data $s(t)$ by $P(s|h(\boldsymbol{\theta}))$, where $\boldsymbol{\theta}$ is the set of parameters that characterizes the gravitational wave signal. Similarly, the probability of no gravitational wave signal present in the data s is denoted by $P(s|0)$. Likelihood ratio $\Lambda(\boldsymbol{\theta})$ is the ratio between these two probabilities

$$\begin{aligned}\Lambda(\boldsymbol{\theta}) &= \frac{P(s|h(\boldsymbol{\theta}))}{P(s|0)} \\ &= e^{<s|h(\boldsymbol{\theta})> - \frac{1}{2}<h(\boldsymbol{\theta})|h(\boldsymbol{\theta})>}.\end{aligned} \tag{11.17}$$

It is conventional to consider rather logarithm of the likelihood ratio as a detection statistic: $L(\boldsymbol{\theta}) = \log \Lambda(\boldsymbol{\theta}) =< s|h(\boldsymbol{\theta}) > -\frac{1}{2} < h(\boldsymbol{\theta})|h(\boldsymbol{\theta}) >$. This is the quantity we want to maximize over the parameter set $\boldsymbol{\theta}$.

The likelihood ratio could be further simplified if we use PW. A single harmonic with polynomial phase up to $\dddot{f}$ order in the source frame takes the following form

$$\mathbf{h}(t) = A_+ \cos(\Phi(t) + \Phi_0)\mathbf{e}_+ + A_\times \sin(\Phi(t) + \Phi_0)\mathbf{e}_\times, \tag{11.18}$$

$$\begin{aligned}\Phi(t) &= 2\pi f(t - t_0) + \pi\dot{f}(t - t_0)^2 \\ &+ \frac{\pi}{3}\ddot{f}(t - t_0)^3 + \frac{\pi}{12}\dddot{f}(t - t_0)^4,\end{aligned} \tag{11.19}$$

where we have omitted harmonic indices l, m, n. After simple algebra, LISA's response to this single harmonic GW signal without noise can be put in a simple form

$$h_I(t) = A^\mu h^I_\mu(t), \quad h_{II}(t) = A^\mu h^{II}_\mu(t) \tag{11.20}$$

where we follow summation convention over repeated indices, and $\mu = 1, 2, 3, 4$. The four amplitude parameters A^{μ} depend only on $(A_{+}, A_{\times}, \Phi_0, \psi)$, which are usually called extrinsic parameters, while $h^{I}_{\mu}(t)$, $h^{II}_{\mu}(t)$ are functions of $(\theta^{S}, \phi^{S}, f, \dot{f}, \ddot{f}, \dddot{f})$, which are usually called intrinsic parameters. From now on, we denote the intrinsic parameters by $\boldsymbol{\theta}$. The extrinsic parameters (being constants in our approximation) can be maximized over analytically [26, 27], which we will show explicitly below. We denote the measured data with noise corresponding to $h_{I}(t), h_{II}(t)$ by $s_{I}(t), s_{II}(t)$. Since the joint probability of a GW signal present in both s_{I} and s_{II} is just the product of the individual probabilities, the joint log likelihood is just the summation of the individual log likelihoods

$$\begin{aligned} L(\boldsymbol{\theta}, A^{\mu}) = &< s_{I}|h_{I}(\boldsymbol{\theta}) > -\frac{1}{2} < h_{I}(\boldsymbol{\theta})|h_{I}(\boldsymbol{\theta}) > \\ &+ < s_{II}|h_{II}(\boldsymbol{\theta}) > -\frac{1}{2} < h_{II}(\boldsymbol{\theta})|h_{II}(\boldsymbol{\theta}) > . \end{aligned} \tag{11.21}$$

Substituting (11.20) into this expression we arrive at

$$\begin{aligned} L(\boldsymbol{\theta}, A^{\mu}) = &A^{\mu} s^{I}_{\mu}(\boldsymbol{\theta}) - \frac{1}{2} A^{\mu} M^{I}_{\mu\nu}(\boldsymbol{\theta}) A^{\nu} \\ &+ A^{\mu} s^{II}_{\mu}(\boldsymbol{\theta}) - \frac{1}{2} A^{\mu} M^{II}_{\mu\nu}(\boldsymbol{\theta}) A^{\nu}, \end{aligned} \tag{11.22}$$

where we have used the following conventions: $s^{I}_{\mu} =< s_{I}|h^{I}_{\mu} >$, $s^{II}_{\mu} =< s_{II}|h^{II}_{\mu} >$, $M^{I}_{\mu\nu} =< h^{I}_{\mu}|h^{I}_{\nu} >$, $M^{II}_{\mu\nu} =< h^{II}_{\mu}|h^{II}_{\nu} >$. We can maximize the log-likelihood over extrinsic parameters by solving

$$\frac{\partial L(\boldsymbol{\theta}, A^{\mu})}{\partial A^{\mu}} = (s^{I}_{\mu} + s^{II}_{\mu}) - (M^{I}_{\mu\nu} + M^{II}_{\mu\nu}) A^{\nu} = 0, \tag{11.23}$$

which is straightforward to find $A^{\mu} = [(M^{I} + M^{II})^{-1}]^{\mu\nu}(s^{I}_{\nu} + s^{II}_{\nu})$. The log-likelihood maximized over the extrinsic parameters is called F-statistic:

$$\begin{aligned} F(\boldsymbol{\theta}) &\equiv \max_{A^{\mu}} L(\boldsymbol{\theta}, A^{\mu}) \\ &= \frac{1}{2}(s^{I}_{\mu} + s^{II}_{\mu})[(M^{I} + M^{II})^{-1}]^{\mu\nu}(s^{I}_{\nu} + s^{II}_{\nu}). \end{aligned} \tag{11.24}$$

Its expectation value is connected to the SNR in the following way

$$E[F(\boldsymbol{\theta})] = \frac{1}{2} SNR^{2} + 2. \tag{11.25}$$

Since $h(\boldsymbol{\theta})$ is narrow band signal, the inner product can be written in the following form

$$< a|b >= \int_{-\infty}^{\infty} \frac{\tilde{a}^*(f)\tilde{b}(f)}{S_n(f_0)} df = \frac{1}{S_n(f_0)} \int_{0}^{T} a(t)b(t)dt, \tag{11.26}$$

where T is the observation time, f_0 is the middle frequency of $h(\boldsymbol{\theta})$. The inner product is a function of T, and so is F-statistic. By varying T from 0 to the total observation time, we define a *cumulative F-statistic* $F(T, \boldsymbol{\theta})$. The cumulative F-statistic for 30 dominant harmonics without detector noise is plotted in Fig. 11.2. The case with the simulated detector noise is shown in Fig. 11.3, the total SNR of the signal in this case is $SNR = 50$. Those are two data sets which we will analyze in the next section.

The cumulative F-statistic provides much more information than F-statistic. Actually, if $\boldsymbol{\theta}_*$ is the true parameter set of the signal, one can argue that

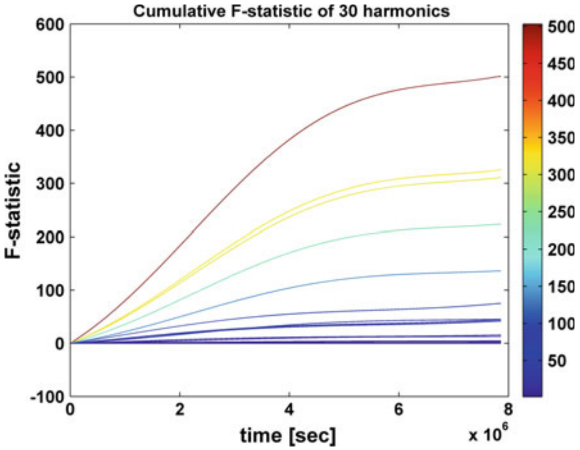

Fig. 11.2 The cumulative F-statistic of 30 dominant harmonics with true parameters without noise. Since there is no noise, the F-statistic is not normalized

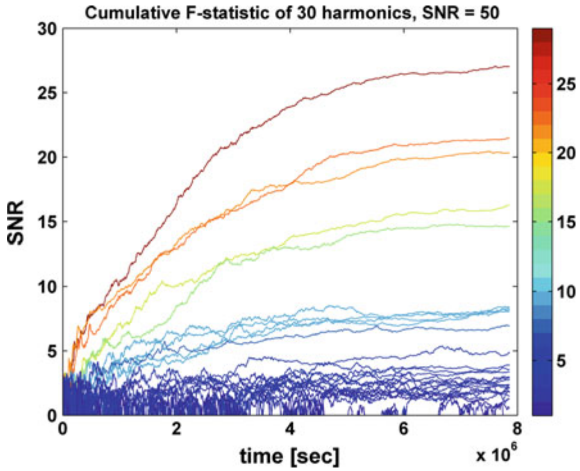

Fig. 11.3 The cumulative F-statistic of 30 dominant harmonics with true parameters and detector noise. Note that the F-statistic is converted to *SNR* in the figure. The strong harmonics are cumulating gradually with local spikes. The low-SNR harmonics behave similar to noise, hence made undetectable

$$E\left[\frac{\partial F(T,\boldsymbol{\theta}_*)}{\partial T}\right] \propto h^2(T)\xi^2(T), \tag{11.27}$$

where $\xi(T) = \sqrt{\xi_+^2(T) + \xi_\times^2(T)}$ is the geometrical mean of the antenna pattern functions for two polarizations. When there is no detector noise, $\frac{\partial F(T,\boldsymbol{\theta}_*)}{\partial T} = E\left[\frac{\partial F(T,\boldsymbol{\theta}_*)}{\partial T}\right]$ is nonnegative. Thus, $E[F(T,\boldsymbol{\theta}_*)]$ is always increasing over the entire time span when the GW signal is present, as can be seen in Fig. 11.2. It is not necessarily so in presence of the noise and during analysis of the data. There are three types of oscillations on the cumulative F-statistic curve $F(T,\boldsymbol{\theta})$. (i) The (non-negative) oscillation due to the oscillatory nature of the gravitational wave signal. It is at twice the GW frequency, which makes it hard to see in Fig. 11.2. (ii) In reality, we do not know the exact true parameters of the GW signal. That means, in most cases, the parameter set $\boldsymbol{\theta}$ we try differs from the true parameter set $\boldsymbol{\theta}_*$. This introduce beat-notes to $F(T,\boldsymbol{\theta})$. This kind of oscillation happens at beat-note frequency, which is much lower than the GW frequency itself. (iii) The third type of oscillation is due the noise. The presence of the noise makes the cumulative F-statistic uneven, see Fig. 11.3. Comparing to the former two types, this kind of oscillation is irregular; it oscillates at all frequencies and could cause temporary (for a short time) decrease in the cumulative F-statistic.

We have found that over three months of simulated data we can consider all harmonics as being completely independent with virtually zero overlap between them, $< h_{lmn}|h_{l'm'n'} >= \delta_{ll'}\delta_{mm'}\delta_{nn'}$. The total F-statistic is therefore a sum of F-statistics from each harmonic. In the next section we describe the search where we use Eq. (11.24) as a detection statistic, and we will use cumulative F-statistic later on to analyze our findings.

11.4 Search with the Phenomenological Waveform

In this section, we use the PW as described above together with the introduced detection statistic. We will use two 3 month worth simulated data sets: with and without noise. We use the same GW signal (based on NK model) in both cases. The total SNR of the source in the noisy case is 50. We have taken the following parameters for the EMRI: the mass of the MBH $M = 10^6 M_\odot$, the mass of the compact object (stellar mass BH) $m = 10M_\odot$, the initial orbital eccentricity $e = 0.4$, the semi-latus rectum $p = 8M$, the inclination angle $\iota = \pi/9$, the spin of the MBH $a = 0.9M$, the sky position of the source $(\theta^S, \phi^S) = (\pi/4, \pi/4)$, the polarization angle $\psi = 0$. In our analysis we assume that the sky location is known. Our primary goal here is to recover the intrinsic parameters of the source. For the Michelson TDI channel h_I, we show the signal and the measurement data with noise in Fig. 11.4. The signal is totally buried in the noise with an instantaneous amplitude much smaller than the noise amplitude. The modulation of the envelop of the signal is due to the time-varying antenna pattern function of the LISA constellation. The time–frequency plane of the measurement data (with an SNR of 50) is shown in Fig. 11.5a, where the signal is

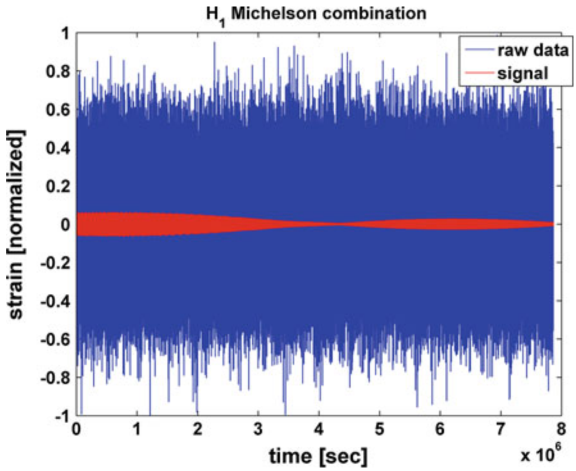

Fig. 11.4 The measurement time series (in *blue*) and the signal time series of SNR 50 (in *red*), for the Michelson TDI channel h_I (color online figure)

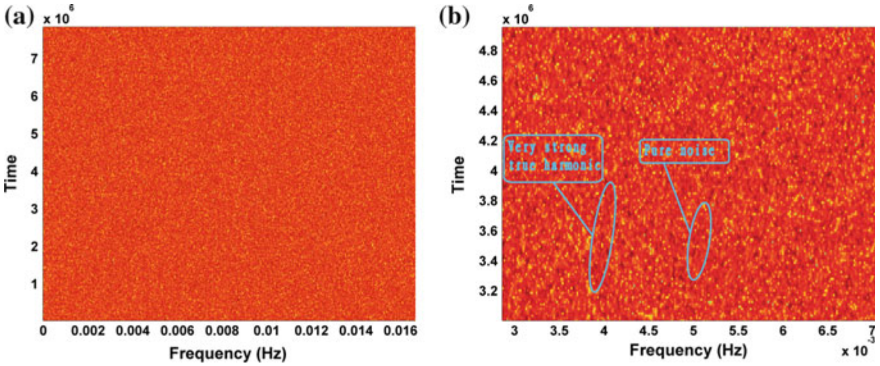

Fig. 11.5 **a** The time–frequency plane of the measurement data (with an SNR of 50). **b** A zoom-in plot of (**a**), where a location of a very strong harmonic and a location of pure noise are indicated. It is very hard to tell the signal by eye in the time–frequency plot

covered by the strong noise. Even in the zoom-in Fig. 11.5b, the location of a very strong harmonic and the location of pure noise are very hard to tell apart.

In the simulation, the noiseless case is used to avoid any possible bias in the final result due to stochastic nature of the noise, and assess possible restrictions of our search technique and PW family. Next, we apply the same search method to the same GW signal buried in the noise, which would justify its effectiveness in practice.

Here, we describe the search for individual harmonics with *Markov chain Monte Carlo* (MCMC) method. For completeness and future references we give a brief introduction to MCMC. Like a standard Monte Carlo integration, MCMC is a random sampling method. It is nothing but Monte Carlo integration with a Markov chain. By properly constructing a Markov chain, MCMC can draw samples from the searching parameter space more efficiently. Among all the methodologies of constructing a Markov chain, the Metropolis-Hastings scheme would be the most general one. The main idea of Metropolis-Hastings algorithm is to cleverly construct a Markov chain that satisfy the detailed balance equation, so that the sampling distribution will converge to the likelihood surface we want to estimate. If the shape of the likelihood surface is known, the parameter set that corresponds to the maximum likelihood is automatically known. Thus, MCMC is also widely used as a stochastic optimization tool in GW data analysis (we refer the reader to a very nice overview and discussion on Bayesian methods in [28], see also references therein).

If the likelihood surface is multimodal (i.e. contains large number of separated local maxima) then simple version of the MCMC finds a maximum and does not move off it to explore larger parameter space. Many ways around this problem were suggested but we will not use any of them here (besides simulated annealing which we will discuss a later). As we will see, a simple Metropolis-Hastings algorithm is sufficient. The likelihood surface of an EMRI signal is very rich in “wall” and “needle” like structures, which make it very hard to find a global maximum. We are interested in detecting as many local maxima as possible. Therefore we run multiple independent chains and harvest the results after they converge to various maxima of the likelihood surface. If we are lucky, the global maximum could be among multiple maxima we have found.

To understand the Metropolis-Hastings algorithm, first consider a stochastic process denoted by $\{\boldsymbol{\theta}_k | k = 0, 1, 2, \ldots\}$ which belongs to the parameter space $\mathcal{B}$ in $\mathbb{R}^n$. Here we defined $\boldsymbol{\theta}_k$ as a set of parameters at step k, which can also be viewed as a point in the parameter space $\mathcal{B}$. If there exists a transition probability $P(\boldsymbol{\theta}_{k+1}|\boldsymbol{\theta}_k)$ depending only on the current point $\boldsymbol{\theta}_k$ for the stochastic process to be in state $\boldsymbol{\theta}_{k+1}$, we call this stochastic process $\{\boldsymbol{\theta}_k | k = 0, 1, 2, \ldots\}$ a *Markov chain* with a transition probability $P(\boldsymbol{\theta}_{k+1}|\boldsymbol{\theta}_k)$. In a Bayesian viewpoint, we can take this transition probability as conditional probability and immediately see that

$$\int_{\mathcal{B}} P(\boldsymbol{\theta}_{k+1}|\boldsymbol{\theta}_k) d\boldsymbol{\theta}_{k+1} = 1. \tag{11.28}$$

A Markov chain satisfying the *detailed balance equation*

$$\Lambda(\boldsymbol{\theta}_k) P(\boldsymbol{\theta}_{k+1}|\boldsymbol{\theta}_k) = \Lambda(\boldsymbol{\theta}_{k+1}) P(\boldsymbol{\theta}_k|\boldsymbol{\theta}_{k+1}) \tag{11.29}$$

will (up to some relatively weak conditions) be equivalent to the samples from the distribution $\Lambda(\boldsymbol{\theta})$ after a certain initial period (often called *burn-in* stage). We can easily estimate the distribution $\Lambda(\boldsymbol{\theta})$ with the Markov chain samples and hence the most probable parameter set $\hat{\boldsymbol{\theta}}$ for given observed data $\mathbf{s}$, where

$$\Lambda(\hat{\boldsymbol{\theta}}|\mathbf{s}) = \max_{\boldsymbol{\theta}} \Lambda(\boldsymbol{\theta}|\mathbf{s}) \tag{11.30}$$

is usually called the maximum likelihood estimator.

By virtue of Metropolis-Hastings algorithm, we can construct a Markov chain that satisfies the detailed balance equation and make use of the corresponding property to estimate our template parameters $\boldsymbol{\theta}$. To do this, we randomly choose a parameter set $\boldsymbol{\theta}_0$ in the parameter space as the starting point. Then one can pick a *proposal distribution* $q(\boldsymbol{\theta}_{k+1}|\boldsymbol{\theta}_k)$ (as long as there is no forbidden region in the prescribed parameter space to the point $\boldsymbol{\theta}_{k+1}$) and sample a candidate point $\boldsymbol{\theta}_{k+1}$ from this distribution. Then we calculate the *acceptance probability* defined by the following formula (we have assumed the uniform priors on parameters)

$$\alpha(\boldsymbol{\theta}_k, \boldsymbol{\theta}_{k+1}) = \min\left(1, \frac{\Lambda(\boldsymbol{\theta}_{k+1})q(\boldsymbol{\theta}_k|\boldsymbol{\theta}_{k+1})}{\Lambda(\boldsymbol{\theta}_k)q(\boldsymbol{\theta}_{k+1}|\boldsymbol{\theta}_k)}\right). \tag{11.31}$$

By accepting the point $\boldsymbol{\theta}_{k+1}$ according to the above probability, we have, in fact, succeeded to construct a transition probability,

$$P(\boldsymbol{\theta}_{k+1}|\boldsymbol{\theta}_k) = q(\boldsymbol{\theta}_{k+1}|\boldsymbol{\theta}_k)\alpha(\boldsymbol{\theta}_k, \boldsymbol{\theta}_{k+1}). \tag{11.32}$$

It is easy to see that the Markov chain generated by the above transition probability satisfies the detailed balance equation:

$$\begin{aligned}\Lambda(\boldsymbol{\theta}_k)P(\boldsymbol{\theta}_{k+1}|\boldsymbol{\theta}_k) &= \min\left(\Lambda(\boldsymbol{\theta}_k)q(\boldsymbol{\theta}_{k+1}|\boldsymbol{\theta}_k), \Lambda(\boldsymbol{\theta}_{k+1})q(\boldsymbol{\theta}_k|\boldsymbol{\theta}_{k+1})\right)\\ &= \min\left(\Lambda(\boldsymbol{\theta}_{k+1})q(\boldsymbol{\theta}_k|\boldsymbol{\theta}_{k+1}), \Lambda(\boldsymbol{\theta}_k)q(\boldsymbol{\theta}_{k+1}|\boldsymbol{\theta}_k)\right)\\ &= \Lambda(\boldsymbol{\theta}_{k+1})P(\boldsymbol{\theta}_k|\boldsymbol{\theta}_{k+1}). \end{aligned} \tag{11.33}$$

Thus, such a Markov chain will eventually serve as a succession of samples from $\Lambda(\boldsymbol{\theta})$. The best performance is achieved if the proposal probability $q(\boldsymbol{\theta}_{k+1}|\boldsymbol{\theta}_k)$ resembles the target distribution $\Lambda(\boldsymbol{\theta})$ over the entire parameter space. Without prior knowledge about the kind of probability distribution around the true parameter location, it is natural to choose it as a multivariate normal distribution centered at the present point $\boldsymbol{\theta}_k$ with covariance matrix $\mathcal{C}$,

$$q(\boldsymbol{\theta}_{k+1}|\boldsymbol{\theta}_k) = \frac{1}{\sqrt{(2\pi)^N \det[\mathcal{C}]}} \exp\left[-\frac{1}{2}(\boldsymbol{\theta}_{k+1} - \boldsymbol{\theta}_k)^{\mathsf{T}}\mathcal{C}^{-1}(\boldsymbol{\theta}_{k+1} - \boldsymbol{\theta}_k)\right], \tag{11.34}$$

where N denotes the dimension of the parameter space and $\det[\mathcal{C}]$ the determinant of the covariance matrix $\mathcal{C}$. The likelihood surface has usually multimodal (multiple local maxima) structure, and, therefore, a single multivariate normal distribution cannot describe the probability density over the entire template space but only a very small region around the local maximum. Since the probability distribution at the local maximum is usually very sharp, a Markov chain easily gets trapped there for many steps. To avoid insignificant maxima we use the so-called *annealing* scheme, originating from simulated annealing. We adopt two types of annealing techniques. (i) We introduce a temperature $\mathcal{T}_1$ to the acceptance rate α [Eq. (11.31)] so as to have a larger possibility to accept the proposal point in the beginning. By combining Eqs. (11.17), (11.24), (11.31), (11.34), the acceptance probability is now written as

$$\alpha(\boldsymbol{\theta}_k, \boldsymbol{\theta}_{k+1}) = \min\left(1, e^{[F(\boldsymbol{\theta}_{k+1}) - F(\boldsymbol{\theta}_k)]/\mathcal{T}_1}\right). \tag{11.35}$$

where the temperature $\mathcal{T}_1 = \mathcal{T}_1(k)$ is a function of the step index k, it starts from some relatively large number and gradually decays to unity. (ii) We introduce a second temperature $\mathcal{T}_2$ to the proposal distribution $q(\boldsymbol{\theta}_{k+1}|\boldsymbol{\theta}_k)$. The covariance matrix $\mathcal{C}$ is replaced by $\mathcal{C} \times \mathcal{T}_2$. Same as $\mathcal{T}_1$, $\mathcal{T}_2$ is also a function of the step index k, decaying gradually to unity. Hence, the chain take large steps in the beginning and explores large volume in the parameter space. Explicitly, we choose $\mathcal{T}_1$ and $\mathcal{T}_2$ both as a linear function of k with negative slope.

Let us summarize the algorithm:

1. $k = 0$. Choose a random parameter set $\boldsymbol{\theta}_0$ as the starting point and calculate the F-statistic $F(\boldsymbol{\theta}_0)$.
2. $k \rightarrow k + 1$. Calculate the temperature $\mathcal{T}_1(k)$, $\mathcal{T}_2(k)$.
3. Generate the next candidate parameter set $\boldsymbol{\theta}_c$ from the proposal distribution with modified covariance $\mathcal{C} \times \mathcal{T}_2$.
4. Calculate the F-statistic of the new parameter set $F(\boldsymbol{\theta}_c)$.
5. Calculate the acceptance probability $\alpha(\boldsymbol{\theta}_k, \boldsymbol{\theta}_c) = \min\left(1, e^{[F(\boldsymbol{\theta}_c) - F(\boldsymbol{\theta}_k)]/\mathcal{T}_1}\right)$.
6. Draw a random number u from unity distribution $\mathcal{U}(0, 1)$. If $u < \alpha$, accept the candidate parameter set $\boldsymbol{\theta}_{k+1} = \boldsymbol{\theta}_c$, else, stay at the current point $\boldsymbol{\theta}_{k+1} = \boldsymbol{\theta}_k$.

In the search we have used a diagonal form of the covariance matrix in the gaussian proposal distribution (11.34), with the following elements: $\mathcal{C} = [\mathrm{diag}(10^{-4}, 10^{-12}, 10^{-20}, 10^{-28})]^2$ corresponding to the parameter set $\{f, \dot{f}, \ddot{f}, \dddot{f}\}$. And $\mathcal{T}_2$ used to scale the covariance matrix decays linearly with the number of members in the chain from 1 to 5×10^{-4}. We have found that the use of the actual Fisher information matrix as $\mathcal{C}$ did not improve significantly the search results. We run about 50 chains on both noiseless data and noisy data. All the parameter sets that generate an SNR larger than a certain threshold (we have used $SNR > 4.5$) are recorded. Notice that there are possibly many such qualified parameter sets in a single chain. Thus, we have hundreds to thousands of qualified parameter sets or local maxima. These local maxima contain information about the signal. We will analyze these local maxima in the next section.

11.5 Analysis of the Search Results and Mapping to the Physical Parameters

In this section we will explain how we use the results of MCMC search described in the previous section and reconstruct harmonics of the GW signal. Furthermore, we use the model of EMRI (NK) to estimate the physical parameters of the system.

11.5.1 Clustering Algorithms

In this subsection we extract information from the local maxima detected by MCMC search. We first focus on the noiseless data to explain the algorithm, then modify it a bit and apply it to the noisy data. Since this work is the first of a series of papers, the main task here is to establish the framework and justify the method. Hence, as mentioned above, we have assumed that the sky position of the source is known and concentrate on the intrinsic parameters only. This will save us some time, yet maintain all the main features of the problem. As a result, each local maximum is characterized only by the frequency and its derivatives $(f, \dot{f}, \ddot{f}, \dddot{f})$.

Let us look at one example to understand how we extract the information about the source from the detected local maxima. We take a particular solution of MCMC search and for each harmonic of PW we can compute cumulative F-statistic according to the prescription given in Sect. 11.3.3. We concentrate only on those harmonics which give significant contribution to the total F-statistic. If the harmonics of PW match perfectly the harmonics of a signal we should observe something similar to Fig. 11.3, however it is rare when we detect a full harmonic (only sometimes for the strongest). More frequently, we detect a part of a harmonic (frequency and derivatives close to true but not exact) or even several harmonics at different instances of time as shown in Fig. 11.6. The black and green curves are two strong harmonics of a signal (black being stronger), and the blue is a harmonic of PW. In the pink regions, our template matches for a short period of time the frequency of a signal (two distinct harmonics at two instances). The corresponding cumulative F-statistic is shown in Fig. 11.7. There are two positive jumps in the accumulation of the F-statistic which correspond to two instances of intersection. Therefore, we can conclude that the positive slope in the cumulative F-statistic (if it happens over a significant duration) corresponds to the part of the frequency and time where a harmonic of PW matches

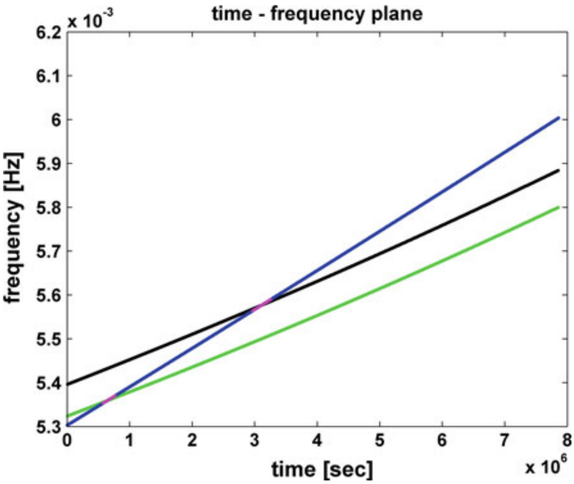

Fig. 11.6 Time–frequency plot of harmonics. The *black* and *green* tracks are two strong harmonics of the EMRI signal (*black* being stronger). The *blue* track corresponds to a harmonic of PW that accumulates a significant F-statistic. It intersects the true harmonics at the *pink* segments, those correspond to times of increase of F-statistic, see Figs. 11.7 and 11.8

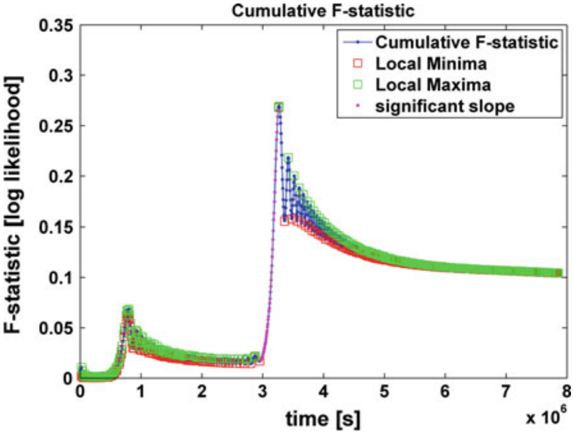

Fig. 11.7 Unfiltered cumulative F-statistic corresponding to the PW harmonic and data given in Fig. 11.6. The F-statistic labeled on the vertical axis has only relative meaning, since we work with the noiseless data. The *green* and *red squares* mark the extremes of the curve, thus distinguishing between the increasing and the decreasing slopes. The large number of the extremes is due to the beating between the true harmonics and the trial harmonic

(at least partially) some harmonics of a signal. We collect such events of matching and display them on the time–frequency plane, resembling the mosaic of a true signal.

The violent oscillation in Fig. 11.7 is one of the three types of oscillations on the cumulative F-statistic curve mentioned in the previous section. In fact, it is the beat note between the true harmonics and the local maximum. Observe that the beat notes happen at relatively higher frequency, while the increasing slopes (where the local maximum matches the frequencies of the true harmonics) have relative low frequency. Thus, we design a third-order Butterworth low pass filter to get rid of the beat notes. After the low-pass filter, the cumulative F-statistic has only few extrema, as shown in Fig. 11.8. After clearing up the cumulative F-statistic, we apply two criteria for identifying a significant F-statistic accumulation: (i) the slope must be larger than certain threshold; (ii) the accumulation time must be over longer than certain period. As it is seen by eye tuning those two parameters should be sufficient to get the right parts of cumulative F-statistic. In our search we have made the following choice for those parameters. In the case of noiseless data, we require the slope to be larger than one-tenth of the largest slope of the cumulative F-statistic of that trial harmonic, and the cumulative time (over which we observe steep positive slope) to be longer than three days.

We plot all recovered patches on the time–frequency plane in Fig. 11.9, where we can identify by eye 13 strong harmonics. For comparison, the time–frequency plane of all the 30 harmonics of the signal without noise is shown in Fig. 11.10, where the F-statistic value of each harmonic is indicated by its color. Although the weaker harmonics are lost in Fig. 11.9, the strong ones retain enough information about the EMRI system evolution, hence allowing us to recover the physical parameters we

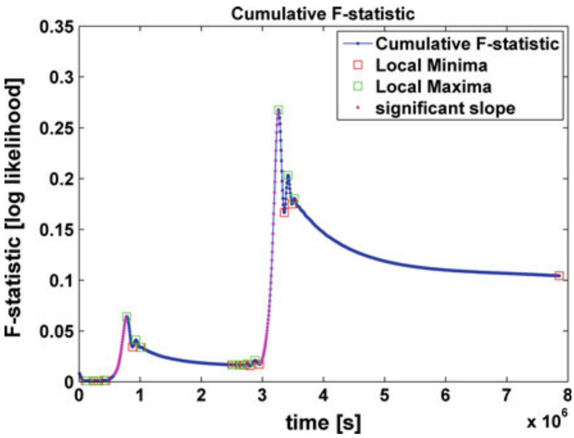

Fig. 11.8 Filtered cumulative F-statistic corresponding to the situation depicted in Fig. 11.6. It is similar to Fig. 11.7, but after applying the low pass filter to remove the beatings (high frequency oscillations)

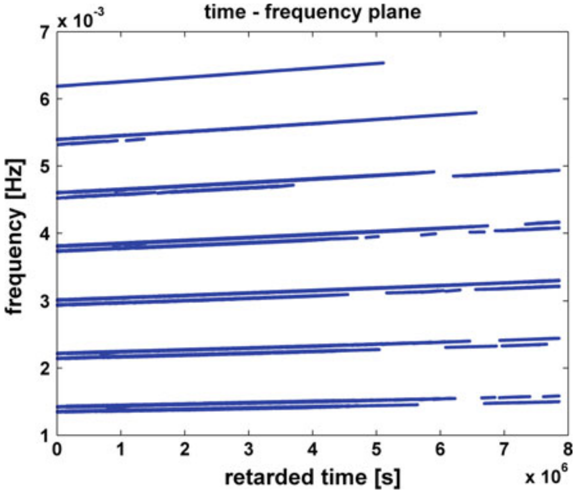

Fig. 11.9 Time–frequency plot of all patches corresponding to strong accumulation of F-statistic. We can identify parts of frequency tracks of 13 EMRI harmonics. Each track in this plot has a finite width coming from different solutions of MCMC search which have different precision of matching the signal

are interested in. Zooming at a specific harmonic in time and frequency, one will see that there are many patches from different results and at each instant we observe a finite spread in the frequencies for a given harmonic. This is due to various solutions from MCMC search matched a given harmonic of a signal with different precision. However, we expect that the distribution of found frequencies at each instant of time will be centered at the true frequency of the signal's harmonic. As an example, we show distribution of found frequencies at a particular instance of time for two harmonics in Fig. 11.11. In that plot we show the histogram of detected frequencies at that time in blue and Gaussian fit as smooth green curves. This is to be compared with frequencies of two harmonics of a signal at the same time in red. As mentioned above, different solutions of MCMC search vary in precision of matching the signal at different instances, and we can use accumulation time as a measure of goodness

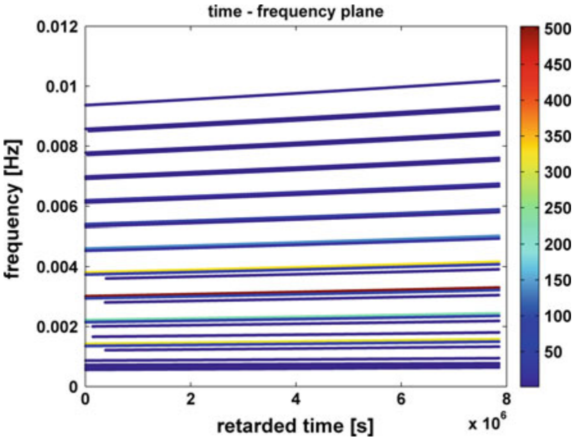

Fig. 11.10 Time–frequency plot of all the 30 harmonics of the signal without noise. The F-statistic of each harmonic is indicated by its color

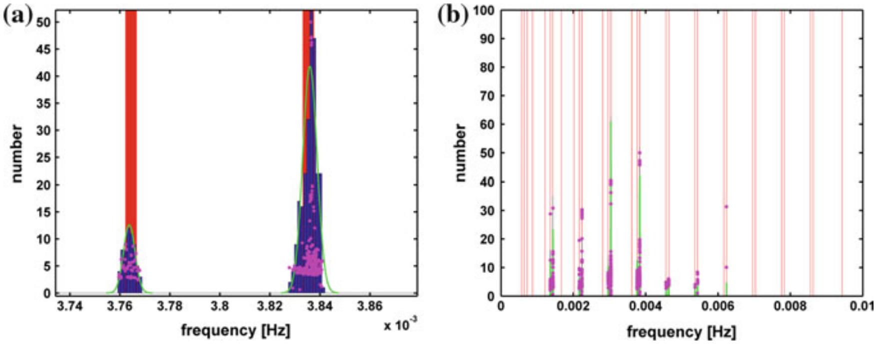

Fig. 11.11 **a** Zoom at two harmonics at a specific instance of time. The *red* stems denote the frequencies of the true harmonics of a signal, while the *blue* histogram shows the detected frequencies at this instant. The *green curves* display the Gaussian fit to the frequency data with re-scaled amplitudes. The vertical axis of *pink points* indicates the relative time over which we have observed strong accumulation of F-statistic for each solution. **b** Similar plot for all the harmonics at the same instant, where 13 harmonics out of 30 are identified

of match of a signal by a given solution. The relative accumulation time of different solutions are shown as pink points in Fig. 11.11. First, one can see that Gaussian fit lies on the top of the true frequency, and second, that the distribution of pink points is similar to the blue histogram, so either can be taken to characterize the found harmonics of a signal. Similarly, we can do at each instance of time for all found tracks in the time–frequency plane. For the noiseless search we picked uniformly 10 instances and made a Gaussian fit around each harmonic. We identify the mean of the Gaussian fit as the most likely frequency of a signal's harmonics at that instance

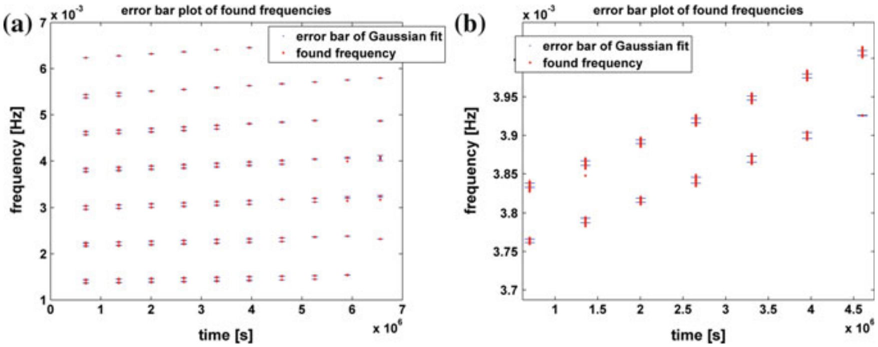

Fig. 11.12 **a** Gaussian fit to the detected frequencies at ten instants. The *red points* represent the mean of a Gaussian fit as shown in Fig. 11.11 for each harmonic at ten instants . The *blue error bars* show the 1σ uncertainties of the Gaussian fits. Note the tiny error bars are along the frequency dimension which indicates that the MCMC search localizes quite well frequencies of the EMRI's harmonics. **b** A zoom-in plot of (**a**) at two strong harmonics. Most of the *red points* are clustered and overlapping with each other (color online figure)

and we identify the spread (standard deviation) of a distribution as an error in our evaluation of a frequency. The result of this clustering is given in Fig. 11.12.

In the case of data with the detector noise, the basics and the strategy are roughly the same as in the noiseless case with minor modifications. In the beginning, we record the local maxima with SNR greater than 4.5. Next, we select the significant increasing slopes of the cumulative F-statistic with three requirements: (i) the maximum F-statistic along the cumulative F-statistic curve is larger than 50, (ii) the minimum slope of the significant increasing segment is larger than $4 \times 10^{-6}\,\mathrm{s}^{-1}$, (iii) the duration of a monotonic increase is longer than about a week. Those conditions are more stringent than for the noiseless case and eliminate several found weak harmonics of the EMRI signal. However, at the same time they significantly reduce the false events (and that is what we want). From this selection, we identify 5 strong harmonics in the noisy case. After that the procedure is similar to the noiseless case.

11.5.2 Search for Physical Parameters

Now we are in a position to recover the physical parameters of the binary system. First, we need to adopt the model for the orbital evolution, and here we have employed the same model as used in the simulation of the data sets. In the noiseless case the only reason for the deviation of recovered parameters from the true values is due to inaccurate identification of the tracks in the time–frequency plane or due to ambiguity in solving the inverse problem (mapping harmonic tracks onto the physical parameters, m/M, a, e, ι, p/M). We have performed the search on the time–frequency plane similar in spirit to [29]. We have used the weighted chi-square test

$$\chi^2 = \sum \min_{f_{lmn}} \left(\frac{f_{lmn} - f_{\mathrm{mean}}}{\sigma_f} \right)^2$$

between the signal tracks (for different parameters) and the recovered tracks (Fig. 11.12). We have used particle swarm optimization (PSO) and genetic algorithm (GA) as two independent search methods to test the robustness of our result. We start with describing the PSO method, and then give brief overview of GA.

Particle swarm optimization (PSO) is a stochastic optimization method introduced by Kennedy and Eberhardt in 1995 [30]. In gravitational wave data analysis, PSO was first applied to a binary inspiral signal [31]. In this section, we briefly describe the algorithm, while further details can be found in the Refs. [30, 31].

The goal of PSO is to find the global minimum/maximum (here we minimize the chi-square test) of a parameterized functional $\kappa(\boldsymbol{\theta})$ and the corresponding parameter set $\boldsymbol{\theta}_*$, where $\boldsymbol{\theta}$ stands for an arbitrary parameter set in $\mathbb{R}^n$. The idea is to evaluate $\kappa(\boldsymbol{\theta}_i)$ simultaneously at different parameter sets $\boldsymbol{\theta}_i$, $i = 1, 2, \ldots,$ treating them as particles in the parameter space, and evolve them according to certain dynamics until the stable solution is reached. Let us denote the ith particle out of a swarm of N_p particles during kth iteration in the search by $\boldsymbol{\theta}_i[k]$. Its position in the parameter space in the next iteration is determined by its velocity in the current iteration $\boldsymbol{v}_i[k]$,

$$\boldsymbol{\theta}_i[k+1] = \boldsymbol{\theta}_i[k] + \boldsymbol{v}_i[k]. \tag{11.36}$$

Usually, the particles start with randomly chosen positions $\boldsymbol{\theta}_i[1]$ and velocities $\boldsymbol{v}_i[1]$. Up to kth iteration, we denote the ith particle's best location by $\boldsymbol{\theta}_i^p[k]$, in the sense that

$$\kappa(\boldsymbol{\theta}_i^p[k]) = \min_{j \le k} \kappa(\boldsymbol{\theta}_i[j]). \tag{11.37}$$

The global best location $\boldsymbol{\theta}_i^g[k]$ up to the kth iteration is defined by

$$\kappa(\boldsymbol{\theta}^g[k]) = \min_{i} \kappa(\boldsymbol{\theta}_i^p[k]). \tag{11.38}$$

Note that particle best locations and the global best location are the best parameters respectively found by the individual particles and the whole swarm in the entirely history of the search up to the kth iteration. They are updated only when a better parameter set is found. These best locations contain a lot of information about the functional $\kappa(\boldsymbol{\theta})$, so they are used to guide the particle's motion in the future. Explicitly, the velocities are updated with the following equation

$$\begin{aligned} \boldsymbol{v}_i[k+1] = {} & w\boldsymbol{v}_i[k] + c_1\chi_1(\boldsymbol{\theta}_i^p[k] - \boldsymbol{\theta}_i[k]) \\ & + c_2\chi_2(\boldsymbol{\theta}^g[k] - \boldsymbol{\theta}_i[k]), \end{aligned} \tag{11.39}$$

where w is called the *inertia weight*, c_1, c_2 are called the *acceleration constants* (we take them to be the same as in [31]) and χ_1, χ_2 are random numbers drawn from $\mathcal{U}(0, 1)$. We run PSO search several times until the return result is confirmed by several searches.

The second search method is called Genetic Algorithm (GA) and there we evolve a number of parameter sets (points in the parameter space $\mathbb{R}^n$). Each parameter set $\boldsymbol{\theta}_i$ is called an organism, individual parameters are called the genes of this organism and the set of organism at kth search iteration step is called kth generation. We evolve generations according to the prescribed rules called "parents selection", "breading" and "mutation". The main idea of this optimization technique is to evolve colony of organisms toward the better fitness (which could be likelihood ratio or, in our case, chi-square value) like in Darwin's theory of natural selection. The strong organisms (with better fitness) participate more often in breading and therefore drag the colony toward the better values (lower) of chi-square. Mutation brings element of randomness in the search and occasional "positive" mutations help to avoid trapping around local minimum. For use of GA in GW data analysis we refer to [32, 33] and references therein.

Let us give few more details specific to the implementation used in here. We use χ^2 value as a measure of fitness for each organism (smaller value is better). In each generation we use the roulette method with the selection probability proportional to the fitness of each organism. For breeding we have used the one random point crossover rule. The probability mutation rate is monotonically decreasing function of the generation number: we have started with high probability of mutation to explore a large part of the parameter space and decrease it gradually as organisms converge to a particular part of the parameter space. We have used "children" and "parents" sorted in the fitness to make a new generation: we use 50 % of the best organisms. We automatically achieve the "elitism" in a way that the best χ^2 value is never increasing from one generation to the next.

We use the multi-step method to accelerate the search. In each step we evolve the colony for 500 generations as described above, but each new step uses the last generation of the previous step as the initial state. We have started evolution in the first step with completely random distribution of the organisms. The evolution of the colony at each step finishes with a very small mutation probability and with organisms confined to a quite small volume of the parameter space. The consequent search steps ensure that the found solution is a robust solution with respect to increase of the mutation probability which disperses organisms forcing them to explore the parameter space for presence of a solution with better fitness. This helps to avoid being trapped in the local minima. The termination condition is the stability of the best solution over several steps of the search.

We have applied both those methods to fit the found tracks on the time frequency plane with the harmonics of EMRI signal. The search is done in 5 dimensional parameter space with quite broad priors on $(e, p/M, \iota, a, \mu = m/M)$, those are the eccentricity, the semi-latus rectum, the orbital inclination angle at the moment of beginning of observation, the spin of the MBH, and, the mass ratio between the stellar BH and the MBH. The total mass is not present here, we have kept it fixed

Table 11.1 Recovered parameters of EMRI against actual parameters used in simulated data sets

Description	$e(t_0)$	$p(t_0)$	$\iota(t_0)$	a	μ
True parameters	0.4	8.0	0.349	0.9	10^{-5}
Recovered parameters (with noise)	0.395	8.029	0.342	0.891	9.79×10^{-6}
Recovered parameters (no noise)	0.402	7.991	0.360	0.901	1.002×10^{-5}

to $M = 10^6 M_\odot$. For a given set of parameters, our search algorithm computes three fundamental orbital frequencies as functions of time, then a weighted chi-square goodness of fit test is preformed on harmonics of the signal. We use the means and standard deviations from the Gaussian fit as found point and its error in the time–frequency plane. The best fit corresponds to the lowest value of χ^2. We have used harmonics of the signal, which are expected to be strong over the large part of the parameter space, and have found this "harmonic table" by intensive monte carlo with NK models generated in the frequency domain. The index table has been truncated by choosing harmonics contributing (in total) 90 % of the overlap with a total signal.[1]

The recovered parameters are given in the Table 11.1.

11.6 Summary

In this paper we have introduced the phenomenological family of waveforms (PW) for detecting EMRI signals in the data from the LISA-like observatory. The template is constructed out of independent (over the time interval we have applied our analysis) harmonics of slowly evolving three orbital frequencies. We have neglected the amplitude evolution and presented the phase as a Taylor series up to the third derivative of frequency. Our analysis was restricted to the case of monotonically increasing frequencies. This condition will break only close to the plunge. The number of harmonics and range of indices were taken from the analysis of dominant harmonics of our model signal, though we have found at the end that the search only weakly depends on the number of used harmonics (only through the accumulated total SNR, which should be sufficient to claim detection).

Constructed phenomenological templates allows us to search for EMRI signals in a model independent way. This way we avoid complexity of accurate modeling the orbital evolution and gravitational waveform during the search. In addition PW

---

[1] The total signal here to be a NK waveform with a large number of harmonics. We still truncate the number of harmonics used to build the signal: we stop if the inclusion of the next harmonic does not change overlap with the already built signal by more than 0.1 %.

cover also all possible small deviations of the background spacetime from the Kerr solution which would influence the signal's phase and could lead even to loss of the signal if the template assumes pure Kerr background geometry.

We have used MCMC based search to find a large number of local maxima of the likelihood surface. We were not that lucky to find the global maximum. We have analyzed the found solutions by means of cumulative F-statistic over the time and identified the patches of the signal which were match by templates. As a result, we have constructed a time–frequency map of (parts of) the signal's harmonics. Each track could be characterized by the best guess and the error bar at each instance of time (by fitting Gaussian profile to found frequencies at that time for each track). The next step is to assume a model for the binary orbital evolution, and check if the found time–frequency picture corresponds to the strongest harmonics of a signal. In other words, we want to find the physical parameters of the binary system which strong GW harmonics could leave the found imprint. We do that by conducting a search using particle swarm optimization techniques and, independently, genetic algorithm. We have used weighted chi-square goodness of fit test to choose the best matching harmonics of the signal. We have assumed the same model as was used in the simulated data, and the recovered parameters are within 2 % of the true values.

We want to make few final remarks.

(i) The found time–frequency tracks of the GW signal from EMRI did not assume any particular model. The mapping of these tracks to the physical parameters could be done in post processing using several models. We have chosen on purpose rather short (3 month) duration of the data. The search procedure could be repeated for each three months and then one can check consistency of a given model or further improve accuracy in the recovered parameters (if our model gives consistent parameters of the system across different data segments). This could be a powerful method to search deviations from "Kerness".

(ii) We have neglected the amplitude evolution of the harmonics which is justifiable on the considered short span of time, where the change in amplitude is small (less than 20 % for the detectable strong harmonics in our case). As mentioned above, for high SNR signals we can analyze the data piecewise. However, for weak signals we need to extend the validity of the PW by introducing the amplitude evolution and higher order derivatives of frequencies. The amplitude evolution is also important in case of the high eccentricity. We will delegate this issue to the next publication.

(iii) In the mapping of the time–frequency tracks to the physical parameters of the binary, we have only weakly used information about the strength of each track/harmonic. We have found that the information stored in the frequency evolution is sufficient to recover parameters of EMRI. However, additional information about the strength of the recovered harmonics and harmonics of the modeled GW signal could give us additional confidence in the result and/or distinguish between several solution, if ambiguity happens.

(iv) Mapping from the found time–frequency tracks onto the physical parameters might turn out to be the most computationally intensive task. However, one might use the information about the strength and a number of found harmonics to restrict a volume of the searched parameter space. In addition, to perform mapping we require mainly the computation of the orbital evolution, not the full waveform. However, it is then important to know which harmonics are the strongest for a given parameter set.

(v) In the future work we intend to include the sky location and the MBH mass into the search and investigate the possibility to differentiate between different models of EMRIs based on the results of MCMC search with PW (as discussed in (i)).

11.7 Supplementary A: Calculate the Evolution of the Fundamental Frequencies of EMRIs and Numerical Kludge waveforms

For test particles, the geodesics in the Kerr spacetime in the Boyer-Lindquist coordinates (r, θ, ϕ, t) can be described by the following set of differential equations

$$\left(\Sigma\frac{\mathrm{d}r}{\mathrm{d}\tau}\right)^2 = [E(r^2+a^2)-L_za]^2 - \Delta[r^2+(L_z-aE)^2+Q] \equiv V_r(r), \tag{11.40}$$

$$\left(\Sigma\frac{\mathrm{d}\theta}{\mathrm{d}\tau}\right)^2 = Q-\cos^2\theta\left[a^2(1-E^2)+\frac{L_z^2}{\sin^2\theta}\right] \equiv V_\theta(\theta), \tag{11.41}$$

$$\Sigma\frac{\mathrm{d}\phi}{\mathrm{d}\tau} = \frac{a}{\Delta}[E(r^2+a^2)-L_za]+\frac{L_z}{\sin^2\theta}-aE \equiv V_\phi(r,\theta) \equiv V_{\phi 1}(r)+V_{\phi 2}(\theta), \tag{11.42}$$

$$\Sigma\frac{\mathrm{d}t}{\mathrm{d}\tau} = \frac{r^2+a^2}{\Delta}[E(r^2+a^2)-L_za]+a(L_z-aE\sin^2\theta) \equiv V_t(r,\theta) \equiv V_{t1}(r)+V_{t2}(\theta), \tag{11.43}$$

where we have defined

$$\Sigma = r^2+a^2\cos^2\theta, \tag{11.44}$$

$$\Delta = r^2-2Mr+a^2, \tag{11.45}$$

and E, L_z, Q respectively denote the energy, the angular momentum along the z-axis and the Carter constant. To prevent the occurrence of closed time-like lines in the spacetime, the spin of the black hole satisfies $a/M \in [0, 1]$. The evolutions of r and θ can be separated by introducing the so-called Mino time λ,

$$\left(\frac{\mathrm{d}r}{\mathrm{d}\lambda}\right)^2 = V_r(r), \tag{11.46}$$

$$\left(\frac{\mathrm{d}\theta}{\mathrm{d}\lambda}\right)^2 = V_\theta(\theta), \tag{11.47}$$

$$\frac{\mathrm{d}\phi}{\mathrm{d}\lambda} = V_\phi(r,\theta) = V_{\phi 1}(r) + V_{\phi 2}(\theta), \tag{11.48}$$

$$\frac{\mathrm{d}t}{\mathrm{d}\lambda} = V_t(r,\theta) = V_{t1}(r) + V_{t2}(\theta). \tag{11.49}$$

For bounded motions, the solutions of r and θ in the Mino time are strictly periodic functions, with periods given by the following

$$T_r = 2\int_{r_{\min}}^{r_{\max}} \frac{\mathrm{d}r}{\sqrt{V_r(r)}}, \tag{11.50}$$

$$T_\theta = 2\int_{\theta_{\min}}^{\pi-\theta_{\min}} \frac{\mathrm{d}\theta}{\sqrt{V_\theta(\theta)}}. \tag{11.51}$$

The corresponding frequencies are defined as

$$F_r = 1/T_r, \tag{11.52}$$

$$F_\theta = 1/T_\theta. \tag{11.53}$$

Since r and θ are strictly periodic functions of λ, the terms $V_\phi(r,\theta)$ and $V_t(r,\theta)$ can be expanded in Fourier series with fundamental frequencies F_r and F_θ in the Mino time λ. Hence, ϕ and t as functions of λ can be easily obtained. Ignoring the oscillating terms, the average accumulating frequency for ϕ is

$$F_\phi = \frac{1}{2\pi}\left[\int_0^{T_r} V_{\phi 1}[r(\lambda)]\frac{\mathrm{d}\lambda}{T_r} + \int_0^{T_\theta} V_{\phi 2}[\theta(\lambda)]\frac{\mathrm{d}\lambda}{T_\theta}\right]. \tag{11.54}$$

The average ratio between the coordinate time t and the Mino time λ can also be calculated

$$R_t = \int_0^{T_r} V_{t1}[r(\lambda)]\frac{\mathrm{d}\lambda}{T_r} + \int_0^{T_\theta} V_{t2}[\theta(\lambda)]\frac{\mathrm{d}\lambda}{T_\theta}. \tag{11.55}$$

Therefore, the three fundamental frequencies of the geodesics are

$$f_r = F_r/R_t, \tag{11.56}$$

$$f_\theta = F_\theta/R_t, \tag{11.57}$$

$$f_\phi = F_\phi/R_t. \tag{11.58}$$

For a given Kerr black hole with mass M and spin a, the three fundamental frequencies of its geodesics can be calculated from the three constants of motion $E,\ L_z,\ Q$, whose evolutions can be obtained from the post-Newtonian formulae in the following form

$$\frac{\mathrm{d}E}{\mathrm{d}t} = f_E(a, M, m, p, e, \iota), \tag{11.59}$$

$$\frac{\mathrm{d}L_z}{\mathrm{d}t} = f_L(a, M, m, p, e, \iota), \tag{11.60}$$

$$\frac{\mathrm{d}Q}{\mathrm{d}t} = f_Q(a, M, m, p, e, \iota). \tag{11.61}$$

To generate numerical kludge waveforms, we need to solve for $r(t)$, $\theta(t)$ and $\phi(t)$ numerically. Once these functions are obtained, the waveforms can be generated with the help of the quadrupole formula or the quadrupole-octupole formula, etc. Here, we will briefly describe the way of calculating $r(t)$, $\theta(t)$ and $\phi(t)$ The derivatives of r and θ can be written as

$$\Sigma\frac{\mathrm{d}r}{\mathrm{d}\tau} = \pm\sqrt{V_r(r)}, \tag{11.62}$$

$$\Sigma\frac{\mathrm{d}\theta}{\mathrm{d}\tau} = \pm\sqrt{V_\theta(\theta)}. \tag{11.63}$$

Due to the flipping signs, these equations cannot be directly integrated. We need to use new variables to avoid the flipping signs. We first define an eccentricity e and a semilatus p as follows

$$p = \frac{2r_{\max}r_{\min}}{r_{\max}+r_{\min}}, \tag{11.64}$$

$$e = \frac{r_{\max}-r_{\min}}{r_{\max}+r_{\min}}, \tag{11.65}$$

which imply the following

$$r_{\min} = \frac{p}{1+e}, \tag{11.66}$$

$$r_{\max} = \frac{p}{1-e}. \tag{11.67}$$

We also define an inclination angle

$$\tan^2\iota = \frac{Q}{L_z^2}. \tag{11.68}$$

Then, we can replace the variable r by ψ through the following relation

$$r = \frac{p}{1+e\cos\psi}. \tag{11.69}$$

This is valid, since the evolutions of e and p are much slower than the evolution of r. Similarly, we wish to replace θ by χ through the following relation

$$\cos^2\theta = z_- \cos^2\chi, \tag{11.70}$$

where z_- is defined by the following formula

$$\begin{aligned} &-a^2(1-E^2)(z_+ - z)(z - z_-) \\ &= a^2(1-E^2)z^2 - z[Q + L_z^2 + a^2(1-E^2)] + Q. \end{aligned} \tag{11.71}$$

Instead of directly evolving r and θ, we evolve ψ and χ. The evolution equations for ψ, χ and ϕ are given by

$$\begin{aligned} \frac{\mathrm{d}\psi}{\mathrm{d}t} &= M\sqrt{1-E^2}[(p - r_3(1+e)) - e(p + r_3(1-e)\cos\psi)]^{1/2} \\ &\quad [(p - r_4(1+e)) + e(p - r_4(1+e)\cos\psi)]^{1/2}/[\gamma + a^2Ez_-\cos^2\chi](1-e^2), \end{aligned} \tag{11.72}$$

$$\frac{\mathrm{d}\chi}{\mathrm{d}t} = \frac{\sqrt{a^2(1-E^2)[z_+ - z_-\cos^2\chi]}}{\gamma + a^2Ez_-\cos^2\chi}, \tag{11.73}$$

$$\frac{\mathrm{d}\phi}{\mathrm{d}t} = \frac{V_\phi}{V_t}, \tag{11.74}$$

where we have defined

$$\gamma = E\left[\frac{(r^2+a^2)^2}{\Delta} - a^2\right] - \frac{2MraL_z}{\Delta}, \tag{11.75}$$

and r_3 and r_4 are defined by the following formula

$$V_r = (1-E^2)(r_{\max} - r)(r - r_{\min})(r - r_3)(r - r_4). \tag{11.76}$$

References

1. L. Barack, C. Cutler, Phys. Rev. D **69**, 082005 (2004). arXiv:gr-qc/0310125
2. L. Barack, C. Cutler, Phys. Rev. D **75**, 042003 (2007). arXiv:gr-qc/0612029
3. S. Babak, J.R. Gair, A. Petiteau, A. Sesana, Class. Quantum Gravity **28**, 114001 (2011). arXiv:gr-qc/1011.2062
4. P. Amaro-Seoane, B. Schutz, C.F. Sopuerta. arXiv:gr-qc/1009.1402
5. P. Amaro-Seoane, S. Aoudia, S. Babak, P. Binetruy, E. Berti et al. arXiv:gr-qc/1202.0839
6. N. Warburton, S. Akcay, L. Barack, J.R. Gair, N. Sago, Phys. Rev. D **85**, 061501 (2012). arXiv:gr-qc/1111.6908
7. L. Barack, N. Sago, Phys. Rev. D **81**, 084021 (2010). arXiv:gr-qc/1002.2386
8. J.R. Gair, E.E. Flanagan, S. Drasco, T. Hinderer, S. Babak, Phys. Rev. D **83**, 044037 (2011). arXiv:gr-qc/1012.5111

9. P. Diener, I. Vega, B. Wardell, S. Detweiler, Phys. Rev. Lett. **108**, 191102 (2012). arXiv:gr-qc/1112.4821
10. P. Eric, A. Pound, I. Vega, Liv. Rev. Relativ. **14**, 7 (2011). http://www.livingreviews.org/lrr-2011-7
11. S. Babak, H. Fang, J.R. Gair, K. Glampedakis, S.A. Hughes, Phys. Rev. D **75**, 024005 (2007). arXiv:gr-qc/0607007
12. J.R. Gair, K. Glampedakis, Phys. Rev. D **73**, 064037 (2006). arXiv:gr-qc/0510129
13. S. Babak, J.R. Gair, E.K. Porter, Class. Quantum Gravity **26**, 135004 (2009). arXiv:gr-qc/0902.4133
14. A. Pound, E. Poisson, Phys. Rev. D **77**, 044013 (2008). arXiv:gr-qc/0708.3033
15. S.A. Teukolsky, Astrophys. J. **185**, 635–647 (1973)
16. K. Martel, Phys. Rev. D **69**, 044025 (2004). arXiv:gr-qc/0311017
17. S. Drasco, S.A. Hughes, Phys. Rev. D **73**, 024027 (2006). arXiv:gr-qc/0509101
18. C.F. Sopuerta, N. Yunes, Phys. Rev. D **84**, 124060 (2011). arXiv:gr-qc/1109.0572
19. C.F. Sopuerta, N. Yunes. arXiv:gr-qc/1201.5715
20. S. Babak et al., Mock LISA data challenge task force. Class. Quantum Gravity **27**, 084009 (2010). arXiv:gr-qc/0912.0548
21. N.J. Cornish, Class. Quantum Gravity **28**, 094016 (2011). arXiv:gr-qc/0804.3323
22. F.B. Estabrook, H.D. Wahlquist, Gen. Relativ. Gravit. **6**, 439 (1975)
23. J.W. Armstrong et al., Time-delay interferometry for space-based gravitational wave searches. ApJ **527**, 814–826 (1999)
24. C. Cutler, Phys. Rev. D, **57**, 7089-7102 (1998). arXiv:gr-qc/9703068
25. L.J. Rubbo, N.J. Cornish, O. Poujade, Phys. Rev. D **69**, 082003 (2004). arXiv:gr-qc/0311069
26. P. Jaranowski, A. Krolak, B.F. Schutz, Phys. Rev. D **58**, 063001 (1998). arXiv:gr-qc/9804014
27. R. Prix, J.T. Whelan, Class. Quantum Gravity **24**, S565-S574 (2007). arXiv:gr-qc/0707.0128
28. T.B. Littenberg, N.J. Cornish, Phys. Rev. D **80**, 063007 (2009). arXiv:gr-qc/0902.0368
29. J.R. Gair, I. Mandel, L. Wen, Class. Quantum Gravity **25**, 184031 (2008). arXiv:gr-qc/0804.1084p
30. J. Kennedy, R.C. Eberhart, in *Proceedings of the IEEE, International Conference on Neural Networks*, vol. 4 (1995) p. 1942. http://ieeexplore.ieee.org
31. Y. Wang, S.D. Mohanty, Phys. Rev. D **81**, 063002 (2010). arXiv:gr-qc/1001.0923
32. J. Crowder, N.J. Cornish, L. Reddinger, Phys. Rev. D **73**, 063011 (2006). arXiv:gr-qc/0601036
33. A. Petiteau, Y. Shang, S. Babak, F. Feroz, Phys. Rev. D **81**, 104016 (2010). arXiv:gr-qc/1001.5380

Chapter 12
Fast Detection and Automatic Parameter Estimation of a Gravitational Wave Signal with a Novel Method

Abstract The detection of gravitational wave usually requires to match the measurement data with a large number of templates, which is computationally very expensive. Compressed sensing methods allow one to match the data with a small number of templates and interpolate the rest. However, the interpolation process is still computationally expensive. In this chapter, we designed a novel method that only requires to match the data with a few templates, yet without needing any interpolation process. The algorithm worked well for signals with relatively high SNRs. It also showed promise for low SNRs signals.

12.1 Introduction

While gravitational wave (GW) signals contain invaluable physical information, extracting this information from the noisy data is quite challenging. Most of the time, GW signals are weaker than the instrumental noise at any instant, but they are predictable and long lived [1]. This gives a way to build up signal-to-noise ratio (SNR) over time by tracking the signals coherently with matched filtering [2]. However, this requires the templates to be exactly the same as the true signal to recover the optimal SNR, or at least resemble the true signal sufficiently in order not to lose much SNR [3]. Since the template waveforms depend on several parameters, one needs to match the data with a huge number of templates in the high dimensional parameter space. Therefore, a normal grid-based search is usually computationally extremely expensive, or even prohibitive. The reduction of the computational cost lies in the center of the modern GW data analysis.

There are several categories of algorithms, successfully reducing the computational cost, such as reduced bases (RB) [4], singular value decomposition (SVD) [5] and principal component analysis (PCA) [6]. These methods make use of the fact that each template is strongly correlated with the templates in its neighbourhood in the parameter space. Therefore, its SNR can be effectively interpolated from the SNRs of the templates in its neighbourhood. In other words, the likelihood surface

Y. Wang, *First-stage LISA Data Processing and Gravitational Wave Data Analysis*,
Springer Theses, DOI 10.1007/978-3-319-26389-2_12

on the grid of the template bank has special properties (sparsity), which allows the compressed sensing [7] algorithms to apply. Instead of using all the templates in the bank, one only needs to calculate the SNRs of a few so-called basis templates (which are different from the original templates), and then interpolate the SNRs of all the other templates in the bank. It is extremely fast to perform matched filtering on that few basis templates comparing to the original bank of templates. However, the interpolation (or sometimes referred to as the reconstruction) process is still computationally expensive.

We wish to design a novel method, which requires to perform matched filtering on a few templates, and in the meantime does not require any interpolation stage (or can automatically reconstruct the parameters of the GW signal). However, this method currently requires a relatively high SNR of the signal. The detailed description of the method and the preliminary simulation results are shown in the following.

12.2 Review of the GW Data Analysis Problem

First of all, we briefly review the convention and notations of the GW data analysis. Usually, the measurement data can be expressed as $s = Ah_* + n$, where n is the noise, A is the amplitude of the signal, h_* is the normalized signal in the measurement, which satisfies $\langle h_*|h_*\rangle = 1$. The inner product of two time series $a(t)$ and $b(t)$ is defined as follows

$$\langle a|b\rangle = \int_{-\infty}^{\infty} \frac{\tilde{a}^*(f)\tilde{b}(f)}{S_n(f)} \mathrm{d}f, \tag{12.1}$$

where $\tilde{a}(f)$, $\tilde{b}(f)$ are the Fourier transforms of $a(t)$ and $b(t)$. $S_n(f)$ is the so-called two-sided noise power spectral density (PSD), usually defined as $\mathrm{E}[\tilde{n}^*(f')\tilde{n}(f)] = S_n(f)\delta(f - f')$.

The GW data analysis problem that we want to solve is formulated as follows. For a set of normalized candidate templates $h_i = h(\Theta_i)$ (we choose the template index $i = 1, \ldots, 2^N$ for convenience) characterized by parameters Θ_i, we want to determine which one is present in the measurement, hence obtaining the parameters Θ_* of the signal. Notice that Θ denotes a set of waveform parameters. For clarity, we require the templates to be nearly independent $\langle h_i|h_j\rangle \ll 1,\ (i \neq j)$. This is not generally true for a whole template bank. However, one can easily divide the entire template bank into a group of smaller template banks, within which the templates are nearly independent.

We assume that the true signal h_* belongs to the template family, $* \in \{1, 2, \ldots, 2^N\}$. The inner product between the measurement data and a template is denoted as

$$\begin{aligned} x_i &\equiv \langle s|h_i\rangle \\ &= A\langle h_*|h_i\rangle + \langle n|h_i\rangle, \end{aligned} \tag{12.2}$$

thus the expectation and the variance are

$$\mathrm{E}(x_i) = A\delta_{*,i} \tag{12.3}$$

$$\begin{aligned} \mathrm{Var}(x_i) &= \mathrm{E}[\langle h_i|n\rangle\langle n|h_i\rangle] \\ &= \langle h_i|h_i\rangle = 1. \end{aligned} \tag{12.4}$$

By identifying the largest inner product x_*, we can detect the signal h_* and estimate its parameters Θ_*. When the inner product x_* is much larger than its standard deviation $\sqrt{\mathrm{Var}(x_*)} = 1$, the significance is high. The above shows a normal search strategy, which requires to perform 2^N inner products.

12.3 The New Algorithm

In this section, we will describe a novel search algorithm. First, we express the waveform indices i in binary, hence each index is an N-digit binary number (e.g. 001011011 . . .). Then, we define N sets $\mathcal{P}_k$ ($k = 1, 2, \ldots, N$) such that $\mathcal{P}_k$ consists of all the indices i whose kth digit is 1. A new template family is defined based on these sets

$$H_k = \sum_{i\in\mathcal{P}_k} h_i. \tag{12.5}$$

The inner products of these new templates with the measurement data are

$$\begin{aligned} X_k &\equiv \langle s|H_k\rangle \\ &= \sum_{i\in\mathcal{P}_k} \langle s|h_i\rangle. \end{aligned} \tag{12.6}$$

The expectation of X_k is

$$\mathrm{E}(X_k) = \begin{cases} A, & * \in \mathcal{P}_k \\ 0, & * \notin \mathcal{P}_k \end{cases} \tag{12.7}$$

The variance can be calculated as follows

$$\begin{aligned} \mathrm{Var}(X_k) &= \mathrm{E}[\langle n|\sum_{i\in\mathcal{P}_k} h_i\rangle^2] \\ &= \sum_{i,j\in\mathcal{P}_k} \langle h_i|h_j\rangle. \end{aligned} \tag{12.8}$$

Since the templates h_i are nearly independent, we have

$$\begin{aligned} \mathrm{Var}(X_k) &= \sum_{i\in\mathcal{P}_k} \langle h_i|h_i\rangle \\ &= 2^{N-1}. \end{aligned} \tag{12.9}$$

Suppose $* \in \mathcal{P}_a$ and $* \notin \mathcal{P}_b$, then

$$\mathrm{E}(X_a - X_b) = A \tag{12.10}$$

$$\begin{aligned} \mathrm{Var}(X_a - X_b) &= \mathrm{E}[\langle n|\sum_{i\in\mathcal{P}_a} h_i - \sum_{j\in\mathcal{P}_b} h_j\rangle] \\ &= \sum_{i\in\{\mathcal{P}_a\cup\mathcal{P}_b-\mathcal{P}_a\cap\mathcal{P}_b\}} \langle h_i|h_i\rangle \\ &= 2^{N-1}. \end{aligned} \tag{12.11}$$

When the expectation A is much larger than the standard deviation $2^{(N-1)/2}$, we can set some threshold $\mathcal{T}$ between A and $2^{(N-1)/2}$. Based on this threshold, a binary number can be obtained as follows: if $X_k > \mathcal{T}$, the kth bit of this binary number is 1, otherwise its kth digit is set as 0. This binary number can be converted to a decimal number i_0. The method identifies the waveform h_{i_0} with parameters Θ_{i_0} to be most probably present in the data. In this new approach, we have used N templates instead of 2^N templates to detect the signal and estimate its parameters. The computational cost is thus reduced from $\mathcal{C}\cdot 2^N$ to $\mathcal{C}\cdot N$. Notice that, if each inner product of the data and a template provides one bit of information (above or below a certain threshold), N is the minimum required number of templates to distinguish 2^N sets of candidate parameters.

12.4 Simulation

To exemplify the performance of the novel method, we consider the following chirp waveform family

$$h(t; f, \dot{f}) = \mathcal{A}\cos(2\pi f t + \pi \dot{f} t^2), \tag{12.12}$$

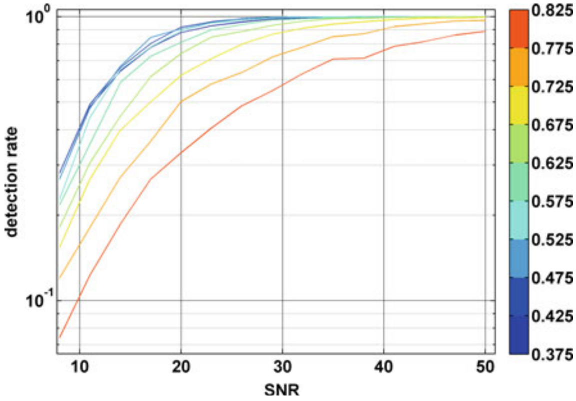

Fig. 12.1 Detection rate at different SNRs and thresholds. The *color bar* indicates the value of the coefficient c. The algorithm achieves the optimal performance, when c is around 0.5. The detection rate is above 99 %, when SNR is above 30

where $\mathcal{A}$ is the normalization constant, f and $\dot{f}$ are the two intrinsic parameters to be estimated. We have simulated 100 s measurement data at 1 kHz with different SNRs. The parameters of the true signal are $f_* = 100\,\text{Hz}$ and $\dot{f}_* = 0.2\,\text{Hz/s}$. We have considered 2^6 candidate waveforms with the parameter mesh grid

$$f = \{70, 80, 90, 100, 110, 120, 130, 140\}\,\text{Hz},$$

$$\dot{f} = \{-0.3, -0.2, -0.1, 0, 0.1, 0.2, 0.3, 0.4\}\,\text{Hz/s}.$$

The threshold is simply chosen as $\mathcal{T} = c \cdot \max(X_k)$, where we have tried several values of the coefficient c. The SNR varies from 8 to 50 with a uniform spacing 3. For each combination of SNR and the threshold, we carried out a Monte Carlo simulation with 1000 different noise realizations. If the algorithm identifies the true signal and its true parameters, the detection is successful. The success rate is called the detection rate. Figure 12.1 shows the detection rate at different SNRs and thresholds, where the color bar indicates the value of the coefficient c. The best performance is realized by setting the coefficient c around 0.5. For signals with SNR higher than 30, the detection rate of the algorithm is above 99 %. Thus, the algorithm with the least number of new templates works efficiently at relatively high SNRs. However, at low SNRs, the detection rate is low. We will see whether we could improve the detection rate by slightly increase the computational cost.

12.5 Features of the Algorithm

Let us take a close look at the features of the algorithm to better understand it. First, we review some concepts and conventions, which will be used later on. The error function $\mathrm{erf}(x)$ is usually defined as follows

$$\mathrm{erf}(x) = \frac{2}{\sqrt{\pi}} \int_0^x e^{-x^2} dx. \tag{12.13}$$

The cumulative distribution function $F(a)$ is defined as follows

$$\begin{aligned} F(a) &= P(x \leq a) \\ &= \int_{-\infty}^{a} p(x) dx, \end{aligned} \tag{12.14}$$

where $p(x)$ is the probability density function. For a Gaussian random variable x with an expectation μ and a standard deviation σ, we denote its cumulative distribution function as $F_{\mu,\sigma}(x)$. It is straightforward to show that

$$F_{\mu,\sigma}(x) = \frac{1}{2}\left[1 + \mathrm{erf}\left(\frac{x-\mu}{\sqrt{2}\sigma}\right)\right]. \tag{12.15}$$

For the set of 2^N independent templates h_i, if 2^N is smaller than the number of samples in the observation data, $x_i = \langle s|h_i \rangle$ are also independent. To characterize the performance of the algorithms, we want to examine to what extent can the noise mimic a signal. Since the signal part of x_i only contributes a DC bias to its probability distribution, we can ignore the DC part and only consider the random part of x_i, which is $\langle n|h_i \rangle$. It can be shown without much effort that the probability density function of the maximum of these 2^N random variables x_i is the following

$$p_{\max}(x) = \frac{2^N}{\sqrt{2^{2^{N+1}-1}\pi}}\left[1 + \mathrm{erf}\left(\frac{x}{\sqrt{2}}\right)\right]^{2^N-1} e^{-\frac{x^2}{2}}. \tag{12.16}$$

Since these random variables follow Gaussian distribution with a zero mean, which is symmetric about the y-axis, the minimum of these random variables has a probability density function as follows

$$p_{\min}(x) = \frac{2^N}{\sqrt{2^{2^{N+1}-1}\pi}}\left[1 + \mathrm{erf}\left(\frac{-x}{\sqrt{2}}\right)\right]^{2^N-1} e^{-\frac{x^2}{2}}. \tag{12.17}$$

By contrast, the random variables X_k are correlated. The analytical expression (if there exists) of the probability density function of the maximum of these random variables is not easy to calculate. Instead, this probability density function is calculated numerically via Monte Carlo simulations later on. If we artificially ignore

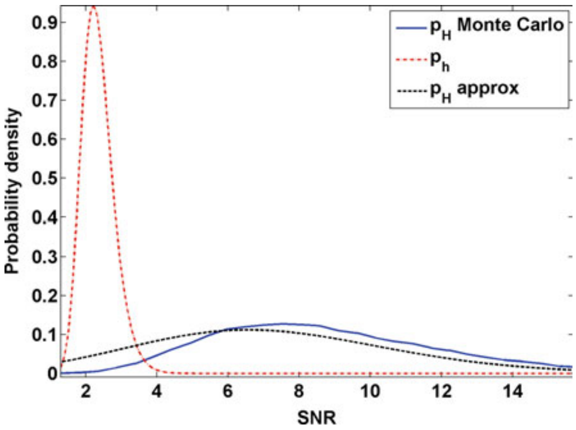

Fig. 12.2 The probability density functions of the random part of x_i and X_k, which are $\langle n|h_i\rangle$ and $\langle n|H_k\rangle$

the correlation between X_k for the moment, an analytical approximate expression can be obtained as follows

$$p_{\max}(X)\ \frac{N}{\sqrt{2^{3N-2}\pi}}\left[1+\operatorname{erf}\left(\frac{X}{\sqrt{2^N}}\right)\right]^{N-1} e^{-\frac{X^2}{2^N}}. \tag{12.18}$$

For the case we considered, we have $N = 6$. The probability density functions of the maximum of the random part of x_i and X_k are shown in Fig. 12.2, where for X_k we have plotted both an analytical approximate curve and the results from Monte Carlo simulation of 5×10^4 different noise realizations. This figure tells us to what extent SNRs could be mimicked by pure noise. As expected, in case of X_k, the noise could mimic larger SNRs. This can also be seen from the larger standard deviation of X_k. In fact, this is the reason for the drop in the detection rate at low SNRs in Fig. 12.1.

Next, let us examine the role of the threshold $\mathcal{T} = \frac{1}{2}\max(X_k)$. In the previous simulations, we have six inner products X_k, $(k = 1, \ldots, 6)$, each corresponding to an SNR achieved by H_i. Since the detection criteria only depends on the ratio between the inner products, it is convenient to look at their pie charts. In Fig. 12.3, we show the pie charts for different SNRs, where the color bar represents the indices of the inner products. Take Fig. 12.3a for instance. The inner products $X_1,\ X_3,\ X_4$ contribute most part of the summation $\sum_{k=1}^{6} X_k$, while $X_2,\ X_5,\ X_6$ are much smaller. According to the criteria we designed before, only $X_1,\ X_3,\ X_4$ are above the threshold. Therefore, we obtain the index $101100_2 = 44$ of the template, which most resembles the signal in the data. Similarly, Fig. 12.3b–e all successfully identify the correct template in case of different SNRs. Figure 12.3f shows a failure case. According to the previous criteria, this pie chart gives a wrong index $101001_2 = 41$. In fact,

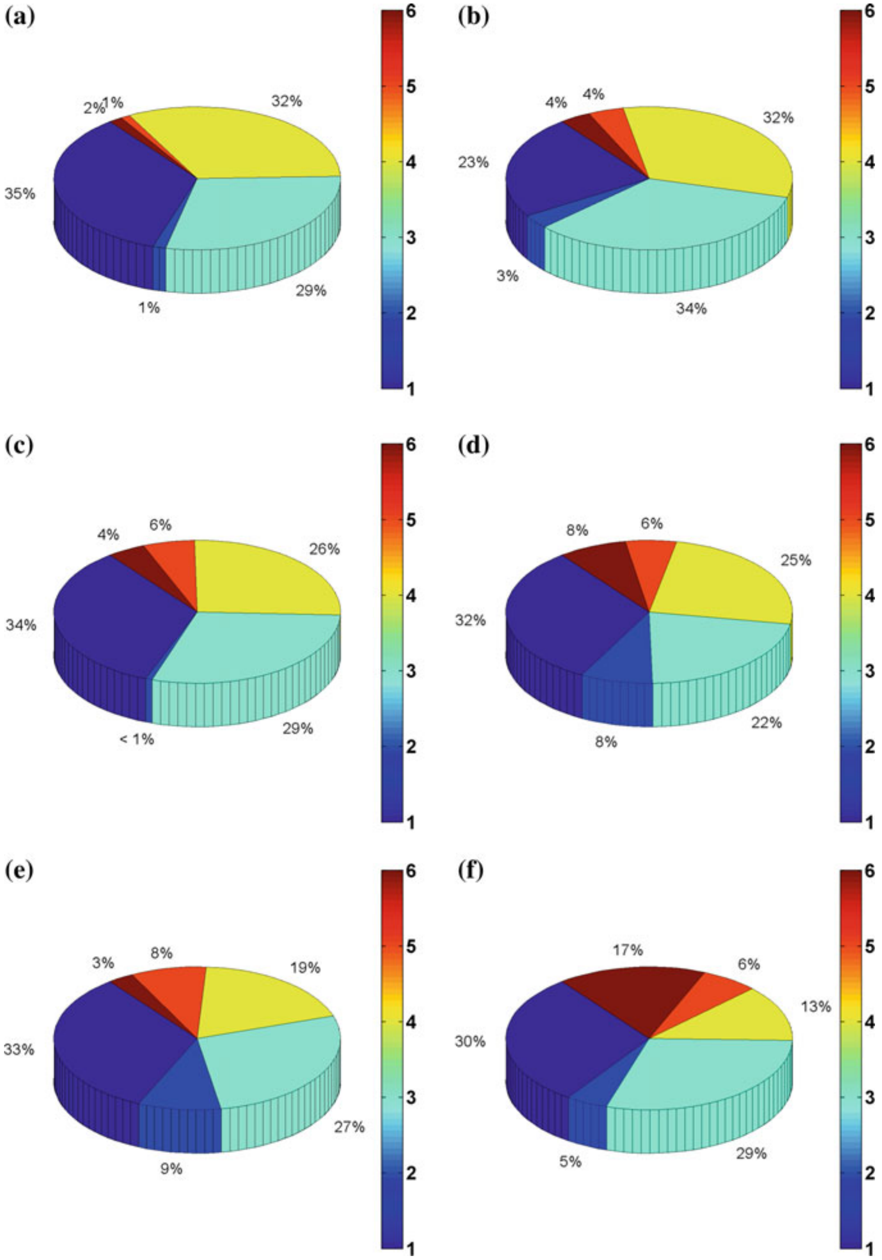

Fig. 12.3 Pie charts of X_k for different SNRs, **e** and **f** are for the same SNR with different noise realizations. The *color bar* denotes the index of X_k. **a** SNR = 50. **b** SNR = 40. **c** SNR = 30. **d** SNR = 20. **e** SNR = 10. **f** SNR = 10

even if one bit of the binary is wrongly determined, we end up with a completely different template (and its corresponding parameters). This is also a main reason why the detection rate at low SNRs drops so quickly. We will discuss how to improve the performance of the algorithm in the next section.

12.6 Improve the Performance of the Algorithm

In this section, we will discuss a simple and straightforward way to improve the performance of the algorithm by slightly increasing the computational cost. Let us look at the failure case in Fig. 12.3f again. The largest inner product is X_1, which contributes 30 % of the entire SNR pie. The threshold, which was set to half of the largest inner product, turns out to be 15 %. Therefore, among the six inner products, $X_1,\ X_3$ are significantly above the threshold, $X_2,\ X_5$ are significantly below, while $X_4,\ X_6$ are close to the threshold. In the end, the binary bits corresponding to X_4 and X_6 were determined wrongly, which leads to a detection failure. However, the binary bits corresponding to $X_1,\ X_2,\ X_3$ and X_5 are correctly determined, and we are confident about that in the blind search. In fact, we are not so confident about the bits corresponding to X_4 and X_6, since they are just slightly above or below the threshold. If we leave these two binary bits undetermined, we end up with a binary number $101\mathrm{y}0\mathrm{y}_2$, where we have used y to denote undetermined bits. It implies that the true signal might match one of the four templates $101000_2 = 40$, $101100_2 = 44$, $101001_2 = 41$ and $101101_2 = 45$. By simply calculating the inner products of the data and these four templates, we will know which one matches the true signal.

Hence, we can modify the algorithm according to the above procedure. In the beginning, we calculate X_k, $(k = 1, \ldots, 6)$ and the threshold $\mathcal{T} = c \cdot \max(X_k)$. Then, we identify two X_k, which are closest to the threshold $\mathcal{T}$, and leave two binary bits corresponding to these two X_k undetermined. We determine other binary bits in the same way as before. A binary number with two unknown bits is thus constructed. It corresponds to four original templates h_i. In the end, we calculate the inner product between the data and these four templates, and detect the signal. Following this procedure, we carry out a similar simulation as before. The detection rate is plotted in Fig. 12.4 with different combinations of c values and SNRs. Comparing with Fig. 12.1, the modified algorithm has significantly improved the performance. The detection rate is increased at all SNRs. We also observe that $c = 0.5$ is still the optimal choice. For the curve $c = 0.5$, the detection rate is 100 % above SNR 30 and 96 % at SNR = 20. This strategy can be easily generalized by assigning a probability to each binary bit according to X_k, hence obtaining the probability of each h_i present in the data. We reserve this for the future work.

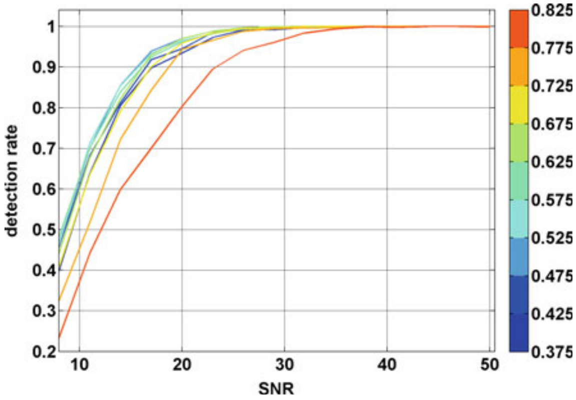

Fig. 12.4 Detection rate at different SNRs and thresholds. The *color bar* indicates the value of the coefficient *c*

12.7 Conclusion and Future Work

We have designed a novel algorithm for GW data analysis. Instead of using 2^N normal waveform templates, this new algorithm uses only N combinations of the original waveforms as the new templates. By calculating the inner products between these N new templates with the data and comparing these inner products with some threshold, we can construct a binary number with N bits. From this binary number, we can determine which normal template in the original template bank best matches the signal in the data, without any reconstruction process. Therefore, this new algorithm can greatly reduce the computational cost in certain circumstances. However, it requires relatively high SNRs. We have discussed a simple and straightforward way to improve the performance of the algorithm. By leaving two most unconfident binary bits undetermined and calculating four additional inner products, we can significantly improve the performance of the algorithm at low SNRs. The detection rate of the modified algorithm is 100 % for 1000 different noise realizations for each SNR larger than 25. For SNR lower than 25, further improvements are demanded. We reserve that for future work.

One possible way to improve the algorithm is to construct additional H_k, $(k = N+1, \ldots)$ for auxiliary use, such as to determine unconfident binary bits, to suppress the noise in X_k, etc. One can also set more sophisticated thresholds. We have used a threshold only depending on the relative values between the inner products X_k for simplicity. A threshold also depending on the absolute values of the inner products would help, since the probability distribution of the random part of X_k depends only on the absolute SNRs.

We have only carried out simulations for a bank of nearly independent templates. In the future, we will do a simulation for an entire template bank. The correlation between templates need also to be studied, since it could be used to reduce the noise in the detection statistic.

References

1. B.S. Sathyaprakash, B.F. Schutz, Physics, astrophysics and cosmology with gravitational waves. Living Rev. Relativ. **12**, 2 (2009). arXiv:0903.0338. http://www.livingreviews.org/lrr-2009-2
2. P. Jaranowski, A. Królak, Gravitational-wave data analysis. Formalism and sample applications: the Gaussian case. Living Rev. Relativ. **15**(4) (2012). http://www.livingreviews.org/lrr-2012-4
3. B. Owen, Search templates for gravitational waves from inspiraling binaries: choice of template spacing. Phys. Rev. D **53**, 6749 (1996)
4. S.E. Field et al., Reduced basis catalogs for gravitational wave templates. Phys. Rev. Lett. **106**, 221102 (2011)
5. K. Cannon et al., Singular value decomposition applied to compact binary coalescence gravitational-wave signals. Phys. Rev. D **82**, 044025 (2010)
6. I.S. Heng, Rotating stellar core-collapse waveform decomposition: a principal component analysis approach. Class. Quantum Gravity **26**, 105005 (2009)
7. E.J. Candes, T. Tao, Near-optimal signal recovery from random projections: universal encoding strategies? IEEE Trans. Inf. Theory **52**, 12 (2006)

Chapter 13
Likelihood Transform: Making Optimization and Parameter Estimation Easier

Abstract Parameterized optimization and parameter estimation is of great importance in almost every branch of modern science, technology and engineering. A practical issue in the problem is that when the parameter space is large and the available data is noisy, the geometry of the likelihood surface in the parameter space is complicated. This makes searching and optimization algorithms computationally expensive, sometimes even beyond reach. In this chapter, we define a likelihood transform (LT) which can make the structure of the likelihood surface much simpler, hence reducing the intrinsic complexity and easing optimization significantly. We demonstrate the properties of LT by applying it to a toy model in gravitational wave data analysis. For the signal with a signal-to-noise ratio 20, LT has made a deterministic template-based search possible for the first time, which turns out to be much more efficient than an exhaustive grid-based search. The method can also be directly applied to similar matched-filtering-based optimization and parameter estimation problems in other fields.

13.1 Introduction

Parameterized optimization and parameter estimation is a general important problem in almost every branch of modern science, technology and engineering [1–5]. The general problem can be described as follows. Let us denote $\boldsymbol{\theta} = (\theta^1, \theta^2, \ldots, \theta^k) \in \mathcal{P}$ as the parameters to be estimated, where $\mathcal{P}$ is the k-dimensional parameter space. The figure of merit $\mathcal{F}(\boldsymbol{\theta}, \mathbf{x}) \equiv \mathcal{M} \cdot (\boldsymbol{\theta}, \mathbf{x})$ is usually some functional of the parameters $\boldsymbol{\theta}$ and the data $\mathbf{x}$ (e.g. measurement data from experiments). In practice, the functional $\mathcal{M}$ can be viewed as a set of operations on the parameters $\boldsymbol{\theta}$ and the data $\mathbf{x}$. The goal is to find the best estimate $\boldsymbol{\theta}_*$ that maximizes the functional $\mathcal{F}(\boldsymbol{\theta}_*, \mathbf{x})$. Since minimization can be cast into maximization by just adding a minus sign, we will focus only on maximization problems. Also, for brevity, we omit $\mathbf{x}$ and denote $\mathcal{F}(\cdot, \mathbf{x})$ as $\mathcal{F}(\cdot)$ from now on. The mapping $\mathcal{M} \cdot (\cdot, \mathbf{x})$ from $\boldsymbol{\theta}$ to $\mathcal{F}$ defines a hypersurface in

Y. Wang, *First-stage LISA Data Processing and Gravitational Wave Data Analysis*,
Springer Theses, DOI 10.1007/978-3-319-26389-2_13

the k-dimensional parameter space $\mathcal{P}$. Hereafter, we refer it as the *likelihood surface* in general, although sometimes it does not have to be related to the likelihood.

By definition, the likelihood surface should peak at the best estimate θ_*. When the peak is broad and smooth, there are less structures in this region. Hence, the search is relatively easy and the resolution is poor (i.e. the error bar in the estimate is large). When the peak is sharp and narrow, the resolution is high, but the search is much more difficult. In general, the structure of the likelihood surface determines the difficulty of the optimization problem. By modifying the surface structure, we may alter the innate difficulty of the problem.

13.2 Likelihood Transform

We introduce a set of functionals $\mathcal{Y}_\varpi$ acting on the mapping functional $\mathcal{M}$, where ϖ can be either a scalar variable or a set of variables.

$$\begin{aligned}\mathcal{F}_\varpi(\cdot) &\equiv \mathcal{Y}_\varpi[\mathcal{M}(\cdot, \mathbf{x})]\\ &= (\mathcal{Y}_\varpi\mathcal{M})(\cdot, \mathbf{x}),\end{aligned} \tag{13.1}$$

By varying ϖ, we obtain a set of modified likelihood surfaces $\mathcal{F}_\varpi(\cdot)$. We want to find a proper set of functionals $\mathcal{Y}_{\varpi(l)}$, where the index $l \in [0, l_*] \subset \mathbb{R}$, such that as l running from l_* to 0, $\mathcal{Y}_{\varpi(l)}$ modifies the sharp narrow peak at the best estimate θ_* gradually (or continuously) to broader and smoother hills. We require that $\mathcal{Y}_{\varpi(l_*)}$ is a unity functional, i.e. $\mathcal{F}_{\varpi(l_*)}(\cdot) = \mathcal{F}(\cdot)$. When such a proper set of functionals is identified, one can search on the broadest and smoothest likelihood surface, $\mathcal{F}_{\varpi(0)}(\cdot)$, since its (local) maximum θ_ϖ is usually easiest to find. Notice that this maximum θ_ϖ needs not to be the global maximum on the modified likelihood surface and it needs not to be exactly at θ_*. However, as l going from 0 to l_*, θ_ϖ should gradually converge to θ_* due to the continuity of the transform. This means after identifying the maximum $\theta_{\varpi(0)}$ in the smoothest likelihood surface, the transform $\mathcal{Y}_{\varpi(l)}$ can help lead us to the best estimate θ_*.

Following the conventions [6] used by the gravitational wave (GW) data analysis community, it is convenient to define the inner product of two time series $a(t), b(t)$ as below

$$\langle a|b\rangle = \int_{-\infty}^{\infty} \frac{\tilde{a}^*(f)\tilde{b}(f)}{S_n(f)} df, \tag{13.2}$$

where $\tilde{a}(f), \tilde{b}(f)$ are the Fourier transforms of $a(t)$ and $b(t)$. $S_n(f)$ is the so-called two-sided power spectral density of Gaussian noise, usually defined as $E[\tilde{n}^*(f')\tilde{n}(f)] = S_n(f)\delta(f - f')$.

We denote the normalized GW waveform with parameters θ by $h(\theta, t)$, thus $\langle h(\theta)|h(\theta)\rangle = 1$. The measured data $x(t)$ containing a GW signal with parameters θ_*

and Gaussian noise $n(t)$ can be expressed as $x(t) = Ah(\theta_*) + n(t)$, where A is the strength of the signal.

The figure of merit is the signal-to-noise ratio (SNR)

$$\begin{aligned}\mathcal{F}(\theta) &= \mathcal{M}(\theta, \mathbf{x}) \\ &\equiv \langle x | h(\theta) \rangle \\ &= \int_{-\infty}^{\infty} \frac{\tilde{x}^*(f)\tilde{h}(\theta, f)}{S_n(f)} df. \end{aligned} \tag{13.3}$$

Although $\mathcal{F}(\theta)$ here is not the likelihood, it is directly related to the likelihood $\mathcal{L}(\theta) \propto \exp[\mathcal{F}(\theta)^2/2]$. The functional $\mathcal{M}$ can be interpreted as two operations: first, to generate a waveform with parameters θ; second, to calculate the inner product of this waveform and the data $\mathbf{x}$. Usually, $\mathcal{F}(\cdot)$ has a sharp narrow peak at the best estimate θ_*. As an example, we define the functionals $\mathcal{Y}_\sigma$ as convolution operators

$$\begin{aligned}\mathcal{F}_\sigma(\theta) &= (\mathcal{Y}_\sigma \mathcal{M})(\theta, \mathbf{x}) \\ &\equiv \langle x | (\mathcal{K}_\sigma \star h)(\theta) \rangle \\ &= (\mathcal{K}_\sigma \star \mathcal{F})(\theta), \end{aligned} \tag{13.4}$$

where $\mathcal{K}_\sigma$ is the kernel function. The last equality is because convolution is a linear operation and $\mathcal{F}(\theta)$ is linear in $h(\theta)$. Since the convolution can be viewed as a smoothing functional, the modified likelihood surface $\mathcal{F}_\sigma(\cdot)$ is smoother than the original one. For brevity's sake, we temporarily assume θ is a scaler parameter and choose the kernel function as one-dimensional Gaussian function $\mathcal{K}_\sigma = \frac{1}{\sqrt{2\pi}\sigma} \exp(-\frac{\theta^2}{2\sigma^2})$. The argument below can be trivially generalized to multi-dimensional case. When σ is large, the kernel is a very broad Gaussian function, hence making the likelihood surface $\mathcal{F}_\sigma(\cdot)$ very smooth. As σ decays to 0, $\mathcal{F}_\sigma(\cdot)$ converges to the original likelihood surface $\mathcal{F}(\cdot)$. Notice that when $\sigma \to 0$, we have $\mathcal{K}_\sigma \to \delta(\theta)$. In practice, we can set $\sigma(l) = \sigma(0)(l_* - l)/l_*$. As l goes from 0 to l_*, $\mathcal{F}_{\sigma(l)}(\cdot)$ evolves gradually from very smooth modified likelihood surface to the original likelihood surface.

From another point of view, $\mathcal{K}_\sigma \star h(\theta)$ in Eq. 13.4 is just a weighted average of many waveforms. Since waveforms with similar parameters are correlated, by using a summation of nearby waveforms one can smooth the original likelihood surface. As the number of averaged waveforms goes to 1, the modified likelihood surface converges to the original likelihood surface.

13.3 How to Use Likelihood Transforms

Likelihood transform $\mathcal{Y}_{\sigma(l)}$ can gradually modify the likelihood surface, hence changing the intrinsic complexity of the optimization problem. In the meantime, it retains the relation between the modified likelihood surfaces and the original likelihood surface. Therefore, likelihood transform can be used in many ways. For instance, it can accelerate stochastic optimization methods, such as Markov chain Monte Carlo [7, 8], particle swarm optimization [8, 9], genetic algorithm [8, 10, 11], etc. It can help design hierarchical search algorithms. In some circumstances, it can even make a deterministic search possible.

13.3.1 Comparison with Simulated Annealing

Likelihood transform is different from simulated annealing [12], which is also a technique to accelerate stochastic optimization algorithms. In the following, we will compare the two. Simulated annealing employs a temperature parameter $\mathcal{T}$ to heat the likelihood surface from $\mathcal{L}(\boldsymbol{\theta}) \propto \exp[\mathcal{F}(\boldsymbol{\theta})^2/2]$ to $\exp[\mathcal{F}(\boldsymbol{\theta})^2/2\mathcal{T}]$. As the stochastic search algorithms proceed, the temperature cools down gradually. Therefore, the heuristics can escape from local maxima more easily and explore the whole parameter space more thoroughly, hence being accelerated. As an example, we simulated a sinusoidal signal with only one parameter $\omega = 0.2$ rad/s buried in white Gaussian noise. The SNR was 9. Figure 13.1a shows how simulated annealing gradually modifies the likelihood surface (or more rigorously the SNR surface). As seen from the figure, the likelihood surface is less spiky at high temperatures. Notice that the number of local maxima (including the global maximum) is the same at all temperatures, and the locations of these maxima are unchanged.

As for likelihood transform, it modifies the likelihood as $\exp[\mathcal{F}_{\boldsymbol{\sigma}(l)}(\boldsymbol{\theta})^2/2]$. For simplicity, we choose the functional $\mathcal{Y}_{\boldsymbol{\sigma}}$ to be convolution operators with a Gaussian kernel. We then applies it to the same simulated data. The modified likelihood surface $\mathcal{F}_{\boldsymbol{\sigma}(l)}(\boldsymbol{\theta})$ are shown in Fig. 13.1b. Notice that both the number of local maxima and their locations are changed by the likelihood transform. In addition, the likelihood surfaces are smoother with less structures comparing to the cases of simulated

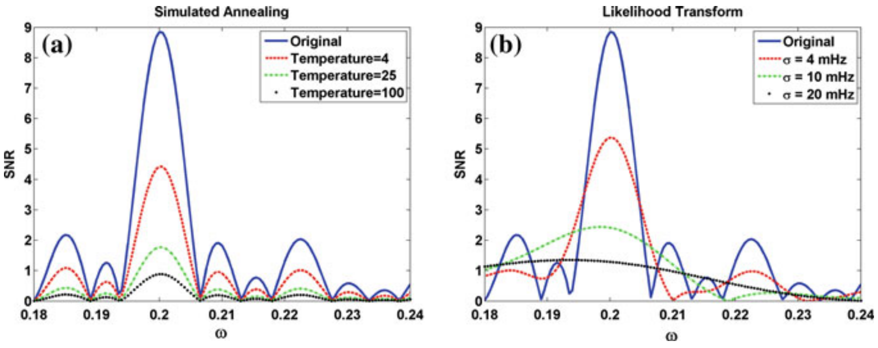

Fig. 13.1 A comparison of simulated annealing (**a**) and likelihood transform (**b**)

annealing. These features of likelihood transform may help accelerate the stochastic optimization algorithms more efficiently.

13.3.2 Manipulation of the Intrinsic Complexity of the Likelihood Surface

In this subsection, we applied likelihood transform to a toy model in gravitational wave data analysis. Although it is a somehow simplified model, it captures important features of the general problem and can demonstrate the method in a more general (less background-dependent) way.

Suppose the normalized gravitational wave chirp signal is in the following form

$$h(\boldsymbol{\theta}, t) = \sqrt{\frac{2}{T}} \cos[\omega_0 \alpha_0(t) + \omega_1 \alpha_1(t)], \tag{13.5}$$

where $\boldsymbol{\theta} = (\omega_0, \omega_1)$ are the two parameters to be estimated, the two time functions are defined as $\alpha_0(t) \equiv t - \frac{T}{2}$ and $\alpha_1(t) \equiv (t - \frac{T}{2})^2$, T is the total observation time, which we choose to be 5120 s in the simulation. We inject a signal with parameters $\omega_0 = 0.0628\,\text{rad/s}$, $\omega_1 = 6.136 \times 10^{-6}\,\text{rad/s}^2$. Notice that ω_0 is an angular frequency. The searching parameter ranges for ω_0 and ω_1 are $(\omega_0^{\text{low}}, \omega_0^{\text{upp}}) = (1.2\,\text{mrad/s}, 0.126\,\text{rad/s})$ and $(\omega_1^{\text{low}}, \omega_1^{\text{upp}}) = (-3.07 \times 10^{-6}\,\text{rad/s}^2, 1.23 \times 10^{-5}\,\text{rad/s}^2)$ respectively.

As an example, we use convolution operators as the functionals $\mathcal{Y}_{\boldsymbol{\sigma}}(l)$ and assume the kernel function to be a Gaussian function with diagonal covariance. Then, we have

$$\begin{aligned}
H_{\boldsymbol{\sigma}(l)}(\boldsymbol{\theta}) &= (\mathcal{K}_{\boldsymbol{\sigma}(l)} \star h)(\boldsymbol{\theta}), \\
&= \int\int \mathcal{K}[\omega_0 - \omega_0', \omega_1 - \omega_1', \sigma_0(l), \sigma_1(l)] \\
&\quad \cdot h(\omega_0', \omega_1') \mathrm{d}\omega_0' \mathrm{d}\omega_1', \\
&= h(\boldsymbol{\theta}) e^{-\frac{1}{2}[\sigma_0(l)^2 \alpha_0(t)^2 + \sigma_1(l)^2 \alpha_1(t)^2]}, \qquad (13.6) \\
\mathcal{F}_{\boldsymbol{\sigma}(l)}(\boldsymbol{\theta}) &= \langle x | H_{\boldsymbol{\sigma}(l)}(\boldsymbol{\theta}) \rangle. \qquad (13.7)
\end{aligned}$$

We set $l_* = 1$ and choose $(\sigma_0(l), \sigma_1(l)) = (1 - l)(\omega_0^{upp} - \omega_0^{low}, \omega_1^{upp} - \omega_1^{low})$ to be a fraction of the entire searching parameter range. We will see how this parameter l can modify the likelihood surface and adjust the difficulty of the optimization problem. In general, the difficulty of the search can be very well described by the required number of templates for a certain mismatch by template-based search. Following conventions, we set the mismatch to be 0.03. By calculating the metric of the likelihood surface on the parameter space [13], it's straightforward to estimate the number of templates required by optimal layout (we choose rectangular layout here). When $l = l_* = 1$, we

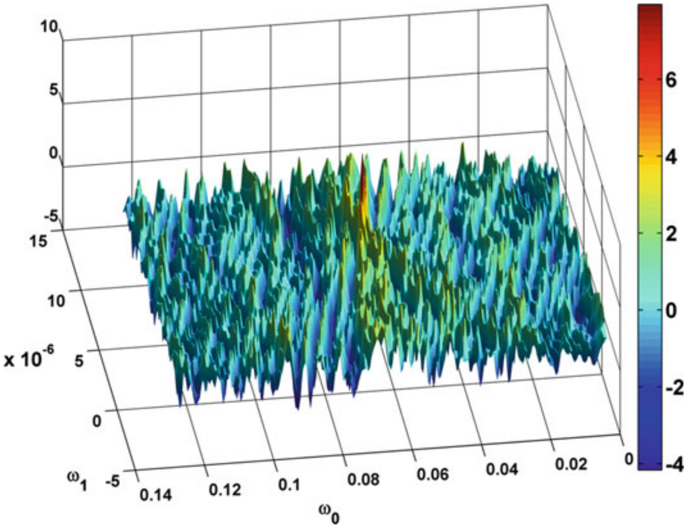

Fig. 13.2 The original likelihood surface $\mathcal{F}(\omega_0, \omega_1)$. It peaks at the true signal parameter with an optimal SNR 8. It is very fluctuant. Optimal template layout requires 69,620 templates

have the original likelihood surface $\mathcal{F}(\omega_0, \omega_1)$ shown in Fig. 13.2. On this likelihood surface, the optimal layout requires 69,620 templates. This large required number is due to the noise-like features of the likelihood surface.

The structure of the likelihood surface can be greatly simplified through the likelihood transform. Figure 13.3a–d shows the several transformed likelihood surfaces $\mathcal{F}_{\varpi(l)}(\omega_0, \omega_1)$ with different values of l. When $l = 3/4$, the modified likelihood surface is very smooth. It is extremely simple to characterize the structure of this likelihood surface or find its maximum. As l increases, more and more structures appear on the likelihood surface $\mathcal{F}_{\varpi(l)}(\omega_0, \omega_1)$. It gradually converges to the original likelihood surface $\mathcal{F}(\omega_0, \omega_1)$. These figures show how the difficulty of the optimization problem can be modified by the likelihood transform. More precisely, we have calculated the required number of templates for different values of l in Fig. 13.4.

For $1 - l > 0.1$, the 0.03-mismatch rule gives an error rectangular, which is comparable to the area of the entire search parameter space. However, the error rectangular may have very different shape from the search parameter space. Therefore, in $1 - l > 0.1$ region, the required number of templates shown in Fig. 13.4 only serves as a rough estimate of the complexity of the modified likelihood surface. In the more interesting $1 - l < 0.1$ region, the dependence of the required number on $1 - l$ roughly follows a power law. The required number decreases rapidly in this region, hence the difficulty of search decreases rapidly.

These features of likelihood transform can potentially help the optimization algorithms. For example, it may help in the design of efficient hierarchical algorithms to search for GW signals.

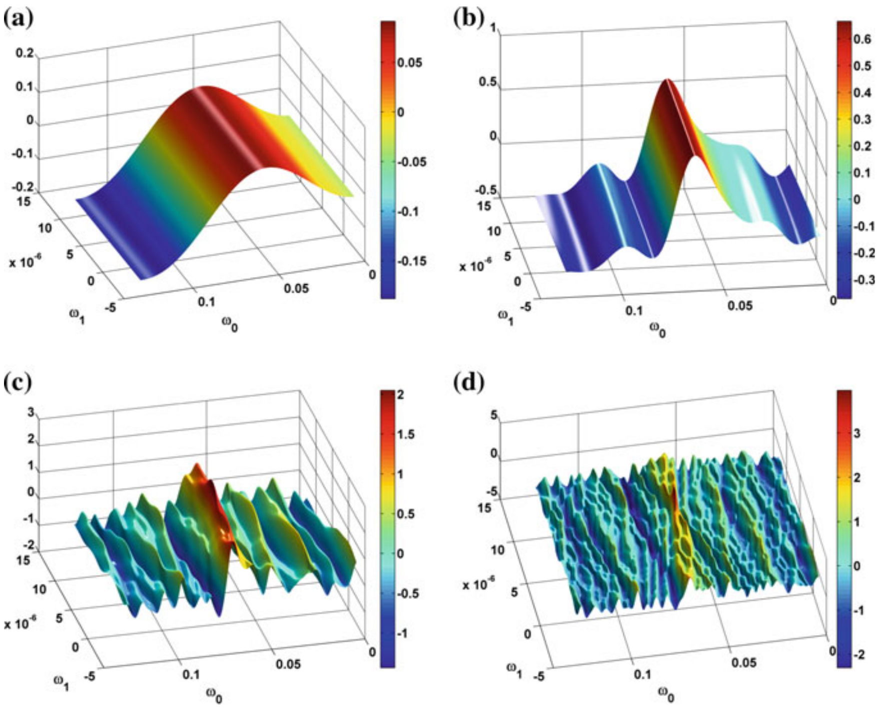

Fig. 13.3 The modified likelihood surfaces $\mathcal{F}_{\sigma(l)}(\omega_0, \omega_1)$ after likelihood transforms. **a** $1 - l = 1/4$. **b** $1 - l = 1/16$. **c** $1 - l = 1/64$. **d** $1 - l = 1/128$

Fig. 13.4 Number of templates required by the optimal layout for different values of l. Notice that the original case $l = 1$ is not plotted here

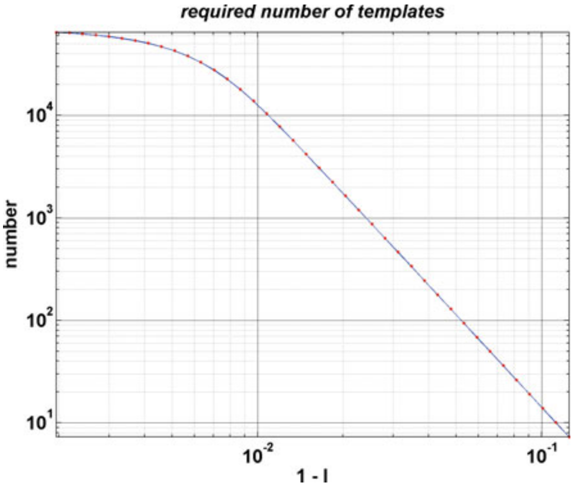

13.3.3 A Deterministic Search

In this subsection, we will show that in some cases the likelihood transform can even make deterministic optimization methods such as Newton's method possible. Hence, the search algorithm will be much more efficient.

In the neighbourhood of a (local) maximum $\mathbb{\theta}_{\varpi(l)}$ on modified likelihood surface $\mathcal{F}_{\varpi(l)}(\cdot)$, the geometry can be described by a Taylor series

$$\mathcal{F}_{\varpi(l)}(\mathbb{\theta}_{\varpi(l)} + \Delta\mathbb{\theta}) = \mathcal{F}_{\varpi(l)}(\mathbb{\theta}_{\varpi(l)}) + \frac{1}{2}\frac{\partial^2 \mathcal{F}_{\varpi(l)}}{\partial\theta^\mu \partial\theta^\nu}\Delta\theta^\mu \Delta\theta^\nu + \mathcal{O}(\Delta\mathbb{\theta}^3). \tag{13.8}$$

where we have assumed the Einstein summation convention. The first derivative vanishes and the modified Fisher information matrix $I^{\varpi(l)}_{\mu\nu} = -\frac{\partial^2 \mathcal{F}_{\varpi(l)}}{\partial\theta^\mu \partial\theta^\nu}|_{\mathbb{\theta}=\mathbb{\theta}_{\varpi(l)}}$ is positive definite due to the fact that $\mathcal{F}(\mathbb{\theta}_{\varpi(l)})$ is a maximum stationary point. Notice that, when $l = l_*$, the Taylor expansion is on the original likelihood surface around the best estimate $\mathbb{\theta}_*$, and $I_{\mu\nu} = I^{\varpi(l*)}_{\mu\nu} = -\frac{\partial^2 \mathcal{F}}{\partial\theta^\mu \partial\theta^\nu}|_{\mathbb{\theta}=\mathbb{\theta}_*}$ is the Fisher information matrix at the best estimate $\mathbb{\theta}_*$. For each modified likelihood surface $\mathcal{F}_{\varpi(l)}(\cdot)$, there exists a neighbourhood $\mathcal{B}_l \subseteq \mathcal{P}$ of $\mathbb{\theta}_{\varpi(l)}$ where the geometry of the likelihood surface can be approximated by a quadratic form quite well (say, the percentage error caused by higher order term is less 1 %). According to our design, the smaller the l the smoother the modified likelihood surface $\mathcal{F}_{\varpi(l)}(\cdot)$, hence the larger the neighbourhood $\mathcal{B}_l$. Sometimes, $\mathcal{B}_0$ can be as large as the entire parameter space $\mathcal{P}$.

Starting from any point $\mathbb{\theta}'_l \in \mathcal{B}_l$ on modified likelihood surface $\mathcal{F}_{\varpi(l)}(\cdot)$, one can easily find the best estimate $\mathbb{\theta}_{\varpi(l)}$ via some deterministic local-search algorithms. For instance, by neglecting higher order terms in Eq. 13.8 and differentiating both sides with respect to θ^ν, we get

$$\frac{\partial \mathcal{F}_{\varpi(l)}(\mathbb{\theta}'_l)}{\partial\theta^\nu} = \frac{\partial^2 \mathcal{F}_{\varpi(l)}}{\partial\theta^\mu \partial\theta^\nu}\Delta\theta^\mu. \tag{13.9}$$

Thus, we calculate the best estimate in just one step

$$\begin{aligned}\theta^\mu_{\varpi(l)} &= \theta'^\mu_l - \Delta\theta^\mu \\ &= \theta'^\mu_l - \left[\frac{\partial^2 \mathcal{F}_{\varpi(l)}}{\partial\theta^\mu \partial\theta^\nu}\right]^{-1} \frac{\partial \mathcal{F}_{\varpi(l)}(\mathbb{\theta}'_l)}{\partial\theta^\nu},\end{aligned} \tag{13.10}$$

where $\frac{\partial^2 \mathcal{F}_{\varpi(l)}}{\partial\theta^\mu \partial\theta^\nu}$ is constant in $\mathcal{B}_l$, so it can be calculated at $\mathbb{\theta}'_l$. Observe that as l gradually runs from 0 to l_*, $\mathcal{B}_l$ shrinks smoothly. Also, since $\mathcal{B}_l$ is roughly a quadratic region, ϖ_l should be near the center of $\mathcal{B}_l$. So, there must exist a smaller region $\mathcal{B}_{l_1}$ (with $l_1 > l$) which contains $\mathbb{\theta}_{\varpi(l)}$ in it. One can take $\mathbb{\theta}_{\varpi(l)}$ as the starting point in $\mathcal{B}_{l_1}$ and repeat Eq. 13.10 to calculate the best estimate $\mathbb{\theta}_{\varpi(l_1)}$ on $\mathcal{F}_{\varpi(l_1)}(\cdot)$. By iterating the above process, one will find the best estimate $\mathbb{\theta}_*$ on the original likelihood surface $\mathcal{F}(\cdot)$.

Usually, we need to study the properties of the neighbourhood $\mathcal{B}_l$ in order to design an efficient deterministic algorithm. However, in some cases, likelihood transform

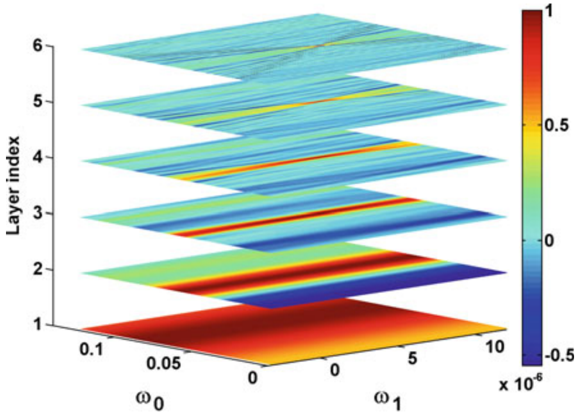

Fig. 13.5 A plot of six transformed likelihood surfaces $\mathcal{F}_{\varpi(l)}$

can change the likelihood surface to be so smooth and regular that we can simply choose a set of $\mathcal{Y}_\varpi$ to perform a deterministic search. As an example, we still use the waveform model introduced in the last subsection and set the SNR to 20. Six transformed likelihood surfaces are shown in Fig. 13.5. Notice that the global maxima on these surfaces are normalized to 1. We start from 10 points in the parameter space uniformly sampled in ω_0 with random ω_1. Then, we calculate the values of $\mathcal{F}_\varpi(\mathbb{\theta})$ at these 10 points on the smoothest transformed likelihood surface. The maximum among these 10 points is set as the initial location for the Newton's method with 10 iterations. Figure 13.6 shows the simulation result of this deterministic algorithm. After 7 iterations, this algorithm converges to the location of the global maximum of the original likelihood surface. In this process, we have only used a few tens of templates. Comparing to 69,620 templates required by a grid-based search algorithm, the deterministic algorithm is about 1,000 times more efficient.

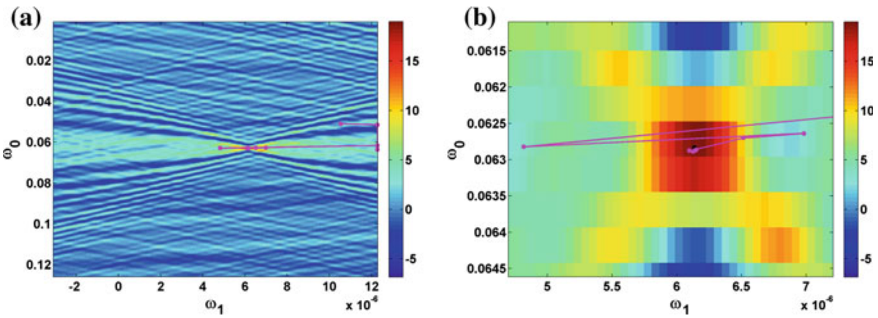

Fig. 13.6 A deterministic search with the help of likelihood transform. The *pink points* identify the trajectory of $\theta^{\mu}_{\varpi(l)}$ (**b**) is a zoom-in version of (**a**)

13.4 Discussion and Further Work

We have introduced the likelihood transform as a general tool to make optimization and parameter estimation easier. The likelihood transform can gradually transform the likelihood surface to a smoother shape with less complex structure. On these modified likelihood surfaces, the local and global maxima are much easier to find. Since these modified likelihood surfaces are directly related to the original likelihood surface by the likelihood transform, one can find the global maximum of the original likelihood surface more efficiently based on knowledge of the transformed likelihood surfaces. We have shown the possibility to use likelihood transform to accelerate stochastic optimization methods. Compared to simulated annealing, likelihood transform gives indications that it would accelerate the heuristics more efficiently. We applied likelihood transform to a GW data analysis problem with a toy waveform model. Simulation results show that likelihood transform can manipulate the structure of the original likelihood surface, hence allowing it to combine with and accelerate a hierarchical search. We have also shown that for the toy waveform model with $\text{SNR} = 20$, likelihood transform make a deterministic search possible, which turns out to be 1,000 times more efficient than the exhaustive grid-based search for GW signals. With the help of likelihood transform, a template-based deterministic search for GW signals is shown to be possible for the first time.

In this work, we have only considered linear functionals, or more specifically, convolutions with Gaussian kernels with uncorrelated covariances. In the future, we will study other linear functionals and even nonlinear functionals $\mathcal{Y}_{\sigma}$, which would potentially exhibit better properties.

References

1. E. Poisson, C.M. Will, Phys. Rev. D **52**, 848–855 (1995)
2. K. Tamura et al., Mol. Biol. Evol. **28**(10), 2731–2739 (2011)
3. T. Bollerslev, J.M. Wooldridge, Econ. Rev. **11**(2), 143–172 (1992)
4. R.O. Schmidt, IEEE Trans. Antennas Propag. **34**(3), 276–280 (1986)
5. S. Johansen, K. Juselius, Oxf. Bull. Econ. Stat. **52**(2), 169–210 (1990). May
6. P. Jaranowski, A. Królak, Gravitational-wave data analysis. Formalism and sample applications: the gaussian case. Liv. Rev. Relativ. 15(4) (2012), http://www.livingreviews.org/lrr-2012-4
7. T.B. Littenberg, N.J. Cornish, Phys. Rev. D **80**, 063007 (2009). arXiv:gr-qc/0902.0368
8. Y. Wang, Y. Shang, S. Babak, Phys. Rev. D **86**, 104050 (2012)
9. Y. Wang, S.D. Mohanty, Phys. Rev. D **81**, 063002 (2010). arXiv:gr-qc/1001.0923
10. J. Crowder, N.J. Cornish, L. Reddinger, Phys. Rev. D **73**, 063011 (2006). arXiv:gr-qc/0601036
11. A. Petiteau, Y. Shang, S. Babak, F. Feroz, Phys. Rev. D **81**, 104016 (2010). arXiv:gr-qc/1001.5380
12. S. Kirkpatrick, C.D. Gelatt Jr, M.P. Vecchi, Science **220**(4598), 671–680 (1983). 13 May 1983
13. B. Owen, Search templates for gravitational waves from inspiraling binaries: choice of template spacing. Phys. Rev. D **53**, 6749 (1996). June

Index

Y. Wang, *First-stage LISA Data Processing and Gravitational Wave Data Analysis*,
Springer Theses, DOI 10.1007/978-3-319-26389-2